EPFL

Thèse n° 10 364

Using Complex Hydrides for Hydrogen Storage and Direct Borohydride Fuel Cells for Electricity Production

Présentée le 17 février 2023

Faculté des sciences de base
Laboratoire des matériaux pour les énergies renouvelables
Programme doctoral en chimie et génie chimique

pour l'obtention du grade de Docteur ès Sciences

par

Youngdon KO

Acceptée sur proposition du jury

Prof. B. Smit, président du jury
Prof. A. Züttel, directeur de thèse
Prof. V. Ramani, rapporteur
Prof. M. Chatenet, rapporteur
Dr J. Van Herle, rapporteur

École polytechnique fédérale de Lausanne

2023

Acknowledgements

I would like to thank a number of people for their assistance and support for my Ph.D. journey and writing of this thesis. Firstly, many thanks to my thesis director, Prof. Andreas Züttel, for giving me opportunity to work in his lab. Numerous scientific instruments, sufficient resources, scientific discussion, and direction for presenting the results would be of great benefit. He often creates group excursion for hiking and skiing to foster group interaction and refresh the mind. In addition, I could participate in a number of international conferences to share research findings and gain insight from the discussions. He gave me the most latitude to explore any scientifically intriguing topics or questions. It affords Ph.D. candidates the opportunity to engage in scientifically challenging work and accomplishments involving problem-solving and exploration.

As the jury members, Prof. Berend Smit, Dr. Jan Van Herle, Prof. Vijay Ramani, and Prof. Marian Chatenet accepted the review and evaluation of my thesis. I appreciate them taking the time to read my thesis and provide feedback.

I would like to thank Dr. Loris Lombardo for his assistance in both the scientific and social aspects of my life in Switzerland. At the beginning of my Ph.D. studies, he taught me how to use a variety of laboratory instruments and provided me with helpful advice. We always had fruitful discussions in the laboratory and beyond. I also value the time we spend in the lab repairing and resolving the issue together. It was also a great time to attend multiple conferences and trips together.

I'd like to express my appreciation to Dr. Liping Zhong. We might be able to find opportunities for collaboration and assistance from sources outside of EPFL thanks to her extensive network. In addition to scientific collaboration with her, other activities outside of the lab make life in Sion enjoyable.

Thank you to Ms. Thi Ha My Pham, who joined the group one year after I did. Not only were lab discussions on electrochemistry interesting and insightful, but we also had a great time participating in numerous activities. She frequently prepares delicious foods and cookies that bring a little joy.

When I joined the group, Dr. Heena Yang helped me in obtaining an interview opportunity and introduced me to the lab. She was my co-supervisor until she left EPFL to pursue her future career. She organized several activities outside the lab to bring people together and integrate the group.

Numerous colleagues and collaborators conducted multiple tests on hydrogen storage materials and direct borohydride fuel cells. Dr. Xiong Zhang is responsible for synthesizing the M-N-C materials. Mr. Junkil Park performed DFT calculations for M-N-C materials' durability. Dr. Liqun Kang measured and analyzed XAS data. Dr. Loris Lombardo teached me with a number of measurements, including DSC, XRD, PCT, and NMR. Dr. Mo Li and Dr. Liping Zhong exerted considerable effort in measuring XPS samples. The SEM and TEM images were measured by Dr. Emad Oveisi, Dr. Victor Boureau, and Ms. Thi Ha My Pham. Dr. Jie Zhang and Dr. Wen Luo always responded to my questions relating electrochemistry. Ms. Yasemen Kuddusi assisted me with XAS measurement in HZB. Dr. Pascal Alexander Schouwink instructed me on the XRD. Training in ICP and NMR from Dr. Natalia Gasilova and Dr. Aurélien Bornet.

During my time in the lab, I also value the presence of other people. Although they are not directly involved in my project, their assistance in the lab is crucial. Dr. Kun Zhao, Mr. Alexandre Borsay, Ms. Pamela Canjura, Dr. Marco Calizzi, Dr. Emanuele Moioli, Dr. Robin Mutschler, and Mr. Yannick Baehler are thanked.

I would like to express my gratitude to Prof. Hobeom Kim, my mentor and pledge brother in Sion. We have fond memories of living abroad and relying on one another for the majority of three years. During my Ph.D. studies, I found many of his insights to be extremely helpful. I also thanks to Mr. Kuang-Jung Hsu. He always has positive energy and patience. We enjoyed our time discussing science and life. In addition, I made many enjoyable memories with members of the Korean community at EPFL.

During my research at EPFL Valais, the assistance of numerous staff members was indispensable and greatly valued. Mr. Stéphane Voeffray and Mr. Robin Délèze are thanked for manufacturing a customized system. Mr. Dennis Ellersiek assisted in the repair of the fuel cell system's electronics. I would like to express my gratitude to Mrs. Ivana Suter, who has always assisted me with numerous requests and complicated paperwork.

I am also grateful to my family, for the endless love and support they have given me throughout my life. With the encouragement and support of many people, I was able to complete my Ph.D. journey.

I gratefully acknowledge the financial support from EPFL, EMPA, and the Swiss Competence Center for Energy Research (SCCER) project.

Sion, 1st December 2022

Abstract

Hydrogen storage and utilization are the technologies to achieve carbon-neutral energy systems with renewable energy sources. The storage and transport of hydrogen is a significant barrier to closing the global energy demand-supply gap. Currently, the high-pressure hydrogen tank and liquid hydrogen are the primary and only methods for transporting hydrogen to a different location. The demand for safe and high-density hydrogen storage methods increasing attention such as material-based hydrogen storage. To find and develop proper materials for hydrogen storage, it is necessary to understand the hydrogen adsorption/absorption mechanism with materials. Among the various materials that have been investigated, complex hydrides are a material exhibiting high gravimetric hydrogen density and operate with hydrogen in a reasonable temperature ranges (Room temperature to 200 °C). To establish a hydrogen-based clean energy system, it is necessary to develop both an electricity production technology using hydrogen and a hydrogen storage technology. Therefore, the objectives of this thesis are to understand the mechanism of the catalyzed hydrogen desorption of complex hydrides and to develop platinum group metal (PGM)-free catalysts for direct borohydride fuel cells (DBFCs). The specific objectives are as follows : (1) decreasing hydrogen release temperature and preventing material expansion on alanate complex hydrides using nickel with porous carbon sheets; (2) replacing palladium catalyst with facilely synthesized nickel catalyst on DBFC anode; (3) replacing platinum catalyst with atomically dispersed transition metal with nitrogen-doped carbon (M-N-C) materials and assessing durability; and (4) H_2O_2 production via 2-electron oxygen reduction reaction (ORR) and identification of the active site of atomically dispersed and nanoparticle cobalt.

Alanate materials, one of the complex hydrides, were investigated as a hydrogen storage material. The combination of nickel-containing porous carbon sheets (Ni-PCS) with various alanates decreased the hydrogen release temperature and prevented volume expansion upon decomposition. The interaction of alanates with Ni-PCS was investigated by means of in-situ X-ray diffraction. It turned out, that the Ni-PCS prevented volume expansion by allowing hydrogen to escape from the liquid layer. The catalytic activity of Ni-PCS is proportional to the electronegativity of the cation in M (Li, Na, or Mg) in $M(AlH_4)$. For cations with a lower electronegativity, the catalyst shows an increased activity.

The nickel catalyst for the DBFC anode was synthesized by precipitation and growth from solution on nickel foam. The nickel catalyst replaces costly palladium catalysts due to its high-selectivity and fuel utilization efficiency. Different types of ionomers regulate the local pH in the reaction. The selective catalytic activity of the nickel catalyst for the borohydride oxidation reaction (BOR) and the hydrogen oxidation reaction (HOR) are the most significant performance-determining factors. Furthermore, fuel utilization and H_2 evolution measurement in a membrane electrode assembly configuration provide information such as chemical energy to electricity conversion and limit of impure fuel usage on the complex anode reaction in DBFC.

The PGM-based catalysts were completely replaced with transition metal catalysts in DBFC. The M-N-C materials are used in the DBFC cathode for hydrogen peroxide reduction reaction (PRR). The Fe-N-C has higher activity on PRR than Co-N-C. Co-N-C is however more stable than Fe-N-C under DBFC operating conditions. Various characterization and DFT calculations are used to compare the degradation of M-N-C. In the DBFC durability test, Fe-N-C shows 18.6% performance loss after accelerated durability test, whereas Co-N-C shows a more stable performance only 6.7% performance loss.

Electrochemical hydrogen peroxide production via 2-electron ORR is demonstrated with Co-N-C catalysts. The H_2O_2 usage and production could be achieved reversibly on-site through the electrochemical reactions. The atomically dispersed CoN_4 site is known as high selective H_2O_2 production. The H_2O_2 production activity of nanoparticle Co and atomically dispersed Co are compared in acidic and alkaline electrolytes. The small amount of cation can influence the selectivity of H_2O_2 production and can differentiate the active site on nanoparticle Co and atomically dispersed Co. The selectivity of H_2O_2 production is enhanced on nanoparticle Co meanwhile, is decreased on atomically dispersed Co by the cation shielding effect.

This thesis promoted hydrogen storage and electricity production using complex hydrides and various catalysts. This knowledge has the potential to be implemented in small devices that generate decentralized electricity, heat energy, and chemical feedstock. This thesis contributes to a fundamental understanding of catalyst preparation for cost-effective hydrogen storage and utilization.

Keywords

Complex hydrides, Electrocatalysis, Direct borohydride fuel cells, Electrochemical hydrogen peroxide production, Nickel catalyst, Single atom catalyst, Fe-N-C, Co-N-C

Résumé

Le stockage et l'utilisation de l'hydrogène sont les technologies permettant de réaliser des systèmes énergétiques neutres en carbone avec des sources d'énergie renouvelables. Le stockage et le transport de l'hydrogène constituent un obstacle important à la réduction de l'écart entre la demande et l'offre énergétiques mondiales. Actuellement, le réservoir d'hydrogène à haute pression est la principale et unique méthode de transport d'hydrogène vers un autre endroit. La demande de méthodes de stockage d'hydrogène sûres et à haute densité attire l'attention, telles que le stockage d'hydrogène à base de matériaux. Pour trouver et développer des matériaux appropriés pour le stockage de l'hydrogène, il est nécessaire de comprendre le mécanisme d'adsorption/absorption de l'hydrogène avec les matériaux. Parmi les différents matériaux qui ont été étudiés, les hydrures complexes peuvent être un matériau candidat pour le stockage d'hydrogène à haute gravimétrie et utilisant des plages de température raisonnables pour l'hydrogène (température ambiante à 200 °C). Pour établir un système d'énergie propre à base d'hydrogène, il est nécessaire de développer à la fois une technologie de production d'électricité utilisant l'hydrogène et une technologie de stockage de l'hydrogène. Par conséquent, les objectifs de cette thèse sont de comprendre le comportement des hydrures complexes avec des catalyseurs et de développer des catalyseurs sans métaux du groupe du platine (PGM) pour les piles à combustible à borohydrure direct (DBFC). Les objectifs spécifiques sont les suivants : (1) diminuer la température de libération d'hydrogène et empêcher l'expansion du matériau sur les hydrures complexes d'alanate en utilisant du nickel avec des feuilles de carbone poreuses ; (2) remplacer le catalyseur au palladium par un catalyseur au nickel facilement synthétisé sur l'anode DBFC ; (3) remplacer le catalyseur au platine par un métal de transition dispersé de manière atomique par des matériaux de carbone dopé à l'azote (M-N-C) et évaluer la durabilité ; et (4) production de H2O2 via une réaction de réduction de l'oxygène à 2 électrons (ORR) et identification du site actif du cobalt atomiquement dispersé et des nanoparticules.

Les matériaux d'alanate, l'un des hydrures complexes, ont été étudiés en tant que matériau de stockage d'hydrogène. La combinaison de feuilles de carbone poreux contenant du nickel (Ni-PCS) avec divers alanates a diminué la température de libération d'hydrogène et a empêché l'expansion volumique lors de la décomposition. La diffraction des rayons X in situ a révélé l'interaction des alanates avec le Ni-PCS. Ni-PCS a empêché les changements de couche en permettant à l'hydrogène de s'échapper de la couche liquide. L'activité catalytique de Ni-PCS est proportionnelle à l'électronégativité du cation dans M (Li, Na ou Mg) dans $M(AlH_4)$. Lorsque les cations ont une électronégativité plus faible, l'effet du catalyseur est plus important.

Le catalyseur au nickel pour l'anode DBFC a été synthétisé à l'aide d'une méthode simple et directe sur de la mousse de nickel. Le catalyseur au nickel peut remplacer les coûteux catalyseurs au palladium en raison de sa sélectivité élevée et de son efficacité d'utilisation du carburant. Différents types d'ionomères régulent les conditions locales de pH. Les activités catalytiques sélectives du catalyseur au nickel pour la réaction d'oxydation du borohydrure (BOR) et la réaction d'oxydation de l'hydrogène (HOR) sont les facteurs déterminants de performance les plus importants. De plus, la mesure de l'utilisation du carburant et de l'évolution de H_2 dans une configuration d'assemblage d'électrodes à membrane fournit plus d'informations sur la réaction complexe de l'anode dans le DBFC.

Ensuite, les catalyseurs à base de PGM sont totalement remplacés par des catalyseurs à base de métaux de transition dans le DBFC. Les matériaux M-N-C sont utilisés dans la cathode DBFC pour la réaction de réduction du

peroxyde d'hydrogène (PRR). Le Fe-N-C a une activité plus élevée sur le PRR que le Co-N-C. Co-N-C est cependant plus stable que Fe-N-C dans les conditions de fonctionnement DBFC. Diverses methodes de carac-térisation et un calcul DFT sont utilisés pour comparer la dégradation du M-N-C. Durant les tests DBFC, Fe-N-C montre une perte de performance de 18,6 % après un test de durabilité accéléré, tandis que Co-N-C montre une performance plus stable avec seulement 6,7 % de perte de performance.

La production électrochimique de peroxyde d'hydrogène via ORR à 2 électrons est démontrée avec des catalyseurs Co-N-C. L'utilisation et la production de H_2O_2 pourraient être réalisées de manière réversible sur site grâce aux réactions électrochimiques. Le site CoN_4 atomiquement dispersé est reconnu comme production hautement sélective de H_2O_2. L'activité de production de H_2O_2 du Co nanoparticule et du Co atomiquement dispersé est comparée dans des électrolytes acides et alcalins. Une petite quantité de cations peut influencer la sélectivité de la production de H_2O_2 et peut différencier le site actif sur la nanoparticule Co et le Co dispersé atomiquement. La sélectivité de la production de H_2O_2 est améliorée sur la nanoparticule Co tandis q'elle est diminuée sur le Co dispersé atomiquement par l'effet de protection cationique.

Cette thèse a promu le stockage d'hydrogène et la production d'électricité à l'aide d'hydrures complexes et de divers catalyseurs. Ces connaissances ont le potentiel d'être mises en œuvre dans de petits appareils qui génèrent de l'électricité décentralisée, de l'énergie thermique et des matières premières chimiques. Cette thèse contribue à une compréhension fondamentale de la préparation des catalyseurs pour le stockage et l'utilisation rentables de l'hydrogène.

Mots-clés

Hydrures complexes, Électrocatalyse, Piles à combustible à borohydrure direct, Production électrochimique de peroxyde d'hydrogène, Catalyseur au nickel, Catalyseur à atome unique, Fe-N-C, Co-N-C

Contents

List of Figures

List of Tables

Chapter 1 Introduction

1.1 Energy source transition toward sustainable energy

Until now, most energy has been produced and supplied based on fossil fuels. Fossil fuels are mostly consumed for heat, electricity, and mobility. Consumption of fossil fuels releases carbon dioxide (CO_2) into the atmosphere and influences global climate change, which is exceeding the bounds of natural variability.[1] The increased atmospheric CO_2 concentration creates a great deal of unpredictability for the planet and its inhabitants because of an increase in catastrophic natural disasters. Comparing the global median temperature anomalies derived from the HadCRUT5 dataset and the atmospheric CO_2 concentration measured at the Mauna Loa Observatory from 1959 to 2021, Figure 1.1 reveals a trend in global warming that is concurrent with the increase in CO_2 concentration.[2,3] The International Panel on Climate Change from the United Nations issued a warning that exceeding a 1.5 °C temperature increase will result in unprecedented flooding, drought, rising sea level, heat waves, and famine.[4] The transition from a reliance on fossil fuels to renewable energy is more crucial than ever.

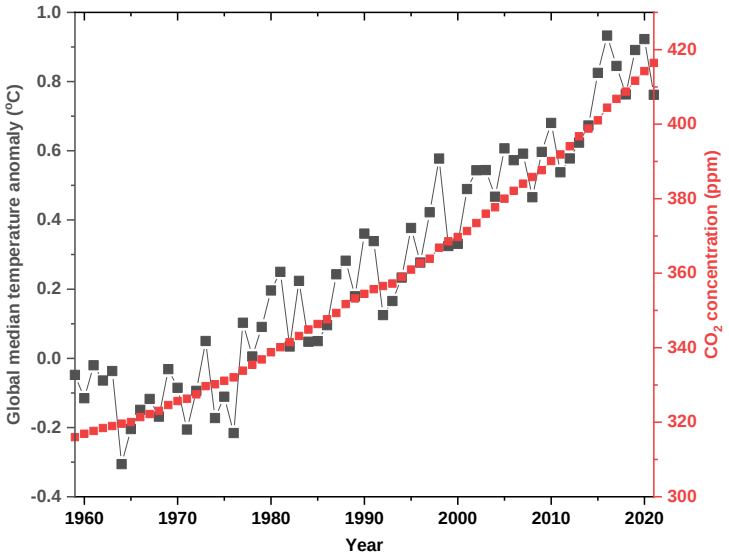

Figure 1.1 Global median temperature anomalies (HadCRUT5 dataset)[2] and atmospheric CO_2 concentration (Mauna Loa Observatory) from 1959 to 2021.[3] Data from Ref 2 and 3.

1.2 Hydrogen storage

1.2.1 Physical storage

Hydrogen is the most abundant element on earth, but the vast majority of it is chemically bound in water molecules, and the remainder is chemically bound to liquid or gaseous hydrocarbons. The clean way to produce hydrogen from water is to use solar energy in combination with photovoltaic cells and water electrolysis (Figure 1.2).[5] The drawback in the use of hydrogen as an energy carrier is often associated with the lack of methods to effectively store it. Hydrogen has a low volumetric energy density (0.7 kJ L^{-1} at 25 °C and atmospheric pressure), and the current mature storage technology involves compressing hydrogen to 700 bars in a carbon fiber-

reinforced composite tank.[6] Hydrogen can also be stored as liquid hydrogen, with a high volumetric density (141.6 kJ L^{-1} at −253 °C), in a cryogenic tank. However, the large amount of energy required for liquefaction and the constant evaporation of hydrogen limit the practical applications of liquid hydrogen storage systems.[7]

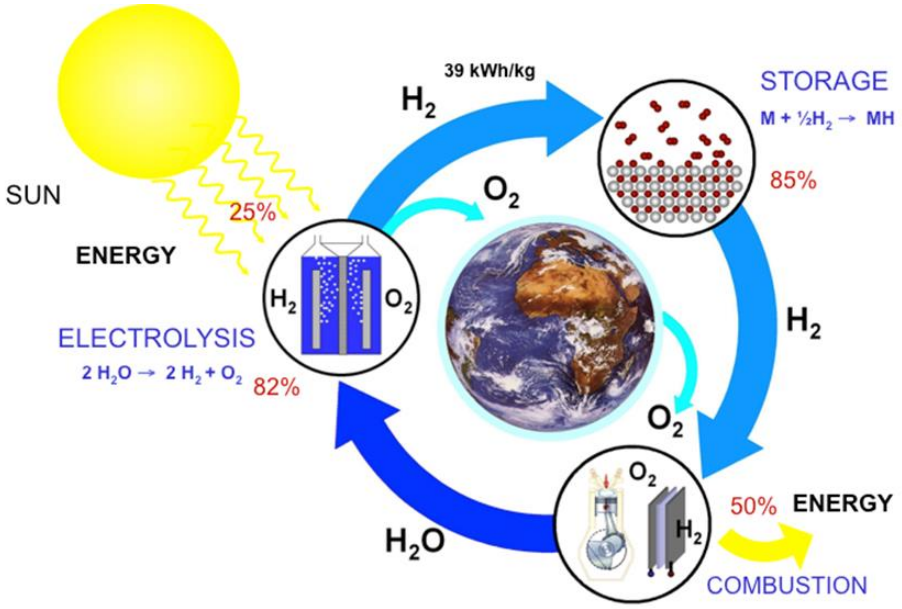

Figure 1.2 Schematic image of a closed hydrogen cycle with renewable energy sources for carbon-free energy storage and utilization. Permission from Ref. 5.

1.2.2 Metal hydrides

Metal hydrides ($LaNi_5$, TiFe, etc.) have been created to offer new and significant opportunities for storing renewable energy with a high volumetric energy density. The metal hydrides are typically designated as AB, AB_2, AB_3, A_2B, AB_5, etc., where A is an element that can form stable metallic hydrides with rare earth and early transition metals, and B is an element that repels hydrogen with rare earth and late transition metals.[8] These metal alloys are capable of safely storing hydrogen at low hydrogen pressures because of their ability to store hydrogen via a simple chemical reaction.[9] In addition, these materials can be utilized in metal hydride hydrogen compressors (MHHC) without the occurrence of vibration, noise, or friction.[8] Commercial MHHC system (HyCo, GRZ Technologies AG, Switzerland) are available in the market.[9]

1.2.3 Carbon and molecular organic frameworks (MOF)

Carbon materials and high surface area materials, such as molecular organic frameworks (MOF), are candidates to provide efficient hydrogen storage properties at a low temperature (77 K). The hydrogen molecules are weekly bound to the surfaces of the materials. Important parameters for the hydrogen storage properties are the MOF pore diameter and volume. In terms of interchangeable structure properties, MOFs are desirable for hydrogen storage applications because of their well-defined porous networks. There are several candidates for hydrogen storage MOFs such as Zn-based MOFs (MOF-5, IRMOF-8, MOF-177), Cu-based MOFs (HKUST-1, MOF-505), Mn-based MOFs, and Al-based MOFs.[10,11]

1.2.4 Complex hydrides

Complex hydrides, such as alanates, borohydrides, and amides, have a high hydrogen gravimetric density ($NaBH_4$: 10.6 wt.%, $NaAlH_4$: 5.6 wt.%) and are, in some cases, commercially available. The decomposition of bo-

rohydride and alanate is depicted in Figure 1.3. The multiple steps of the hydrogen desorption process result in the irreversible storage of hydrogen.[12] In 1996, Bogdanovic presented the initial results of experiments involving reversible hydrogen storage in Ti-catalyzed $NaAlH_4$.[13] Based on the local structure and thermodynamic considerations, only the Ti catalyst exhibits reversible hydrogen sorption properties with alanates, despite the large number of publications in alanate materials.[14] Additional Ti distributed throughout the alanate may facilitate the mass transfer of Al or NaH. Considering the rehydrogenation of NaH and Al particles, Na_3AlH_6 must be formed as an intermediate at the interfaces between NaH and Al particles, where gaseous hydrogen molecules must be activated for the reaction. The Na_3AlH_6 intermediate undergoes additional reactions with Al and H_2 to regenerate $NaAlH_4$.[6]

Several methods have been suggested for decreasing the temperature of hydrogen release from metal hydride. When Mg and Al are milled together, the enthalpy of hydrogen release decreases from 75 kJ mol^{-1} to 70 kJ mol^{-1}. In addition, decreasing the particle size alters the kinetics and stability of complex hydrides (Figure 1.4a). The basic strategy for designing hydrogen storage materials is described in Figure 1.4b.[6] The form of hydrogen, i.e., as atomic (H), hydride (H^-), protide (H^+), or a combination, is chosen to lead to a low reversible energy path. Hydrogen frequently forms stable hydrides with other elements, releasing their hydrogen at elevated temperatures. The common strategy involves adjustment of the reaction enthalpy by combining the chosen hydride with elements forming unstable hydrides. The introduction of a catalyst to the hydride may promote the dissociative absorption and recombination of hydrogen during desorption. The hydrogen dissociation rate of the catalyst should be sufficiently high, whereas its hydrogen binding strength should be relatively low, to facilitate hydrogen release/absorption from the hydride material. Therefore, the difficulty in modifying the properties of hydrogen storage materials lies in the necessity of simultaneously enhancing thermodynamics and kinetics without reducing the hydrogen storage capacity. In Chapter 2 of this dissertation, a nickel-containing porous carbon sheet (Ni-PCS) is introduced to alanate materials to prevent material volume expansion and decrease hydrogen release temperature. The catalytic activity of Ni-PCS is dependent on the electronegativity of the cation (Li, Na, or Mg) in alanate. The catalyst has a stronger effect when the cations have lower electronegativity.

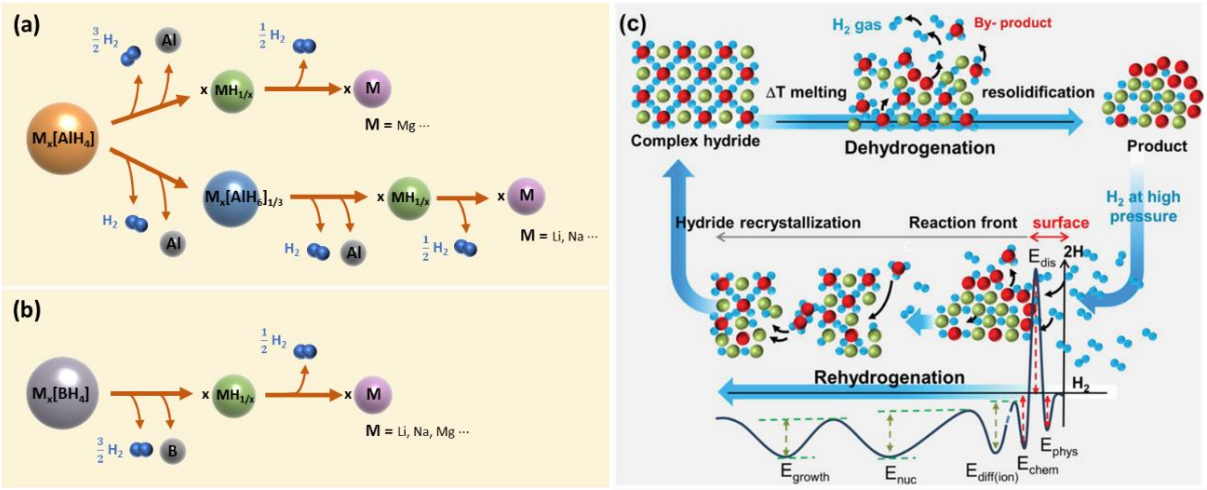

Figure 1.3 Schematic description of the hydrogen adsorption/absorption principles in complex hydrides. General decomposition path of (a) alanate and (b) borohydrides. (c) hypothetic mechanisms for hydrogen release and uptake in complex hydrides and associated Lennard-Jones potential diagram corresponding to the successive energy barriers encountered by hydrogen during absorption. E_{phys}: energy for hydrogen physisorption, E_{dis}: energy for hydrogen dissociation, E_{chem}: energy for hydrogen chemisorption, E_{pen}: energy for hydrogen penetration in the subsurface, $E_{diff(ion)}$: energy for ionic diffusion, and E_{nuc} and E_{growth}: energy for the nucleation and growth of the hydride. In complex hydrides, the reaction is believed to occur at the interface of segregated elements. Permission from Ref. 6.

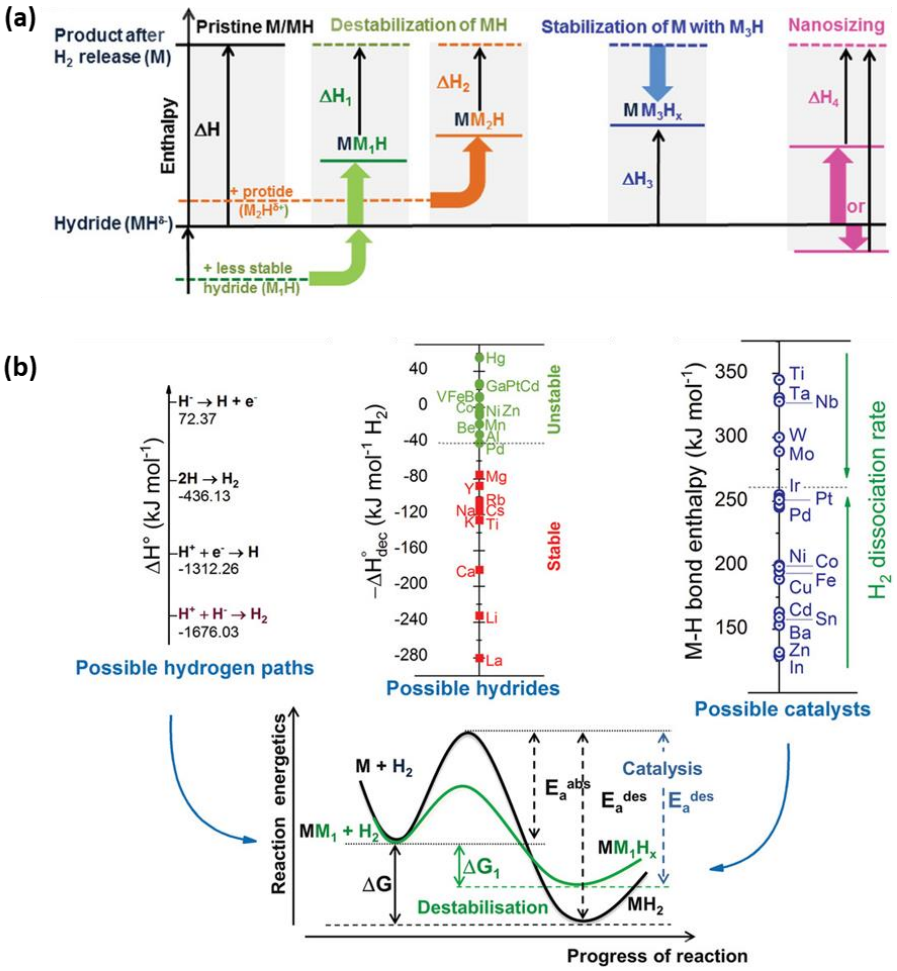

Figure 1.4 (a) Generalized enthalpy diagram illustration by alloy formation with less stable hydrides, e.g., Fe, Ni (green); the reaction of a hydride, e.g., LiH, MgH_2, $NaBH_4$, $NaAlH_4$, with a corresponding protide, e.g., $LiNH_2$, NH_3 (orange); stabilization of the decomposition products (blue); and nanosizing (pink). To enable room-temperature hydrogen storage, ΔH should be brought down while ΔS remains constant. (b) Designing hydrogen storage materials by the combination of hydrogen paths, hydrides, and catalysts. Permission from Ref. 6.

1.3 Fuel cells

1.3.1 Proton exchange membrane fuel cells (PEMFCs)

A fuel cell is a device designed to convert chemical energy directly to electrical energy.[15] Proton exchange membrane fuel cells (PEMFC) use hydrogen as a fuel and generate electricity and heat through an electrochemical reaction involving hydrogen and oxygen. In PEMFCs, the polymeric proton exchange membrane functions as the solid electrolyte. This membrane is typically composed of a hydrophobic perfluorinated sulfonic acid polymer backbone with hydrophilic sulfonic acid groups (i.e., Nafion). Hydrogen reacts at the anode, and proton ions transport through the membrane to the cathode, while electrons circulate in an external circuit. The overall reaction for PEMFCs is described below.

Anode: $2H_2 \rightarrow 4H^+ + 4e^-$ ($E^{0,a}$ = 0.00 V vs. SHE) (1)

Cathode: $O_2 + 4H^+ + 4e^- \rightarrow 2H_2O$ ($E^{0,c}$ = 1.23 V vs. SHE) (2)

Overall: $2H_2 + O_2 \rightarrow 2H_2O$ (E^0 = 1.23 V vs. SHE) (3)

The reaction enthalpy (−ΔH) amounts to 285.8 kJ mol^{-1}, and the Gibbs free energy (−ΔG) of the reaction amounts to 237.1 kJ mol^{-1}. The maximum attainable thermodynamic efficiency of energy conversion in a PEMFC is 83%.[15] The thermodynamic potential of a PEMFC at a temperature of 25 °C is 1.23 V. However, the general open circuit potential (OCP) has values between 0.9 and 1 V, depending on the temperature and device configuration. Platinum is a well-known electrochemical reaction catalyst at the anode and cathode of PEMFCs. Platinum is deposited on highly dispersed carbon, allowing for increased utilization efficiency and decreased metal content in the electrode. The membrane electrode assembly (MEA) of interest herein was developed by Gottesfeld and Zawodzinski at Los Alamos National Laboratory and by Srinivasan at the Center for Electrochemical Systems and Hydrogen Research, Texas A&M University.[16,17] The catalyst ink is a mixture of Pt/C, ionomer, alcohol, and water, which can be sprayed directly onto Nafion to manufacture MEA.

In the PEMFC, the oxygen reduction reaction (ORR) at the cathode is sluggish and performance-determining. Pt and its alloys are the most commonly used catalysts for the ORR process. The ORR activity can be plotted as a function of O or OH binding energy, which gives the volcano plot. Metals that have either stronger or weaker binding energy of oxygen than Pt are poorer oxygen reduction catalysts.[18] Currently, the technical goal of the U.S. Department of Energy is to minimize the use of Pt catalysts or improve catalytic activity by controlling the shape of Pt, alloying Pt, and synthesizing hollow nanoparticle structures.[19]

Platinum group metal (PGM)-free catalysts in PEMFCs have significantly enhanced ORR activity and initial fuel cell performance, especially with M-N-C catalysts. The highest performing ORR active catalyst among the M-N-C catalysts is the Fe-N-C catalyst. Despite massive efforts to increase activity, the stability of Fe-N-C catalysts under practical fuel cell conditions remains unsatisfactory.[20] Recent advancements in highly stable and active Fe-N-C with control of the local carbon structure and conversion of unstable pyrrolic N-coordinated Fe to stable pyridinic N-coordinated Fe may provide a solution to the stability problem of M-N-C catalysts.[21]

In PEMFC operation, many other parameters, such as water management, heat management, and partial pressure of the reactant gas, must be considered to obtain high-performance devices. Excess water at the cathode electrode may cause flooding of the pores of the active layers, with oxygen reaching the catalyst's active site. Dehydration of the membrane, in contrast, raises the ohmic resistance due to the low proton ion transport through the membrane. During the operation of fuel cells with a high current density, a substantial amount of heat is generated. In particular, effective heat management is a crucial aspect of the PEMFC stack. For efficient heat transfer, the temperature of the heat-transfer medium must be at least 10 °C lower than the PEMFC operating temperature. The residual heat can be utilized for heating as well.

1.3.2 Direct borohydride fuel cells (DBFCs)

Direct methanol fuel cells are historically the first liquid fuel-fed fuel cell using methanol as fuel. Isopropanol has recently been considered for the fuel in direct isopropanol fuel cells (DIFC).[22] The product of DIFCs at the anode is acetone, which does not emit CO_2 at the anode exit. Liquid fuels are considerably more convenient and less dangerous than high-pressure hydrogen. Such advantages of the liquid-fed fuel cell are highlighted in small portable devices. The different properties of PEMFCs and DBFCs are illustrated in Figure 1.5.

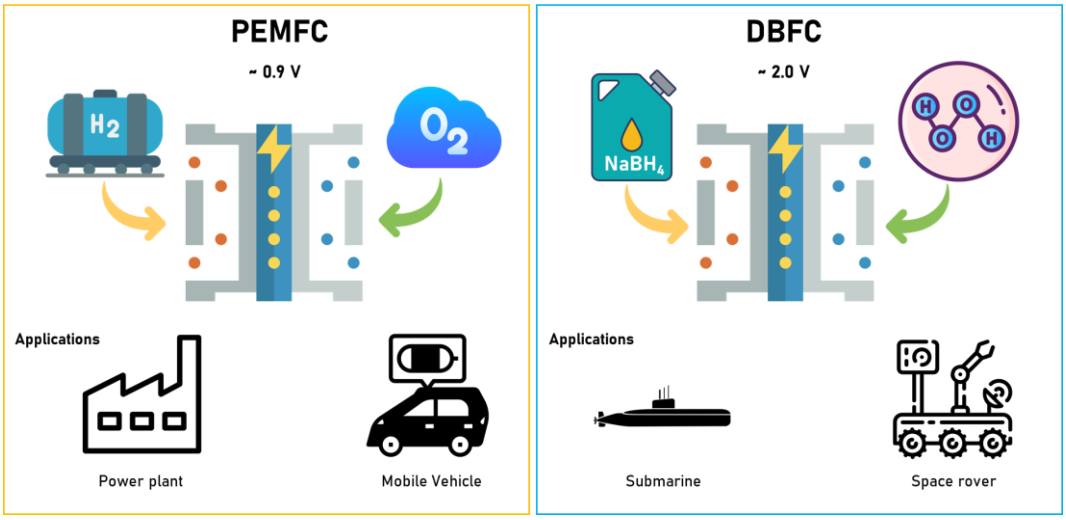

Figure 1.5 The operational differences between PEMFC and DBFC. The DBFC utilized liquid fuels (Borohydride solution and hydrogen peroxide solution), whereas the PEMFC utilizes hydrogen stored in a high-pressure tank.

Direct borohydride fuel cells (DBFC) are one type of fuel cell that uses liquid fuel on both the anode and cathode. The theoretical OCP of DBFC is 3.01 V, with an anode potential of 1.24 V and a cathode potential of 1.77 V. However, because of the contribution of mixed potential at the cathode and liquid junction potential loss, the typical measured OCP from the DBFC is around 2 V. The mixed potential at the cathode will be discussed in Chapter 4. Figure 1.6 depicts a schematic of the DBFC system. The main reaction at the anode is the borohydride oxidation reaction (BOR). The main reaction at the cathode is the hydrogen peroxide reduction reaction (PRR). Some DBFCs use O_2 as the cathode oxidant instead of H_2O_2. Nevertheless, the operating voltage is lower compared to H_2O_2-fed DBFCs.

$$\text{Anode: } BH_4^- + 8OH^- \rightarrow BO_2 + 6H_2O + 8e^- \qquad (E^{0,a} = -1.24 \text{ V vs. SHE}) \qquad (4)$$

$$\text{Cathode: } 4H_2O_2 + 8H^+ + 8e^- \rightarrow 8H_2O \qquad (E^{0,c} = 1.77 \text{ V vs. SHE}) \qquad (5)$$

$$\text{Overall: } BH_4^- + 4H_2O_2 + 8H^+ + 8OH^- \rightarrow BO_2^- + 14H_2O \qquad (E^0 = 3.01 \text{ V}) \qquad (6)$$

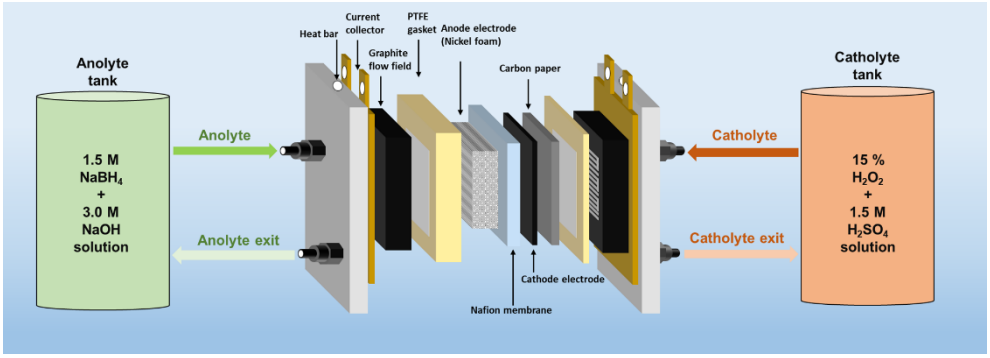

Figure 1.6 Schematic image of direct borohydride fuel cell. Two tanks are used as a liquid fuel reservoir for anolyte (1.5 M $NaBH_4$ with 3 M NaOH solution) and catholyte (15% H_2O_2 with 1.5 M H_2SO_4 solution). The nickel foam is used as an anode electrode. The gas diffusion layer and carbon-based catalyst are used as cathode electrodes.

1.3.3 Borohydride oxidation reaction (BOR) catalysts

The BOR is the main reaction that occurs in the DBFC anode. The optimal catalyst for the DBFC anode has a high activity for the BOR, but a low activity for heterogeneous hydrolysis of BH_4, the hydrogen evolution reaction (HER), and the hydrogen oxidation reaction.[23]

$$BH_4^- + 8OH^- \rightarrow BO_2^- + 6H_2O + 8e^- \qquad (E^0 = -1.24\ V\ vs.\ SHE) \qquad (4)$$

$$BH_4^- + 2H_2O \rightarrow BO_2^- + 4H_2 \qquad (7)$$

$$H_2O + 2e^- \rightarrow H_2 + 2OH^- \qquad (E^0 = 0\ V\ vs.\ SHE) \qquad (8)$$

$$H_2 + 2OH^- \rightarrow 2H_2O + 2e^- \qquad (E^0 = 0\ V\ vs.\ SHE) \qquad (9)$$

The BOR is investigated for various catalysts, including Pt, Pd, Au, etc. Chatenet et al. reported the BOR mechanisms and poisoning effects on Au, Pt, and Pd electrodes.[24] The kinetic model and activity show that a more significant poisoning effect occurs for Pt than Au and Pd by the intermediate reactive products such as BH_{ads} or $BH_{3,ads}$. In addition, Pd maintains promising BOR kinetics, even at high $NaBH_4$ concentrations, whereas Au consistently demonstrates the lowest BOR activity. In terms of activity in the DBFC anode, the Pd catalyst is therefore regarded as a promising BOR catalyst. Ramani et al. demonstrated the pH-gradient-enabled microscale bipolar interfaces (PMBI) with a Pd catalyst and two different ionomers (cation or anion exchange ionomer) in DBFCs (Figure 1.7).[25] They prepared PMBIs using a Pd/C catalyst covered with anion exchange ionomer and examined the ability to control the local pH gradient at the catalyst reaction site. The PMBI-based DBFC demonstrates a current density of 330 mA cm^{-2} at 1.5 V and a peak power density of 630 mW cm^{-2} at 1.0 V. The DBFC with PMBI configuration paves the way for the development of high-performance DBFCs and the comprehension of the catalyst-ionomer interface under local pH conditions. In addition, reactant-transport engineering (890 mW cm^{-2}) further improved the state-of-the-art DBFC performance.[26]

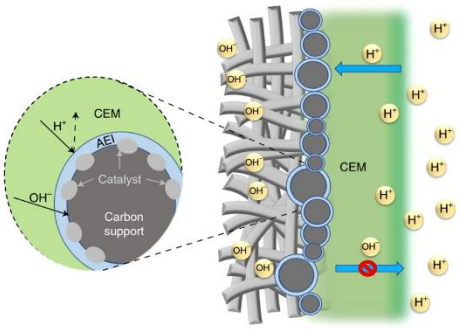

Figure 1.7 The PMBI forms at the junction between the cation exchange membrane (CEM) and the anion exchange ionomer (AEI) binder. The reaction sites on the catalyst particle surface are covered by the AEI binder, which allows for the selective transport of hydroxide ions. Permission from Ref. 25.

In the context of DBFC development, Suda et al. published the first paper to use Ni catalyst with PTFE binder for the BOR.[27] They claim that the BOR reaction on the Ni catalyst is followed by a four-electron process rather than an eight-electron reaction. Oshchepkov et al. reported that metallic Ni has significant BOR activity but partially oxidized Ni has significantly low BOR activity, which correlates with its higher HER activity.[28] In addition, they measured the performance of the fuel cell with a metallic Ni catalyst at the anode, which revealed a higher OCP

and power density than a Pt-based catalyst.[28,29] Chapter 3 describes the utilization of Ni catalyst to replace Pd in DBFCs.

1.3.4 Hydrogen peroxide reduction (PRR) catalysts

H_2O_2 is generally an unstable chemical, which easily decomposes to oxygen and water, as shown in Figure 1.8.[30] Higher H_2O_2 concentrations are therefore metastable, but there are still two ways in which H_2O_2 can be formed. One is the electrochemical oxidation of water, represented by the green line. The other is 2-electron ORR, denoted by the red line, which also establishes the maximum H_2O_2 concentration that can be attained at a given potential. The potential between the red and green lines in Figure 1.8, indicates that H_2O_2 may decompose through electrochemical oxidation to oxygen and reduction to water. The most important drawbacks of utilizing H_2O_2 in DBFC cathode are the side reaction of the decomposition of H_2O_2 and the slow kinetics of PRR on the non-noble catalyst. The activity of PRR is higher on the Pt catalyst than M-N-C catalyst, and at the same time, the decomposition of H_2O_2 is also severe on the Pt catalyst.[31] The degradation of M-N-C catalyst in H_2O_2 with H_2SO_4 solution is also a critical challenge in DBFC cathode. The H_2O_2 and reactive oxygen species induce the demetallation of the active site and carbon oxidation in M-N-C catalysts.[32] In Chapter 4, the activity and durability of Fe-N-C and Co-N-C are compared.

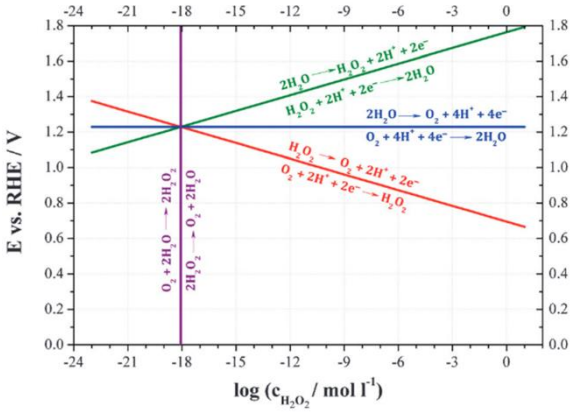

Figure 1.8 Equilibrium potentials for hydrogen peroxide oxidation (red) and reduction (green) as a function of H_2O_2 concentration at 1 bar of O_2. For comparison, the equilibrium potential for dissociative oxygen reduction (blue) and the equilibrium concentration for the nonelectrochemical H_2O_2 formation/decomposition (purple) are also shown. The thermodynamically favorable reactions are indicated. Permission from Ref. 30.

1.4 Electrochemical H_2O_2 production via oxygen reduction reaction

The electrochemical H_2O_2 production via 2-electron ORR has emerged as a promising alternative for decentralized production and on-site applications.[33] H_2O_2 is essential in a variety of fields, including chemical synthesis, wastewater treatment, rocket propulsion, pulp, and paper bleaching, etc. (Figure 1.9). The ORR consists of two reactions. The first is a 4-electron route to H_2O, and the second is a 2-electron route to H_2O_2, which is less thermodynamically favorable. Furthermore, the produced H_2O_2 can be further reduced to water via PRR, significantly decreasing H_2O_2 production yield. Therefore, several requirements are necessary regarding the catalytic properties (activity, selectivity, and stability) for practical applications.

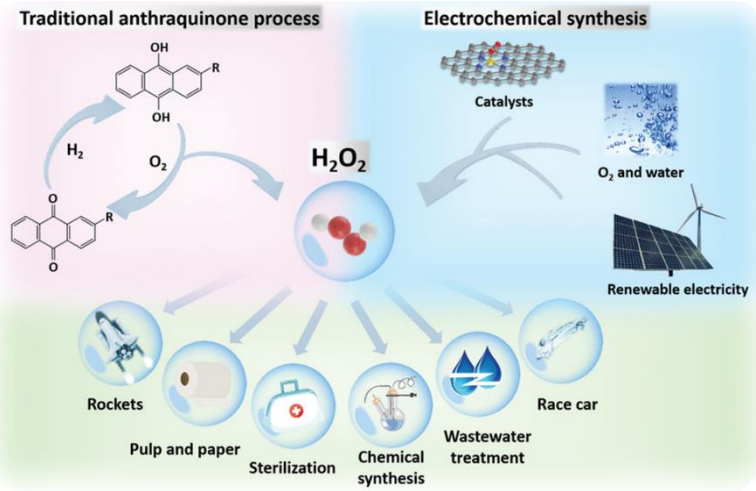

Figure 1.9 Hydrogen peroxide synthesis methods and application in various areas. Permission from Ref. 33.

The H_2O_2 production via 2-electron ORR has been extensively studied in pristine carbon, nitrogen-doped carbon, and metal with nitrogen-doped carbon materials.[33,34] It was discovered that the various properties of carbon materials (surface area, zeta potential, and defect) play a crucial role in determining the H_2O_2 production activity and selectivity.[34] The M-N-C materials can overcome the low ORR activity to produce H_2O_2 under acidic conditions. The schematic illustration of 2-electron and 4-electron ORR is shown in Figure 1.10a. When the binding energy between an active metal site (*) with the intermediate OOH (i.e., *OOH) is weaker than the O–OH bond, the *OOH bond tends to be broken for a favorable $2e^-$ pathway. In contrast, if the *OOH bond is stronger than the O–OH, and the $4e^-$ pathway is preferable because of the relatively facile O–OH cleavage.[35] In addition, the proton affinity to the detached *OOH increases by decreasing the potential with the active site of a single cobalt atom catalyst, thereby increasing the H_2O_2 production selectivity. Among the catalysts indicated in Figure 1.10c and d, the Co-N-C catalyst showed the highest H_2O_2 selectivity and lowest electron transfer number for ORR.

The atomically dispersed Co that coordinates with N has a high selectivity for H_2O_2 production via ORR. Conversely, the ORR activity of Co nanoparticles has not been investigated. The active site identification for H_2O_2 production is demonstrated on atomically dispersed Co and nanoparticle Co with two different catalysts. Wang et al. demonstrated the cation effect of H_2O_2 production at high current density, near industrial levels. The cation shielding effect at the surface of the electrochemical catalysts suppresses the proceeding H_2O formation, which enhances the selectivity of H_2O_2 production. In Chapter 5, the cation shielding effect is used to investigate the different active sites on atomically dispersed Co and Co nanoparticles using a rotating ring disk electrode (RRDE) for the measurement. The atomically dispersed Co with nitrogen bonding exhibits intrinsically selective 2-electrons ORR activity. Moreover, the ORR produced H_2O at the Co nanoparticles situated on a nitrogen-doped carbon catalyst.

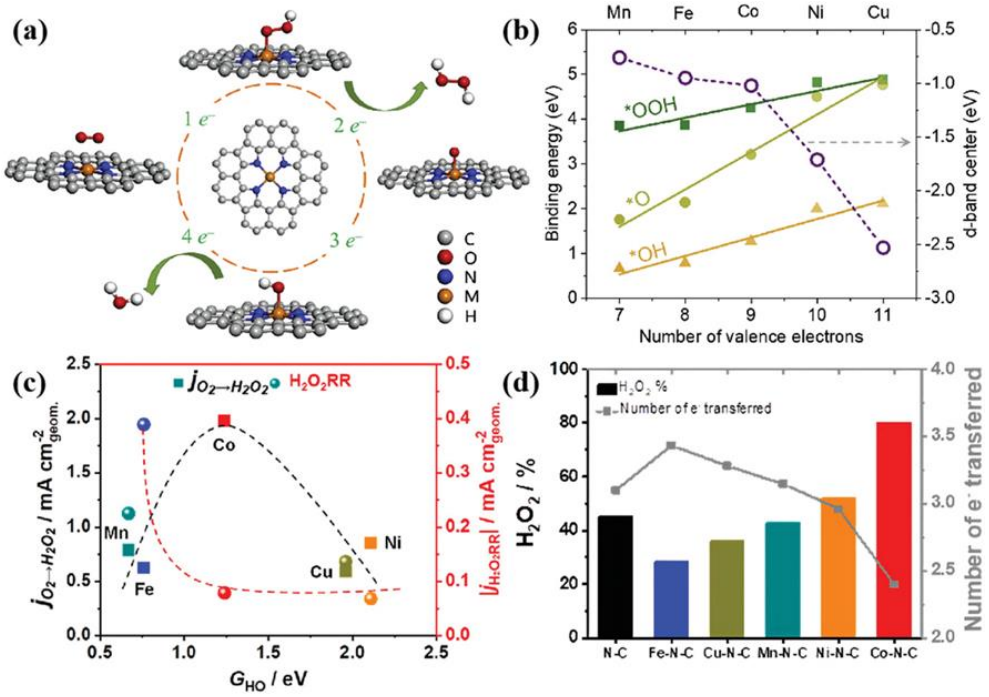

Figure 1.10 An activity–selectivity trend in various M−N−C catalysts (M = Mn, Fe, Co, Ni, and Cu) has been evaluated. (a) Schematic illustration of ORR pathways, and (b) the corresponding binding energy of *OOH, *O, and *OH on the M−N−C catalyst and d-band center of M atom. (c) H_2O_2 production current as a function of the binding energy of *OH intermediate, and (d) H_2O_2 selectivity and the electrons transfer number at 0.1 V vs. reversible hydrogen electrode (RHE) for different M-N-C catalysts. Permission from Ref. 33.

1.5 Characterization methods

1.5.1 Catalyst characterization and evaluation

Electron microscopy such as scanning electron microscopy (SEM), transmission electron microscopy (TEM), and scanning transmission electron microscopy-energy dispersive X-ray analysis (STEM-EDX) are commonly used for characterizing particle size, morphology, and catalyst distribution on support materials. The atomically dispersed metal with nitrogen-doped carbon samples is first checked for the existence of nanoparticle agglomeration by TEM. After checking the non-existence of nanoparticles, the aberration-corrected STEM (AC-STEM) is used to find the bright dots which are the atomically dispersed metals in carbon layers. Observing a single atom in the carbon support requires a technique called “beam shower”. The electron beam spreads over a large area for at least 30 min, which prevents carbon deposition on the interested area during the measurement.

X-ray diffraction (XRD) is used to evaluate the crystalline phase of catalysts, phase composition, and grain size. The crystalline phase of the sample is compared with the database (JCPDS, COD). The phase composition is calculated by fitting the measured pattern with Rietveld refinement.[36] X-ray photoelectron spectroscopy (XPS) is used to characterize the chemical bonding of exposed surfaces. The element at the catalyst's surface can be assessed qualitatively and quantitatively using XPS.

Nitrogen adsorption and desorption isotherms can be measured to determine the specific surface area of materials. For calculating specific surface area, the Brunauer–Emmett–Teller theory is commonly used. The Barrett–Joyner–Halenda method is the appropriate method to measure the mesopore size distribution of material.

Raman spectroscopy and Fourier transform-infrared spectroscopy (FT-IR) measure the vibrational and rotational motions of molecules. Raman spectroscopy and FT-IR are commonly used to provide a structural fingerprint of molecules and their chemical bonding.

Thermogravimetric analysis (TGA) and differential scanning calorimetry (DSC) measure the physical properties of a sample as they change over time, as well as their dependence on temperature. TGA analysis measures the sample weight change under an inert or oxidation condition. DSC is used to measure the difference in the amount of heat required to increase the temperature of a sample and a reference.

Pressure composition isotherm measurements are used to calculate hydrogen capacity for metal hydrides. The measurements are divided into dynamic (mass-flow) and Sievert's types at different temperatures and flow rates.[37] The amounts of hydrogen release are measured using a flow meter at a certain temperature or increase in temperature.

An RRDE is generally composed of a Pt ring and a glassy carbon (GC) disk electrode. The RRDE is used to measure ORR activity and the selectivity of the catalyst. The catalyst is deposited on a disk electrode, and the potential is swept under the O_2-saturated electrolyte. The potential of the Pt ring electrode is fixed at 1.2 V to measure the anodic current of H_2O_2 that is produced from the disk electrode to measure 2-electron ORR activity. A modified RRDE was used to measure the activity of the nickel catalyst on nickel foam, and the additional GC is attached to measure the durability of the M-N-C catalyst.

MEA performance is obtained by the fuel cell station. The fuel cell station has a load, heat controller, and mass-flow control system. The parameters of fuel cell measurement are controlled and recorded by the system. MEA fabrication is one of the key skills that must be optimized, along with membrane thickness, catalyst amount in the electrode, and gasket thickness.

X-ray absorption spectroscopy (XAS) has been used to gather spectroscopic information about atomic energy level structure. X-ray absorption near edge structure (XANES) information provides insights regarding the valence state, energy bandwidth, and bond angles. Extended X-ray absorption fine structure (EXAFS) information can indicate the interatomic distances, near neighbor coordination numbers, and lattice dynamics. Both XANES and EXAFS are powerful tools for analyzing atomically dispersed metal catalysts. Furthermore, XAS can measure the oxidation state of the catalyst during the electrochemical process, which makes it possible to observe the intermediate catalyst state.

1.6 Challenges and objectives of this thesis

This thesis investigated various catalysts applied to hydrogen storage materials and DBFCs. The hydrogen storage method was investigated in various ways. One of the promising hydrogen storage materials, complex hydride, has a high gravimetric density of hydrogen. The hydrogen release temperature of complex hydride generally does not match the operating temperature of PEMFC. The introduction of a catalyst to the complex hydride can assist the dissociative absorption and recombination of hydrogen during desorption. In Chapter 2, the nickel metal doped on a porous carbon sheet is introduced to the aluminum-based-complex hydride (alanate). The hydrogen release temperature of alanate is decreased and the material expansion is prevented during the reaction.

The high activity of the catalyst is the key component for a high-performance fuel cell that operated at a low temperature (60–80 °C). In addition, the cost of catalysts, generally PGM-group metals have high activity for the reaction in the fuel cell. The replacement of the PGM-group metal in the fuel cell is a challenge to reduce the

cost of the fuel cell. In Chapter 3, the facile synthesis method of nickel with ionomer is introduced and utilized in the DBFC anode. The nickel catalyst is a more proper catalyst for selective BOR than the palladium catalyst.

The replacement of the platinum catalyst at the DBFC cathode is described in Chapter 4. The metal with nitrogen-doped carbon materials is applied to replace the Pt catalyst. The active site of M-N-Cs is known as atomically dispersed metal coordinated with nitrogen. The durability of the catalyst needs to be evaluated for practical fuel cell operation. The Fe-N-C has high activity, but Co-N-C is more stable for the hydrogen PRR under harsh conditions than Fe-N-C.

Hydrogen peroxide production via electrochemical 2-electron ORR is studied in Chapter 5. High-selective 2-electron ORR is a key property of the H_2O_2 production catalyst. The atomically dispersed Co coordinated with N is known as the active site for electrochemical H_2O_2 production. However, the Co nanoparticles may affect the selectivity of H_2O_2 production. A small amount of cation is added to the electrolyte for differentiating the active site on atomically dispersed Co and Co nanoparticles.

References

(1) Karl, T. R.; Trenberth, K. E. Modern Global Climate Change. *Science* **2003**, *302* (5651), 1719–1723. https://doi.org/10.1126/science.1090228.

(2) Morice, C. P.; Kennedy, J. J.; Rayner, N. A.; Winn, J. P.; Hogan, E.; Killick, R. E.; Dunn, R. J. H.; Osborn, T. J.; Jones, P. D.; Simpson, I. R. An Updated Assessment of Near-Surface Temperature Change From 1850: The HadCRUT5 Data Set. *Journal of Geophysical Research: Atmospheres* **2021**, *126* (3), e2019JD032361. https://doi.org/10.1029/2019JD032361.

(3) Keeling, R. F.; Keeling, C. D. Atmospheric Monthly in Situ CO2 Data-Mauna Loa Observatory, Hawaii. *Scripps CO2 program data* **2017**.

(4) Holechek, J. L.; Geli, H. M. E.; Sawalhah, M. N.; Valdez, R. A Global Assessment: Can Renewable Energy Replace Fossil Fuels by 2050? *Sustainability* **2022**, *14* (8), 4792. https://doi.org/10.3390/su14084792.

(5) Schlapbach, L.; Züttel, A. Hydrogen-Storage Materials for Mobile Applications. In *Materials for Sustainable Energy*; Co-Published with Macmillan Publishers Ltd, UK, 2010; pp 265–270. https://doi.org/10.1142/9789814317665_0038.

(6) Lai, Q.; Sun, Y.; Wang, T.; Modi, P.; Cazorla, C.; Demirci, U. B.; Fernandez, J. R. A.; Leardini, F.; Aguey-Zinsou, K.-F. How to Design Hydrogen Storage Materials? Fundamentals, Synthesis, and Storage Tanks. *Advanced Sustainable Systems* **2019**, *3* (9), 1900043. https://doi.org/10.1002/adsu.201900043.

(7) Züttel, A. Materials for Hydrogen Storage. *Materials Today* **2003**, *6* (9), 24–33. https://doi.org/10.1016/S1369-7021(03)00922-2.

(8) Peng, Z.; Li, Q.; Ouyang, L.; Jiang, W.; Chen, K.; Wang, H.; Liu, J.; Li, Z.; Wang, S.; Zhu, M. Overview of Hydrogen Compression Materials Based on a Three-Stage Metal Hydride Hydrogen Compressor. *Journal of Alloys and Compounds* **2022**, *895*, 162465. https://doi.org/10.1016/j.jallcom.2021.162465.

(9) Bellosta von Colbe, J.; Ares, J.-R.; Barale, J.; Baricco, M.; Buckley, C.; Capurso, G.; Gallandat, N.; Grant, D. M.; Guzik, M. N.; Jacob, I.; Jensen, E. H.; Jensen, T.; Jepsen, J.; Klassen, T.; Lototskyy, M. V.; Manickam, K.; Montone, A.; Puszkiel, J.; Sartori, S.; Sheppard, D. A.; Stuart, A.; Walker, G.; Webb, C. J.; Yang, H.; Yartys, V.; Züttel, A.; Dornheim, M. Application of Hydrides in Hydrogen Storage and Compression: Achievements, Outlook and Perspectives. *International Journal of Hydrogen Energy* **2019**, *44* (15), 7780–7808. https://doi.org/10.1016/j.ijhydene.2019.01.104.

(10) Hu, Y. H.; Zhang, L. Hydrogen Storage in Metal–Organic Frameworks. *Advanced Materials* **2010**, *22* (20), E117–E130. https://doi.org/10.1002/adma.200902096.

(11) Rosi, N. L.; Eckert, J.; Eddaoudi, M.; Vodak, D. T.; Kim, J.; O'Keeffe, M.; Yaghi, O. M. Hydrogen Storage in Microporous Metal-Organic Frameworks. *Science* **2003**, *300* (5622), 1127–1129. https://doi.org/10.1126/science.1083440.

(12) Orimo, S.; Nakamori, Y.; Eliseo, J. R.; Züttel, A.; Jensen, C. M. Complex Hydrides for Hydrogen Storage. *Chem. Rev.* **2007**, *107* (10), 4111–4132. https://doi.org/10.1021/cr0501846.

(13) Bogdanović, B.; Schwickardi, M. Ti-Doped Alkali Metal Aluminium Hydrides as Potential Novel Reversible Hydrogen Storage Materials1Invited Paper Presented at the International Symposium on Metal–Hydrogen Systems, Les Diablerets, August 25–30, 1996, Switzerland.1. *Journal of Alloys and Compounds* **1997**, *253–254*, 1–9. https://doi.org/10.1016/S0925-8388(96)03049-6.

(14) Züttel, A.; Mauron, P.; Kato, S.; Callini, E.; Holzer, M.; Huang, J. Storage of Renewable Energy by Reduction of CO2 with Hydrogen. *CHIMIA* **2015**, *69* (5), 264–264. https://doi.org/10.2533/chimia.2015.264.

(15) The Working Principles of a Fuel Cell. In *Fuel Cells*; John Wiley & Sons, Ltd, 2012; pp 5–24. https://doi.org/10.1002/9781118191323.ch1.

(16) Gottesfeld, S.; Zawodzinski, T. A. Polymer Electrolyte Fuel Cells. In *Advances in Electrochemical Science and Engineering*; John Wiley & Sons, Ltd, 1997; pp 195–301. https://doi.org/10.1002/9783527616794.ch4.

(17) Parthasarathy, A.; Martin, C. R.; Srinivasan, S. Investigations of the O 2 Reduction Reaction at the Platinum/Nafion® Interface Using a Solid-State Electrochemical Cell. *J. Electrochem. Soc.* **1991**, *138* (4), 916. https://doi.org/10.1149/1.2085747.

(18) Nørskov, J. K.; Rossmeisl, J.; Logadottir, A.; Lindqvist, L.; Kitchin, J. R.; Bligaard, T.; Jónsson, H. Origin of the Overpotential for Oxygen Reduction at a Fuel-Cell Cathode. *J. Phys. Chem. B* **2004**, *108* (46), 17886–17892. https://doi.org/10.1021/jp047349j.

(19) Mølmen, L.; Eiler, K.; Fast, L.; Leisner, P.; Pellicer, E. Recent Advances in Catalyst Materials for Proton Exchange Membrane Fuel Cells. *APL Materials* **2021**, *9* (4), 040702. https://doi.org/10.1063/5.0045801.

(20) He, Y.; Wu, G. PGM-Free Oxygen-Reduction Catalyst Development for Proton-Exchange Membrane Fuel Cells: Challenges, Solutions, and Promises. *Acc. Mater. Res.* **2022**, *3* (2), 224–236. https://doi.org/10.1021/accountsmr.1c00226.

(21) Liu, S.; Li, C.; Zachman, M. J.; Zeng, Y.; Yu, H.; Li, B.; Wang, M.; Braaten, J.; Liu, J.; Meyer, H. M.; Lucero, M.; Kropf, A. J.; Alp, E. E.; Gong, Q.; Shi, Q.; Feng, Z.; Xu, H.; Wang, G.; Myers, D. J.; Xie, J.; Cullen, D. A.; Litster, S.; Wu, G. Atomically Dispersed Iron Sites with a Nitrogen–Carbon Coating as Highly Active and Durable Oxygen Reduction Catalysts for Fuel Cells. *Nat Energy* **2022**, 1–12. https://doi.org/10.1038/s41560-022-01062-1.

(22) Hauenstein, P.; Seeberger, D.; Wasserscheid, P.; Thiele, S. High Performance Direct Organic Fuel Cell Using the Acetone/Isopropanol Liquid Organic Hydrogen Carrier System. *Electrochemistry Communications* **2020**, *118*, 106786. https://doi.org/10.1016/j.elecom.2020.106786.

(23) Oshchepkov, A. G.; Braesch, G.; Bonnefont, A.; Savinova, E. R.; Chatenet, M. Recent Advances in the Understanding of Nickel-Based Catalysts for the Oxidation of Hydrogen-Containing Fuels in Alkaline Media. *ACS Catal.* **2020**, *10* (13), 7043–7068. https://doi.org/10.1021/acscatal.0c00101.

(24) Braesch, G.; Bonnefont, A.; Martin, V.; Savinova, E. R.; Chatenet, M. Borohydride Oxidation Reaction Mechanisms and Poisoning Effects on Au, Pt and Pd Bulk Electrodes: From Model (Low) to Direct Borohydride Fuel Cell Operating (High) Concentrations. *Electrochimica Acta* **2018**, *273*, 483–494. https://doi.org/10.1016/j.electacta.2018.04.068.

(25) Wang, Z.; Parrondo, J.; He, C.; Sankarasubramanian, S.; Ramani, V. Efficient PH-Gradient-Enabled Microscale Bipolar Interfaces in Direct Borohydride Fuel Cells. *Nature Energy* **2019**, *4* (4), 281–289. https://doi.org/10.1038/s41560-019-0330-5.

(26) Wang, Z.; Sankarasubramanian, S.; Ramani, V. Reactant-Transport Engineering Approach to High-Power Direct Borohydride Fuel Cells. *Cell Reports Physical Science* **2020**, *1* (7), 100084. https://doi.org/10.1016/j.xcrp.2020.100084.

(27) Liu, B. H.; Li, Z. P.; Suda, S. Anodic Oxidation of Alkali Borohydrides Catalyzed by Nickel. *J. Electrochem. Soc.* **2003**, *150* (3), A398. https://doi.org/10.1149/1.1553785.

(28) Oshchepkov, A. G.; Braesch, G.; Ould-Amara, S.; Rostamikia, G.; Maranzana, G.; Bonnefont, A.; Papaefthimiou, V.; Janik, M. J.; Chatenet, M.; Savinova, E. R. Nickel Metal Nanoparticles as Anode Electrocatalysts for Highly Efficient Direct Borohydride Fuel Cells. *ACS Catal.* **2019**, 8520–8528. https://doi.org/10.1021/acscatal.9b01616.

(29) Braesch, G.; Oshchepkov, A. G.; Bonnefont, A.; Asonkeng, F.; Maurer, T.; Maranzana, G.; Savinova, E. R.; Chatenet, M. Nickel 3D Structures Enhanced by Electrodeposition of Nickel Nanoparticles as High Performance Anodes for Direct Borohydride Fuel Cells. *ChemElectroChem* **2020**, *7* (7), 1789–1799. https://doi.org/10.1002/celc.202000254.

(30) Katsounaros, I.; B. Schneider, W.; C. Meier, J.; Benedikt, U.; Ulrich Biedermann, P.; A. Auer, A.; J. Mayrhofer, K. J. Hydrogen Peroxide Electrochemistry on Platinum: Towards Understanding the Oxygen Reduction Reaction Mechanism. *Physical Chemistry Chemical Physics* **2012**, *14* (20), 7384–7391. https://doi.org/10.1039/C2CP40616K.

(31) Amirfakhri, S. J.; Pascone, P.-A.; Meunier, J.-L.; Berk, D. Fe–N-Doped Graphene as a Superior Catalyst for H2O2 Reduction Reaction in Neutral Solution. *Journal of Catalysis* **2015**, *323*, 55–64. https://doi.org/10.1016/j.jcat.2014.12.020.

(32) Bae, G.; Chung, M. W.; Ji, S. G.; Jaouen, F.; Choi, C. H. PH Effect on the H2O2-Induced Deactivation of Fe-N-C Catalysts. *ACS Catal.* **2020**, *10* (15), 8485–8495. https://doi.org/10.1021/acscatal.0c00948.

(33) Yang, X.; Zeng, Y.; Alnoush, W.; Hou, Y.; Higgins, D.; Wu, G. Tuning Two-Electron Oxygen-Reduction Pathways for H2O2 Electrosynthesis via Engineering Atomically Dispersed Single Metal Site Catalysts. *Advanced Materials* **2022**, *34* (23), 2107954. https://doi.org/10.1002/adma.202107954.

(34) Sun, Y.; Sinev, I.; Ju, W.; Bergmann, A.; Dresp, S.; Kühl, S.; Spöri, C.; Schmies, H.; Wang, H.; Bernsmeier, D.; Paul, B.; Schmack, R.; Kraehnert, R.; Roldan Cuenya, B.; Strasser, P. Efficient Electrochemical Hydrogen Peroxide Production from Molecular Oxygen on Nitrogen-Doped Mesoporous Carbon Catalysts. *ACS Catal.* **2018**, *8* (4), 2844–2856. https://doi.org/10.1021/acscatal.7b03464.

(35) Zhao, X.; Liu, Y. Origin of Selective Production of Hydrogen Peroxide by Electrochemical Oxygen Reduction. *J. Am. Chem. Soc.* **2021**, *143* (25), 9423–9428. https://doi.org/10.1021/jacs.1c02186.

(36) Rietveld, H. M. A Profile Refinement Method for Nuclear and Magnetic Structures. *J Appl Cryst* **1969**, *2* (2), 65–71. https://doi.org/10.1107/S0021889869006558.

(37) Canjura Rodriguez, P.; Gallandat, N.; Züttel, A. Accurate Measurement of Pressure-Composition Isotherms and Determination of Thermodynamic and Kinetic Parameters of Metal Hydrides. *International Journal of Hydrogen Energy* **2019**, *44* (26), 13583–13591. https://doi.org/10.1016/j.ijhydene.2019.03.224.

(38) Liu, B. H.; Li, Z. P.; Zhu, J. K. Sodium Borohydride Formation When Mg Reacts with Hydrous Sodium Borates under Hydrogen. *Journal of Alloys and Compounds* **2009**, *476* (1), L16–L20. https://doi.org/10.1016/j.jallcom.2008.09.057.

Chapter 2 Interfacial effect between aluminium-based complex hydrides and nickel-containing porous carbon sheets

Youngdon Ko[1, 2], Loris Lombardo[1, 2], Mo Li[1, 2], Emad Oveisi[3], Heena Yang[1, 2]*, Andreas Züttel[1, 2]

[1] Laboratory of Materials for Renewable Energy (LMER), Institute of Chemical Sciences and Engineering (ISIC), Basic Science Faculty (SB), École Polytechnique Fédérale de Lausanne (EPFL) Valais/Wallis, Energypolis, Rue de l'Industrie 17, 1951 Sion, Switzerland

[2] Empa Materials Science and Technology, 8600 Dübendorf, Switzerland

[3] Interdisciplinary Centre for Electron Microscopy (CIME), École Polytechnique Fédérale de Lausanne (EPFL), 1015 Lausanne, Switzerland

*Corresponding author: heena.yang@epfl.ch

Postprint version: this section has been published as a full-length article in *ACS Applied Energy Materials* **2020**, 3, 10, 9685−9695. DOI: 10.1021/acsaem.0c01262.

Edit: caption numbers of figures, tables, and equations were edited to match the thesis chapter number.

Permission to reproduce: reproduced with permission from the publisher.

Abstract

Supported aluminum-based complex hydrides (alanates) were investigated in view of their interaction at the interface. A nickel-containing porous carbon sheets (Ni-PCS) was combined with various alanates, resulting in a decreased of the decomposition temperature and reduced volume expansion of the upon decomposition. The interaction of alanates and alanates with Ni-PCS were observed by in situ X-ray diffraction (XRD), which found that alanate expanded during thermolysis and that Ni-PCS prevented layer changes by creating a path for hydrogen to escape from the liquid layer. The thermal desorption properties of $LiAlH_4$, $NaAlH_4$, and $Mg(AlH_4)_2$ containing Ni-PCS were investigated and compared. The catalytic activity of Ni-PCS depends on the electronegativity of the cation (Li, Na or Mg) in $M(AlH_4)$. We observed that the catalyst had stronger effects when the cations have lower electronegativity. Thus, $NaAlH_4$, which has the lowest electronegativity value among the examined alanates, was greatly affected by the Ni catalyst, with an onset decomposition temperature decreased from 140°C to 111°C.

2.1 Introduction

In the near future, with the rapid increase in renewable energy production, energy storage technology will be the primary challenge. Hydrogen, which can store large amounts of energy at low costs, is regarded as an important technology.[1] Hydrogen storage in a solid material is considered to be a potential storage method for mobile and stationary applications.[2] Complex hydrides have high gravimetric and volumetric capacities among the various solid-state hydrogen storage materials. Several types of complex hydrides combine alkali and alkaline earth salts with alanates, amides, and borohydrides.[3–5] Alanates have attracted increasing attention ever since Bogdanovic and Schwickardi discovered a method to reversibly hydrogenate $NaAlH_4$ with titanium doping on

aluminum.[6] Based on that research, a lithium alanate rehydrogenation reaction was also investigated, using Ti doping.[7–10] In general, rehydrogenation of complex hydrides is challenging, but new facile and low cost methods techniques have been recently reported.[11–14] Although many rehydrogenation studies have been performed using Ti catalysts, studies examining the hydrogen desorption of alanates at low temperatures have also been performed with various catalysts to reach the temperatures used in proton exchange membrane fuel cells (PEMFC, < 80°C). Various additives can be used to reduce the hydrogen desorption temperatures of complex hydrides. For example, V, Fe, Ni, Ce, Pt, Mn, C, and ionic liquids have previously been studied.[15–23] Another method is nano-sizing complex hydrides by confining them into host materials.[24–34] The impregnation and direct synthesis of complex hydrides inside of pores have been used to prepare nanoconfined hydrides.[26,30,31,35]

Carbon-based materials have been extensively investigated as adsorbent, supporting material, catalyst, photocatalyst.[36–40] Especially, porous carbon structure with high surface area has an admirable capability to remove toxic gas with a highly accessible active site.[41–44] In this paper, the porous carbon sheets (PCS) is a supporting material for the distribution of the nickel catalyst. Additionally, we investigated the interfacial behavior between PCS and alanate during thermolysis.

Nickel has been used as a catalyst in various fields, including the hydrogenation of CO_2, steam reforming processes, and carbon nanotube (CNT) synthesis.[45–48] In the field of hydrogen storage, Ni with a carbon structure has been investigated for hydrogen storage through the hydrogen spill-over effect.[49–53] Ni was used as a catalyst for the dissociation of hydrogen gas, using the hydrogen spillover effect and carbon materials as storage media, due to their high specific surface areas. A Ni catalyst has also been used to reduce the hydrogen desorption temperatures of complex hydrides.[17,54–56] Additionally, Ni plays a role in the AB_5 and AB_2 metal hydrides alloys that have long been used for batteries and hydrogen storage. In these alloys, Ni belongs to the B component, which improves the reversibility of the metal hydride by preventing the oxidation of the A component.[57] The catalytic activity of Ni in alanates is associated with its electronegativity value of 1.91. Nakamori et al. demonstrated that the exchange of cations with higher electronegativity values than sodium to $NaBH_4$ can modify the dehydrogenation properties.[58]

In this study, we synthesized a nickel-containing porous carbon sheets (Ni-PCS) as a catalyst for enhancing the hydrogen release of alanates at low temperatures. We investigated three different alanates: lithium alanate ($LiAlH_4$), sodium alanate ($NaAlH_4$), and magnesium alanate [$Mg(AlH_4)_2$]. The electronegativity values of the cations bound to the alanates used in this study are 0.98, 0.93, and 1.31 for Li, Na, and Mg, respectively.[59] The hydrogen desorption and activation energy of each alanate were compared.

2.2 Experimental section

2.2.1 Synthesis of porous carbon sheets and doping nickel nanoparticle

Phosphorous pentoxide (98%) and sucrose (99%) were purchased from Sigma-Aldrich and used as received. The PCS was produced using the method described by Chen et al.[60] Phosphorous pentoxide and sucrose were mixed with a mortar and pestle, for 30 min, under argon atmosphere. The mixed powder was placed in a 200 mL Teflon-lined autoclave and heated in an oven at 200°C, for 6 h. The obtained black powder was calcined at 450°C under argon gas for 1 h, using a ramp rate of 3°C·min^{-1}, and heated to 900°C for 3 h, using a ramp rate of 5 °C·min^{-1}. A total of 0.1 g of the synthesized PCS was dispersed in 46 mL ethylene glycol (99%), using a sonicator. After dissolving 0.92 g nickel chloride in 2 mL ethylene glycol and sonicating for 2 h, the $NiCl_2$ solution was added to the PCS dispersed solution. After 2 h stirring, the solution was heated to 140°C, and 0.1 g of $NaBH_4$ was added, with continuous stirring for 1 h. The mixture was cooled to room temperature, washed two times with deionized water, and dried in a vacuum oven at 60°C, overnight.

2.2.2 Preparation of aluminum-based hydrides with Ni-PCS

Commercial $LiAlH_4$ (95%), $NaAlH_4$ (93%), and $MgCl_2$ (99.9%) were purchased from Sigma-Aldrich and used as received. For the synthesis of $LiAlH_4$ with Ni-PCS, $LiAlH_4$ and Ni-PCS were mixed with a mortar for 15 min. The amount of Ni-PCS in $LiAlH_4$ was 5 wt%. The mixed powder was then placed into a stainless-steel milling jar, with a stainless-steel ball, and high energy ball-milled (SPEX M8000 Mixer/Mill) for 15 min. The ball to powder weight ratio was maintained at 40:1. The $LiAlH_4$ and $LiAlH_4$ ball-milled samples correspond to bulk $LiAlH_4$ and ball-milled samples, without additional materials, using the same ball-to-powder weight ratio. For $LiAlH_4$ with PCS, the same method was employed, using 5 wt% PCS as an additive. $NaAlH_4$ with Ni-PCS was synthesized using the same method. $LiAlH_4$ and $MgCl_2$ were used to synthesize $Mg(AlH_4)_2$, using the metathesis method. The molar ratio of $MgCl_2$ to $LiAlH_4$ was 1:2. After mixing $MgCl_2$ and $LiAlH_4$ with a mortar, the powder was ball-milled for 90 min. The addition of Ni-PCS used the same procedure used to generate $LiAlH_4$ with Ni-PCS and $NaAlH_4$ with Ni-PCS. All sample preparations were performed using a high-purity glove box (MBRAUN) filled with Ar (Ar < 0.1 ppm, H_2O < 0.1 ppm).

2.2.3 Characterization

The morphologies of synthesized PCS and Ni-PCS were characterized by transmission electron microscopy (TEM, JEOL JEM-3010 and FEI Tecnai G2 Spirit Twin). Selected area diffraction pattern (SADP) for the Ni-PCS were experimentally obtained at 120 kV and compared with simulated pattern. Morphology of the samples were characterized by scanning electron microscopy (SEM, FEI Teneo). Image J was used to measure the particle sizes of sample by first setting the scale according to the SEM scale bar. Thermogravimetric analysis (TGA, TA Q-Series TGA Q500) curves were obtained for synthesized PCS and Ni-PCS. Samples were loaded onto a tared platinum pan. The airflow rate was 25 mL·min^{-1}, with heating at a rate of 10°C·min^{-1}. The Brunauer-Emmett-Teller (BET) specific surface area of PCS was estimated using N_2 adsorption, at 77 K (Micrometrics, Tristar II 3020). X-ray photoelectron spectroscopy (XPS, SPECS GmbH, Phoibos 100) experiments were performed in an ultra-high vacuum (UHV) chamber, equipped with a Mg Kα (hv = 1253.6 eV) X-ray source and a hemispherical energy analyzer. The XPS spectra were recorded using a pass energy of 20 eV for narrow scans. Binding energies were referenced against the C1s binding energy of adventitious carbon (284.5 eV). The Ni concentration of $LiAlH_4$ with Ni-PCS was confirmed using inductively coupled plasma optical emission spectrometry (ICP-OES, Agilent 5110). The crystal phases of the alanate materials were determined by X-ray diffraction (XRD, Bruker D8 Discover), using copper, CuKα (λ = 0.1543 nm) radiation (40 kV and 40 mA), at a heating rate of 0.5°C·min^{-1}, in a home-made *in situ* cell under vacuum.[61] Differential scanning calorimetry (DSC, Mettler Toledo HP DSC827^e) was performed at different heating rates under Ar flow. Fourier transform infrared spectroscopy (FT-IR, PerkinElmer Spectrum Two) spectra of the alanates were recorded in the range of 400 to 4000 cm^{-1}. The hydrogen desorption properties were measured by an advanced gas analyzing system (AGAS Mano, GRZ Technologies). All experiments were conducted under vacuum, and the temperature was increased to 500°C, using a heating rate of 5°C·min^{-1}, and maintained for 20 min. The hydrogen gas flow was recorded to calculate the hydrogen amount in each sample. The volume change was measured the height of pellets under 1 bar Ar, and the temperature was increased to 200°C.

2.3 Results and discussion

2.3.1 Nickel with porous carbon sheets catalyst

The microstructure and texture of the synthesized Ni-PCS were examined using several characterization methods. TEM images of the PCS and Ni-PCS are shown in Figure 2.1a and b, respectively. The PCS is a turbostratic-activated carbon, with a thickness of 6–10 nm (Figure S2.1). N_2 isotherm adsorption and the pore size distribution plot confirmed a high specific surface area of 2,572 m^2·g^{-1}, with an average pore sizes of 2.8 nm (Figure

2.1d). The PCS contains many micropores throughout the entire structure, creating a high specific surface area. We can observe the pores in the TEM image, as shown in Figure 2.1a. The Ni-PCS TEM image shows that Ni has been successfully doped onto the PCS (Figure 2.1b). SADP of Ni-PCS was conducted to identify the crystalline phase structure (Figure S2.2). In the figure S2.2b, experimentally obtained SADP ring pattern and simulated SADP ring pattern are compared. Mostly the nickel particle consists of metallic Ni and small amount of NiO phase. The XRD peaks for the Ni-PCS (Figure 2.1c) allow us to estimate an average crystalline Ni nanoparticle size of 4.3 nm, using the Scherrer equation.[62] The amount of Ni nanoparticles on the PCS was estimated using thermogravimetric analysis. The difference in weight between the PCS and the Ni-PCS was 27 wt%, which corresponds to the Ni amount in the Ni-PCS (Figure S2.3). The chemical status on the surface of the Ni-PCS was investigated by XPS (Figure S2.4). Three peaks can be deconvoluted in the C1s spectra (Figure S2.4a), at approximately 284.8, 286.7, and 289.2 eV. These peaks can be assigned to C-C bonds and carbon atoms bound to one oxygen atom by either a single bond (C-O) or a double bond (C=O), respectively.[63] The O1s peaks (Figure S2.4b) at 531.7 and 533.1 eV were assigned to C=O and C-O, respectively.[63] The Ni $2p_{3/2}$ spectrum displayed at 856.2 eV, with a satellite peak at 861.9 eV, whereas the Ni $2p_{1/2}$ spectrum appeared at 874.8 eV, with a satellite peak at 881.1 eV, as shown in Figure S2.4c.[64] These peaks could be ascribed to the NiO phase. The surface of Ni remains oxide groups because no reduction treatment was performed after synthesis. However, according to the XRD results, Ni has a metallic crystal structure, which confirms that only the surface contains oxide groups, while the inside is composed of metal.

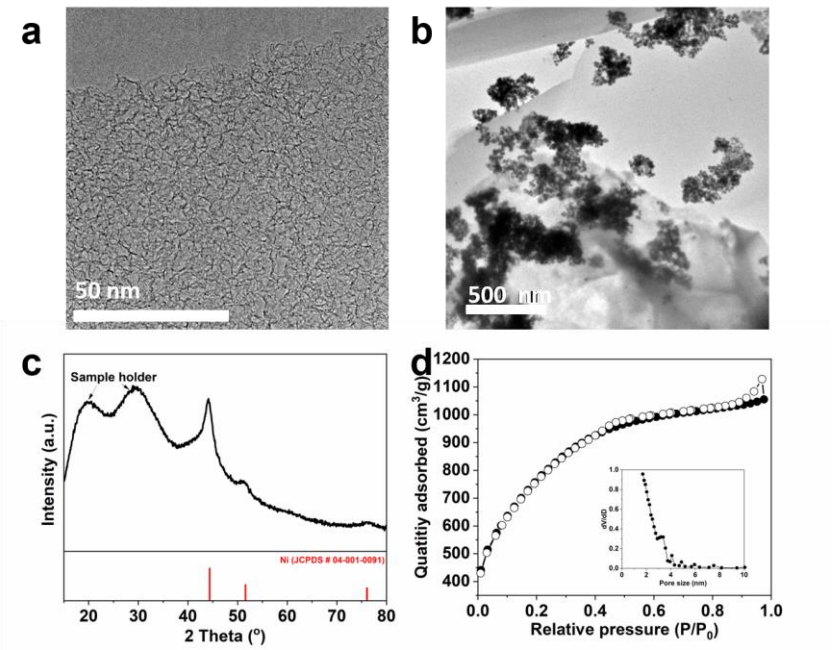

Figure 2.1 TEM image of (a) porous carbon sheets and (b) nickel-containing porous carbon sheets (Ni-PCS). (c) XRD patterns of Ni-PCS. (d) N_2 adsorption isotherms, with pore size distribution graph for PCS in the inset.

2.3.2 Lithium alanate and the catalytic effect of Ni-PCS

The crystal structures of $LiAlH_4$ and $LiAlH_4$ with Ni-PCS were determined by *in situ* XRD. In Figure 2.2, the XRD peaks for $LiAlH_4$ are listed, depending on the *in situ* cell temperature. At 140°C, Li_3AlH_6 and Al characteristic peaks appeared, due to the decomposition of $LiAlH_4$ (Figure 2.2a). Li_3AlH_6 characteristic peaks appeared until 190°C (Figure 2.2b). During the *in situ* XRD measurements of bulk $LiAlH_4$, only the copper (Cu) sample holder characteristic peaks (2θ = 43.1° and 50.2°) were observed at 200°C. The alanate decomposition process exhibits internal friction and dynamic elastic modulus, which indicates an irreversible layer change transformation for the

alanate sample in the XRD cell, as shown in Figure S2.5a and b. According to Levi et al., the nucleation and growth of a new phase in alanate materials cause internal friction effects.[65] The observed transformation may be caused by the melting of $LiAlH_4$ to form a liquid layer. Therefore, the liquid layer of $LiAlH_4$ blocks hydrogen gas from escaping, and a Li_3AlH_6 solid is formed simultaneously. Interestingly, in the $LiAlH_4$ with Ni-PCS sample, the $LiAlH_4$ layer change in the XRD cell was barely observable (Figure S2.5c and d). A schematic image of the interfacial behavior between $LiAlH_4$ and the $LiAlH_4$ with Ni-PCS layer during *in situ* XRD is shown in Figure 2.3. During the $LiAlH_4$ decomposition reaction, the solid $LiAlH_4$ layer at the bottom changes to a liquid $LiAlH_4$ layer at 150°C. Then, at 160°C, the bottom liquid layer releases hydrogen and changes phase, to form a solid Li_3AlH_6 layer. Simultaneously, hydrogen gas bubbles through the liquid $LiAlH_4$ layer. The solid Li_3AlH_6 layer puffs up from the sample holder at 200°C. For $LiAlH_4$ with Ni-PCS, decomposition started at 94°C.

As shown in Figure S2.5d, $LiAlH_4$ with Ni-PCS displayed no layer changes during the entire reaction. The Ni-PCS might prevent the expansion of $LiAlH_4$ with increasing temperatures and create a path for hydrogen to escape. The characteristic peaks for Al appear in the $LiAlH_4$ with Ni-PCS samples before heating, as shown in Figure 2.2c. A part of the alanate in $LiAlH_4$ with Ni-PCS decomposed during ball-milling and reduced nickel oxide and the PCS. The thermal decomposition of $LiAlH_4$ with Ni-PCS continues until 150°C (Figure 2.2c and d). The hydrogen desorption temperature of $LiAlH_4$ with Ni-PCS significantly decreased to 94°C, compared with 150°C for $LiAlH_4$. Although XRD could not confirm the crystal structure of Ni inside the $LiAlH_4$ with Ni-PCS sample, 0.8 mol% of Ni was present, as determined by ICP-OES. The addition of Ni-PCS to $LiAlH_4$ serves as a catalyst for the destabilization of $LiAlH_4$. The electronegativity value of Ni is 1.91, which is higher than that of Li (0.98). Therefore, destabilization by charge transfer occurred, which decreased the decomposition temperature of $[AlH_4]^-$. The intensity of the Li_3AlH_6 characteristic peaks in the $LiAlH_4$ with Ni-PCS sample decreased from 150°C to 210°C, and only the LiH characteristic peak remained (Figure 2.2d and e). After increasing the temperature to 260°C, the *in situ* XRD cell was cooled to room temperature. The Al peak intensity of the $LiAlH_4$ with Ni-PCS sample increased, due to the crystallization of Al and the contraction of the sample to the focal point of the X-ray.

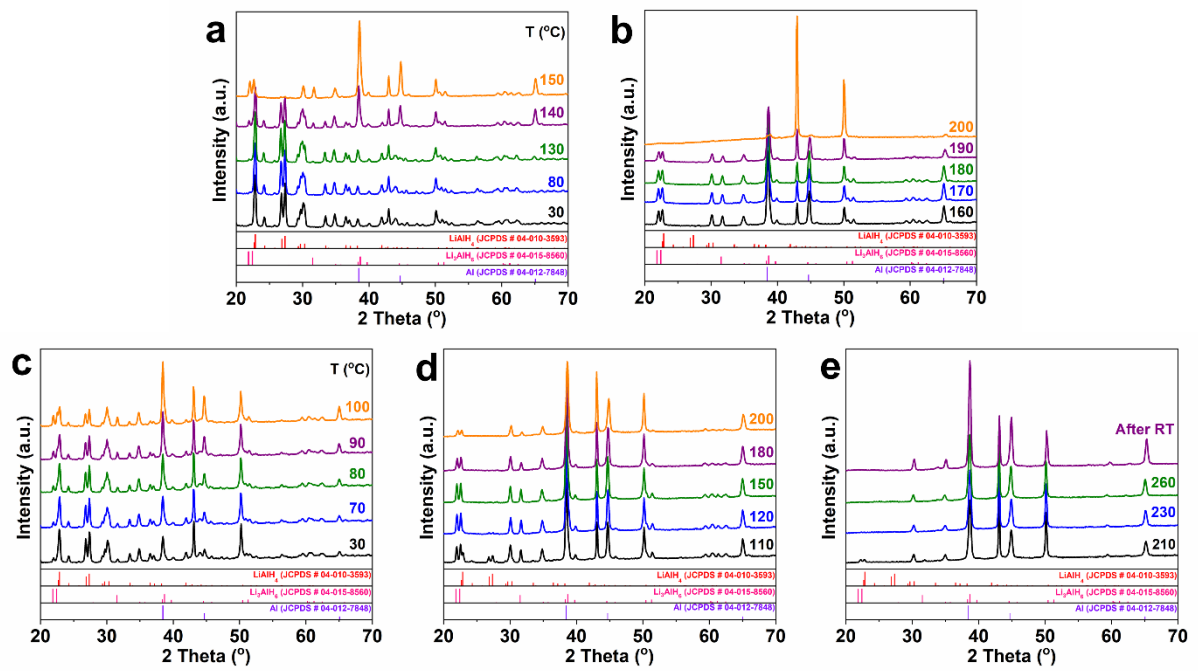

Figure 2.2 *In situ* powder XRD spectra of (a) $LiAlH_4$ at the temperature region, 30°C – 150°C, (b) 160°C – 200°C, and (c) $LiAlH_4$ with Ni-PCS at the temperature region, 30°C – 100°C, (d) 110°C – 200°C, (e) 210°C – 260°C with after cooling down to room temperature. The JCPDS of $LiAlH_4$, Li_3AlH_6, and Al were indicated below the spectra.

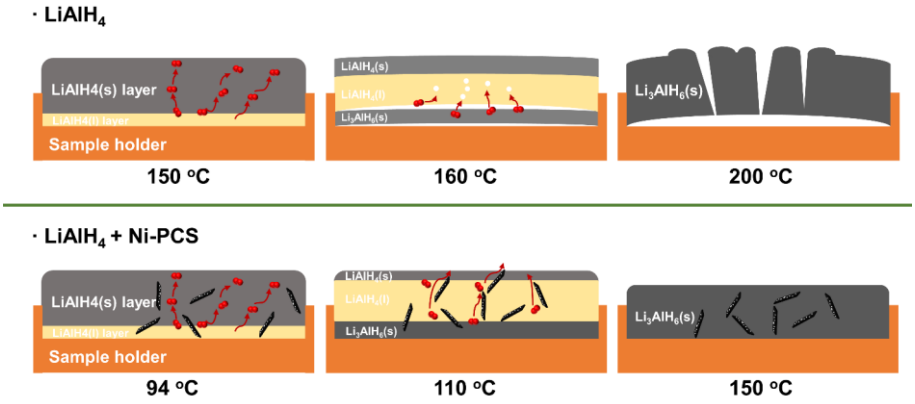

Figure 2.3 Schematic image showing the interfacial behavior of $LiAlH_4$ and $LiAlH_4$ with Ni-PCS during decomposition.

The thermal decomposition behaviors of $LiAlH_4$, ball-milled $LiAlH_4$, $LiAlH_4$ with PCS, and $LiAlH_4$ with Ni-PCS were investigated at different heating rates by DSC. The results are presented in Figures 2.4 and S2.6. Two exothermic peaks and three endothermic peaks were observed for $LiAlH_4$.[66,67] The first, small exothermic peak at 149°C corresponds to the interaction between $LiAlH_4$ and surface hydroxyl impurities. The following endothermic peak, at 170°C, was attributed to the melting of $LiAlH_4$ (R1). After the melting peak of $LiAlH_4$, the exothermic peak at 209°C is due to the hydrogen evolution in liquid $LiAlH_4$ (R2). The next endothermic peak, at 256°C, corresponds to the decomposition of Li_3AlH_6 (R3). The last endothermic peak corresponds to the decomposition of LiH (R4). The DSC spectra of samples, using a 10°C·min^{-1} heating rate, are shown in Figure 2.4. Compared with the other samples, the surface hydroxyl impurities peak for $LiAlH_4$ with Ni-PCS is reduced by 34°C. Additionally, the melting peak (R1, 164°C) enthalpy of $LiAlH_4$ with Ni-PCS was the lowest among the samples. This phenomenon creates an overlap between the exothermic R2 peak and the $LiAlH_4$ melting peak (R1). In addition, the Li_3AlH_6 decomposition peak (R3) has the lowest temperature, of 211°C, which is 45°C lower than the maximum value of 256°C. The activation energy of hydrogen desorption in liquid $LiAlH_4$ was calculated by Kissinger's equation (Figure S2.7a)[68] and was found to be 57 kJ·mol^{-1} for $LiAlH_4$ with Ni-PCS, which is significantly lower than the 79 kJ·mol^{-1} for $LiAlH_4$. And the activation energies of ball-milled $LiAlH_4$ (70 kJ·mol^{-1}) and $LiAlH_4$ with PCS (73 kJ·mol^{-1}) were also decreased compared with that of $LiAlH_4$, but in smaller extent. However, the calculated activation energy of the Li_3AlH_6 decomposition step did not decrease in any sample, except Li_3AlH_6 with Ni-PCS (Figure S2.7b). The Li_3AlH_6 decomposition step corresponds to the release of hydrogen from liquid $LiAlH_4$ and the formation of the bulk foam solid Li_3AlH_6. Therefore, no additional size effect is provided by the ball-mill procedure. Interestingly, the activation energy of Li_3AlH_6 with Ni-PCS decreased to 81 kJ·mol^{-1}, which is lower than the 111 kJ·mol^{-1} for the Li_3AlH_6 sample. Therefore, Ni also affects the decomposition of Li_3AlH_6.

$$LiAlH_4\,(s) \rightarrow LiAlH_4\,(l) \quad (R1)$$

$$LiAlH_4\,(l) \rightarrow Li_3AlH_6\,(s) + 2\,Al + 3\,H_2 \quad (R2)$$

$$Li_3AlH_6\,(s) + 2\,Al \rightarrow 3\,LiH\,(s) + 3\,Al + 1.5\,H_2 \quad (R3)$$

$$LiH\,(s) \rightarrow Li\,(s) + \tfrac{1}{2}\,H_2 \quad (R4)$$

The dehydrogenation properties of the $LiAlH_4$ samples were investigated using a flow meter inside an AGAS (Figure 2.5a-c). Four different flow plots, with equal sample masses but different additives and synthesis methods, are shown in Figures 2.5a and b and S2.8. The flow plots for all samples were similar, except for $LiAlH_4$ with Ni-

PCS. The flow plot for $LiAlH_4$ with Ni-PCS shows three well-divided peaks, compared with the others (Figure 2.5b). These three peaks derive from hydrogen desorption, in agreement with the three decomposition steps, R2 - R4, observed by DSC. The flow plot for $LiAlH_4$ also consists of three peaks but does not show a sharp peak for the decomposition of Li_3AlH_6. Additionally, the R4 step is not finished at 500°C (Figure 2.5a). The hydrogen desorption capacity of each sample was calculated by the hydrogen flow plot, as shown in Figure 2.5c. The onset temperature of $LiAlH_4$ was 150°C, and the hydrogen desorbed amounts at R2, R3, and R4 were 4.73 wt%, 2.3 wt%, and 1.3 wt%, respectively (Table 2.1). In contrast, the R2 step of $LiAlH_4$ with Ni-PCS started at 94°C, and the R3 step also started at 160°C, as shown in Figure 2.5b. The hydrogen desorption temperature of $LiAlH_4$ with Ni-PCS decreased due to the Ni catalytic effect. Also, the ball-milling affects the decrease of decomposition temperature by increasing the interfacial surface area of $LiAlH_4$ particles. Zhu et al.[69] demonstrated the dominant role of the interface region for the hydrogenation and dehydrogenation conditions, such as temperature and pressure.

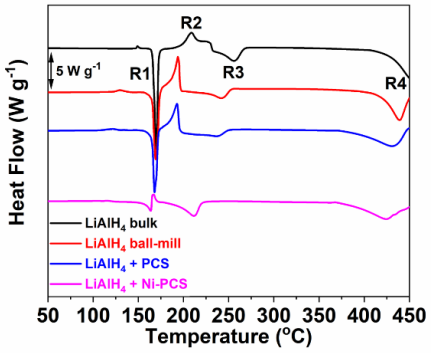

Figure 2.4 DSC profiles of $LiAlH_4$ bulk, ball-milled $LiAlH_4$, $LiAlH_4$ with PCS, and $LiAlH_4$ with Ni-PCS, using a 10°C·min^{-1} heating rate.

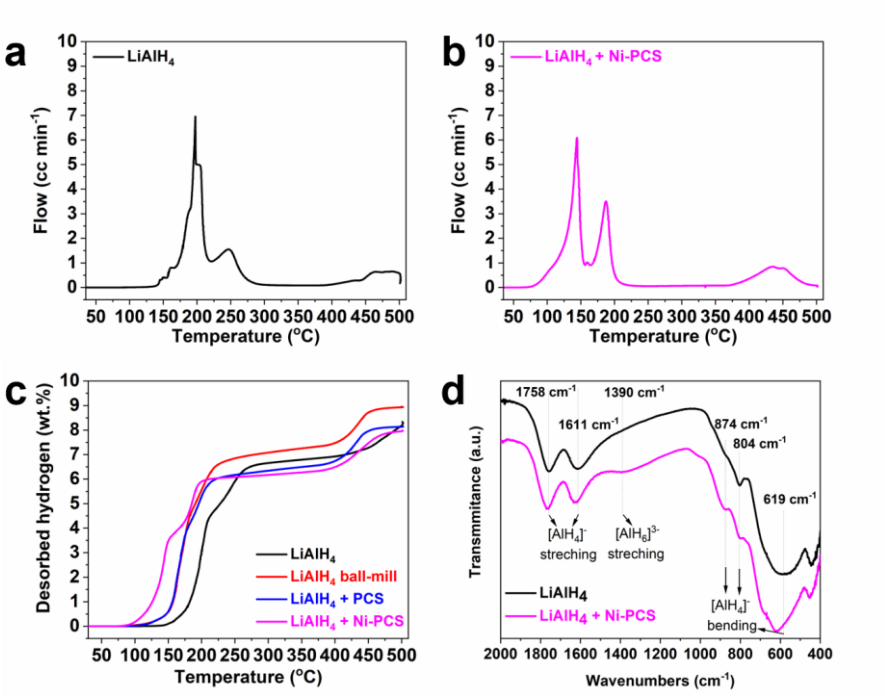

Figure 2.5 (a) Thermal desorption curves for $LiAlH_4$ and (b) $LiAlH_4$ with Ni-PCS. (c) Hydrogen desorption capacity curves. (d) FT-IR spectra for $LiAlH_4$ and $LiAlH_4$ with Ni-PCS.

Table 2.1. Decomposition temperatures and hydrogen desorption amounts for each sample.

Sample	$LiAlH_4$ T_{onset}[a]	R2 hydrogen (wt%)	Li_3AlH_6 T_{onset}	R3 hydrogen (wt%)	LiH T_{onset}	R4 hydrogen (wt%)	Total hydrogen (wt%)
$LiAlH_4$	150	4.73	220	2.3	416	1.3	8.33
$LiAlH_4$ ball-mill	115	4.59	183	2.77	383	1.59	8.95
$LiAlH_4$ + PCS	120	4.03	179	2.53	376	1.58	8.14
$LiAlH_4$ + Ni-PCS	94	3.84	160	2.49	371	1.64	7.97

[a] $LiAlH_4$ T_{onset}: the temperature at which 0.1 wt% hydrogen desorbed

2.3.3 Sodium alanate and the catalytic effect of Ni-PCS

In addition to $LiAlH_4$, the Ni-PCS catalytic effects on $NaAlH_4$ decomposition were investigated. The hydrogen desorption amounts for ball-milled $NaAlH_4$ and $NaAlH_4$ with Ni-PCS (Figure 2.6a) were calculated based on hydrogen flow, as shown in Figure S2.11. The decomposition onset temperature of ball-milled $NaAlH_4$ was 140°C, and the desorbed amount of hydrogen was 5.67 wt%. NaH decomposition started at 300°C, and the desorbed amount of hydrogen was 1.57 wt%. The total amount of hydrogen desorbed from ball-milled $NaAlH_4$ was 7.24 wt%. $NaAlH_4$ with Ni-PCS started to decompose at 111°C, 29°C below ball-milled $NaAlH_4$, and NaH decomposition started at 288°C. The hydrogen desorbed amount for the two steps was 4.74 wt% and 1.5 wt% respectively. The total amount of hydrogen desorbed in $NaAlH_4$ with Ni-PCS was 6.24 wt%, which is 1 wt% lower than for ball-milled $NaAlH_4$. The onset temperatures and hydrogen desorbed amounts for the $NaAlH_4$ samples are provided in Table 2.2.

The *in situ* XRD results for ball-milled $NaAlH_4$ and $NaAlH_4$ with Ni-PCS were compared, as shown in Figure S2.12. The XRD peaks for ball-milled $NaAlH_4$ are listed according to the *in situ* cell temperatures (Figure S2.12a and b). For ball-milled $NaAlH_4$, the XRD peak intensity of $NaAlH_4$ gradually decreased from 130°C to 180°C, followed by peaks shift at 190°C. The change in the XRD peak shape at 190°C can be explained by the same layer mechanism described in Scheme 1 for $LiAlH_4$. Based on DSC analysis (Figure S2.14a), the endothermic peak at 186°C represents the melting of $NaAlH_4$. Therefore, the increased peak intensity of Cu from the sample holder is due to sample displacement. As Na_3AlH_6 continued to decompose, the swollen sample contracted again and returned to the X-ray focal point, reducing the XRD peak of the sample holder. Figure S2.13a shows the shrinkage of the ball-milled $NaAlH_4$ sample after *in situ* XRD. For $NaAlH_4$ with Ni-PCS, all the decomposition steps were clearly observed by XRD (Figure S2.12c and d). The XRD peak for $NaAlH_4$ continuously decreased, until 200°C with the formation of Na_3AlH_6, followed by a large Na_3AlH_6 phase change at 210°C. The next step is the decomposition of Na_3AlH_6 to NaH, starting at 220°C. Once again, we confirmed that Ni-PCS prevented the expansion of the alanate. Figure S2.13b shows the unchanged layer of the $NaAlH_4$ with Ni-PCS sample after thermolysis.

The thermal decomposition properties of ball-milled $NaAlH_4$ and $NaAlH_4$ with Ni-PCS were measured by DSC, and the results are shown in Figures S2.14. The DSC spectra of ball-milled $NaAlH_4$ and $NaAlH_4$ with Ni-PCS differ between 220°C and 300°C. One exothermic and five endothermic peaks are observed for ball-milled $NaAlH_4$. The first, small exothermic peak, at 162°C, represents a small amount of hydroxide that exists at the surface of ball-milled $NaAlH_4$. The following endothermic peak. at 187°C, corresponded to the melting of $NaAlH_4$. The next three endothermic peaks, at 246°C, 276°C, and 297°C, were related to the decomposition of $NaAlH_4$, the structural transformation (α to β) of Na_3AlH_6, and the decomposition of Na_3AlH_6, respectively. The NaH decomposition step

corresponds to the last endothermic peak, at 358°C. The DSC spectra of $NaAlH_4$ with Ni-PCS shows one exothermic peak and three endothermic peaks. The exothermic peak at 168°C represents the surface hydroxide on the alanate. Unlike ball-milled $NaAlH_4$, the three endothermic peaks at 184°C, 246°C, and 359°C correspond to the melting of $NaAlH_4$, the decomposition of $NaAlH_4$, and the decomposition of NaH, respectively. The decomposition of $NaAlH_4$, the structural transformation of Na_3AlH_6, and the decomposition of Na_3AlH_6 were merged into one endothermic peak, at 246°C, due to the catalytic effect of Ni. The *in situ* XRD results for $NaAlH_4$ with Ni-PCS also showed that $NaAlH_4$ changes rapidly to Na_3AlH_6 at 210°C. The DSC results of ball-milled $NaAlH_4$ and $NaAlH_4$ with Ni-PCS were measured at various heating rates (Figure S2.14b and c). The activation energy of the first dehydrogenation step in liquid $NaAlH_4$ was calculated using Kissinger's equation (Figure 2.6b). The decomposition activation energies for ball-milled $NaAlH_4$ were found to be 109 kJ·mol^{-1} and 163·kJ mol^{-1}, for the decomposition of $NaAlH_4$ and Na_3AlH_6, respectively (Figure 2.6b and S2.14d). Compared with ball-milled $NaAlH_4$, $NaAlH_4$ with Ni-PCS has a 15 kJ·mol^{-1} lower activation energy during $NaAlH_4$ decomposition. However, the activation energy of Na_3AlH_6 in $NaAlH_4$ with Ni-PCS could not be calculated, due to the overlap of the peaks.

FT-IR spectra of ball-milled $NaAlH_4$ and $NaAlH_4$ with Ni-PCS were compared, in Figure S2.15. The stretching vibration frequency of Al-H appeared at 1,664 cm^{-1}. Two bending vibration frequencies, at 901 cm^{-1} and 535 cm^{-1}, can be observed. Compared with ball-milled $NaAlH_4$ the $NaAlH_4$ with Ni-PCS bending vibration peak has a broad and reduced intensity, due to the decomposition of $NaAlH_4$ during the ball-mill process.

The morphology of ball-milled $NaAlH_4$ and $NaAlH_4$ with Ni-PCS are shown in SEM images (Figure S2.16). Mean particle size of both samples are similar after ball-mill (7.0 µm and 6.9 µm for ball-milled $NaAlH_4$ and $NaAlH_4$ with Ni-PCS). On the other hand, the $NaAlH_4$ crystalline size of $NaAlH_4$ with Ni-PCS decreased to 27.7 nm compared to 37.2 nm for ball-milled $NaAlH_4$ due to the decomposition of $NaAlH_4$ during ball-milling with the presence of Ni.

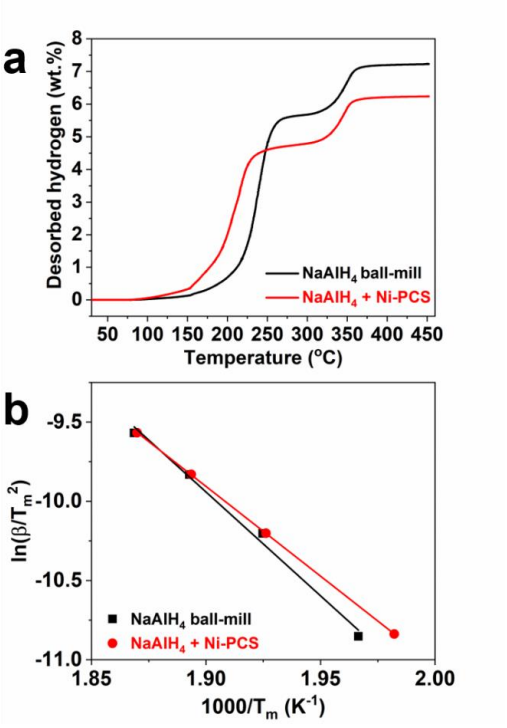

Figure 2.6 (a) Hydrogen desorption capacity curves of ball-milled $NaAlH_4$ and $NaAlH_4$ with Ni-PCS. (b) Kissinger's plots for dehydrogenation of ball-milled $NaAlH_4$ (■, E_a: 109 kJ·mol^{-1}) and $NaAlH_4$ with Ni-PCS (●, E_a: 94 kJ·mol^{-1}).

Table 2.2 Decomposition temperatures and hydrogen desorption amounts for each $NaAlH_4$ sample.

Sample	$NaAlH_4$ T_{onset}[a]	$NaAlH_4$ + Na_3AlH_6 hydrogen (wt%)	NaH T_{onset}	NaH hydrogen (wt%)	Total hydrogen (wt%)
$NaAlH_4$ ball-mill	140	5.67	300	1.57	7.24
$NaAlH_4$ + Ni-PCS	111	4.74	288	1.5	6.24

[a] $NaAlH_4$ T_{onset}: the temperature at which 0.1 wt% hydrogen desorbed

2.3.4 Magnesium alanate and the catalytic effect of Ni-PCS

The catalytic effects of Ni-PCS on $Mg(AlH_4)_2$ were also investigated. $Mg(AlH_4)_2$ differs from $LiAlH_4$ and $NaAlH_4$ because of the presence of LiCl. As mentioned in the experimental section, $Mg(AlH_4)_2$ was synthesized using the metathesis method, from $LiAlH_4$ and $MgCl_2$. Therefore, the $Mg(AlH_4)_2$ sample has a relatively small amount of hydrogen desorption (3.87 wt%) compared with the theoretical amount (9.3 wt%)[70], due to the weight of LiCl in the sample. $Mg(AlH_4)_2$ is a kinetically stabilized hydride, with a high equilibrium pressure at room temperature.[71] Kinetically stabilized hydrides decompose even at room temperature, and experience rapid hydrogen desorption when a certain temperature is reached. Therefore, only two decomposition steps are present for $Mg(AlH_4)_2$. As shown in Figure S2.17, the thermal desorption curves show two distinct peaks. The first step is the decomposition of $Mg(AlH_4)_2$, and the second step represents MgH_2 decomposition. The total desorbed hydrogen amount for ball-milled $Mg(AlH_4)_2$ was 3.87 wt% (Figure 2.7a), consisting of 2.89 wt% and 0.98 wt% for the first and second steps, at onset temperatures of 146°C and 219°C, respectively. Compared with ball-milled $Mg(AlH_4)_2$, the onset temperature of $Mg(AlH_4)_2$ with Ni-PCS decreased, to 125°C, due to the catalytic effect of Ni-PCS, similar to the effect observed for $LiAlH_4$ and $NaAlH_4$. The total hydrogen desorption amount for $Mg(AlH_4)_2$ with Ni-PCS was 3.34 wt%, with 2.46 wt% and 0.88 wt%, hydrogen desorption occurring during the first and second steps, respectively. Hydrogen desorption amounts and onset temperatures for the $Mg(AlH_4)_2$ samples are summarized in Table 2.3.

The crystal phases and layer changes in ball-milled $Mg(AlH_4)_2$ and $Mg(AlH_4)_2$ with Ni-PCS were observed by *in situ* XRD, as shown in Figure S2.18. The crystal phase of $Mg(AlH_4)_2$ started to decrease at 150°C in ball-milled $Mg(AlH_4)_2$ (Figure S2.18a). Additionally, the crystal phase of LiCl decreased after 160°C, confirming the layer change during hydrogen desorption. The crystal phase of MgH_2 appeared after $Mg(AlH_4)_2$ decomposition. For $Mg(AlH_4)_2$ with Ni-PCS, the intensity of $Mg(AlH_4)_2$ started to decrease at 120°C, and small MgH_2 peaks were observed at 200°C (Figure S2.18e). Unlike ball-milled $Mg(AlH_4)_2$, almost no change in peak intensity was observed for LiCl as the temperature increases, which indicated that the layer did not change due to the effects of Ni-PCS. Additionally, the MgH_2 hydrogen desorption was finished before 250°C, due to the catalytic effects of Ni. Therefore, the MgH_2 peak was not observed after reducing the temperature of the *in situ* cell (Figure S2.18f).

The thermal decomposition behaviors of the $Mg(AlH_4)_2$ samples were observed by DSC, as shown in Figure S2.19a. In previous studies, the enthalpy change during the decomposition of $Mg(AlH_4)_2$ was sometimes described as endothermic and sometimes as exothermic. Fitchtner et al.[72] reported that the decomposition of $Mg(AlH_4)_2$ was endothermic, at 41 $kJ{\cdot}mol^{-1}$, and Cho et al.[73] reported an exothermic enthalpy change of -20.4 $kJ{\cdot}mol^{-1}$. For ball-milled $Mg(AlH_4)_2$, the decomposition of $Mg(AlH_4)_2$ shows an exothermic reaction. In contrast, the decomposition of $Mg(AlH_4)_2$ is endothermic for $Mg(AlH_4)_2$ with Ni-PCS. The catalytic effect of Ni may be combined with the exothermic peak and the following broad endothermic peak observed for ball-milled

$Mg(AlH_4)_2$. Additionally, the endothermic peak of MgH_2 shifted to a lower temperature. The activation energy of $Mg(AlH_4)_2$ decomposition was calculated by Kissinger's equation (Figure 2.7b). The exothermic peak was used to calculate the activation energy of ball-milled $Mg(AlH_4)_2$, and the endothermic peak was used to calculate the activation energy for $Mg(AlH_4)_2$ with Ni-PCS, as shown in Figure S2.19b and c, respectively. The activation energies of $Mg(AlH_4)_2$ decomposition was estimated to be 118 $kJ \cdot mol^{-1}$ and 103 $kJ \cdot mol^{-1}$ for ball-milled $Mg(AlH_4)_2$ and $Mg(AlH_4)_2$ with Ni-PCS, respectively.

The FT-IR spectra of ball-milled $Mg(AlH_4)_2$ and $Mg(AlH_4)_2$ with Ni-PCS were compared, in Figure S2.19d. The stretching vibration frequency of Al-H, at 1,818 cm^{-1}, and the bending vibration frequency, at 616 cm^{-1}, are consistent with previous reports.[73,74]

The morphology of ball-milled $Mg(AlH_4)_2$ and $Mg(AlH_4)_2$ with Ni-PCS are shown in SEM images (Figure S2.20). Mean particle size of $Mg(AlH_4)_2$ with Ni-PCS is 6.9 µm, which is bigger than 5.3 µm for ball-milled $Mg(AlH_4)_2$. The increase of the mean particle size compared to ball-milled $Mg(AlH_4)$ could come from small particles surrounding the Ni-PCS.

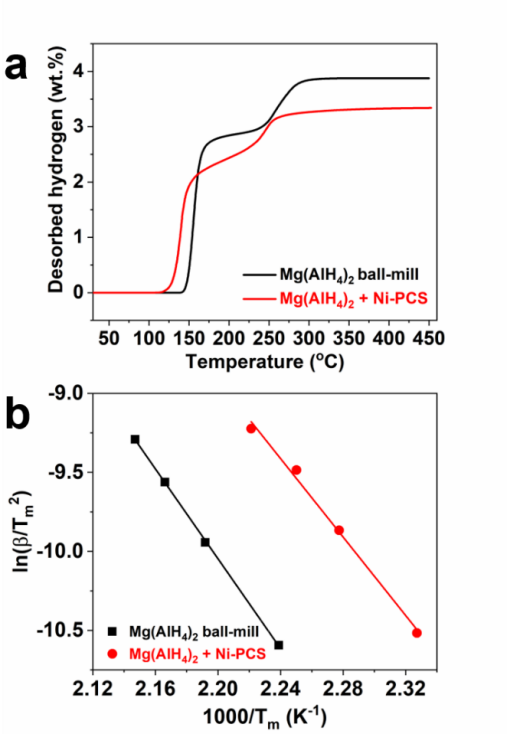

Figure 2.7 (a) Hydrogen desorption capacity curves of ball-milled $Mg(AlH_4)_2$, and $Mg(AlH_4)_2$ with Ni-PCS (b) Kissinger's plots for dehydrogenation of ball-milled $Mg(AlH_4)_2$ (■, E_a: 118 $kJ \cdot mol^{-1}$) and $Mg(AlH_4)_2$ with Ni-PCS (●, E_a: 103 $kJ \cdot mol^{-1}$).

Table 2.3 Decomposition temperatures and hydrogen desorption amounts for each $Mg(AlH_4)_2$ sample.

Sample	$Mg(AlH_4)_2$ T_{onset}[a]	$Mg(AlH_4)_2$ hydrogen (wt%)	MgH_2 T_{onset}	MgH_2 hydrogen (wt%)	Total hydrogen (wt%)
$Mg(AlH_4)_2$ ball-mill	146	2.89	219	0.98	3.87
$Mg(AlH_4)_2$ + Ni-PCS	125	2.46	204	0.88	3.34

[a] $Mg(AlH_4)_2$ T_{onset}: the temperature at which 0.1 wt% hydrogen desorbed

2.3.5 Ni-PCS dual functionality on alanate

The improvements of alanate property with addition of Ni-PCS were explained by *in situ* XRD, DSC, and hydrogen desorption measurement. First, the decrease of decomposition temperature was observed depending on the electronegativity difference between the cation of alanate and Ni (Figure 2.8a). In Figure 2.8a, the difference in electronegativity leads to effect on decreasing alanate decomposition temperature. Among the samples, the largest average decomposition temperature reduction is 30.5°C in $NaAlH_4$, which has the largest electronegativity difference, 0.98, between Ni and cation. The average decomposition temperature reduction is 26.2°C and 15°C for $LiAlH_4$ and $Mg(AlH_4)_2$. The electronegativity difference between Ni and cation is 0.93 and 0.6, Li and Mg, respectively. Therefore, the electronegativity difference between Ni and cation is the key parameter of catalytic activity in alanate.

The second functionality of Ni-PCS is to suppress the expansion of alanate during the thermolysis process. As mentioned before, the alanate expansion were compared for each alanate with and without Ni-PCS during thermolysis by *in situ* XRD. The alanate expansion was obviously observed through the sample displacement out of X-ray focus at the hydrogen desorption temperature. On the other hand, the alanate with Ni-PCS samples displayed no layer changes during the entire reaction. Also, the alanate expansion were observed from compacted pellets of ball-milled $LiAlH_4$, $NaAlH_4$, and $Mg(AlH_4)_2$ by measuring height change in function of temperature (Figure 2.8b, S2.21). The compacted pellet composed of ball-milled $NaAlH_4$ expands by 420 % of the original pellet height. After the pellet expansion reaches the peak, it contracted to 165 % of the original pellet height. On the other hand, the compacted pellet volume of $NaAlH_4$ with Ni-PCS expands only by 49 % and then contracted to 45 % of the original pellet height. Both results of volume expansion and *in situ* XRD clearly show that Ni-PCS prevents the expansion of the alanate. The volume expansion measurements of $LiAlH_4$ and $Mg(AlH_4)_2$ samples also confirmed that Ni-PCS is a great inhibitor of alanate expansion (Figure S2.21).

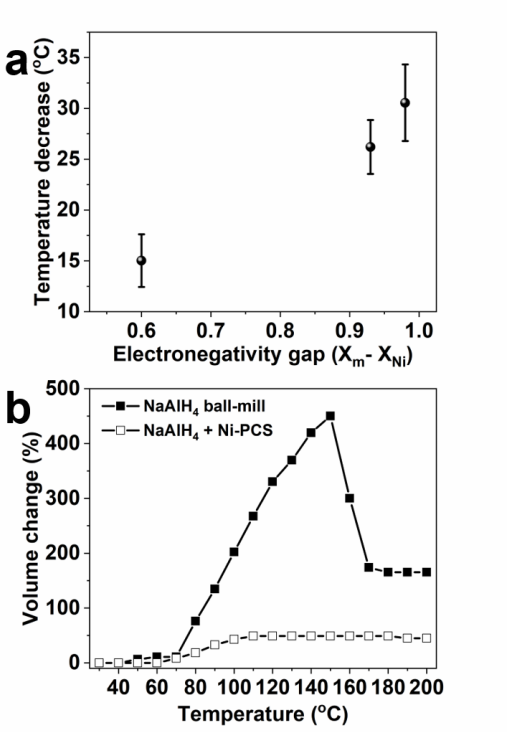

Figure 2.8 (a) Correlation between electronegativity gap (X_m - X_{Ni}) and alanate decomposition temperature decrease. (b) Volume change of the pellets of ball-milled $NaAlH_4$ and $NaAlH_4$ with Ni-PCS.

2.4 Conclusions

The catalytic effects of Ni-PCS on alanate materials were investigated for $LiAlH_4$, $NaAlH_4$, and $Mg(AlH_4)_2$, with a focus on electronegativity of the cation. The Ni-PCS played the dual role of preventing alanate layer changes and decreasing the decomposition temperature. We observed alanate layer and phase changes induced by heating, using *in situ* XRD, and found that these changes depended on the electronegativity values of the cation in the alanate. $NaAlH_4$, which has a higher electronegativity gap with Ni, was more strongly affected (greater decomposition temperature difference). Ni acts as a destabilizing agent on the alanates, reduces their decomposition temperatures and activation energy. The Ni catalyst in alanate was effective for lowering the activation energy by 13 - 15 $kJ \cdot mol^{-1}$. Also, the suppression of expansion with the addition of Ni-PCS was attributed to the creation of exit paths for hydrogen release. The understanding of alanate expansion mechanism through this study may applied to remain alanate structurally intact over the lifetime of a hydrogen storage system.

References

(1) Ehteshami, S. M. M.; Chan, S. H. The Role of Hydrogen and Fuel Cells to Store Renewable Energy in the Future Energy Network – Potentials and Challenges. *Energy Policy* **2014**, *73*, 103–109. https://doi.org/10.1016/j.enpol.2014.04.046.

(2) Schlapbach, L.; Züttel, A. Hydrogen-Storage Materials for Mobile Applications. *Nature* **2001**, *414* (6861), 353–358. https://doi.org/10.1038/35104634.

(3) Orimo, S.; Nakamori, Y.; Eliseo, J. R.; Züttel, A.; Jensen, C. M. Complex Hydrides for Hydrogen Storage. *Chem. Rev.* **2007**, *107* (10), 4111–4132. https://doi.org/10.1021/cr0501846.

(4) Ley, M. B.; Jepsen, L. H.; Lee, Y.-S.; Cho, Y. W.; Bellosta von Colbe, J. M.; Dornheim, M.; Rokni, M.; Jensen, J. O.; Sloth, M.; Filinchuk, Y.; Jørgensen, J. E.; Besenbacher, F.; Jensen, T. R. Complex Hydrides for Hydrogen Storage – New Perspectives. *Materials Today* **2014**, *17* (3), 122–128. https://doi.org/10.1016/j.mattod.2014.02.013.

(5) Schüth, F.; Bogdanović, B.; Felderhoff, M. Light Metal Hydrides and Complex Hydrides for Hydrogen Storage. *Chemical Communications* **2004**, *0* (20), 2249–2258. https://doi.org/10.1039/B406522K.

(6) Bogdanović, B.; Schwickardi, M. Ti-Doped Alkali Metal Aluminium Hydrides as Potential Novel Reversible Hydrogen Storage Materials1Invited Paper Presented at the International Symposium on Metal–Hydrogen Systems, Les Diablerets, August 25–30, 1996, Switzerland.1. *Journal of Alloys and Compounds* **1997**, *253–254*, 1–9. https://doi.org/10.1016/S0925-8388(96)03049-6.

(7) Liu, X.; Langmi, H. W.; Beattie, S. D.; Azenwi, F. F.; McGrady, G. S.; Jensen, C. M. Ti-Doped LiAlH4 for Hydrogen Storage: Synthesis, Catalyst Loading and Cycling Performance. *J. Am. Chem. Soc.* **2011**, *133* (39), 15593–15597. https://doi.org/10.1021/ja204976z.

(8) Liu, X.; McGrady, G. S.; Langmi, H. W.; Jensen, C. M. Facile Cycling of Ti-Doped LiAlH4 for High Performance Hydrogen Storage. *J. Am. Chem. Soc.* **2009**, *131* (14), 5032–5033. https://doi.org/10.1021/ja809917g.

(9) Graetz, J.; Wegrzyn, J.; Reilly, J. J. Regeneration of Lithium Aluminum Hydride. *J. Am. Chem. Soc.* **2008**, *130* (52), 17790–17794. https://doi.org/10.1021/ja805353w.

(10) Langmi, H. W.; McGrady, G. S.; Liu, X.; Jensen, C. M. Modification of the H2 Desorption Properties of LiAlH4 through Doping with Ti. *J. Phys. Chem. C* **2010**, *114* (23), 10666–10669. https://doi.org/10.1021/jp102641p.

(11) Ouyang, L.; Chen, W.; Liu, J.; Felderhoff, M.; Wang, H.; Zhu, M. Enhancing the Regeneration Process of Consumed NaBH4 for Hydrogen Storage. *Advanced Energy Materials* **2017**, *7* (19), 1700299. https://doi.org/10.1002/aenm.201700299.

(12) Chen, K.; Ouyang, L.; Zhong, H.; Liu, J.; Wang, H.; Shao, H.; Zhang, Y.; Zhu, M. Converting H + from Coordinated Water into H − Enables Super Facile Synthesis of LiBH 4. *Green Chemistry* **2019**, *21* (16), 4380–4387. https://doi.org/10.1039/C9GC01897B.

(13) Zhu, Y.; Ouyang, L.; Zhong, H.; Liu, J.; Wang, H.; Shao, H.; Huang, Z.; Zhu, M. Closing the Loop for Hydrogen Storage: Facile Regeneration of NaBH4 from Its Hydrolytic Product. *Angewandte Chemie International Edition* **2020**, *59* (22), 8623–8629. https://doi.org/10.1002/anie.201915988.

(14) Xian, K.; Gao, M.; Li, Z.; Gu, J.; Shen, Y.; Wang, S.; Yao, Z.; Liu, Y.; Pan, H. Superior Kinetic and Cyclic Performance of a 2D Titanium Carbide Incorporated 2LiH + MgB2 Composite toward Highly Reversible Hydrogen Storage. *ACS Appl. Energy Mater.* **2019**, *2* (7), 4853–4864. https://doi.org/10.1021/acsaem.9b00557.

(15) Blanchard, D.; Brinks, H. W.; Hauback, B. C.; Norby, P. Desorption of LiAlH4 with Ti- and V-Based Additives. *Materials Science and Engineering: B* **2004**, *108* (1), 54–59. https://doi.org/10.1016/j.mseb.2003.10.114.

(16) Varin, R. A.; Parviz, R. The Effects of the Micrometric and Nanometric Iron (Fe) Additives on the Mechanical and Thermal Dehydrogenation of Lithium Alanate (LiAlH4), Its Self-Discharge at Low Temperatures and Rehydrogenation. *International Journal of Hydrogen Energy* **2012**, *37* (11), 9088–9102. https://doi.org/10.1016/j.ijhydene.2012.02.182.

(17) Varin, R. A.; Zbroniec, L. The Effects of Nanometric Nickel (n-Ni) Catalyst on the Dehydrogenation and Rehydrogenation Behavior of Ball Milled Lithium Alanate (LiAlH4). *Journal of Alloys and Compounds* **2010**, *506* (2), 928–939. https://doi.org/10.1016/j.jallcom.2010.07.119.

(18) Varin, R. A.; Zbroniec, L. Fast and Slow Dehydrogenation of Ball Milled Lithium Alanate (LiAlH4) Catalyzed with Manganese Chloride (MnCl2) as Compared to Nanometric Nickel Catalyst. *Journal of Alloys and Compounds* **2011**, *509*, S736–S739. https://doi.org/10.1016/j.jallcom.2010.09.068.

(19) Choi, J.; Ha, T.; Park, J.; Lee, Y.-S.; Han, H. N.; Lee, J.; Shim, J.-H. Mechanochemical Synthesis of Ce3Al11 Powder and Its Catalytic Effect on the Hydrogen Sorption Properties of NaAlH4. *Journal of Alloys and Compounds* **2019**, *784*, 313–318. https://doi.org/10.1016/j.jallcom.2019.01.045.

(20) Tan, C.-Y.; Tsai, W.-T. Catalytic and Inhibitive Effects of Pd and Pt Decorated MWCNTs on the Dehydrogenation Behavior of LiAlH4. *International Journal of Hydrogen Energy* **2015**, *40* (32), 10185–10193. https://doi.org/10.1016/j.ijhydene.2015.06.106.

(21) Yang, H.; Lombardo, L.; Luo, W.; Kim, W.; Züttel, A. Hydrogen Storage Properties of Various Carbon Supported NaBH4 Prepared via Metathesis. *International Journal of Hydrogen Energy* **2018**, *43* (14), 7108–7116. https://doi.org/10.1016/j.ijhydene.2018.02.142.

(22) Lombardo, L.; Yang, H.; Züttel, A. Destabilizing Sodium Borohydride with an Ionic Liquid. *Materials Today Energy* **2018**, *9*, 391–396. https://doi.org/10.1016/j.mtener.2018.07.001.

(23) Lombardo, L.; Yang, H.; Züttel, A. Study of Borohydride Ionic Liquids as Hydrogen Storage Materials. *Journal of Energy Chemistry* **2019**, *33*, 17–21. https://doi.org/10.1016/j.jechem.2018.08.011.

(24) Schneemann, A.; White, J. L.; Kang, S.; Jeong, S.; Wan, L. F.; Cho, E. S.; Heo, T. W.; Prendergast, D.; Urban, J. J.; Wood, B. C.; Allendorf, M. D.; Stavila, V. Nanostructured Metal Hydrides for Hydrogen Storage. *Chem. Rev.* **2018**, *118* (22), 10775–10839. https://doi.org/10.1021/acs.chemrev.8b00313.

(25) Fichtner, M. Nanoconfinement Effects in Energy Storage Materials. *Physical Chemistry Chemical Physics* **2011**, *13* (48), 21186–21195. https://doi.org/10.1039/C1CP22547B.

(26) Wang, L.; Rawal, A.; Quadir, M. Z.; Aguey-Zinsou, K.-F. Nanoconfined Lithium Aluminium Hydride (LiAlH4) and Hydrogen Reversibility. *International Journal of Hydrogen Energy* **2017**, *42* (20), 14144–14153. https://doi.org/10.1016/j.ijhydene.2017.04.104.

(27) Wang, L.; Rawal, A.; Aguey-Zinsou, K.-F. Hydrogen Storage Properties of Nanoconfined Aluminium Hydride (AlH3). *Chemical Engineering Science* **2019**, *194*, 64–70. https://doi.org/10.1016/j.ces.2018.02.014.

(28) Baldé, C. P.; Hereijgers, B. P. C.; Bitter, J. H.; Jong, K. P. de. Facilitated Hydrogen Storage in NaAlH4 Supported on Carbon Nanofibers. *Angewandte Chemie International Edition* **2006**, *45* (21), 3501–3503. https://doi.org/10.1002/anie.200504202.

(29) Li, Y.; Zhou, G.; Fang, F.; Yu, X.; Zhang, Q.; Ouyang, L.; Zhu, M.; Sun, D. De-/Re-Hydrogenation Features of NaAlH4 Confined Exclusively in Nanopores. *Acta Materialia* **2011**, *59* (4), 1829–1838. https://doi.org/10.1016/j.actamat.2010.11.049.

(30) Christian, M. L.; Aguey-Zinsou, K.-F. Core–Shell Strategy Leading to High Reversible Hydrogen Storage Capacity for NaBH4. *ACS Nano* **2012**, *6* (9), 7739–7751. https://doi.org/10.1021/nn3030018.

(31) Yan, Y.; S. Au, Y.; Rentsch, D.; Remhof, A.; Jongh, P. E. de; Züttel, A. Reversible Hydrogen Storage in Mg(BH 4) 2 /Carbon Nanocomposites. *Journal of Materials Chemistry A* **2013**, *1* (37), 11177–11183. https://doi.org/10.1039/C3TA12222K.

(32) Yu, X.; Tang, Z.; Sun, D.; Ouyang, L.; Zhu, M. Recent Advances and Remaining Challenges of Nanostructured Materials for Hydrogen Storage Applications. *Progress in Materials Science* **2017**, *88*, 1–48. https://doi.org/10.1016/j.pmatsci.2017.03.001.

(33) Wang, S.; Gao, M.; Xian, K.; Li, Z.; Shen, Y.; Yao, Z.; Liu, Y.; Pan, H. LiBH4 Nanoconfined in Porous Hollow Carbon Nanospheres with High Loading, Low Dehydrogenation Temperature, Superior Kinetics, and Favorable Reversibility. *ACS Appl. Energy Mater.* **2020**, *3* (4), 3928–3938. https://doi.org/10.1021/acsaem.0c00325.

(34) Lai, Q.; Milanese, C.; Aguey-Zinsou, K.-F. Stabilization of Nanosized Borohydrides for Hydrogen Storage: Suppressing the Melting with TiCl3 Doping. *ACS Appl. Energy Mater.* **2018**, *1* (2), 421–430. https://doi.org/10.1021/acsaem.7b00082.

(35) Gao, J.; Adelhelm, P.; Verkuijlen, M. H. W.; Rongeat, C.; Herrich, M.; van Bentum, P. J. M.; Gutfleisch, O.; Kentgens, A. P. M.; de Jong, K. P.; de Jongh, P. E. Confinement of NaAlH4 in Nanoporous Carbon: Impact on H2 Release, Reversibility, and Thermodynamics. *J. Phys. Chem. C* **2010**, *114* (10), 4675–4682. https://doi.org/10.1021/jp910511g.

(36) Li, J.-S.; Zhang, S.; Sha, J.-Q.; Wang, H.; Liu, M.-Z.; Kong, L.-X.; Liu, G.-D. Confined Molybdenum Phosphide in P-Doped Porous Carbon as Efficient Electrocatalysts for Hydrogen Evolution. *ACS Appl. Mater. Interfaces* **2018**, *10* (20), 17140–17146. https://doi.org/10.1021/acsami.8b01541.

(37) Zhang, T.; Sun, Y.; Hang, L.; Bai, Y.; Li, X.; Wen, L.; Zhang, X.; Lyu, X.; Cai, W.; Li, Y. Large-Scale Synthesis of Co/CoOx Encapsulated in Nitrogen-, Oxygen-, and Sulfur-Tridoped Three-Dimensional Porous Carbon as Efficient Electrocatalysts for Hydrogen Evolution Reaction. *ACS Appl. Energy Mater.* **2018**, *1* (11), 6250–6259. https://doi.org/10.1021/acsaem.8b01272.

(38) Lv, Z.; Li, X.; Chen, X.; Li, X.; Wu, M.; Li, Z. One-Step Site-Specific Activation Approach for Preparation of Hierarchical Porous Carbon Materials with High Electrochemical Performance. *ACS Appl. Energy Mater.* **2019**, *2* (12), 8767–8782. https://doi.org/10.1021/acsaem.9b01729.

(39) Yao, L.; Peng, Y.; Zhang, Y. Rational Assembly of Hierarchically Porous CoxFe1–XS2@Carbon Superparticles for Efficient Hydrogen Evolution. *ACS Appl. Energy Mater.* **2020**, *3* (5), 4139–4143. https://doi.org/10.1021/acsaem.0c00387.

(40) Wang, C.; Liu, G.; Song, K.; Wang, X.; Wang, H.; Zhao, N.; He, F. Three-Dimensional Hierarchical Porous Carbon/Graphitic Carbon Nitride Composites for Efficient Photocatalytic Hydrogen Production. *ChemCatChem* **2019**, *11* (24), 6364–6371. https://doi.org/10.1002/cctc.201901598.

(41) Kan, X.; Chen, X.; Chen, W.; Mi, J.; Zhang, J.-Y.; Liu, F.; Zheng, A.; Huang, K.; Shen, L.; Au, C.; Jiang, L. Nitrogen-Decorated, Ordered Mesoporous Carbon Spheres as High-Efficient Catalysts for Selective Capture and Oxidation of H2S. *ACS Sustainable Chem. Eng.* **2019**, *7* (8), 7609–7618. https://doi.org/10.1021/acssuschemeng.8b05852.

(42) Liu, F.; Huang, K.; Wu, Q.; Dai, S. Solvent-Free Self-Assembly to the Synthesis of Nitrogen-Doped Ordered Mesoporous Polymers for Highly Selective Capture and Conversion of CO2. *Advanced Materials* **2017**, *29* (27), 1700445. https://doi.org/10.1002/adma.201700445.

(43) Kong, W.; Liu, F.; Liu, Y. Design of Nitrogen-Doped Graphitized 2D Hierarchical Porous Carbons as Efficient Solid Base Catalysts for Transesterification to Biodiesel. *Green Chemistry* **2020**, *22* (3), 903–912. https://doi.org/10.1039/C9GC03960K.

(44) Liang, S.; Mi, J.; Liu, F.; Zheng, Y.; Xiao, Y.; Cao, Y.; Jiang, L. Efficient Catalytic Elimination of COS and H2S by Developing Ordered Mesoporous Carbons with Versatile Base N Sites via a Calcination Induced Self-Assembly Route. *Chemical Engineering Science* **2020**, *221*, 115714. https://doi.org/10.1016/j.ces.2020.115714.

(45) Jalama, K. Carbon Dioxide Hydrogenation over Nickel-, Ruthenium-, and Copper-Based Catalysts: Review of Kinetics and Mechanism. *Catalysis Reviews* **2017**, *59* (2), 95–164. https://doi.org/10.1080/01614940.2017.1316172.

(46) Rathod, V.; Bhale, P. V. Experimental Investigation on Biogas Reforming for Syngas Production over an Alumina Based Nickel Catalyst. *Energy Procedia* **2014**, *54*, 236–245. https://doi.org/10.1016/j.egypro.2014.07.267.

(47) Bepari, S.; Kuila, D. Steam Reforming of Methanol, Ethanol and Glycerol over Nickel-Based Catalysts-A Review. *International Journal of Hydrogen Energy* **2019**. https://doi.org/10.1016/j.ijhydene.2019.08.003.

(48) Dupuis, A.-C. The Catalyst in the CCVD of Carbon Nanotubes—a Review. *Progress in Materials Science* **2005**, *50* (8), 929–961. https://doi.org/10.1016/j.pmatsci.2005.04.003.

(49) Kim, B.-J.; Lee, Y.-S.; Park, S.-J. A Study on the Hydrogen Storage Capacity of Ni-Plated Porous Carbon Nanofibers. *International Journal of Hydrogen Energy* **2008**, *33* (15), 4112–4115. https://doi.org/10.1016/j.ijhydene.2008.05.077.

(50) Zieliński, M.; Wojcieszak, R.; Monteverdi, S.; Mercy, M.; Bettahar, M. M. Hydrogen Storage in Nickel Catalysts Supported on Activated Carbon. *International Journal of Hydrogen Energy* **2007**, *32* (8), 1024–1032. https://doi.org/10.1016/j.ijhydene.2006.07.004.

(51) Wang, L.; Yang, R. T. Hydrogen Storage on Carbon-Based Adsorbents and Storage at Ambient Temperature by Hydrogen Spillover. *Catalysis Reviews* **2010**, *52* (4), 411–461. https://doi.org/10.1080/01614940.2010.520265.

(52) Zieliński, M.; Wojcieszak, R.; Monteverdi, S.; Mercy, M.; Bettahar, M. M. Hydrogen Storage on Nickel Catalysts Supported on Amorphous Activated Carbon. *Catalysis Communications* **2005**, *6* (12), 777–783. https://doi.org/10.1016/j.catcom.2005.07.001.

(53) Zhong, Z. Y.; Xiong, Z. T.; Sun, L. F.; Luo, J. Z.; Chen, P.; Wu, X.; Lin, J.; Tan, K. L. Nanosized Nickel(or Cobalt)/Graphite Composites for Hydrogen Storage. *J. Phys. Chem. B* **2002**, *106* (37), 9507–9513. https://doi.org/10.1021/jp020151j.

(54) Wahab, M. A.; Beltramini, J. N. Catalytic Nanoconfinement Effect of In-Situ Synthesized Ni-Containing Mesoporous Carbon Scaffold (Ni-MCS) on the Hydrogen Storage Properties of LiAlH4. *International Journal of Hydrogen Energy* **2014**, *39* (32), 18280–18290. https://doi.org/10.1016/j.ijhydene.2014.09.010.

(55) Xu, J.; Li, Y.; Cao, J.; Meng, R.; Wang, W.; Chen, Z. Preparation of Graphene-Supported Highly Dispersed Nickel Nanoparticles for the Improved Generation of Hydrogen from Ball-Milled LiBH 4. *Catalysis Science & Technology* **2015**, *5* (3), 1821–1828. https://doi.org/10.1039/C4CY01276C.

(56) Ngene, P.; Zwienen, M. (Rien) van; Jongh, P. E. de. Reversibility of the Hydrogen Desorption from LiBH 4 : A Synergetic Effect of Nanoconfinement and Ni Addition. *Chemical Communications* **2010**, *46* (43), 8201–8203. https://doi.org/10.1039/C0CC03218B.

(57) *Space Electrochemical Research and Technology: Proceedings of a Conference Held at NASA Lewis Research Center, Cleveland, Ohio, April 14-15, 1993*; National Aeronautics and Space Administration, Office of Management, Scientific and Technical Information Program, 1993.

(58) Nakamori, Y.; Li, H.-W.; Kikuchi, K.; Aoki, M.; Miwa, K.; Towata, S.; Orimo, S. Thermodynamical Stabilities of Metal-Borohydrides. *Journal of Alloys and Compounds* **2007**, *446–447*, 296–300. https://doi.org/10.1016/j.jallcom.2007.03.144.

(59) Electronegativities of the Elements (Data Page). *Wikipedia*; 2019.

(60) Lei, W.; Deng, Y.-P.; Li, G.; Cano, Z. P.; Wang, X.; Luo, D.; Liu, Y.; Wang, D.; Chen, Z. Two-Dimensional Phosphorus-Doped Carbon Nanosheets with Tunable Porosity for Oxygen Reactions in Zinc-Air Batteries. *ACS Catal.* **2018**, *8* (3), 2464–2472. https://doi.org/10.1021/acscatal.7b02739.

(61) Mauron, Ph.; Bielmann, M.; Remhof, A.; Züttel, A. High-Pressure and High-Temperature x-Ray Diffraction Cell for Combined Pressure, Composition, and Temperature Measurements of Hydrides. *Review of Scientific Instruments* **2011**, *82* (6), 065108. https://doi.org/10.1063/1.3600668.

(62) Scherrer, P. Bestimmung der inneren Struktur und der Größe von Kolloidteilchen mittels Röntgenstrahlen. In *Kolloidchemie Ein Lehrbuch*; Zsigmondy, R., Ed.; Chemical Technology in; Springer: Berlin, Heidelberg, 1912; pp 387–409. https://doi.org/10.1007/978-3-662-33915-2_7.

(63) Song, S.; Ma, F.; Wu, G.; Ma, D.; Geng, W.; Wan, J. Facile Self-Templating Large Scale Preparation of Biomass-Derived 3D Hierarchical Porous Carbon for Advanced Supercapacitors. *Journal of Materials Chemistry A* **2015**, *3* (35), 18154–18162. https://doi.org/10.1039/C5TA04721H.

(64) Ganesan, P.; Sivanantham, A.; Shanmugam, S. Inexpensive Electrochemical Synthesis of Nickel Iron Sulphides on Nickel Foam: Super Active and Ultra-Durable Electrocatalysts for Alkaline Electrolyte Membrane Water Electrolysis. *J. Mater. Chem. A* **2016**, *4* (42), 16394–16402. https://doi.org/10.1039/C6TA04499A.

(65) Campari, E. G.; Bonetti, E.; Casagrande, A.; Ferrari, L.; Levi, G. Mechanical Spectroscopy Observation of LiAlH4 Decomposition. *Journal of Alloys and Compounds* **2020**, *814*, 152242. https://doi.org/10.1016/j.jallcom.2019.152242.

(66) Ismail, M.; Zhao, Y.; Yu, X. B.; Dou, S. X. Effects of NbF5 Addition on the Hydrogen Storage Properties of LiAlH4. *International Journal of Hydrogen Energy* **2010**, *35* (6), 2361–2367. https://doi.org/10.1016/j.ijhydene.2009.12.178.

(67) Li, L.; Xu, Y.; Wang, Y.; Wang, Y.; Qiu, F.; An, C.; Jiao, L.; Yuan, H. NbN Nanoparticles as Additive for the High Dehydrogenation Properties of LiAlH4. *Dalton Trans.* **2013**, *43* (4), 1806–1813. https://doi.org/10.1039/C3DT52313F.

(68) Kissinger, H. E. Reaction Kinetics in Differential Thermal Analysis. *Anal. Chem.* **1957**, *29* (11), 1702–1706. https://doi.org/10.1021/ac60131a045.

(69) Ouyang, L. Z.; Ye, S. Y.; Dong, H. W.; Zhu, M. Effect of Interfacial Free Energy on Hydriding Reaction of Mg–Ni Thin Films. *Appl. Phys. Lett.* **2007**, *90* (2), 021917. https://doi.org/10.1063/1.2428877.

(70) Fossdal, A.; Brinks, H. W.; Fichtner, M.; Hauback, B. C. Determination of the Crystal Structure of Mg(AlH4)2 by Combined X-Ray and Neutron Diffraction. *Journal of Alloys and Compounds* **2005**, *387* (1), 47–51. https://doi.org/10.1016/j.jallcom.2004.06.050.

(71) Graetz, J. New Approaches to Hydrogen Storage. *Chemical Society Reviews* **2009**, *38* (1), 73–82. https://doi.org/10.1039/B718842K.

(72) Fichtner, M.; Engel, J.; Fuhr, O.; Glöss, A.; Rubner, O.; Ahlrichs, R. The Structure of Magnesium Alanate. *Inorg. Chem.* **2003**, *42* (22), 7060–7066. https://doi.org/10.1021/ic034160y.

(73) Kim, Y.; Lee, E.-K.; Shim, J.-H.; Cho, Y. W.; Yoon, K. B. Mechanochemical Synthesis and Thermal Decomposition of Mg(AlH4)2. *Journal of Alloys and Compounds* **2006**, *422* (1), 283–287. https://doi.org/10.1016/j.jallcom.2005.11.063.

(74) Liu, Y.; Pang, Y.; Zhang, X.; Zhou, Y.; Gao, M.; Pan, H. Synthesis and Hydrogen Storage Thermodynamics and Kinetics of Mg(AlH4)2 Submicron Rods. *International Journal of Hydrogen Energy* **2012**, *37* (23), 18148–18154. https://doi.org/10.1016/j.ijhydene.2012.09.081.

Supporting information

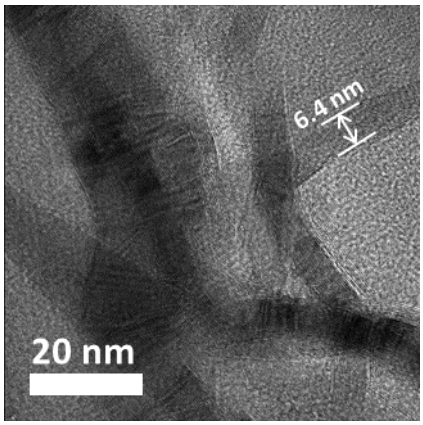

Figure S2.1 TEM image of cross section in porous carbon sheets.

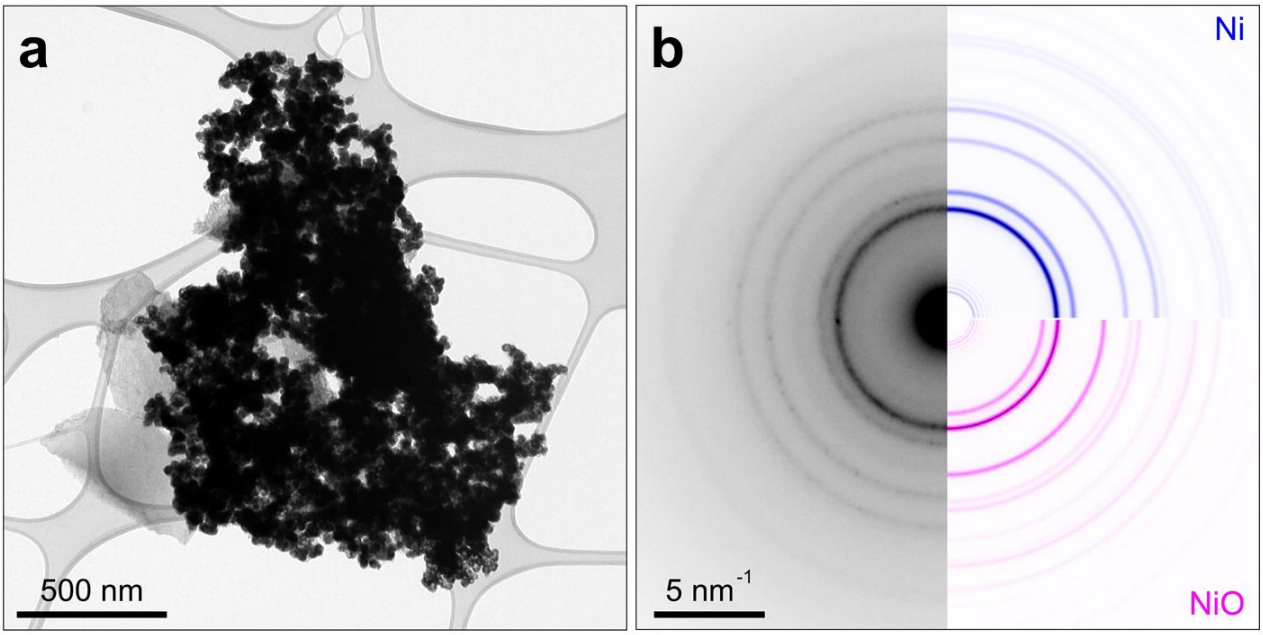

Figure S2.2 (a) TEM image of Ni-PCS and (b) selected area diffraction pattern (SADP) of Ni-PCS (Left: experimental ring pattern, right: simulated Ni and NiO ring pattern)

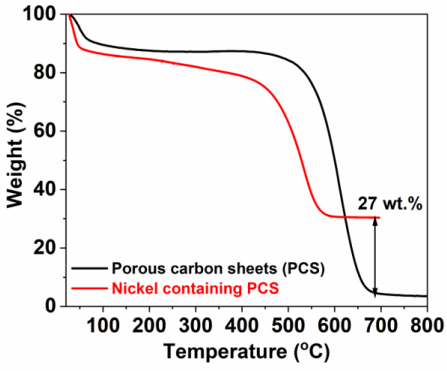

Figure S2.3 Thermogravimetric analysis plot of porous carbon sheets (PCS) and Ni-PCS.

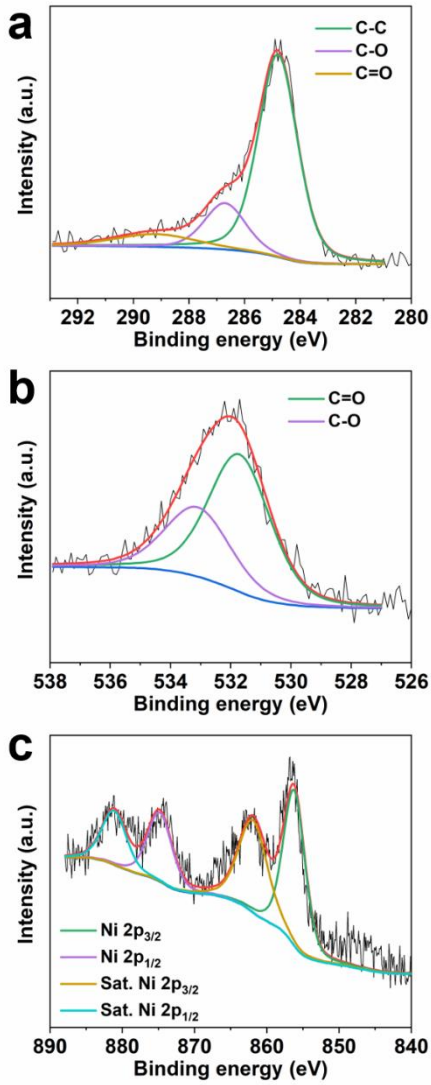

Figure S2.4 XPS spectra of (a) C 1s, (b) O 1s, and (c) Ni 2p about Ni-PCS (The background subtraction method was used Shirley type. The ratio of Gaussian and Lorentzian contribution to the peak shape is GL (30) for the deconvoluted peaks).

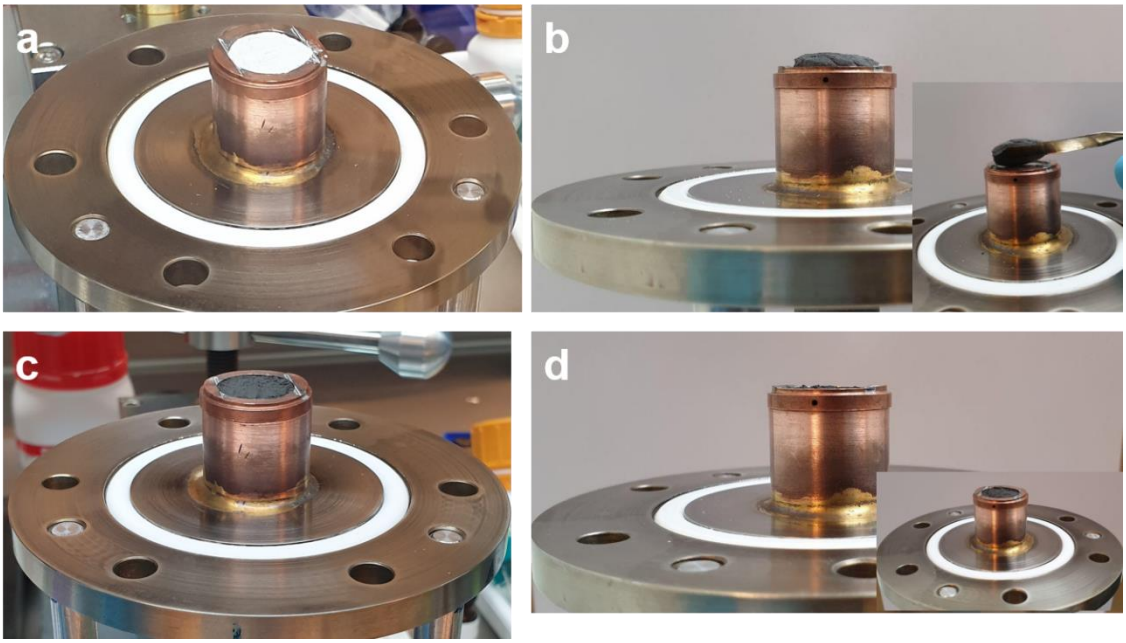

Figure S2.5 Photograph of (a) $LiAlH_4$ in glove box for *in situ* XRD, (b) $LiAlH_4$ after *in situ* XRD, (c) $LiAlH_4$ with Ni-PCS in glove box, and (d) $LiAlH_4$ with Ni-PCS after *in situ* XRD.

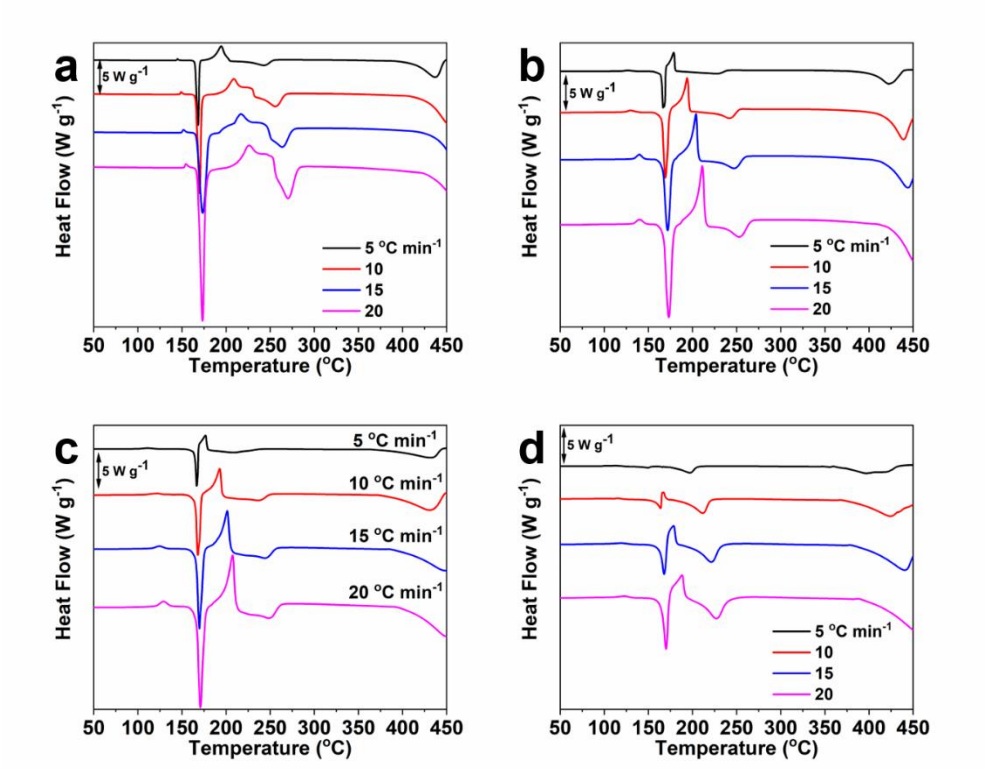

Figure S2.6 DSC profiles at various heating rate of (a) $LiAlH_4$, (b) $LiAlH_4$ ball-mill, (c) $LiAlH_4$ with PCS, and (d) $LiAlH_4$ with Ni-PCS.

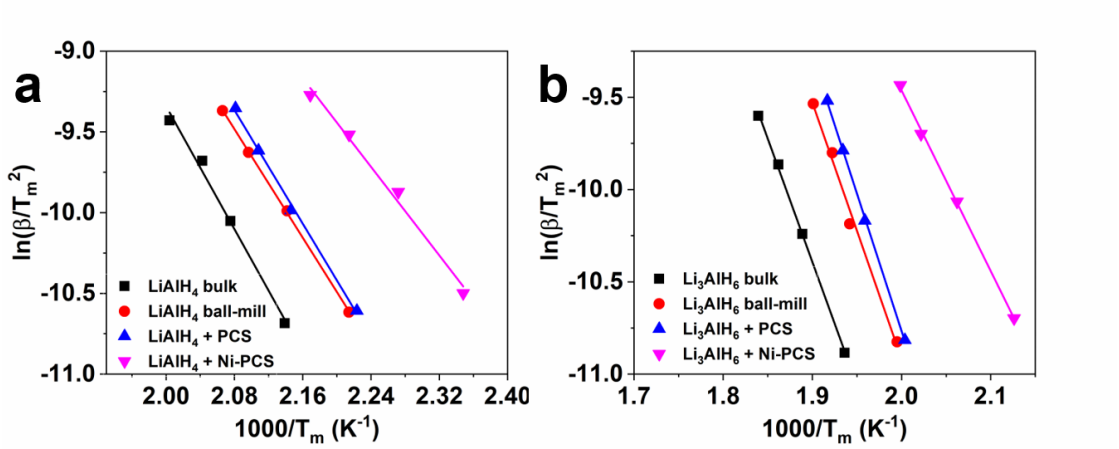

Figure S2.7 (a) Kissinger's plots showing the dehydrogenation of liquid $LiAlH_4$ in $LiAlH_4$ bulk (■, E_a: 79 kJ·mol^{-1}), ball-milled $LiAlH_4$ (●, E_a: 70 kJ·mol^{-1}), $LiAlH_4$ with PCS (▲, E_a: 73 kJ·mol^{-1}), and $LiAlH_4$ with Ni-PCS (▼, E_a: 57 kJ·mol^{-1}). (b) Dehydrogenation of Li_3AlH_6 in $LiAlH_4$ bulk (E_a: 111 kJ·mol^{-1}), ball-milled $LiAlH_4$ (E_a: 115 kJ·mol^{-1}), $LiAlH_4$ with PCS (E_a: 124 kJ·mol^{-1}), and $LiAlH_4$ with Ni-PCS (E_a: 81 kJ·mol^{-1}).

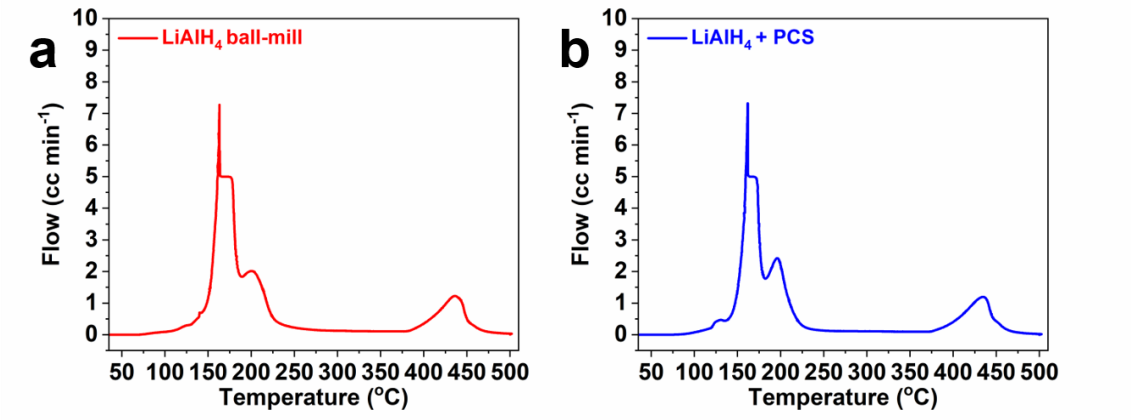

Figure S2.8 (a) Thermal desorption curves of (a) $LiAlH_4$ ball-mill and (b) $LiAlH_4$ with PCS.

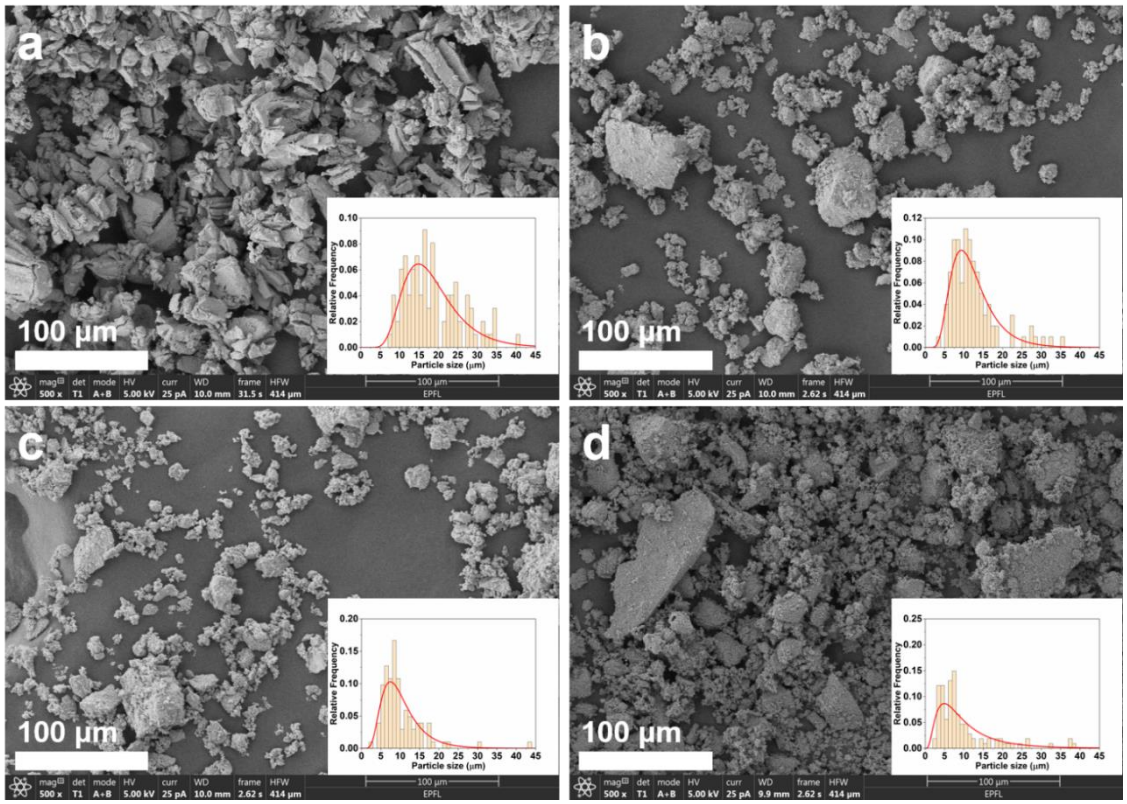

Figure S2.9 SEM image and particle size distribution graph of (a) $LiAlH_4$, (b) $LiAlH_4$ ball-mill, (c) $LiAlH_4$ with PCS, and (d) $LiAlH_4$ with Ni-PCS.

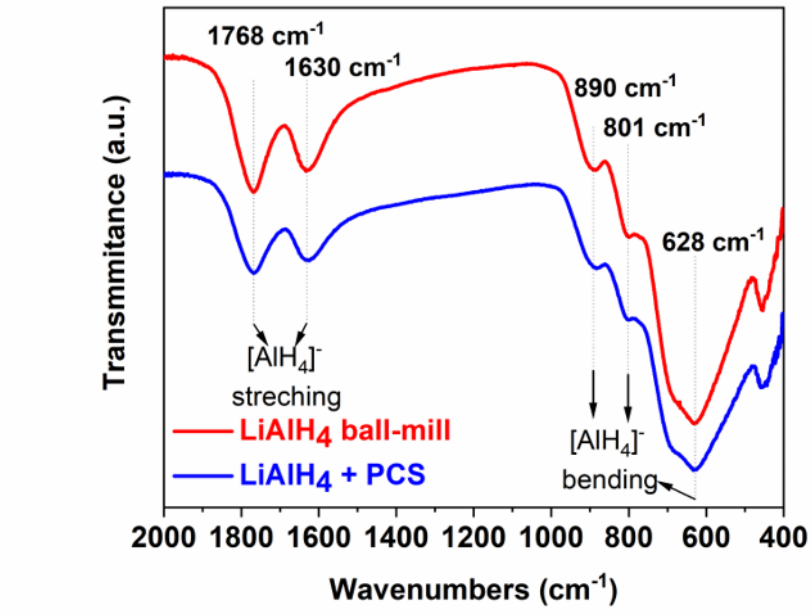

Figure S2.10 FT-IR spectra of $LiAlH_4$ ball-mill and $LiAlH_4$ with PCS.

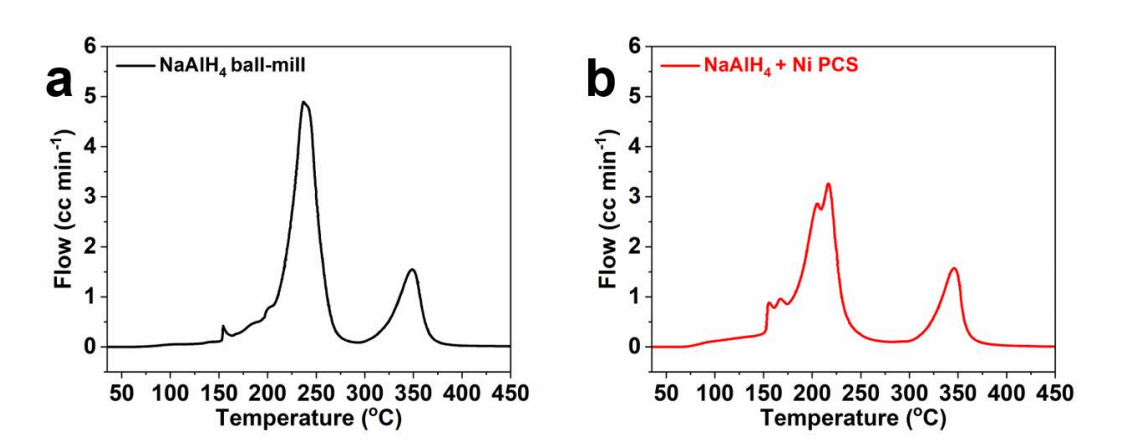

Figure S2.11 (a) Thermal desorption curves of (a) $NaAlH_4$ ball-mill and (b) $NaAlH_4$ with Ni-PCS.

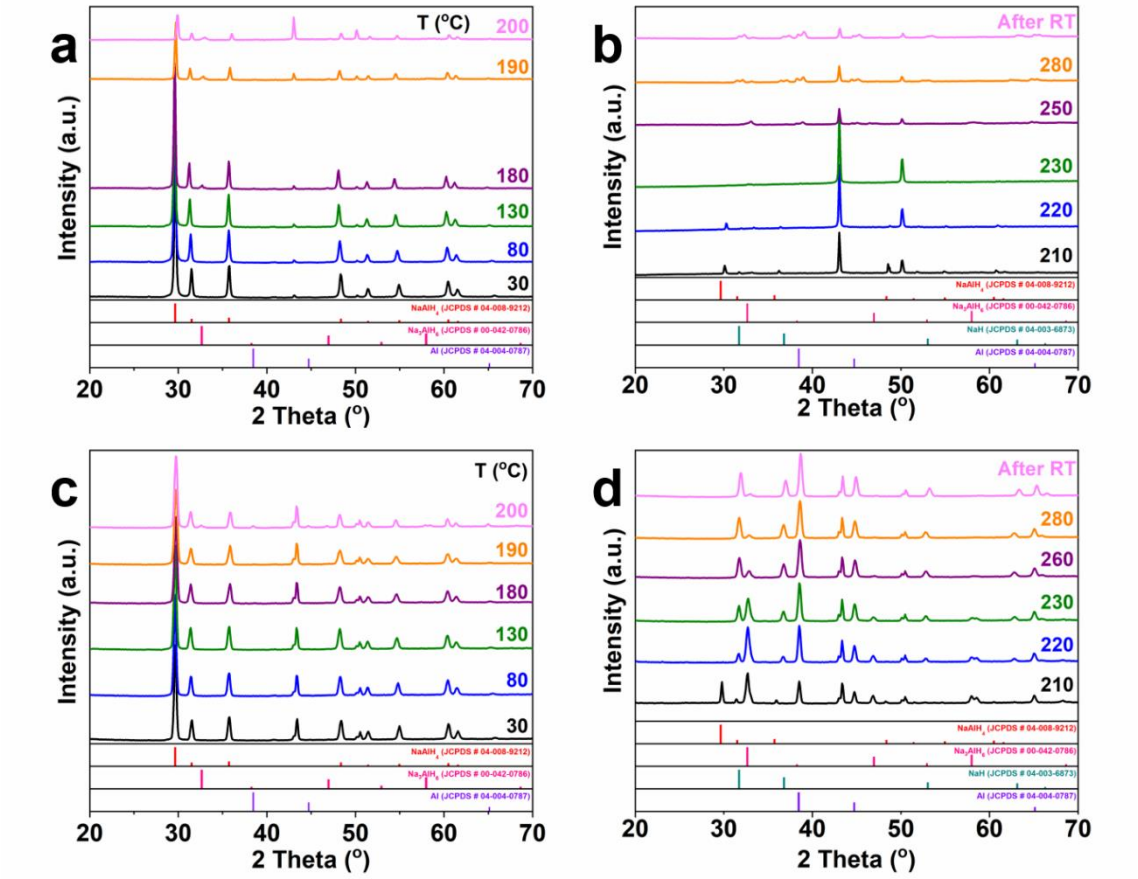

Figure S2.12 *In situ* powder XRD spectra of (a) $NaAlH_4$ ball-mill at the temperature region, 30°C – 200°C, (b) 210°C – 280°C. (c) $NaAlH_4$ with Ni-PCS at the temperature region, 30°C – 200°C, (d) 210°C – 280°C with after cooling down to room temperature. The JCPDS of $NaAlH_4$, Na_3AlH_6, and Al were indicated below the spectra.

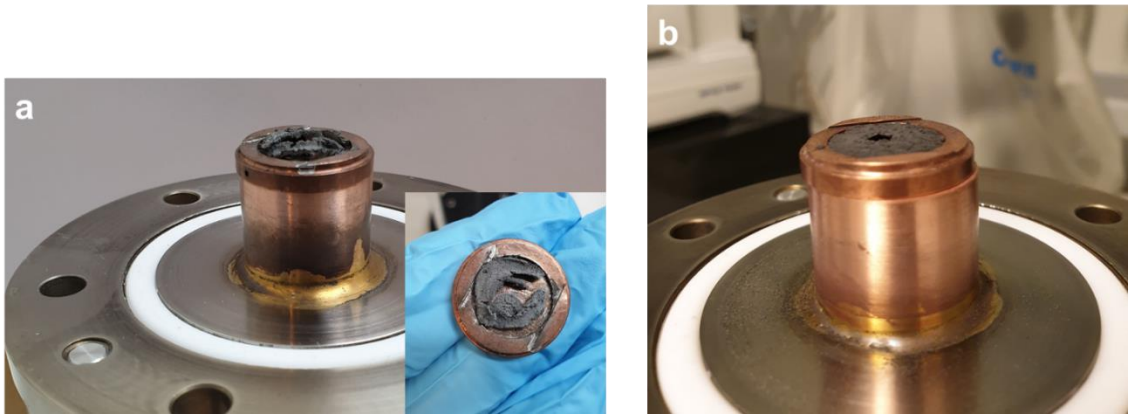

Figure S2.13 Photograph of (a) $NaAlH_4$ ball mill after *in situ* XRD and (b) $NaAlH_4$ with Ni-PCS after *in situ* XRD.

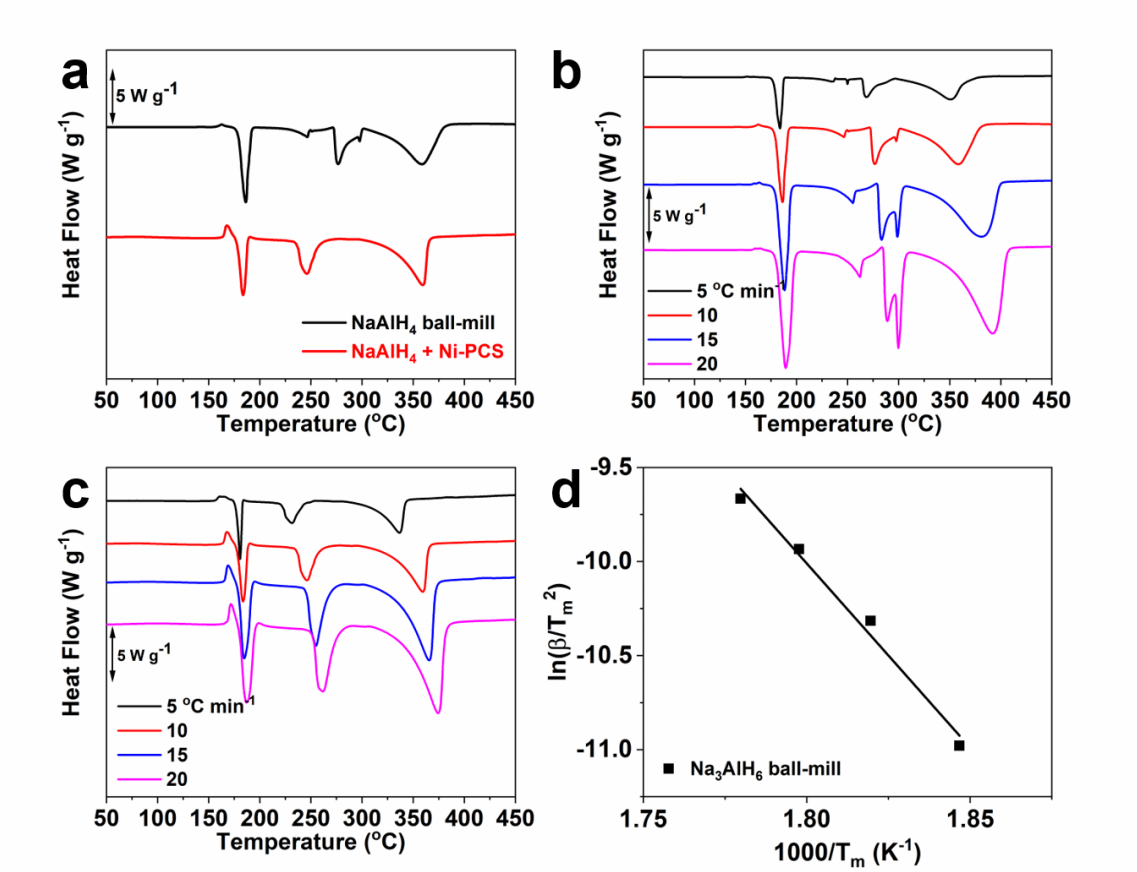

Figure S2.14 (a) DSC profiles of prepared samples, using a 10°C·min^{-1} heating rate. (b) various heating rate of DSC profiles for ball-milled $NaAlH_4$ and (c) $NaAlH_4$ with Ni-PCS. (d) Kissinger's dehydrogenation plots for Na_3AlH_6 peak in ball-milled $NaAlH_4$ (■, E_a: 163 kJ·mol^{-1}).

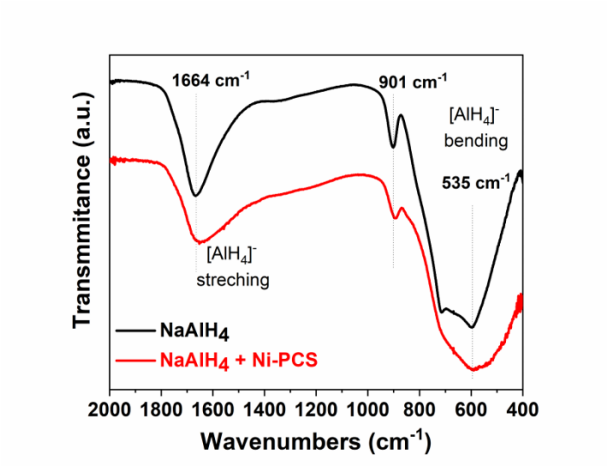

Figure S2.15 FT-IR spectra of ball-milled $NaAlH_4$ and $NaAlH_4$ with Ni-PCS.

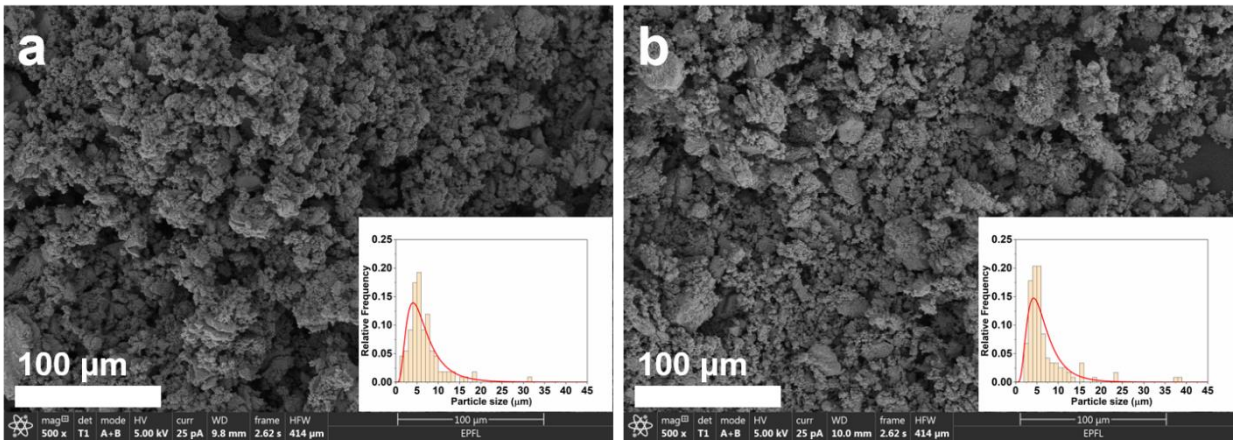

Figure S2.16 SEM image and particle size distribution graph of (a) $NaAlH_4$ ball-mill and (b) $NaAlH_4$ with Ni-PCS.

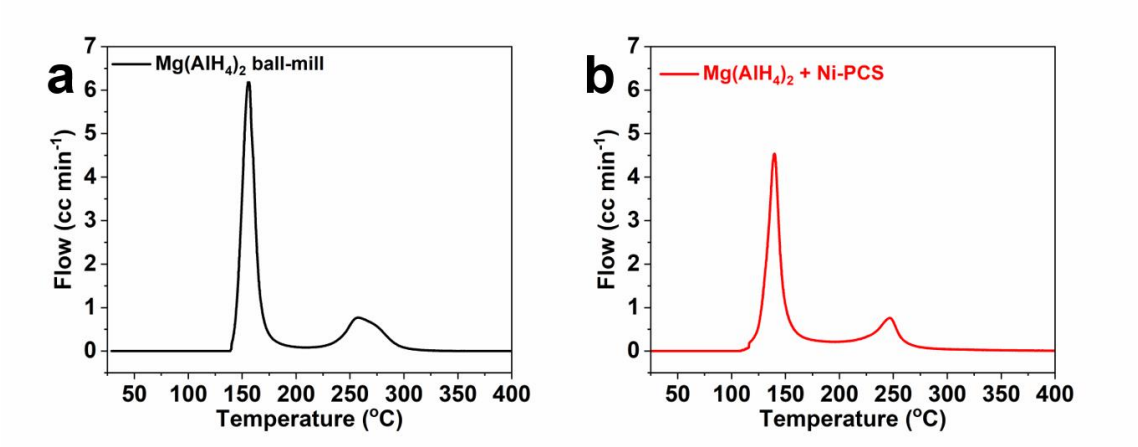

Figure S2.17 Thermal desorption curves of (a) $Mg(AlH_4)_2$ ball-mill and (b) $Mg(AlH_4)_2$ with Ni-PCS.

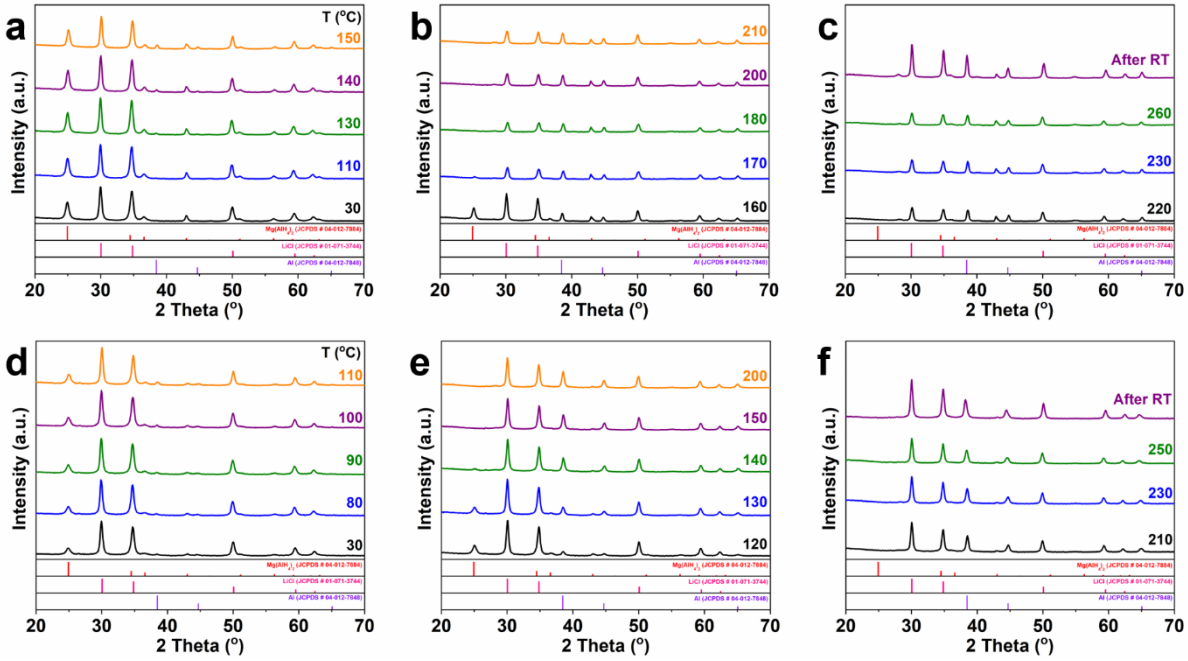

Figure S2.18 *In situ* powder XRD spectra of (a) $Mg(AlH_4)_2$ ball-mill at the temperature region, 30°C – 150°C, (b) 160°C – 210°C, (c) 220°C – 260°C. (d) $Mg(AlH_4)_2$ with Ni-PCS at the temperature region, 30°C – 110°C, (e) 120°C – 200°C (f) 210°C – 250°C with after cooling down to room temperature. The JCPDS of $Mg(AlH_4)_2$, LiCl, and Al were indicated below the spectra.

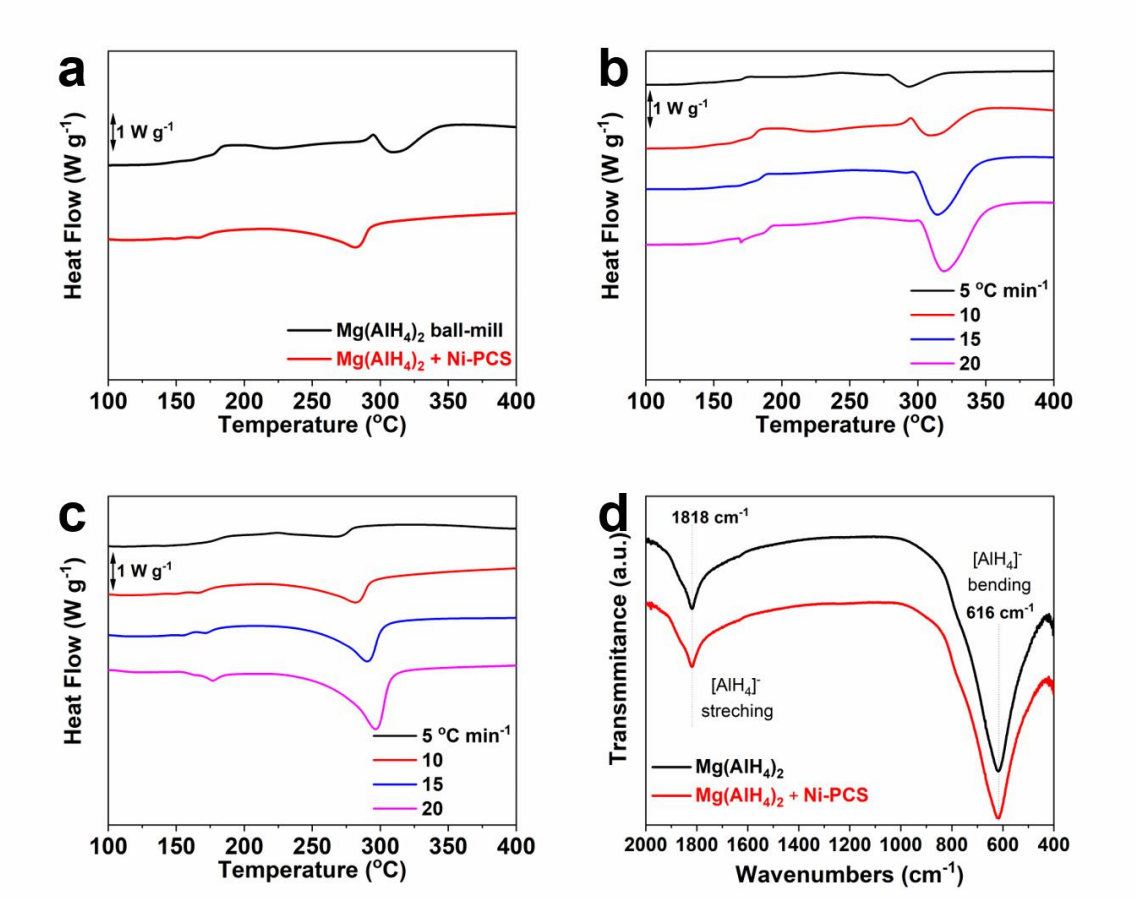

Figure S2.19 (a) DSC profiles of prepared samples, using a 10°C·min^{-1} heating rate. (b) Various heating rate of DSC profiles of $Mg(AlH_4)_2$ ball-mill and (c) $Mg(AlH_4)_2$ with Ni-PCS. (d) FT-IR spectra of $Mg(AlH_4)_2$ ball-mill and $Mg(AlH_4)_2$ with Ni-PCS.

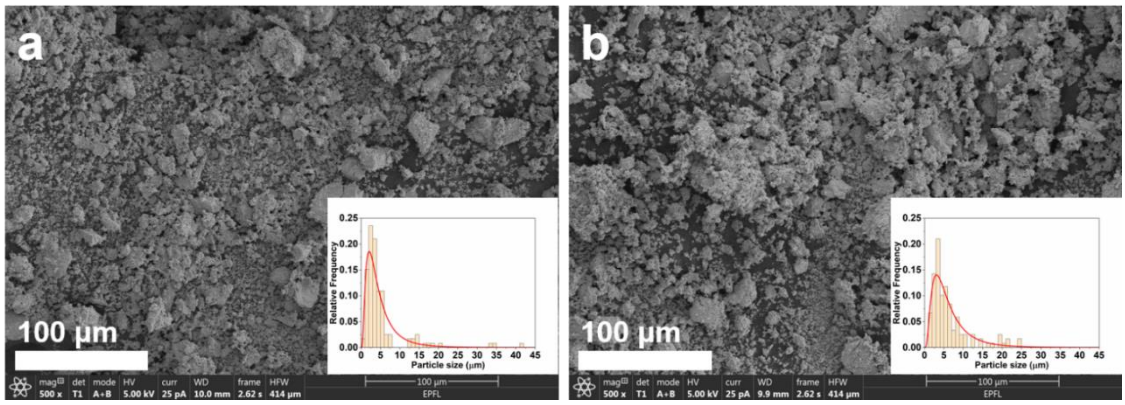

Figure S2.20 SEM image and particle size distribution graph of (a) $Mg(AlH_4)_2$ ball-mill and (b) $Mg(AlH_4)_2$ with Ni-PCS.

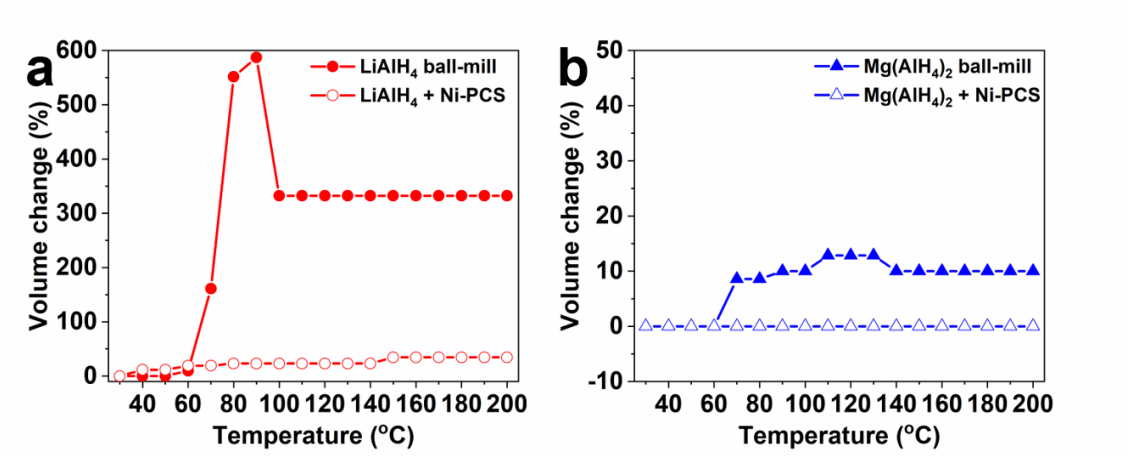

Figure S2.21 Volume change of the pellets of (a) ball-milled $LiAlH_4$ and $LiAlH_4$ with Ni-PCS and (b) ball-milled $Mg(AlH_4)_2$ and $Mg(AlH_4)_2$ with Ni-PCS.

Table S2.1 Particle and crystalline size for alanate samples.

Sample	Particle size[a] (μm)	Crystalline size[b] (nm)
$LiAlH_4$	18.6[c]	26.4
$LiAlH_4$ ball-mill	12.4	26.9
$LiAlH_4$ + PCS	10.5	25.8
$LiAlH_4$ + Ni-PCS	11.6	25.7
$NaAlH_4$ ball-mill	7.0	37.2
$NaAlH_4$ + Ni-PCS	6.9	27.7
$Mg(AlH_4)_2$ ball-mill	5.3	15.0
$Mg(AlH_4)_2$ + Ni-PCS	6.9	12.9

[a] Mean particle size was calculated based on SEM image

[b] Crystalline sizes were calculated by Scherrer equation based on XRD

[c] Rod shape particle size was determined to volume equivalent sphere diameter

Table S2.2 Hydrogen storage properties of alanates.

Sample	hydrogen[a] (wt %)	Dehydrogenation T_{onset} (°C)	Activation energy[b] (kJ·mol^{-1})	Ref
$LiAlH_4$	7.9	150-175		[1]
$LiAlH_4$ ball-mill	7.3	145	115	[1]
$LiAlH_4$ (with $TiCl_3$)	7.0	75	-	[2]
$LiAlH_4$ with Ni/C	6.5	48	61.9	[3]
$LiAlH_4$	7.0	150	79	This work
$LiAlH_4$ ball-mill	7.4	115	70	This work
$LiAlH_4$ with PCS	6.6	120	73	This work
$LiAlH_4$ with Ni-PCS	6.3	94	57	This work
$NaAlH_4$	5.5	200-210	118-132	[4–6]
$NaAlH_4$ (with Ti)	4.5	90	72-100	[5–7]
$NaAlH_4$ with carbon	4	160	88	[8]
$NaAlH_4$ ball-mill	5.7	140	109	This work
$NaAlH_4$ with Ni-PCS	4.7	111	94	This work
$Mg(AlH_4)_2$ ball-mill	5.5	120-170	-	[9]
$Mg(AlH_4)_2$ ball -mill (with $TiCl_3$)	4.5	120-150	-	[9]
$Mg(AlH_4)_2$ nanorods	6.7	100	97.3	[10]
$Mg(AlH_4)_2$ ball-mill (with NaCl)	2.8	115	-	[11]
$Mg(AlH_4)_2$ ball-mill (with LiCl)	2.9	146	118	This work
$Mg(AlH_4)_2$ with Ni-PCS (with LiCl)	2.5	125	103	This work

[a] $LiAlH_4 \rightarrow LiH + Al + 3/2H_2$;
$NaAlH_4 \rightarrow NaH + Al + 3/2H_2$;
$Mg(AlH_4)_2 \rightarrow MgH_2 + 2Al + 3H_2$; hydrogen desorbed amount in the reaction

[b] $3LiAlH_4 \rightarrow Li_3AlH_6 + 2Al + 3H_2$;

[c] $3NaAlH_4 \rightarrow Na_3AlH_6 + 2Al + 3H_2$;
$Mg(AlH_4)_2 \rightarrow MgH_2 + 2Al + 3H_2$; activation energy in the reaction

REFERENCES

(1) Ares, J. R.; Aguey-Zinsou, K.-F.; Porcu, M.; Sykes, J. M.; Dornheim, M.; Klassen, T.; Bormann, R. Thermal and Mechanically Activated Decomposition of LiAlH4. *Materials Research Bulletin* **2008**, *43* (5), 1263–1275. https://doi.org/10.1016/j.materresbull.2007.05.018.

(2) Langmi, H. W.; McGrady, G. S.; Liu, X.; Jensen, C. M. Modification of the H2 Desorption Properties of LiAlH4 through Doping with Ti. *J. Phys. Chem. C* **2010**, *114* (23), 10666–10669. https://doi.org/10.1021/jp102641p.

(3) Zang, L.; Liu, S.; Guo, H.; Chang, X.; Xu, X.; Jiao, L.; Yuan, H.; Wang, Y. In Situ Synthesis of 3D Flower-Like Nanocrystalline Ni/C and Its Effect on Hydrogen Storage Properties of LiAlH4. *Chemistry – An Asian Journal* **2018**, *13* (3), 350–357. https://doi.org/10.1002/asia.201701649.

(4) Schüth, F.; Bogdanović, B.; Felderhoff, M. Light Metal Hydrides and Complex Hydrides for Hydrogen Storage. *Chemical Communications* **2004**, *0* (20), 2249–2258. https://doi.org/10.1039/B406522K.

(5) Sandrock, G.; Gross, K.; Thomas, G. Effect of Ti-Catalyst Content on the Reversible Hydrogen Storage Properties of the Sodium Alanates. *Journal of Alloys and Compounds* **2002**, *339* (1), 299–308. https://doi.org/10.1016/S0925-8388(01)02014-X.

(6) Kircher, O.; Fichtner, M. Kinetic Studies of the Decomposition of NaAlH4 Doped with a Ti-Based Catalyst. *Journal of Alloys and Compounds* **2005**, *404–406*, 339–342. https://doi.org/10.1016/j.jallcom.2004.11.121.

(7) Wang, T.; Wang, J.; Ebner, A. D.; Ritter, J. A. Reversible Hydrogen Storage Properties of NaAlH4 Catalyzed with Scandium. *Journal of Alloys and Compounds* **2008**, *450* (1), 293–300. https://doi.org/10.1016/j.jallcom.2006.10.072.

(8) Li, Y.; Fang, F.; Fu, H.; Qiu, J.; Song, Y.; Li, Y.; Sun, D.; Zhang, Q.; Ouyang, L.; Zhu, M. Carbon Nanomaterial-Assisted Morphological Tuning for Thermodynamic and Kinetic Destabilization in Sodium Alanates. *Journal of Materials Chemistry A* **2013**, *1* (17), 5238–5246. https://doi.org/10.1039/C3TA00102D.

(9) Fichtner, M.; Fuhr, O.; Kircher, O. Magnesium Alanate—a Material for Reversible Hydrogen Storage? *Journal of Alloys and Compounds* **2003**, *356–357*, 418–422. https://doi.org/10.1016/S0925-8388(02)01236-7.

(10) Pang, Y.; Liu, Y.; Gao, M.; Ouyang, L.; Liu, J.; Wang, H.; Zhu, M.; Pan, H. A Mechanical-Force-Driven Physical Vapour Deposition Approach to Fabricating Complex Hydride Nanostructures. *Nature Communications* **2014**, *5* (1), 3519. https://doi.org/10.1038/ncomms4519.

(11) Kim, Y.; Lee, E.-K.; Shim, J.-H.; Cho, Y. W.; Yoon, K. B. Mechanochemical Synthesis and Thermal Decomposition of Mg(AlH4)2. *Journal of Alloys and Compounds* **2006**, *422* (1), 283–287. https://doi.org/10.1016/j.jallcom.2005.11.063.

Chapter 3 Selective Borohydride Oxidation Reaction on Nickel Catalyst with Anion and Cation Exchange Ionomer for High-Performance Direct Borohydride Fuel Cells

Youngdon Ko[1, 2], Loris Lombardo[1, 2], Mo Li[1, 2], Thi Ha My Pham[1, 2] Heena Yang[1, 2, 3], Andreas Züttel[1, 2*]

[1] Laboratory of Materials for Renewable Energy (LMER), Institute of Chemical Sciences and Engineering (ISIC), Basic Science Faculty (SB), École Polytechnique Fédérale de Lausanne (EPFL) Valais/Wallis, Energypolis, Rue de l'Industrie 17, 1951 Sion, Switzerland

[2] Empa Materials Science and Technology, 8600 Dübendorf, Switzerland

[3] Korea Water Resources Corporation, Daedeok-Gu, 34350 Daejeon, Republic of Korea.

[*]Corresponding author: heena.yang@epfl.ch

Postprint version: this section has been published as a full-length article in *Advanced Energy Materials* **2022**, 12, 16, 2103539. DOI: 10.1002/aenm.202103539.

Edit: caption numbers of figures, tables, and equations were edited to match the thesis chapter number.

Abstract

Direct borohydride fuel cells (DBFCs) operate with liquid H_2O_2 and high–energy-density $NaBH_4$ solution. The facile, direct synthesis method using a non-noble nickel catalyst for the DBFC anode is shown. The complex anode reaction with anion-exchange ionomer (AEI) and cation-exchange ionomer (CEI) is evaluated in half-cell and single-cell configurations. The ionomer type produces high (AEI) or low local pH (CEI) at the active site of the catalyst in the single-cell configuration, generating different catalytic reactions. The performance of nickel catalyst is compared to palladium catalyst. The selective catalytic activities for the borohydride oxidation reaction (BOR) and hydrogen oxidation reaction (HOR) are the key parameters for achieving good performance. Furthermore, fuel utilization and H_2 evolution measurement in a single-cell configuration provide more information on the complex anode reaction in DBFC. The nickel catalyst with CEI on nickel foam (NiF@CEI-Ni) shows the highest DBFC peak power density (0.59 W cm^{-2}) with a non-noble metal anode catalyst.

3.1 Introduction

Fuel cells are clean energy conversion devices that produce electricity (and heat) through an electrochemical reaction with hydrogen-based fuel and an oxidant. Proton-exchange membrane fuel cells (PEMFCs) have a wide range of uses, such as in automobiles and power plants. However, PEMFC systems are still relatively pricy due to the high platinum content and the high-pressure hydrogen tank.[1,2] In the quest for a reduction/suppression of precious metals, alkaline-based fuel cells are considered a preferred system due to the activity of non-noble

metal catalysts under alkaline conditions.[3,4] To allow safer and easier hydrogen storage at ambient conditions, material-based hydrogen storage methods have been investigated.[5,6] For example, hydrogen storage in complex hydrides is getting more attention due to their high capacity and better safety. Complex hydrides (alanates, amides, and borohydrides) are complex anions combined with an alkali metal or alkaline earth metal.[7] They can release hydrogen via hydrolysis and thermolysis to supply hydrogen for the PEMFC[5,6,8–10]. On the other hand, a stabilized borohydride in an alkaline aqueous solution can be directly used as a fuel with direct borohydride fuel cells (DBFCs). The DBFC system offers the advantages of convenient storage and easy charging of stabilized borohydride are over the compressed hydrogen tanks generally used in PEMFC systems. The most studied borohydride is sodium borohydride ($NaBH_4$), which exhibits high gravimetric hydrogen density (10.8%), and has an affordable price among borohydride materials. Also, the by-product of borohydride oxidation reaction (BOR), sodium metaborate ($NaBO_2{\cdot}xH_2O$), is environmentally benign and recyclable.[11] BOR is the main reaction in DBFCs, and occurs at the anode (Equation (1)). However, the competitive hydrolysis (Equation 2), hydrogen evolution reaction (HER, Equation 3, below 0 V vs. RHE), and hydrogen oxidation reaction (HOR, Equation 4, above 0 V vs. RHE) can also take place, decreasing the overall fuel and chemical energy efficiency.[12]

$$BH_4^- + 8OH^- \rightarrow BO_2^- + 6H_2O + 8e^- \qquad (E^0 = -1.24\ \text{V vs SHE}) \qquad (1)$$

$$BH_4^- + 2H_2O \rightarrow BO_2^- + 4H_2 \qquad (2)$$

$$H_2O + 2e^- \rightarrow H_2 + 2OH^- \qquad (E^0 = 0\ \text{V vs SHE}) \qquad (3)$$

$$H_2 + 2OH^- \rightarrow 2H_2O + 2e^- \qquad (E^0 = 0\ \text{V vs SHE}) \qquad (4)$$

Platinum-group metals (PGMs) are currently used as the catalyst on both electrode sides in DBFCs, with palladium being suitable for the anode catalyst.[12–16] Gold and platinum have also been considered for the anode catalyst.[12,17,18] These catalysts are scarce, however, and also in demand for many other industrial reactions. Their high cost and low abundance hence limit their practical applicability in DBFCs. Nickel, in contrast, is abundant and used in various catalytic reactions as well as in batteries.[10,19–22] It is considered an alternative catalyst for catalytic reactions involving PGMs, especially in alkaline conditions. Recently, the Chatenet group reported several results on Ni-based anode electrodes for DBFC application.[23–26] They synthesized the Ni catalyst by electrodeposition on carbon, or directly on chemically reduced nickel forms. The reported electrodeposited Ni on etched Ni-felt (Ni_{ED}/eNFT-D) anode electrode has a peak power density of 446 mW cm^{-2} with 2.0 V open circuit voltage (OCV).[24] Despite its high performance, electrodeposition has a big hurdle for the fabrication of large electrodes. Easier synthesis methods for nickel and ionomer composites are addressed in this study and could be easily applied to large electrodes. Indeed, this noble metal-free Ni-based composite demonstrated a great activity as anode catalyst for DBFC, with a direct and easy activation method.

Ramani et al. demonstrated a pH-gradient-enabled microscale bipolar interface (PMBI) in DBFCs with $NaBH_4$ and H_2O_2 reactants.[14] The PMBI configuration, which creates a local pH gradient on the anode (high pH), opens a new way to obtain remarkable performance (0.63 W cm^{-2}).[15,16,24] In addition, the state-of-the-art DBFC performance was further improved by reactant-transport engineering (0.89 W cm^{-2}).[15] However, their design involves a high-cost Pd catalyst at the anode side, which limits practicability. In this study, we use Pd and Ni as catalysts and two different types of ionomer. Even though the Ni catalyst has higher loading (10 mg cm^{-2}) than the Pd catalyst (0.5 mg cm^{-2}), the high Pd price makes the Ni catalyst more economically promising (~3000 times cheaper in the market). In addition, we focus on a commercial anion exchange ionomer (AEI, Fumion FAA-3A, Fumatech), a polyaromatic polymer functionalized quaternary ammonium group, to fabricate a PMBI configuration. We also use a cation exchange ionomer (CEI, Nafion, Dupont) to compare the properties of nickel catalyst on low local pH, or without-PMBI configuration. This allows us to determine the role of the ionomer on Ni and Pd catalysts,

and to understand their different catalytic natures. We compared Pd and Ni catalyst properties based on electrochemical half-cell measurement to observe BOR and HOR/HER. Synthesized Ni catalyst with ionomer composite on nickel foam shows a higher selectivity for BOR compared to Pd catalyst. The fuel utilization and hydrogen evolution amounts were measured at a certain point of the polarization curve, and a model was fitted to understand the complex phenomena inside a DBFC anode single-cell. Fuel cycling tests were conducted to understand the effect of impurities in the fuel on the performance of two different ionomers with nickel catalyst in DBFC.

3.2 Experimental section

3.2.1 Chemicals and materials

Deionized (DI) water from a Milli-Q system (18.2Ω, Millipore) was used for anolyte/catholyte and washing the DBFC cell. The following chemicals were used without purification: nickel chloride ($NiCl_2$, 98 %, Sigma-Aldrich), platinum on graphitized carbon (Pt/C, 40 wt% Pt loading, Sigma-Aldrich), palladium on activated carbon (Pd/C, 20 wt% Pd loading, Alfa Aesar), isopropanol (IPA, 99.5 %, Fisher Scientific), sulfuric acid (H_2SO_4, 95–98 %, Sigma-Aldrich), sodium hydroxide (NaOH, 98 %, Reactolab), sodium borohydride ($NaBH_4$, 98% Sigma-Aldrich), sodium metaborate tetrahydrate ($NaBO_2{\cdot}4H_2O$, 98% Alfa-Aesar), hydrogen peroxide (H_2O_2, 30 wt%, Fisher Scientific), and nickel foam (5mm, ZOPIN Group). The anion exchange ionomer (Fumion FAA-3, 10 wt%, FuMA-Tech), cation exchange ionomer (Nafion D521 1100 EW, 5 wt%, Dupont), Nafion 115 (127 µm, Dupont), carbon fiber paper (Sigracet 28AA, 190 µm, SGL Carbon), and PTFE gasket were purchased from the fuel cell store.

3.2.2 Preparation of the anode electrode with nickel catalyst and palladium catalyst

0.2 g of $NiCl_2$ was dispersed in 1 g of the anion exchange ionomer (AEI) or 2 g of the cation exchange ionomer (CEI) with 5 ml IPA. The mixture was sonicated for 10 min and stirred 1 h before use. The mixture was sprayed to nickel foam on a hot plate at 80 °C to reach 22 mg cm^{-2} of $NiCl_2$. The coated nickel foam was calcinated at different temperatures (between 200 to 400 °C) for 3 h in N_2 flow. The samples calcinated at 200 °C are denoted NiF@AEI-$NiCl_2$ for nickel chloride with anionic ionomer on nickel foam and NiF@CEI-$NiCl_2$ for nickel chloride with cationic ionomer on nickel foam. For the anode electrodes made of palladium catalyst, the catalyst inks were prepared the same way as the nickel catalyst. The amount of Pd metal loading was fixed to 0.5 mg cm^{-2} on two different inks (AEI-Pd/C and CEI-Pd/C). The palladium on activated carbon with anionic ionomer on nickel foam (NiF@AEI-Pd/C) and palladium on activated carbon with cationic ionomer on nickel foam (NiF@CEI-Pd/C) were used as anode electrodes without calcination.

3.2.3 Preparation of the DBFC single cell

Firstly, the Nafion membrane was activated with 0.5 M H_2SO_4 and DI water 2 h each at 80 °C water bath. The commercial 40 wt% Pt/C catalyst powder and predetermined Nafion amount were mixed with 3 ml of IPA to make the cathode catalyst ink. The glass vial containing the mixture was sonicated and stirred for 30 min each. The Nafion membrane was fixed on a hot plate at 70 °C, and the mixed catalyst ink was directly sprayed on the membrane. The total Pt loading at the cathode was 1 mg cm^{-2}. Next, a carbon fiber paper was placed over the cathode electrode. Finally, the prepared nickel foam was assembled on the anode side of the membrane. After that, the bolts and nuts are tightened with the torque wrench until the 6.2 Nm is reached. The gasket was constructed to surround the membrane electrode assembly (MEA). The thickness of the anode gasket is 4.95 mm which makes the anode contact well to the Nafion membrane (anode electrode thickness: 5 mm). The schematic image of DBFC single-cell assembly is described in Figure S8b. The active area of the DBFC single cell is 9 cm^2. The graphite flow fields were three-channel serpentine at both sides of the cathode and anode.

3.2.4 Activation of anode catalyst and DBFC performance test

DBFC was operated with liquid electrolyte on both anode and cathode sides. Before activation, the MEA was conditioned with pre-electrolyte 10 min at 80 °C. Pre-anolyte and pre-catholyte are 3 M NaOH solution and 1.5 M H_2SO_4 solution, respectively. To activate the NiF@AEI-$NiCl_2$ and NiF@CEI-$NiCl_2$, the anolyte (1.5 M $NaBH_4$ in 3 M NaOH) and the catholyte (15 % H_2O_2 in 1.5 M H_2SO_4) were flown to the anode and cathode, respectively. The electrolyte flow was fixed to 7 ml min^{-1} on both anode and cathode sides by a peristaltic pump (Reglo ICC, Ismatec). At the same time, the voltage cycled from open circuit potential (OCP) to 0.35 V for 30 min. During this activation step, the NiF@AEI-$NiCl_2$ and NiF@CEI-$NiCl_2$ were reduced to metallic nickel. Therefore, the notation changed to nickel catalyst with anionic ionomer on nickel foam (NiF@AEI-Ni) and nickel catalyst with cationic ionomer on nickel foam (NiF@CEI-Ni). The fuel cell performance was conducted with a test station (SMART2, WonA-Tech). The experimental error and average performance data are obtained by three different samples at the same conditions. The high-frequency resistances (HFRs) are obtained for the iR corrected polarization curves by the Nyquist semi-circle fit. Electrochemical impedance spectra (EIS) were measured by a potentiostat (PGSTAT302N, Metrohm Autolab) enhanced with a 10 A booster. The Nyquist plots are measured in potentiostatic mode by sweeping frequencies over the range of 10 kHz to 1 Hz with 10 points per decade. The amplitude of the perturbating AC voltage was always kept at 100 mV. For measuring fuel utilization of anolyte, the current was fixed at the desired current density and stabilized for 3 min. Then, the anolyte exit product was collected for 2 min to measure ^{11}B nuclear magnetic resonance spectroscopy (NMR, Bruker 400 MHz AVIII HD). ^{11}B NMR was conducted for the calculation of fuel utilization after the reaction at the anode electrode from DBFC single cell. The 0.4 ml of collected anolyte at the exit and 0.1 ml deuterium oxide (D_2O) were mixed together to measure ^{11}B NMR. The peak integration value of BH_4^- and BO_2^- were compared to obtain fuel utilization. The hydrogen evolution amount from the anode exit was also measured volumetrically. The durability test was performed at 1 V potentiostatic mode with the same conditions as the single-cell performance test. The fuel cycling test was also conducted at 1 V for 8 h (total volume of 450 ml: 7 ml min^{-1} and 30 ml for line residual for both anolyte and catholyte).

3.2.5 Catalyst characterization and electrochemical measurements

Thermogravimetric analysis (TGA, TG 209 F1 Libra, NETZSCH) measured the stability of CEI and AEI under N_2 flow. Scanning electron microscopy (SEM, Thermo-Scientific Teneo), transmission electron microscopy (TEM, Thermo-Scientific Tecnai G2 Spirit Twin) and high-angle annular dark-field scanning transmission electron microscopy (HAADF-STEM, Thermo-Scientific Tecnai Osiris) with energy-dispersive X-ray spectroscopy (EDX, Super-X SDD) were used to observe the morphology of the synthesized anode catalysts. The TEM samples were prepared as follows: each nickel foam was sonicated with IPA for 20 min to detach the catalyst; after that, the solution was dropped and let it dry on a TEM grid. X-ray photoelectron spectroscopy (XPS) spectra were collected in a Kratos Axis Supra system (analysis chamber base pressure 1×10^{-9} mbar) equipped with a monochromated Al Kα (1486.61 eV) X-ray source at a nominal power of 225 W. The fixed analyzer transmission (FAT) mode was used for spectra acquisition with pass energies of 160 eV for the survey and 20 eV for the narrow scans. The samples were insulated from the sample holder for charge compensation using a flood gun. The binding energies (BEs) were referenced to the C 1s BE of adventitious carbon on sample surface at 284.8 eV. Quantification of Ni-containing components was performed by deconvolution of Ni $2p_{3/2}$ peaks of corresponding samples after a linear-type background subtraction using CasaXPS software. Individual measurements of Ni metal, $NiCl_2$, $Ni(OH)_2$, and Nafion film were carried out to provide standard peak models for the deconvolution. Electrochemical half-cell tests were conducted using a modified rotating disk electrode (RDE) as a working electrode, with Pt wire as a counter electrode, and 1 M NaOH filled Hg/HgO as a reference electrode. The disk part of RDE was replaced by a nickel rod with enough space to mount the 1 mm thick nickel foam. The nickel foam catalyst was prepared and

fitted to the RDE as 3 mm diameter and 1 mm thickness. The modified RDE was connected with the constant rotating system (RRDE-3A, ALS), and electrochemical measurements were performed with a potentiostat (Model 2325, ALS). The cyclic voltammograms (CV) were obtained in 1 M NaOH solution at 50 mV s^{-1} under N_2 atmosphere. After 40 cycles of CV measurement, HOR/HER and BOR performances were measured in the following condition: HOR/HER: 1 M NaOH; BOR: 1 M NaOH with 50 mM $NaBH_4$ at 20 mV s^{-1} and 1600 rpm under N_2 atmosphere. The fuel impurity tolerance measurement is performed with 10% interval steps. The fuel impurity condition was made with different mixing ratios of $NaBH_4$ and $NaBO_2{\cdot}4H_2O$ in 1 M NaOH solution. The measured performances are normalized by the 0% impurity performance. The experimental error and average performance data are obtained by three different samples at the same conditions.

3.3 Results and discussion

3.3.1 Synthesis and morphology of catalysts

As shown in Figure 3.1a, nickel catalyst with anionic ionomer on nickel foam (NiF@AEI-Ni) and nickel catalyst with cationic ionomer on nickel foam (NiF@CEI-Ni) were prepared by simple solution spraying, followed by reduction reaction during the activation stage of the single-cell test. First, the mixed solution of AEI-$NiCl_2$ and CEI-$NiCl_2$ was coated onto nickel foam as shown in the SEM images (Figure S3.1b, c). The composites AEI-$NiCl_2$ and CEI-$NiCl_2$ have needle structures due to the spraying preparation technique and the high viscosity of ionomer dispersion, as shown in the TEM images (Figure S3.2a, b). The NiF@AEI-$NiCl_2$ and NiF@CEI-$NiCl_2$ were calcinated at 200 °C. After that, the electrode was activated in the membrane electrode assembly. During the activation/reduction process, the $NaBH_4$ in the anolyte spontaneously reduces the coated $NiCl_2$ composites to Ni metal nanoparticles on NiF; these metallic nickel particles are the active sites of the anode reaction. The calcination temperature affects the crystallinity and size of metallic nickel particles (Figure S3.3a-c). The optimum calcination temperature is 200 °C. When calcination temperatures above 200 °C are used, the Ni particle size increased, declining the DBFC performance (Figure S3.5, Table S3.1). This phenomenon may be attributed to the decomposition temperature of the ionomer. The decomposition temperatures of AEI and CEI, measured by Thermogravimetric analysis (TGA), start at 225 °C and 280 °C, respectively. (Figure S3.6). Before AEI decomposition begins, the solvent, which mainly consists of N-methyl-2-pyrrolidone, evaporates. For the CEI, the solvent is 1-propanol and ethanol, which evaporates more rapidly and is less viscous than AEI. The nickel particles, combined with ionomer, are covering the NiF surface, as shown in the scanning electron microscopy (SEM) images (Figure 3.1b, e). Transmission electron microscopy (TEM) images of AEI-Ni and CEI-Ni show that the metallic nickel particles are surrounded by ionomer and keep their nanoscale size (Figure 3.1c, f). High-angle annular dark-field scanning transmission electron microscopy (HAADF-STEM) and energy dispersive X-ray (EDX) mapping images confirm that Ni is well distributed and incorporated with ionomer (Figure 3.1d, g). Bromine (Br) consists of the counter ion of AEI which confirms that Ni is bound together with AEI (Figure 3.1d). Also, fluorine (F) is constructed the CEI polymer chain which is bound as well with Ni (Figure 3.1g).

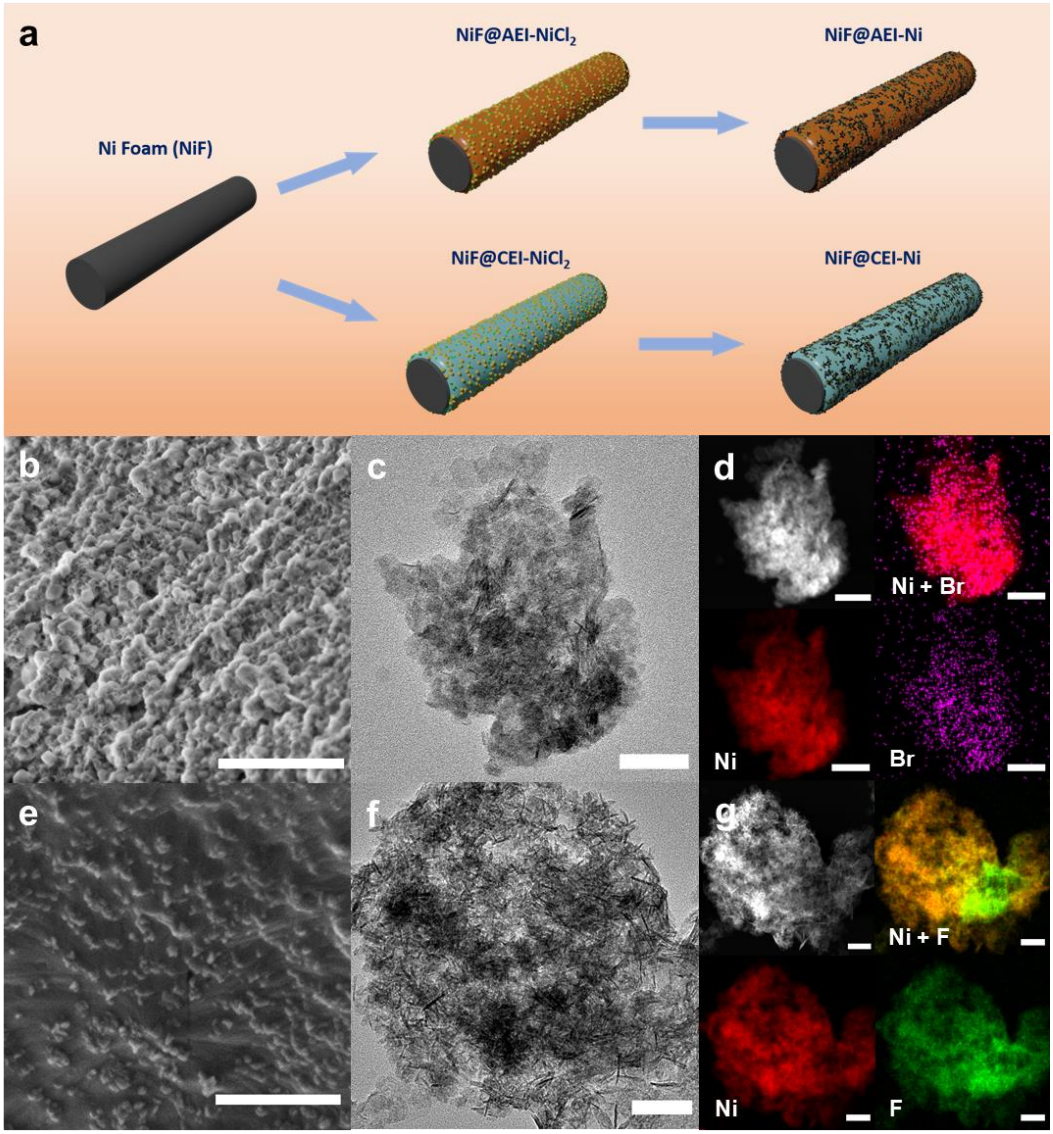

Figure 3.1 (a) Schematic illustration for the synthesis of nickel catalyst with anionic ionomer on nickel foam (NiF@AEI-Ni) and nickel catalyst with cationic ionomer on nickel foam (NiF@CEI-Ni) by solution spraying and reduction of nickel chloride. (b, c, d) SEM, TEM, HAADF-STEM image and the corresponding EDX map of the NiF@AEI-Ni (Ni: red, Br: magenta), (e, f, g) NiF@CEI-Ni (Ni: red, F: green). Scale bar: 1 µm for SEM and 50 nm for TEM, HAADF-STEM, and EDX images.

The surface compositions of NiF@AEI-Ni and NiF@CEI-Ni were characterized by XPS (Figure 3.2a, b). The peaks were fitted by using the standard spectra of Ni metal, $NiCl_2$, $Ni(OH)_2$, and Nafion film. The standard spectrum of Nafion film was used to extract the contribution of fluorine Auger electron spectra (F $KL_1L_{2,3}$). The different Ni species in NiF@CEI-Ni were calculated by excluding the contribution of the F $KL_1L_{2,3}$. Three Ni-containing compositions are detected for NiF@AEI-Ni:9.8wt% metallic Ni, 32.9wt% $Ni(OH)_2$, and 57.3wt% $NiCl_2$. The NiF@CEI-Ni surface consists of 4.0wt% metallic Ni, 25.2wt% $Ni(OH)_2$, and 70.8wt% $NiCl_2$. Therefore, some of the $NiCl_2$ are reduced to metallic Ni or changed to $Ni(OH)_2$, but some $NiCl_2$ remains. The Ni loading quantity is assumed to be 10 mg cm^{-2} on the NiF, even though the 22 mg cm^{-2} of $NiCl_2$ was not totally reduced.

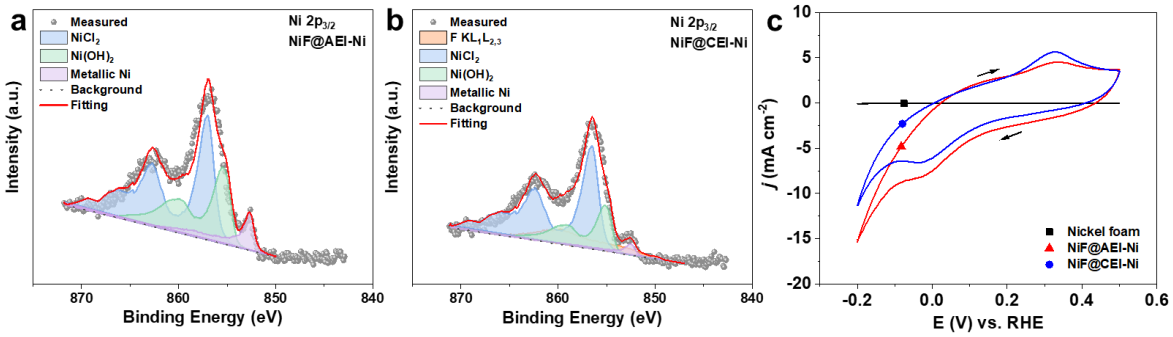

Figure 3.2 (a) Ni $2p_{3/2}$ XPS spectra of NiF@AEI-Ni, and (b) NiF@CEI-Ni. (c) Cyclic voltammetry of NiF, NiF@AEI-Ni, and NiF@CEI-Ni electrode, under N_2 atmosphere in 1 M NaOH, v = 50 mV s^{-1}.

Compared to the electrochemical deposition method on nickel foam, this synthesis method allows the creation of metallic nickel active sites without reducing the nickel oxide layer of nickel foam by acid solution.[24,25] The electrochemical active surface area (ECSA) of the nickel catalyst was calculated based on the anodic peak at 0.3 V on the cyclic voltammetry (CV) curve (Figure 3.2c). These curves were obtained through 40 cycles from −0.2 to 0.5 V versus RHE. Oshchepkov et al. estimated ECSA based on the use of the full anodic charge under the peak of reversible α-$Ni(OH)_2$ formation (0.3 V versus RHE); the corresponding specific charge is 514 µC cm^{-2}.[26] The ECSA of Pd was calculated using the full cathodic charge under the peak of palladium oxide reduction (0.6 V versus RHE); the corresponding specific charge is 420 µC cm^{-2} (Figure S3.4a).[27] After that, the surface area is divided by the catalyst metal loading (Pd: 0.5 mg cm^{-2}, Ni: 10 mg cm^{-2}). The ECSA of non-treated nickel foam cannot be calculated due to the presence of stable oxide at the electrode surface. The ECSA values for the NiF@AEI-Ni and NiF@CEI-Ni are 0.075 ± 0.002 m^2 g_{cat}^{-1} and 0.143 ± 0.004 m^2 g_{cat}^{-1}, respectively. For the Pd catalyst, the ECSA value of NiF@AEI-Pd/C and NiF@CEI-Pd/C are 2.08 ± 0.12 m^2 g_{cat}^{-1} and 1.99 ± 0.11 m^2 g_{cat}^{-1}, respectively (Figure S3.4b). There may be several estimation errors of the ECSA on Ni and Pd, we used the modified RDE to measure the CV curves of Ni and Pd/C catalyst on the nickel foam. The schematic configuration of the modified RDE is shown in Figure S3.8a. In the modified RDE, 1 mm thick nickel foam with catalyst is inserted. The catalyst is deposited onto the 2D surface in a normal RDE system. However, the 3D structure of nickel foam could affect the result due to the complex structure compared to the 2D planar structure. Nonetheless, the ECSA of NiF@AEI-Ni and NiF@CEI-Ni helps understand the active metallic Ni site. The ECSA of NiF@CEI-Ni is two times higher than that of NiF@AEi-Ni, which relates to the performance of the DBFC single-cell test in the latter. Indeed, the non-normalized surface area (not divided by metal loading) can be used to compare the activity (NiF@AEI-Pd/C: 0.74 ± 0.04 cm^2, NiF@CEI-Pd/C: 0.70 ± 0.04 cm^2, NiF@AEI-Ni: 0.53 ± 0.01 cm^2, and NiF@CEI-Ni: 1.01 ± 0.03 cm^2).

3.3.2 Differences between nickel and palladium catalyst for BOR and HOR/HER reaction

Figure 3.3 shows the different catalytic properties of Ni and Pd in 1 M NaOH (HER/HOR condition) or 1 M NaOH with 50 mM $NaBH_4$ (BOR condition). In the HOR reaction with Ni catalyst, the anodic currents of NiF@AEI-Ni and NiF@CEI-Ni show similar performance (AEI: 2.1 ± 0.4 mA cm^{-2}, CEI: 1.6 ± 0.3 mA cm^{-2} at 0.3 V versus RHE, Figure 3.3a). Oshchepkov et al. described how the HOR/HER kinetics between metallic nickel and surface oxide species co-exist within metal Ni sites.[26,28,29] Compared to only metallic nickel species on the surface, the mixture of oxide species with metallic nickel shows higher HOR/HER reaction activity. Although the HOR activity is relatively high for the mixture of metallic and oxide species, it is still low compared to the Pd catalyst, despite the lower Pd metal loading (Figure 3.3c). The different catalytic natures of Pd and Ni play an important role (Figure 3.3e).

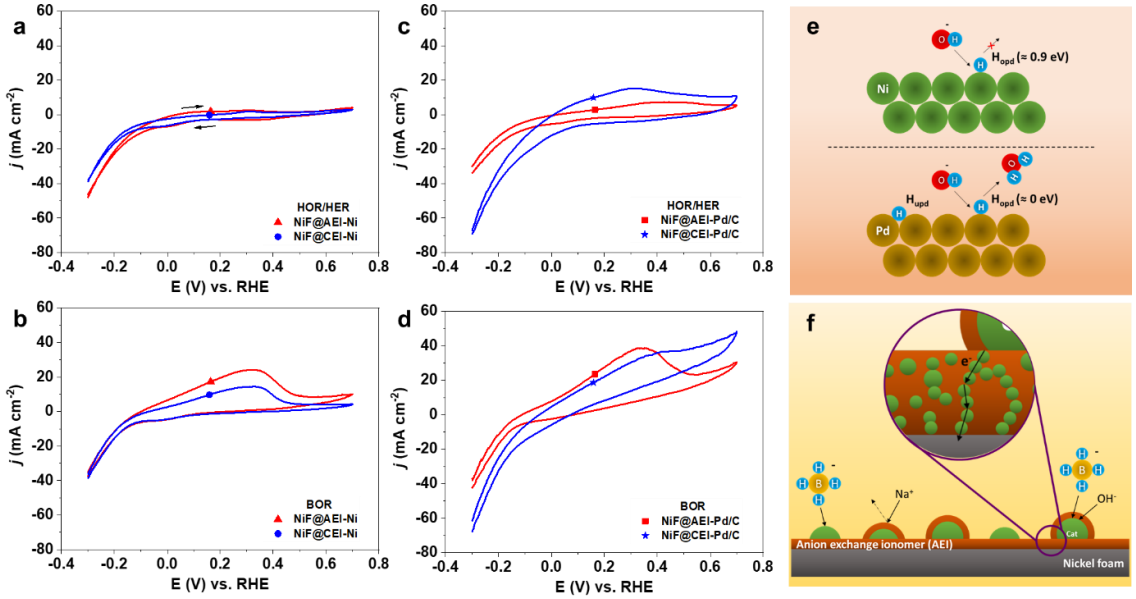

Figure 3.3 (a, b) Cyclic voltammetry of HER/HOR and BOR over NiF@AEI-Ni and NiF@CEI-Ni, (c, d) NiF@AEI-Pd/C and NiF@CEI-Pd/C electrode under N_2 atmosphere in the difference electrolyte (HER/HOR: 1 M NaOH, BOR: 1 M NaOH with 50 mM $NaBH_4$; v = 20 mV s^{-1}, ω = 1600 rpm). (e) Schematic diagram of different catalytic properties of Ni and Pd in hydrogen oxidation reaction (HOR). (f) Schematic diagram of selective ion transport by AEI coating on the catalyst and the catalyst network for conducting electrons to the current collector (NiF).

Pd possesses two hydrogen adsorption modes: under potentially deposited hydrogen (H_{upd}), adsorbed in multi-fold hollow sites, and over potentially deposited hydrogen (H_{opd}), adsorbed at the surface. H_{upd} cannot act as the HOR/HER intermediate because of its strong binding energy. Thus, it is the weakly adsorbed hydrogen H_{opd} that participates in hydrogen oxidation electrocatalysis, with the Gibbs free energy of H_{opd} on Pd catalyst close to zero. On the other hand, H_{opd} on the Ni catalyst has a higher Gibbs free energy (≈ 0.9 eV), making its involvement in the HOR rather unlikely.[26] Furthermore, the HOR activity is also influenced by the nature of the ionomer. A significant HOR activity difference is observed for AEI-Pd/C and CEI-Pd/C, originating from the different ions transported through the ionomer. Na^+ ions are transported by the CEI-Pd/C catalyst in the 1 M NaOH rather than H^+ ions. Koper et al. explained the HER enhancement with a high cation concentration on the catalyst.[30] The quantity of cations surrounding the CEI plays a central role in stabilizing the rate-determining Volmer step by interacting with the dissociating water molecule. This clarified the higher concentration of hydrogen evolved below 0 V vs. RHE with the CEI-Pd/C (Figure 3.3c). Thus, the HOR current is higher in CEI-Pd/C than AEI-Pd/C. For NiF@AEI-Pd/C, the current density at 0.3 V versus RHE is 5.2 ± 0.5 mA cm^{-2}. For NiF@CEI-Pd/C, the current density at 0.3 V versus RHE is 15.2 ± 0.1 mA cm^{-2}, which is almost 3 times higher than NiF@AEI-Pd/C. From those results, we can clearly identify the influence of the ionomer on the catalytic HOR performance of Pd.

The CV curves for BOR are generally similar in shape except for the NiF@CEI-Pd/C electrode (Figure 3.3b, d). The CV curve of NiF@CEI-Pd/C has a shoulder at 0.4 V versus RHE that gradually increases, indicating that the BOR or HOR occurs differently than for the other samples. The other three CV curves have a peak at 0.3 V versus RHE that could be explained by the OH^- adsorption on the catalyst surface. According to kinetic modeling by Oshchepkov et al., the surface coverage of metallic Ni with H_{ad} is high even under N_2 atmosphere, with adsorbed H atoms dominating on the surface until 0.2 V versus RHE. Moreover, the formation of α-$Ni(OH)_2$ proceeds through the OH adsorption, resulting in the blocking of the Ni active sites.[26] Therefore, the anodic peak at 0.3 V versus RHE is due to the limited number of Ni active sites for borohydrides. On the other hand, the Pd catalyst surface phenomena differ between AEI-Pd/C and CEI-Pd/C. For the AEI-Pd/C case, AEI transports OH^- ions to the

catalyst, so the Pd surface is saturated by OH^-, similar to the Ni catalyst case (Figure 3.3d). On the other hand, the catalyst surface of CEI-Pd/C is not limited by OH^- due to the recombination reaction of adsorbed OH^- with H^+ that forms water. The H^+ ion is supplied from the BOR. Furthermore, as long as H_2 easily accessed the Pd surface, HOR will continuously occur. The catalytic activity for BOR should be considered along with the HOR activity, as HOR activity is inherent during BOR measurement. The HOR activity cannot be the same in 1 M NaOH as it is in 1 M NaOH with 50 mM $NaBH_4$ solution, but the BOR activity can be approximated by deducing the current densities via two different data sets. The deduced BOR currents are 21.5 ± 2.7 mA cm^{-2} and 12.3 ± 1.4 mA cm^{-2} for NiF@AEI-Ni and NiF@CEI-Ni, respectively. In the case of Pd/C, similar results are also obtained. The deduced BOR currents for NiF@AEI-Pd/C and NiF@CEI-Pd/C are 29.7 ± 3.2 mA cm^{-2} and 12.8 ± 1.7 mA cm^{-2}, respectively. Thus, the BOR activity is enhanced with AEI-coated catalyst, thanks to the facilitated OH^- ion transportation. In the view of the electron conduction, the anode electrode consists of the ionomer and catalyst composite. The catalyst network inside the ionomer is used as an electron conducting pathway toward the NiF current collector (Figure 3.3f).

We compared the Levich plots of the two different ionomers with Ni and Pd (Figure S3.7). To calculate the electron transfer number (*n*) during the reaction, the diffusion coefficient (*D*) and kinematic viscosity (*v*) of electrolyte are required. Chatenet et al. reported the diffusion coefficient value by the transit-time determination technique with gold rotating ring–disk electrodes, and kinematic viscosity by micro-viscosimeter.[31] However, the reported diffusion coefficient of $NaBH_4$ for the Levich plot is based on a 1 M NaOH with 10 mM $NaBH_4$ solution, which does not match our 1 M NaOH with 50 mM $NaBH_4$ solution. In addition, the surface area is hard to estimate with the Levich equation, which is designed for planar surfaces, due to the complex nickel foam structure with catalyst. Although these limitations, the relative electron transfer number between the two different ionomer composites can be compared because they possess similar configurations, except for the ionomer. In the anode reaction of DBFC, the BOR and HOR occur together during the electron transfer reaction. The BOR and HOR are known as 8-electrons and 2-electrons transfer reactions, respectively. Thus, when the Levich plot is steeper, *n* is larger, indicating that the BOR reaction is more active than the HOR reaction. The slope of the Levich plot for NiF@AEI-Ni (6.4×10^{-5}) and NiF@AEI-Pd/C (1.1×10^{-4}) are higher than NiF@CEI-Ni (6.8×10^{-6}) and NiF@CEI-Pd/C (3.4×10^{-5}), as shown in Figure S3.7. These results signify that the BOR is preferred when the catalyst is covered by AEI, thanks to the boosted OH^- ion transportation. This observation is supported by a previous study. Ramani et al. explained the effect of the electrode binder composition with OCV for CEI and AEI with Pd/C using a recessed planar electrode.[14] The AEI with Pd/C has high OCV compared to CEI with Pd/C due to the higher BOR activity compared to HOR.

3.3.3 Single-cell performance, fuel utilization, and hydrogen evolution measurements

The DBFC single-cell performances were measured at 80 ˚C, and the flow rate for both cathode (15 % H_2O_2 in 1.5 M H_2SO_4) and anode (1.5 M $NaBH_4$ in 3 M NaOH) was 7 ml min^{-1} (Figure 3.4). Among all the samples, the highest peak power density is achieved with NiF@CEI-Ni (0.59 W cm^{-2}) with an OCV of 1.93 V (Figure 3.4c). This peak power density value is one of the highest ever reported for non-noble metal anode catalysts. (Table 3.1, S3.2). In comparison, the peak power density of NiF@AEI-Ni is 0.45 W cm^{-2}, and the OCV is 1.95 V (Figure 3.4a). We observed that the polarization curve of NiF@AEI-Ni at high current areal density (> 0.6 A cm^{-2}) fluctuates due to the significant presence of the H_2 evolution reaction. Although the peak power density of NiF@AEI-Ni is not the highest among the other samples, its OCV is the highest. This phenomenon may be due to the dominance of BOR compared to HOR and BH_4^- hydrolysis under the OCV condition. The Pd/C catalysts with different ionomers show distinct differences in peak power density and OCV. The peak power density of NiF@AEI-Pd/C is 0.38 W cm^{-2}, and OCV is 1.88 V (Figure 3.4b). On the other hand, the peak power density of NiF@CEI-Pd/C is 0.05 W cm^{-2}, which is significantly lower than for NiF@AEI-Pd/C (Figure 3.4d). The reason for this low peak power density

could be explained by Pd poisoning with intermediate states of BH_4^- (BH_x^*, BH_xOH^{-*}, x = 1 to 3) and H_2 evolution.[12] Therefore, a much lower OCV (1.29 V) was observed for NiF@CEI-Pd/C than for NiF@AEI-Pd/C (1.88 V). The open-circuit voltage (OCV) and peak power density of DBFC single-cell measurement are summarized in Figure 3.5a.

To better understand the anode electrode reaction in DBFC, we measured fuel utilization and hydrogen evolution (Figure 3.5b). Fuel utilization amounts are calculated using ^{11}B NMR, comparing the integrated areas of the BH_4^- peaks and BO_2^- peak (Figure S3.9). Fuel utilization is an important factor in the DBFCs. The amount of fuel consumed depends on the current at the DBFC. This information can help to understand the unveiled reaction inside the DBFC. Fuel utilization calculation based on ^{11}B NMR is for the first time conducted as far as we know, highlighting the importance of this study. H_2 evolution amounts are measured volumetrically from the anode exhaust line. An exponential model fits both the fuel utilization and H_2 evolution. The coefficient of the exponential term (a) is fixed to 3 for fuel utilization and 20 for H_2 evolution fitting to compare the difference of catalytic properties with the exponential factor (R_0). The R_0 represents the rate of the fuel utilization (fuel consumption) and H_2 evolution with different catalyst and ionomer configurations. It is possible to compare the activity of catalysts even with different metal loadings. Also, we can predict and distinguish the reactions happening in the single-cell using those fitted curves.

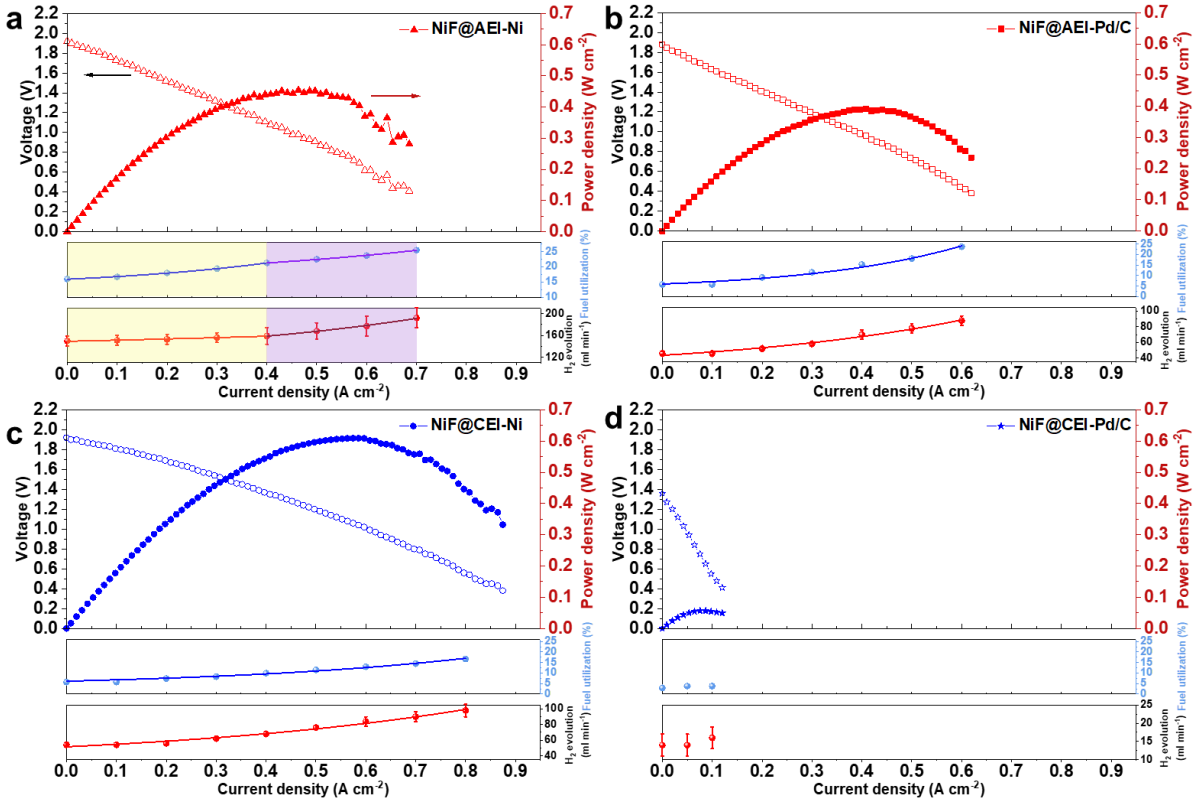

Figure 3.4 DBFC single-cell performances of (a) NiF@AEI-Ni (Fuel utilization fit: j < 0.4 A cm^{-2}; $y = 12.9 + 3e^{2.6x}$, j > 0.4 A cm^{-2}; $y = 15.3 + 3e^{1.7x}$, H_2 evolution fit: j < 0.4 A cm^{-2}; $y = 129 + 20e^{0.95x}$, j > 0.4 A cm^{-2}; $y = 116 + 20e^{1.9x}, R^2 = 0.99$), (b) NiF@AEI-Pd/C (Fuel utilization fit: $y = 2.9 + 3e^{3.3x}$, H_2 evolution fit: $y = 23.5 + 20e^{2x}, R^2 = 0.98$), (c) NiF@CEI-Ni (Fuel utilization fit: $y = 3.1 + 3e^{1.9x}$, H_2 evolution fit: $y = 31.5 + 20e^{1.5x}, R^2 = 0.99$), and (d) NiF@CEI-Pd/C correlated with fuel utilization and H_2 evolution. (Anolyte: 1.5 M $NaBH_4$ in 3 M NaOH, Catholyte: 15 % H_2O_2 in 1.5 M H_2SO_4, flow rate: 7 ml min^{-1} on both anode and cathode)

Table 3.1 Summary of the polarization, fuel utilization fit, and H_2 evolution fit curves.

Samples		Polarization curve		Fuel utilization $(y = y_0 + ae^{R_0 x})$		H_2 evolution $(y = y_0 + ae^{R_0 x})$	
		OCV (V)	Peak power density (W cm^{-2})	$y_0 + a$ (%)	R_0 (cm^2 A^{-1})	$y_0 + a$ (ml min^{-1})	R_0 (cm^2 A^{-1})
NiF@AEI-Ni	j < 0.4 A cm^{-2}	1.95 ± 0.02	0.45 ± 0.01	15.9 ± 0.1	2.56 ± 0.03	149.4 ± 0.4	0.95 ± 0.06
	j > 0.4 A cm^{-2}			18.3 ± 0.1	1.75 ± 0.03	136.1 ± 1.5	1.89 ± 0.04
NiF@CEI-Ni		1.93 ± 0.01	0.59 ± 0.02	6.1 ± 0.2	1.92 ± 0.04	51.5 ± 0.1	1.53 ± 0.04
NiF@AEI-Pd/C		1.88 ± 0.01	0.38 ± 0.02	5.9 ± 0.5	3.26 ± 0.08	43.5 ± 1.2	1.97 ± 0.06
NiF@CEI-Pd/C		1.29 ± 0.08	0.05 ± 0.01	-	-	-	-

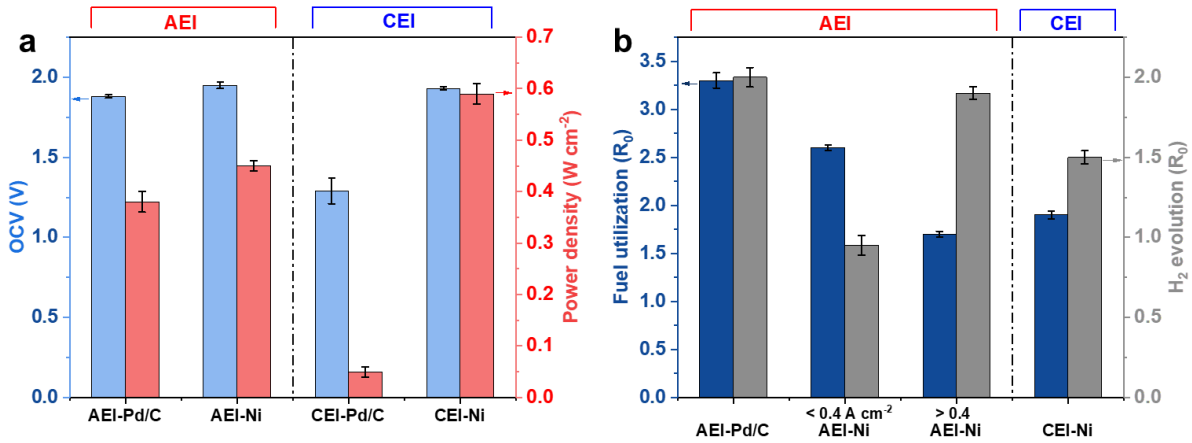

Figure 3.5 (a) Open circuit voltage and peak power density of DBFC single-cells depending on ionomers and catalysts. (b) Fuel utilization and H_2 evolution exponential factor (R_0).

The fuel utilization and H_2 evolution for NiF@AEI-Ni are fitted piecewise, over two domains: one below 0.4 A cm^{-2} current density, and the other above 0.4 A cm^{-2}. The change at 0.4 A cm^{-2} is due to the BOR activity shift toward BH_4^- hydrolysis or high hydrogen evolution. The fuel utilization amount at zero load (0 A cm^{-2}, OCV) is 15.9%, meaning that nickel with the AEI interface is notably active for BOR. Furthermore, the H_2 evolution amounts highly correlate with the fuel utilization amount. In other words, the H^+ ions produced from the BOR do not cross the membrane but participate in the formation of H_2 gas. The H^+ ion for the cathode may be produced at the interfacial area of the membrane and anode by H_2O dissociation. Kohl et al. explained the water dissocia-

tion at the interface of AEM/PEM to supply H^+ ions to the cathode and OH^- ions to the anode.[32] Indeed, the BH_4^- hydrolysis is observed at current densities above 0.4 A cm^{-2} due to the change in R_0 and H_2 evolution. The fuel utilization (R_0) decreased from 2.56 to 1.75, and the one for H_2 evolution increased from 0.95 to 1.89. These values confirm the decrease in BOR activity and increase in BH_4^- hydrolysis activity, as the current density rises beyond 0.4 A cm^{-2}.

Comparison of Ni and Pd catalyst is possible for NiF@AEI-Ni and NiF@AEI-Pd/C with single-cell performance, fuel utilization, and H_2 evolution. The peak power density difference is only 73 mW cm^{-2} between NiF@AEI-Ni and NiF@AEI-Pd/C. However, the difference in fuel utilization at zero load is 10%, which comes from the extent of metal loading in the Ni and Pd catalysts. The amount of Ni metal in NiF@AEI-Ni is 10 mg cm^{-2}, in contrast to only 0.5 mg cm^{-2} for Pd in NiF@AEI-Ni. Thus, even if the fuel utilization exponential factor of NiF@AEI-Ni (R_0 = 2.56) is lower than that of NiF@AEI-Pd/C (R_0 = 3.26), the fuel consumption is higher on NiF@AEI-Ni (Table 3.1, Figure 3.5b). The different catalytic nature of Ni and Pd under the low local pH condition (CEI) stands out more conspicuously than under the high local pH condition (AEI). As shown in Figure 5a, the peak power density of NiF@CEI-Ni is ten times higher than for NiF@CEI-Pd/C. In the case of Ni catalyst, the low HOR activity at both low local pH (CEI) and high local pH (AEI) implies that BOR is dominant independently of the pH. On the other hand, active sites of Pd catalyst need to be protected by high local pH (AEI) to prevent the competitive HER/HOR to take place, highlighting the importance of the ionomer choice for this catalyst (Figure S3.10).

When comparing the two different local pH conditions on the Ni catalyst, we note that the peak power density of NiF@AEI-Ni and NiF@CEI-Ni is 0.45 W cm^{-2} and 0.59 W cm^{-2}, respectively. There may be three reasons for the lower power density of NiF@AEI-Ni. The ECSA value for the NiF@AEI-Ni (0.075 ± 0.002 $m^2\ g_{cat}^{-1}$) is lower than NiF@CEI-Ni (0.143 ± 0.004 $m^2\ g_{cat}^{-1}$). And rapid BH_4^- hydrolysis after 0.4 A cm^{-2} increases the hydrogen evolved, limiting the BH_4^- diffusion or transport to the active site. Second, the water depletion at the AEI/PEM interface could also hinder the performance. As mentioned before, the hydrogen and hydroxide ions dissociated from water in the membrane supply ions to the cathode and anode. Therefore, if the water supply inside the membrane is limited, there is a paucity of hydroxide and hydrogen ions, decreasing the single-cell measurement performance. Third, the ionic conductivity of AEI is lower than CEI, raising the resistance of the whole single-cell membrane electrode assembly. The iR corrected polarization curves of NiF@AEI-Ni and NiF@CEI-Ni are additionally compared in Figure S3.11. The high-frequency resistances (HFRs) were obtained from the Nyquist semi-circle fit. The HFRs of the AEI-Ni are high in all the ranges compared to CEI-Ni. The NiF@AEI-Ni has higher HFRs than NiF@CEI-Ni. However, the iR corrected DBFC performance of NiF@AEI-Ni is still lower than NiF@CEI-Ni. This lower performance, even after the iR correction, might come from the gas permeability difference between CEI and AEI. Jaouen et al. explained that the lower gas permeability in AEIs compared to Nafion might decrease the electrochemical performance.[33] In our case, the low gas permeability inhibits the hydrogen gas evacuation, potentially blocking the active site of BOR. In addition, the fluctuation of single-cell performance in NiF@AEI-Ni might be attributed to the low gas permeability in AEI. In addition, the fuel utilization of NiF@AEI-Ni (R_0 = 2.56) and NiF@CEI-Ni (R_0 = 1.92) indicate that the CEI is the preferred ionomer for Ni catalyst.

In conclusion, the NiF@CEI-Ni has an efficient fuel consumption with limited side reactions, such as BH_4^- hydrolysis, compared to Pd catalyst and AEI condition. Indeed, the fuel utilization of NiF@CEI-Ni at the OCV is 6.1%, which is significantly lower than the value for NiF@AEI-Ni. Therefore, Ni is a suitable non-noble metal catalyst for the DBFC anode. From the view of performance and fuel utilization, NiF@CEI-Ni is the best configuration. Although the goal is to minimize the conversion of BH_4^- to H_2, the hydrogen produced from DBFCs can be used for electricity production with a PEMFC or heat generation by catalytic combustion. Combining a DBFC with a PEMFC could maximize the conversion of borohydride to electricity, generating a promising system.

3.3.4 Durability and fuel cycling test

Durability and fuel cycling tests were further conducted to investigate the stability and endurance of the catalyst. Durability was measured under the same conditions as the performance test, but at 1 V potentiostatic mode (Figure 3.6a). For the NiF@AEI-Ni, the power density dropped only by 4.2% after 60 min. However, the power density for NiF@CEI-Ni dropped by 35.2% after 60 min. This greater performance decrease originates from the adsorption of the intermediate states of BH_4^- (BH_x^*, BH_xOH^{-*}, x = 1 to 3) on the active site of Ni. A clear difference is observed due to the local pH on the catalyst surface. There is unavoidable catholyte crossover through the membrane in the single-cell configuration, inducing the low local pH at the catalyst on the NiF@CEI-Ni. Due to the lack of OH^- in the low local pH condition, the borohydride oxidation reaction is incomplete, generating intermediate states of BH_4.[17] The evidence for the adsorption of intermediate products was confirmed in Figure 3.6b. After the durability test at 1 V, the single-cell with NiF@CEI-Ni was cycled 10 times from OCV to 0.35 V. The peak power density recovered 99% of the starting power density. During the cycling, the intermediates detached or were consumed to form BO_2^-. The electro-osmotic drag force changes during voltage cycling allow sufficient OH^- supply to the catalyst. The Na concentration increase in the catholyte exhaust with the current density increase supports the change of electro-osmotic drag forces (Figure S3.12). On the other hand, the power density of NiF@AEI-Ni shows stable performance due to the complete BOR (BH_4^- to BO_2^-) at Ni active site with a high local pH condition (OH^-). The fuel cycling test with NiF@AEI-Ni and NiF@CEI-Ni was conducted to observe the effect of fuel impurity (BO_2^-) on the catalyst. The purpose is to maximize the conversion of BH_4^- chemical energy to electricity. The anolyte and catholyte amount were fixed to 450 ml for 1 cycle in 1 h. The power density decay curve during the cycling test could be modeled as an exponential decay (Figure 3.6c, d, S3.13), which can then be used to determine the reaction rate as a function of the amount of fuel remaining. The half-lives for powder density decay are 1.6 h and 2.5 h for the NiF@AEI-Ni and NiF@CEI-Ni, respectively (Table 3.2), indicating that the NiF@CEI-Ni is more durable than NiF@AEI-Ni.

Although the NiF@CEI-Ni shows a power density drop during the durability test, the limited power density decay during fuel recycling is primordial for practical application. Indeed, the fuel utilization amount after 8 h is 68.7% for NiF@CEI-Ni, substantially greater than the 47.6% for NiF@AEI-Ni. The NiF@CEI-Ni can operate with BH_4^- fuel containing a high impurity level (BO_2^-). Fitting a sigmoidal logistic function to the fuel utilization can predict the maximum operating limits using impure fuel, for both NiF@AEI-Ni and NiF@CEI-Ni. The NiF@AEI-Ni could be operated with up to 50.5% BO_2^-, while NiF@CEI-Ni could be operated with impurity concentrations as high as 74.7%. The effect of fuel impurity is also investigated in the half-cell configuration to evaluate only the anode electrode. The BOR current at 0.3 V in the different concentration ratios of $NaBH_4$ and $NaBO_2$ are normalized in Figure S3.14. The normalized single-cell (unit-cell) power density is compared to the half-cell. The impurity tolerance is clearly shown in both half-cell and single-cell conditions. The stiff performance drop is shown from 0% to 40% impure fuel condition at NiF@AEI-Ni configuration. On the other hand, the performance of NiF@CEI-Ni decreases continuously until 70% impure fuel condition. In other words, the NiF@CEI-Ni can be operated under more impure conditions. There is some difference observed in half-cell and single-cell conditions at NiF@AEI-Ni. The performance on half-cell condition varies a lot and has not dropped as much as the single-cell condition, because the evolution of hydrogen could affect more the performance and interfere with the BOR measurement in the half-cell than in the single-cell. The conversion of chemical energy to electrical energy is calculated based on the power density decay with fuel utilization (Equation 4). The theoretical enthalpy of the overall reaction occurring in the DBFC is −788.4 kJ mol^{-1} (Equation 5).[14] The amount of $NaBH_4$ in the anolyte (1.5 M $NaBH_4$ with 3 M NaOH solution, 450 ml) is 0.675 mol. The chemical energy conversion of $NaBH_4$ for NiF@CEI-Ni is 21.4%. The rest of the chemical energy in $NaBH_4$ is converted to heat and H_2 gas. The anolyte fuel crossover and intermixing amount of catholyte and anolyte is not considered in the calculation. Compared to the NiF@CEI-Ni, the NiF@AEI-Ni achieves only 19.7% conversion. Even though the fuel utilization of NiF@AEI-Ni (47.6%) after

8 h is closer to the maximum operation condition of fuel (50.5%), the lower $NaBH_4$ chemical energy conversion comes from the H_2 evolution side-reaction. Therefore, the NiF@CEI-Ni is a more promising configuration with high efficiency of fuel utilization, high power density, and tolerance of impurity.

$$\text{Energy conversion (\%)} = \frac{\text{Power}}{NaBH_4 \times \text{Fuel utilization} \times \text{Enthalphy change}} \quad (4)$$

$$NaBH_4 + 4H_2O_2 \rightarrow NaBO_2 + 6H_2O \quad (5)$$

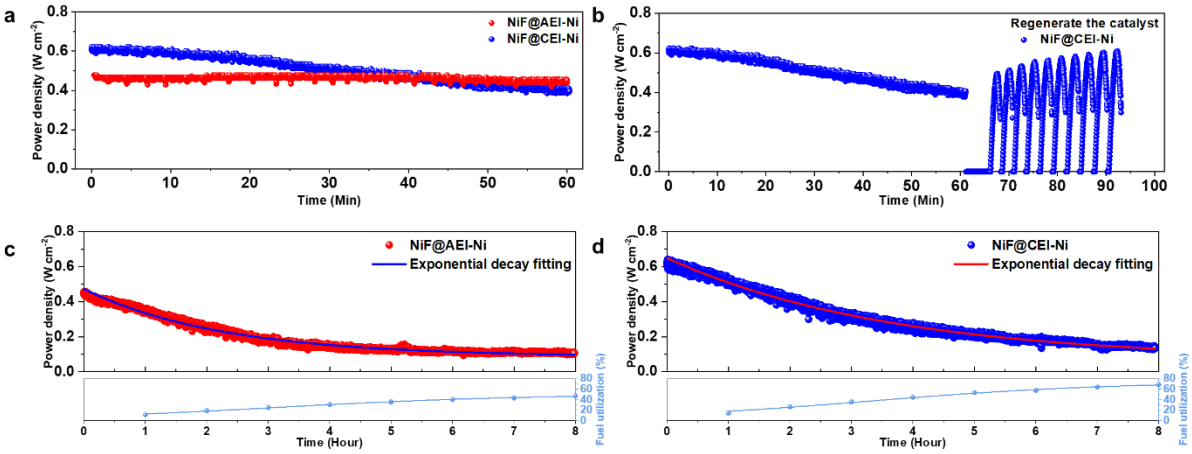

Figure 3.6 (a) Durability test of NiF@AEI-Ni and NiF@CEI-Ni single-cell at 1 V. (b) Regeneration process of the NiF@CEI-Ni catalyst after durability test. (c) Power density decay of single-cell at 1 V ($y = 0.09 + 0.39e^{(-\frac{x}{2.3})}, t_{\frac{1}{2}} = 1.6, R^2 = 0.99$), fuel utilization of NiF@AEI-Ni ($y = \frac{50.5}{(1+e^{-0.5(x-3.1)})}, R^2 = 0.99$), (d) power density decay of NiF@AEI-Ni ($y = 0.07 + 0.58e^{(-\frac{x}{3.6})}, t_{\frac{1}{2}} = 2.5, R^2 = 0.99$), and fuel utilization ($y = \frac{74.7}{(1+e^{-0.5(x-3.3)})}, R^2 = 0.99$) during fuel cycling.

Table 3.2 Summary of power density decay, fuel utilization, and chemical energy conversion during fuel cycling test.

Samples	Fuel cycling test					
	Power density decay half-life ($t_{1/2}$, h)	Fuel utilization after 8 h (%)	Fuel utilization ($y = \frac{a}{1+e^{-k(x-x_c)}}$)		Electrical energy (kJ)	$NaBH_4$ chemical energy conversion (%)
			Maximum operation condition (a, %)	Half-life to reach a (x_c, h)		
NiF@AEI-Ni	1.6	47.6	50.5 ± 1.0	3.1 ± 0.1	49.9	19.7
NiF@CEI-Ni	2.5	68.7	74.7 ± 1.7	3.3 ± 0.2	78.1	21.4

3.4 Conclusions

A facile synthesis method of Ni catalyst on NiF with different ionomers was demonstrated and evaluated. The ionomers' effects on Ni and Pd catalyst were compared using half-cell and single-cell measurements. Because of the differing BOR and HOR catalytic activities on Ni and Pd catalysts, single-cell performance varies significantly. The single-cell performance of NiF@CEI-Pd/C is far lower than for NiF@AEI-Pd/C due to the dominance of HOR at the Pd/C active site rather than BOR. On the other hand, Ni catalyst is less influenced by the ionomer type than Pd, because the activity of HOR on Ni is limited. Therefore, the active sites of Ni are selective for BOR. Indeed, the fuel utilization and H_2 evolution explain the phenomena inside the veiled single-cell measurement. The AEI layer produces a high local pH that facilitates the BOR on the active site of Pd and Ni. Although the AEI-Ni shows a higher activity for BOR than the CEI-Ni in half-cell configuration, the single-cell performance was lower than CEI-Ni. This is due to the high H_2 evolution, BH_4^- concentration loss at the interface of catalyst, high ionic resistance relative to CEI, and the water depletion on the membrane electrode interface. The durability test shows that the CEI-Ni adsorbs intermediate states of BH_4^- with evidence for 99% performance recovery after voltage cycling. The fuel cycling test proved that the CEI-Ni configuration tolerates better fuel impurity (BO_2^-) than AEI-Ni. Moreover, the higher chemical energy conversion of BH_4^- fuel to electricity on CEI-Ni is more promising. From this study, the practical applications of DBFC are becoming more realistic thanks to the utilization of non-noble Ni catalyst.

References

(1) Wang, Y.-J.; Long, W.; Wang, L.; Yuan, R.; Ignaszak, A.; Fang, B.; P. Wilkinson, D. Unlocking the Door to Highly Active ORR Catalysts for PEMFC Applications: Polyhedron-Engineered Pt-Based Nanocrystals. *Energy & Environmental Science* **2018**, *11* (2), 258–275. https://doi.org/10.1039/C7EE02444D.

(2) Hua, T. Q.; Ahluwalia, R. K.; Peng, J.-K.; Kromer, M.; Lasher, S.; McKenney, K.; Law, K.; Sinha, J. Technical Assessment of Compressed Hydrogen Storage Tank Systems for Automotive Applications. *International Journal of Hydrogen Energy* **2011**, *36* (4), 3037–3049. https://doi.org/10.1016/j.ijhydene.2010.11.090.

(3) Li, X.; Popov, B. N.; Kawahara, T.; Yanagi, H. Non-Precious Metal Catalysts Synthesized from Precursors of Carbon, Nitrogen, and Transition Metal for Oxygen Reduction in Alkaline Fuel Cells. *Journal of Power Sources* **2011**, *196* (4), 1717–1722. https://doi.org/10.1016/j.jpowsour.2010.10.018.

(4) Lu, S.; Pan, J.; Huang, A.; Zhuang, L.; Lu, J. Alkaline Polymer Electrolyte Fuel Cells Completely Free from Noble Metal Catalysts. *PNAS* **2008**, *105* (52), 20611–20614. https://doi.org/10.1073/pnas.0810041106.

(5) Schlapbach, L.; Züttel, A. Hydrogen-Storage Materials for Mobile Applications. *Nature* **2001**, *414* (6861), 353–358. https://doi.org/10.1038/35104634.

(6) Züttel, A. Materials for Hydrogen Storage. *Materials Today* **2003**, *6* (9), 24–33. https://doi.org/10.1016/S1369-7021(03)00922-2.

(7) Orimo, S.; Nakamori, Y.; Eliseo, J. R.; Züttel, A.; Jensen, C. M. Complex Hydrides for Hydrogen Storage. *Chem. Rev.* **2007**, *107* (10), 4111–4132. https://doi.org/10.1021/cr0501846.

(8) Lombardo, L.; Yang, H.; Züttel, A. Destabilizing Sodium Borohydride with an Ionic Liquid. *Materials Today Energy* **2018**, *9*, 391–396. https://doi.org/10.1016/j.mtener.2018.07.001.

(9) Lombardo, L.; Yang, H.; Züttel, A. Study of Borohydride Ionic Liquids as Hydrogen Storage Materials. *Journal of Energy Chemistry* **2019**, *33*, 17–21. https://doi.org/10.1016/j.jechem.2018.08.011.

(10) Ko, Y.; Lombardo, L.; Li, M.; Oveisi, E.; Yang, H.; Züttel, A. Interfacial Effect between Aluminum-Based Complex Hydrides and Nickel-Containing Porous Carbon Sheets. *ACS Appl. Energy Mater.* **2020**. https://doi.org/10.1021/acsaem.0c01262.

(11) Zhu, Y.; Ouyang, L.; Zhong, H.; Liu, J.; Wang, H.; Shao, H.; Huang, Z.; Zhu, M. Closing the Loop for Hydrogen Storage: Facile Regeneration of NaBH4 from Its Hydrolytic Product. *Angewandte Chemie International Edition* **2020**, *59* (22), 8623–8629. https://doi.org/10.1002/anie.201915988.

(12) Braesch, G.; Bonnefont, A.; Martin, V.; Savinova, E. R.; Chatenet, M. Borohydride Oxidation Reaction Mechanisms and Poisoning Effects on Au, Pt and Pd Bulk Electrodes: From Model (Low) to Direct Borohydride Fuel Cell Operating (High) Concentrations. *Electrochimica Acta* **2018**, *273*, 483–494. https://doi.org/10.1016/j.electacta.2018.04.068.

(13) Grimmer, C.; Grandi, M.; Zacharias, R.; Cermenek, B.; Weber, H.; Morais, C.; Napporn, T. W.; Weinberger, S.; Schenk, A.; Hacker, V. The Electrooxidation of Borohydride: A Mechanistic Study on Palladium (Pd/C) Applying RRDE, 11B-NMR and FTIR. *Applied Catalysis B: Environmental* **2016**, *180*, 614–621. https://doi.org/10.1016/j.apcatb.2015.07.028.

(14) Wang, Z.; Parrondo, J.; He, C.; Sankarasubramanian, S.; Ramani, V. Efficient PH-Gradient-Enabled Microscale Bipolar Interfaces in Direct Borohydride Fuel Cells. *Nature Energy* **2019**, *4* (4), 281–289. https://doi.org/10.1038/s41560-019-0330-5.

(15) Wang, Z.; Sankarasubramanian, S.; Ramani, V. Reactant-Transport Engineering Approach to High-Power Direct Borohydride Fuel Cells. *Cell Reports Physical Science* **2020**, *1* (7), 100084. https://doi.org/10.1016/j.xcrp.2020.100084.

(16) Wang, Z.; Mandal, M.; Sankarasubramanian, S.; Huang, G.; Kohl, P. A.; Ramani, V. K. Influence of Water Transport Across Microscale Bipolar Interfaces on the Performance of Direct Borohydride Fuel Cells. *ACS Appl. Energy Mater.* **2020**, *3* (5), 4449–4456. https://doi.org/10.1021/acsaem.0c00145.

(17) Rostamikia, G.; J. Janik, M. Direct Borohydride Oxidation : Mechanism Determination and Design of Alloy Catalysts Guided by Density Functional Theory. *Energy & Environmental Science* **2010**, *3* (9), 1262–1274. https://doi.org/10.1039/C0EE00115E.

(18) Gu, L.; Luo, N.; Miley, G. H. Cathode Electrocatalyst Selection and Deposition for a Direct Borohydride/Hydrogen Peroxide Fuel Cell. *Journal of Power Sources* **2007**, *173* (1), 77–85. https://doi.org/10.1016/j.jpowsour.2007.05.005.

(19) Bepari, S.; Kuila, D. Steam Reforming of Methanol, Ethanol and Glycerol over Nickel-Based Catalysts-A Review. *International Journal of Hydrogen Energy* **2019**. https://doi.org/10.1016/j.ijhydene.2019.08.003.

(20) Zhou, G.; Barrio, L.; Agnoli, S.; Senanayake, S. D.; Evans, J.; Kubacka, A.; Estrella, M.; Hanson, J. C.; Martínez-Arias, A.; Fernández-García, M.; Rodriguez, J. A. High Activity of Ce1−xNixO2−y for H2 Production through Ethanol Steam Reforming: Tuning Catalytic Performance through Metal–Oxide Interactions. *Angewandte Chemie International Edition* **2010**, *49* (50), 9680–9684. https://doi.org/10.1002/anie.201004966.

(21) Ouyang, L. Z.; Ye, S. Y.; Dong, H. W.; Zhu, M. Effect of Interfacial Free Energy on Hydriding Reaction of Mg–Ni Thin Films. *Appl. Phys. Lett.* **2007**, *90* (2), 021917. https://doi.org/10.1063/1.2428877.

(22) Vogt, C.; Groeneveld, E.; Kamsma, G.; Nachtegaal, M.; Lu, L.; Kiely, C. J.; Berben, P. H.; Meirer, F.; Weckhuysen, B. M. Unravelling Structure Sensitivity in CO2 Hydrogenation over Nickel. *Nat Catal* **2018**, *1* (2), 127–134. https://doi.org/10.1038/s41929-017-0016-y.

(23) Oshchepkov, A. G.; Braesch, G.; Ould-Amara, S.; Rostamikia, G.; Maranzana, G.; Bonnefont, A.; Papaefthimiou, V.; Janik, M. J.; Chatenet, M.; Savinova, E. R. Nickel Metal Nanoparticles as Anode Electrocatalysts for Highly Efficient Direct Borohydride Fuel Cells. *ACS Catal.* **2019**, 8520–8528. https://doi.org/10.1021/acscatal.9b01616.

(24) Braesch, G.; Wang, Z.; Sankarasubramanian, S.; G. Oshchepkov, A.; Bonnefont, A.; R. Savinova, E.; Ramani, V.; Chatenet, M. A High Performance Direct Borohydride Fuel Cell Using Bipolar Interfaces and Noble Metal-Free Ni-Based Anodes. *Journal of Materials Chemistry A* **2020**. https://doi.org/10.1039/D0TA06405J.

(25) Braesch, G.; Oshchepkov, A. G.; Bonnefont, A.; Asonkeng, F.; Maurer, T.; Maranzana, G.; Savinova, E. R.; Chatenet, M. Nickel 3D Structures Enhanced by Electrodeposition of Nickel Nanoparticles as High Performance Anodes for Direct Borohydride Fuel Cells. *ChemElectroChem* **2020**, *7* (7), 1789–1799. https://doi.org/10.1002/celc.202000254.

(26) Oshchepkov, A. G.; Braesch, G.; Bonnefont, A.; Savinova, E. R.; Chatenet, M. Recent Advances in the Understanding of Nickel-Based Catalysts for the Oxidation of Hydrogen-Containing Fuels in Alkaline Media. *ACS Catal.* **2020**, *10* (13), 7043–7068. https://doi.org/10.1021/acscatal.0c00101.

(27) Singh, R. K.; Davydova, E. S.; Douglin, J.; Godoy, A. O.; Tan, H.; Bellini, M.; Allen, B. J.; Jankovic, J.; Miller, H. A.; Alba-Rubio, A. C.; Dekel, D. R. Synthesis of CeOx-Decorated Pd/C Catalysts by Controlled Surface Reactions for Hydrogen Oxidation in Anion Exchange Membrane Fuel Cells. *Advanced Functional Materials* **2020**, *30* (38), 2002087. https://doi.org/10.1002/adfm.202002087.

(28) Oshchepkov, A. G.; Bonnefont, A.; Parmon, V. N.; Savinova, E. R. On the Effect of Temperature and Surface Oxidation on the Kinetics of Hydrogen Electrode Reactions on Nickel in Alkaline Media. *Electrochimica Acta* **2018**, *269*, 111–118. https://doi.org/10.1016/j.electacta.2018.02.106.

(29) Oshchepkov, A. G.; Bonnefont, A.; Saveleva, V. A.; Papaefthimiou, V.; Zafeiratos, S.; Pronkin, S. N.; Parmon, V. N.; Savinova, E. R. Exploring the Influence of the Nickel Oxide Species on the Kinetics of Hydrogen Electrode Reactions in Alkaline Media. *Top Catal* **2016**, *59* (15), 1319–1331. https://doi.org/10.1007/s11244-016-0657-0.

(30) Goyal, A.; Koper, M. T. M. The Interrelated Effect of Cations and Electrolyte PH on the Hydrogen Evolution Reaction on Gold Electrodes in Alkaline Media. *Angewandte Chemie International Edition* **2021**, *60* (24), 13452–13462. https://doi.org/10.1002/anie.202102803.

(31) Chatenet, M.; Molina-Concha, M. B.; El-Kissi, N.; Parrour, G.; Diard, J.-P. Direct Rotating Ring-Disk Measurement of the Sodium Borohydride Diffusion Coefficient in Sodium Hydroxide Solutions. *Electrochimica Acta* **2009**, *54* (18), 4426–4435. https://doi.org/10.1016/j.electacta.2009.03.019.

(32) Ünlü, M.; Zhou, J.; Kohl, P. A. Hybrid Anion and Proton Exchange Membrane Fuel Cells. *J. Phys. Chem. C* **2009**, *113* (26), 11416–11423. https://doi.org/10.1021/jp903252u.

(33) G. Santori, P.; N. Mondal, A.; R. Dekel, D.; Jaouen, F. The Critical Importance of Ionomers on the Electrochemical Activity of Platinum and Platinum-Free Catalysts for Anion-Exchange Membrane Fuel Cells. *Sustainable Energy & Fuels* **2020**, *4* (7), 3300–3307. https://doi.org/10.1039/D0SE00483A.

Supporting information

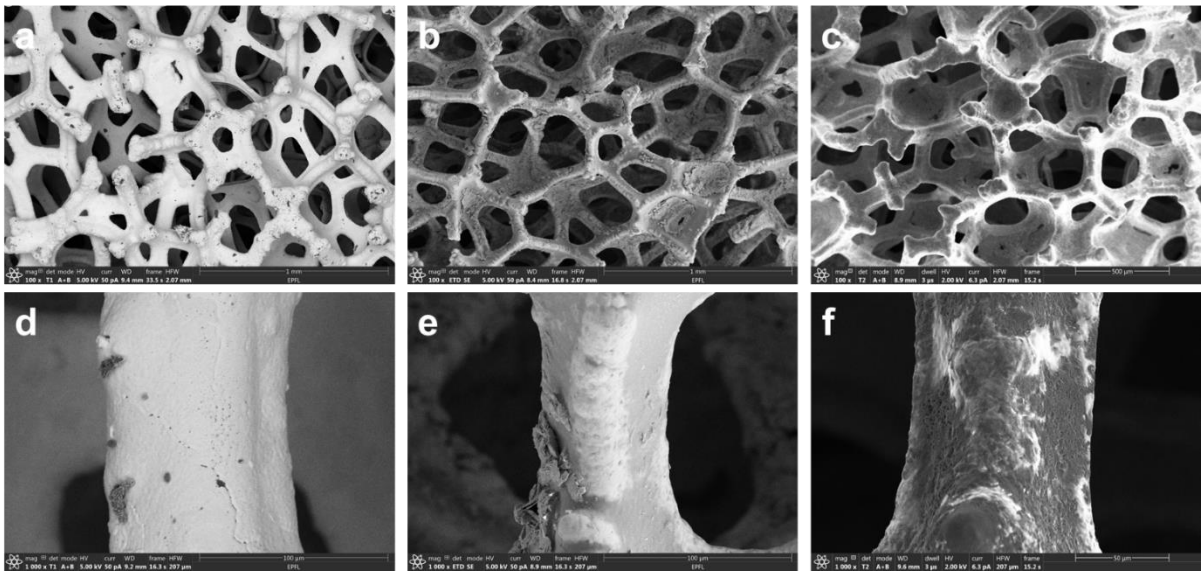

Figure S3.1 SEM images of (a, d) nickel foam (NiF), (b, e) nickel chloride with anionic ionomer on nickel foam (NiF@AEI-$NiCl_2$), and (c, f) nickel chloride with cationic ionomer on nickel foam (NiF@CEI-$NiCl_2$).

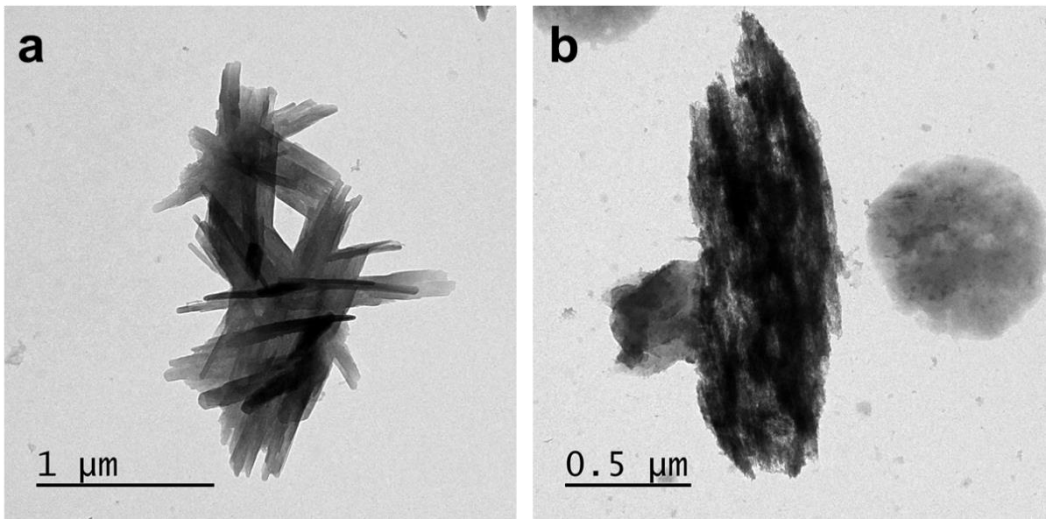

Figure S3.2 TEM images of (a) AEI-$NiCl_2$, and (b) CEI-$NiCl_2$.

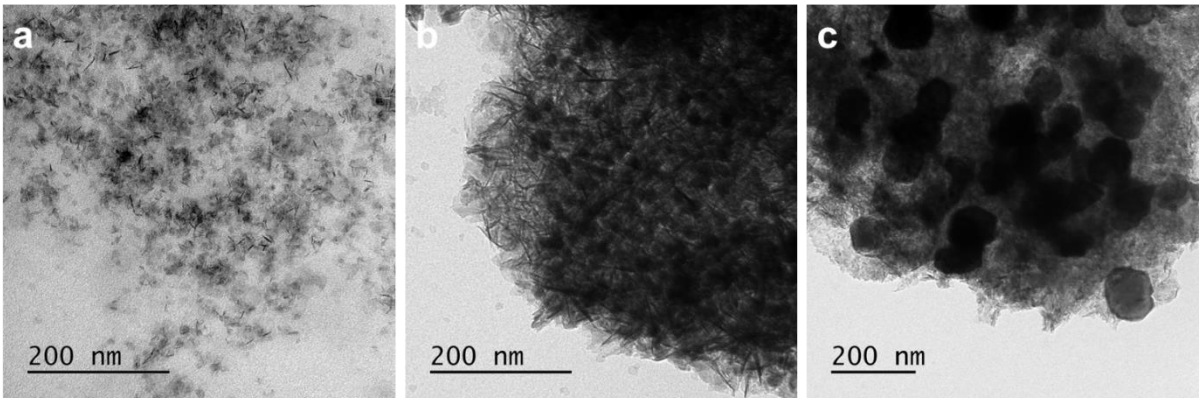

Figure S3.3 TEM images of nickel catalyst with anionic ionomer after activation/reduction process that affected by different calcination temperature under N_2 atmosphere (a) 200 ˚C, (b) 300 ˚C, and (c) 400 ˚C.

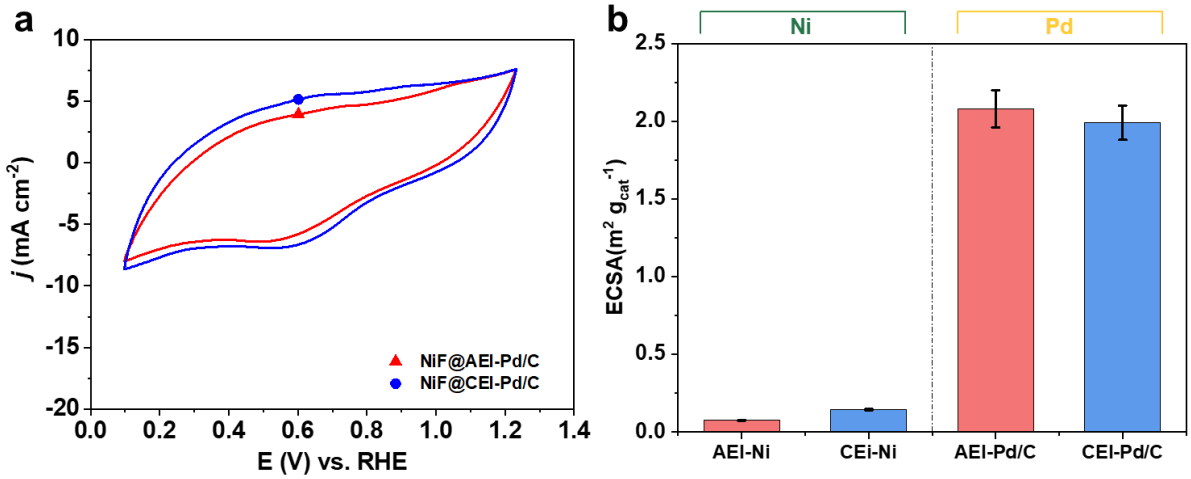

Figure S3.4 (a) Cyclic voltammetry of NiF@AEI-Pd/C and NiF@CEI-Pd/C, under N_2 atmosphere in 1 M NaOH, v = 50 mV s^{-1}. (b) The electrochemical active surface area (ECSA) comparison graph of AEI-Ni (0.075 ± 0.002 m^2 g_{cat}^{-1}), CEI-Ni (0.143 ± 0.004 m^2 g_{cat}^{-1}), AEI-Pd/C (2.08 ± 0.12 m^2 g_{cat}^{-1}), and CEI-Pd/C (1.99 ± 0.11 m^2 g_{cat}^{-1}); Pd metal amount: 0.5 mg cm^{-2}, Ni metal amount 10 mg cm^{-2}.

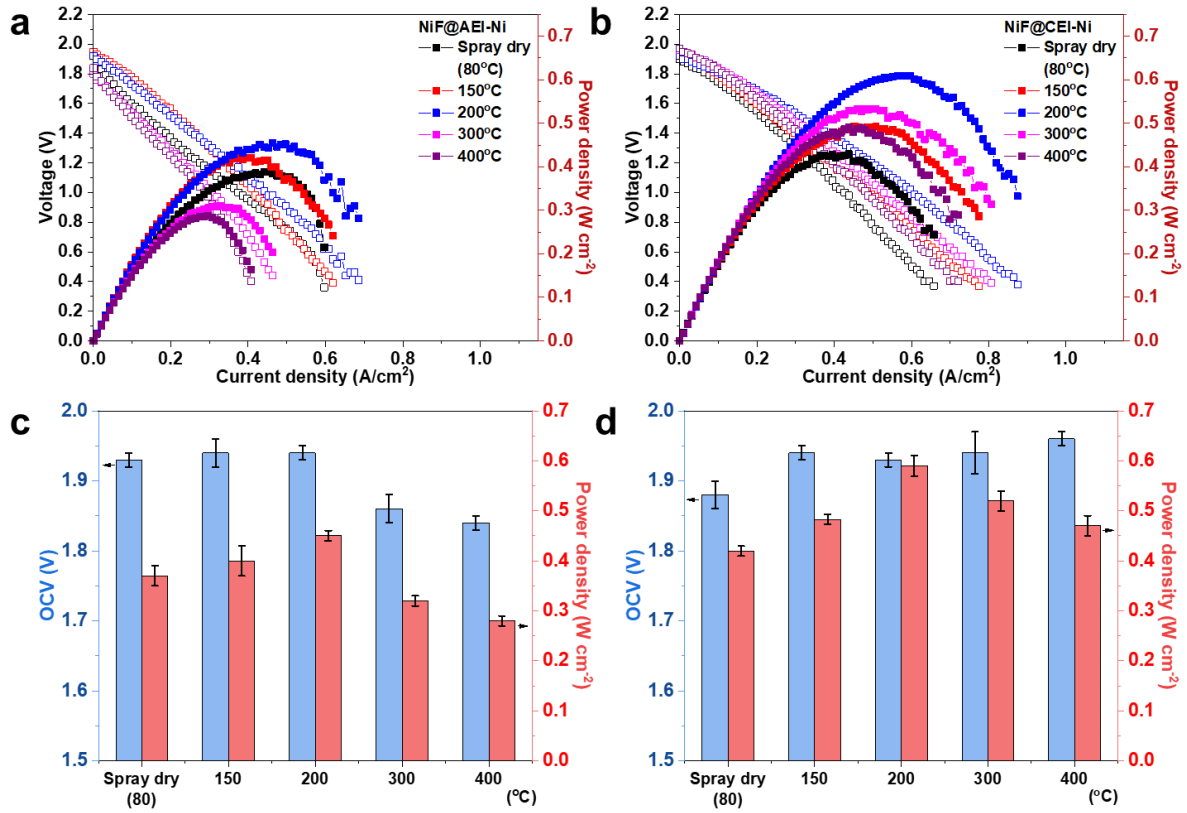

Figure S3.5 DBFC single-cell performances of (a) NiF@AEI-Ni and (b) NiF@CEI-Ni samples at different calcination temperatures under N_2 atmosphere. (c) The comparison of open circuit potential (OCV) and peak power density for NiF@AEI-Ni and (d) NiF@CEI-Ni.

Table S3.1 Comparison of open circuit potential (OCV) and peak power density at NiF@AEI-Ni and NiF@CEI-Ni

Samples	OCV (V)	Peak power density (W cm^{-2})
	NiF@AEI-Ni	
Spray dry (80 ˚C)	1.93 ± 0.01	0.37 ± 0.02
150 ˚C	1.94 ± 0.02	0.40 ± 0.03
200 ˚C	1.94 ± 0.01	0.45 ± 0.01
300 ˚C	1.86 ± 0.02	0.32 ± 0.01
400 ˚C	1.84 ± 0.01	0.28 ± 0.01
	NiF@CEI-Ni	
Spray dry (80 ˚C)	1.88 ± 0.02	0.42 ± 0.01
150 ˚C	1.94 ± 0.01	0.48 ± 0.01
200 ˚C	1.93 ± 0.01	0.59 ± 0.02
300 ˚C	1.94 ± 0.03	0.52 ± 0.02
400 ˚C	1.96 ± 0.01	0.47 ± 0.02

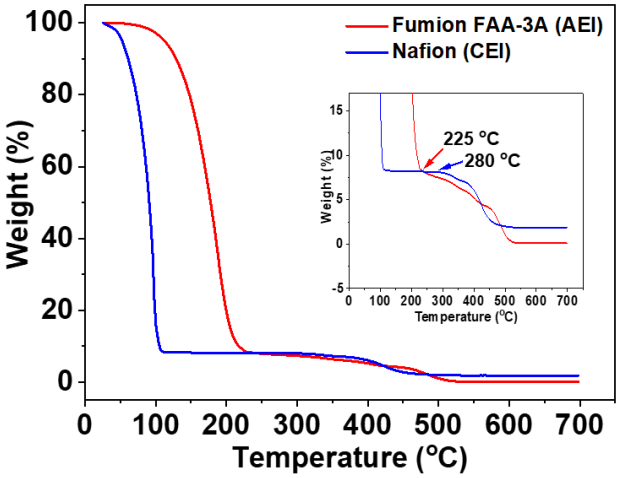

Figure S3.6 Thermogravimetric analysis (TGA) curves of Fumion FAA-3A ionomer (AEI) and Nafion ionomer (CEI).

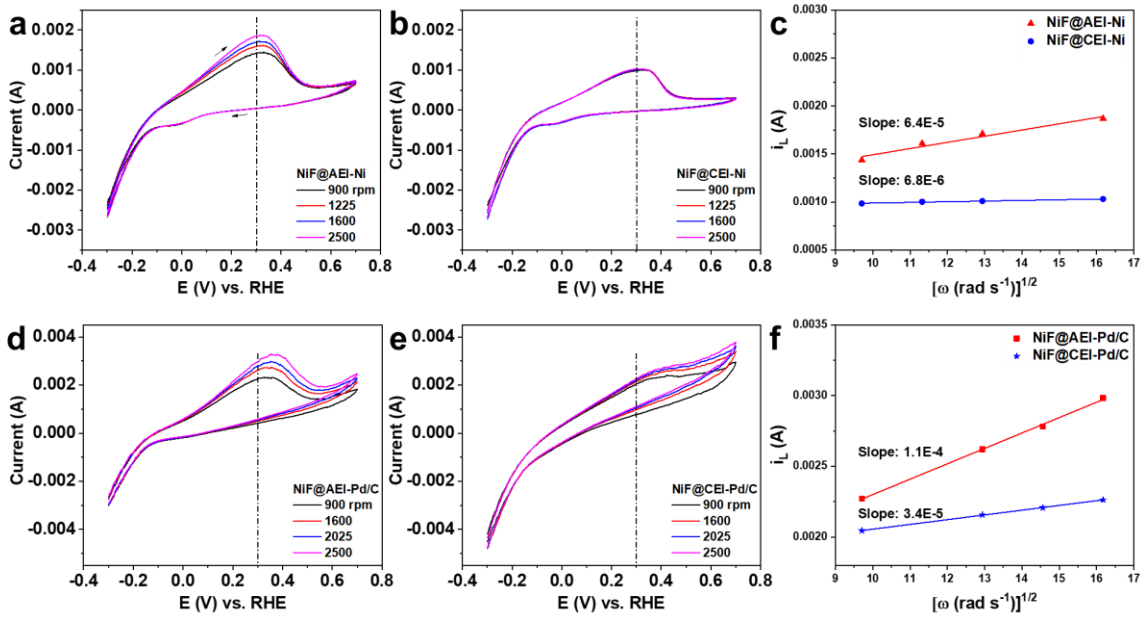

Figure S3.7 Cyclic voltammetry of BOR activity at different rotation rates for (a) NiF@AEI-Ni, (b) NiF@CEI-Ni, (d) NiF@AEI-Pd/C, and (e) NiF@CEI-Pd/C under N_2 atmosphere in 1M NaOH with 50 mM $NaBH_4$ electrolyte. Levich plots of (c) NiF@AEI-Ni and NiF@CEI-Ni, (f) NiF@AEI-Pd/C and NiF@CEI-Pd/C.

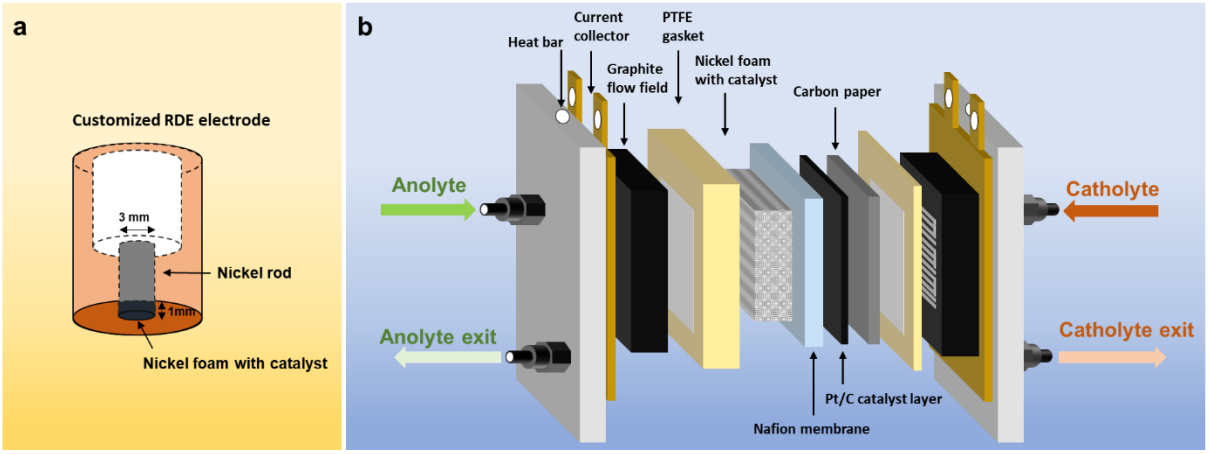

Figure S3.8 Schematic image of (a) modified RDE and (b) DBFC single-cell assembly.

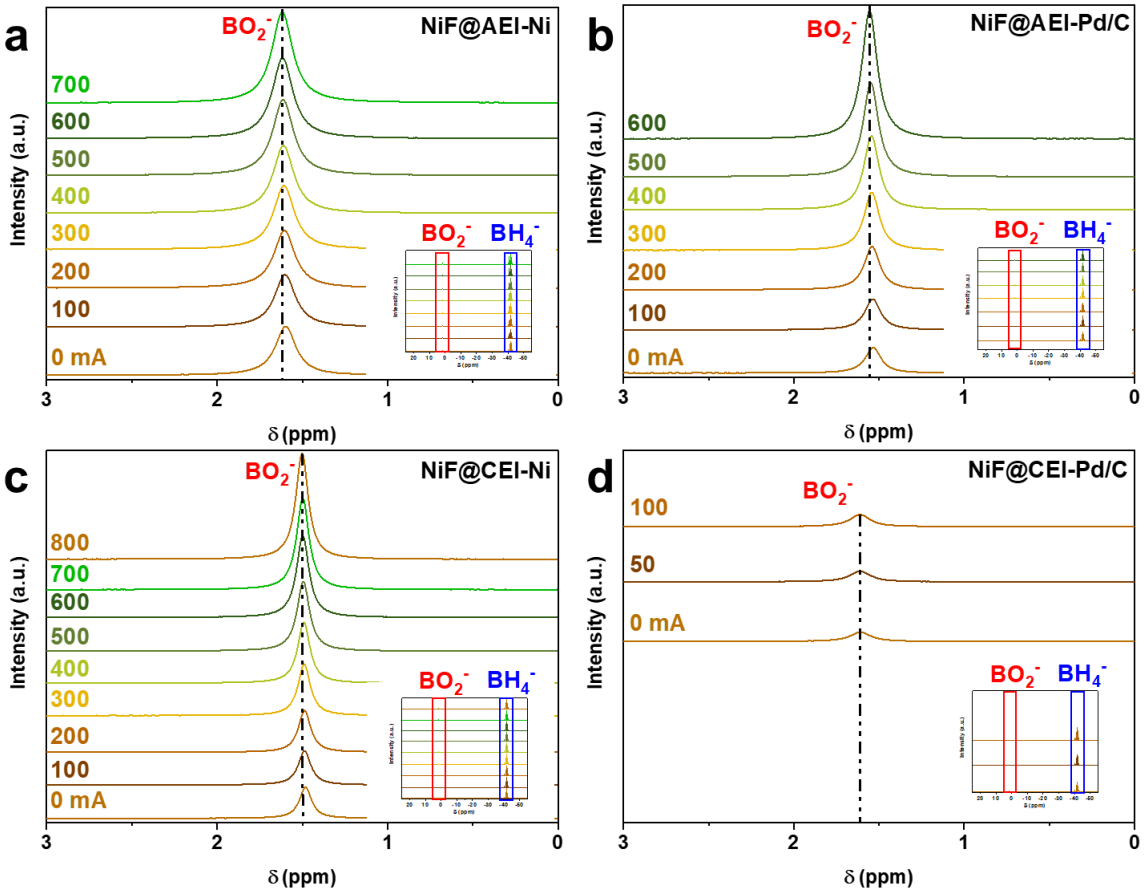

Figure S3.9 ^{11}B NMR of outlet anolyte after the galvanostatic test for (a) NiF@AEI-Ni, (b) NiF@AEI-Pd/C, (c) NiF@CEI-Ni, and (d) NiF@CEI-Pd/C (solvent: D_2O).

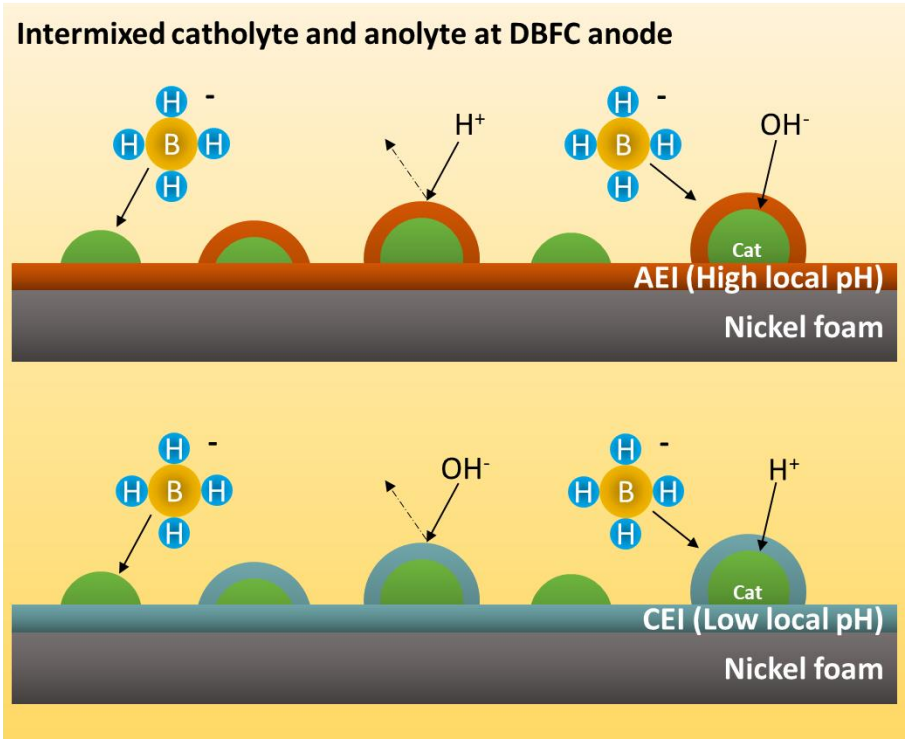

Figure S3.10 Schematic image of local pH condition at catalyst surface with AEI and CEI. The catholyte and anolyte intermixing at DBFC anode in single-cell configuration.

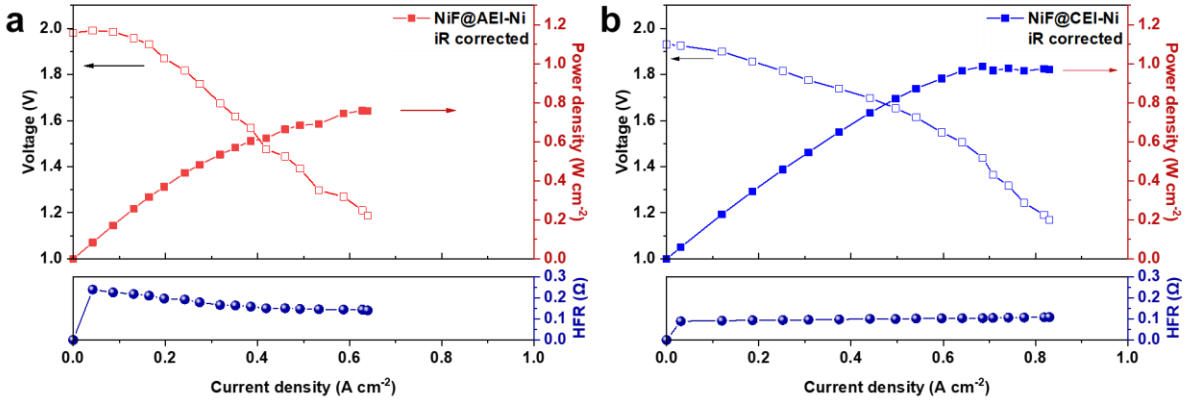

Figure S3.11 iR corrected polarization curve of (a) NiF@AEI-Ni and (b) NiF@CEI-Ni (HFR: high frequency resistance).

Table S3.2 Comparison of recent DBFC performance data (PGMs based, noble metal free anode).

Anode (loading, mg cm^{-2})	Cathode (loading, mg cm^{-2})	Separator (thickness, μm)	Oxidant	Operation temperature (°C)	P_{max} (mW cm^{-2})	OCV (V)	Year published
Au/C (2)	Pt/C (2)	Nafion 117 (175)	O_2	85	72	1.0	2006[1]
Ni-Pt/C (10)	$Co(OH)_2$-PPY-C (5)	Nafion 117 (183)	O_2	80	550	1.1	2012[2]
Pt/C (0.3)	Pt/C (0.3)	Nafion 117 (183)	H_2O_2	25	275	1.67	2015[3]
Pd/C (0.3)	Pt/C (0.3)	Nafion 117 (183)	H_2O_2	25	211	1.72	2015[3]
Pd/C (3) + Ni	Pt/C (3)	Bipolar interface (175)	H_2O_2	70	630	1.95	2019[4]
Pd/C (3) + Ni	Pt/C (3)	Bipolar interface (175)	H_2O_2	70	890	1.96	2020[5]
Pd/C (0.5) + Ni	Pt/C (1)	Nafion 115 (127)	H_2O_2	80	50	1.29	This work
Pd/C (0.5) + Ni	Pt/C (1)	Bipolar interface (127)	H_2O_2	80	376	1.88	This work
Noble metal free anode (loading, mg cm^{-2})	Cathode (loading, mg cm^{-2})	Separator (thickness, μm)	Oxidant	Operation temperature (°C)	P_{max} (mW cm^{-2})	OCV (V)	Year published
Ni powder (167)	Pt/C (1)	Nafion 211 (25)	Air	40	40	1.0	2005[6]
Os/C (1.7)	Pt/C (4)	Nafion 117 (175)	O_2	60	109	1.1	2012[7]
NiB/C (70)	$LaNi_{0.9}Ru_{0.1}O_3$/C (7.5)	Nafion	O_2	25	180	1.09	2018[8]
Ni_{ED}/C (0.6)	Pt/C (2)	Nafion 212 (50)	O_2	60	240	1.21	2019[9]
NiED/eNFT (1.2)	Pt/C (2)	Nafion 212 (50)	O_2	60	180	1.24	2020[10]
u-SnO_2/Co_3O_4 (10)	$LaNiO_3$ (7.5)	Poly fiber mem-brane (140)	Air	25	52	1.02	2020[11]
$Co(OH)_2$-PPy-BP (5)	$Co(OH)_2$-PPy-BP (5)	Cu-AEM (120)	O_2	60	403	1.05	2020[12]
Ni_{ED}/eNFT-D	Pt/C (1)	Bipolar interface (175)	H_2O_2	70	446	2.0	2020[13]
NiF@AEI-Ni (10)	Pt/C (1)	Bipolar interface (127)	H_2O_2	80	449	1.94	This work
NiF@CEI-Ni (10)	Pt/C (1)	Nafion 115 (127)	H_2O_2	80	593	1.93	This work

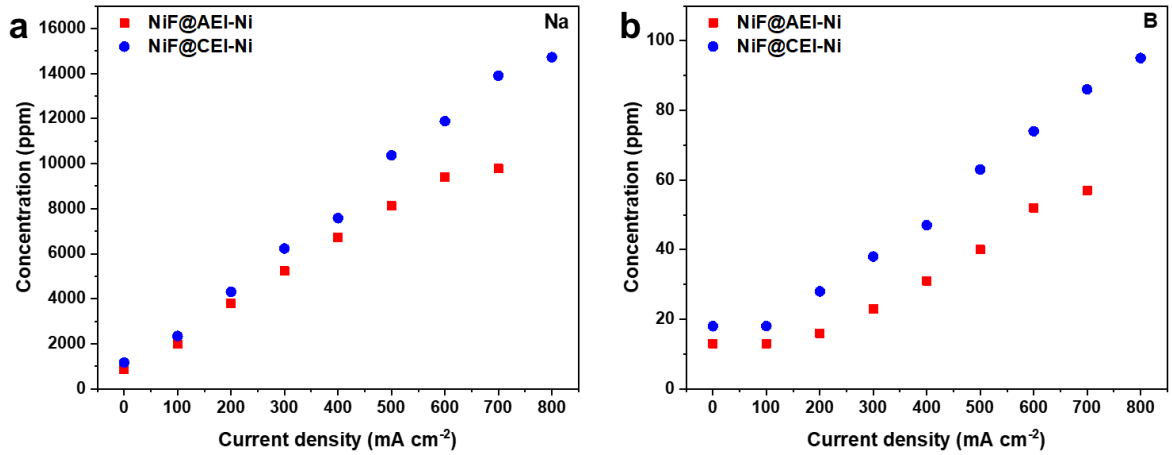

Figure S3.12 The element concentration of outlet catholyte for (a) Na and (b) B by ICP-OES analysis. (Na concentration in catholyte and anolyte: 7 ppm and 81,797 ppm, B concentration in catholyte and anolyte: 0 ppm and 18,159 ppm)

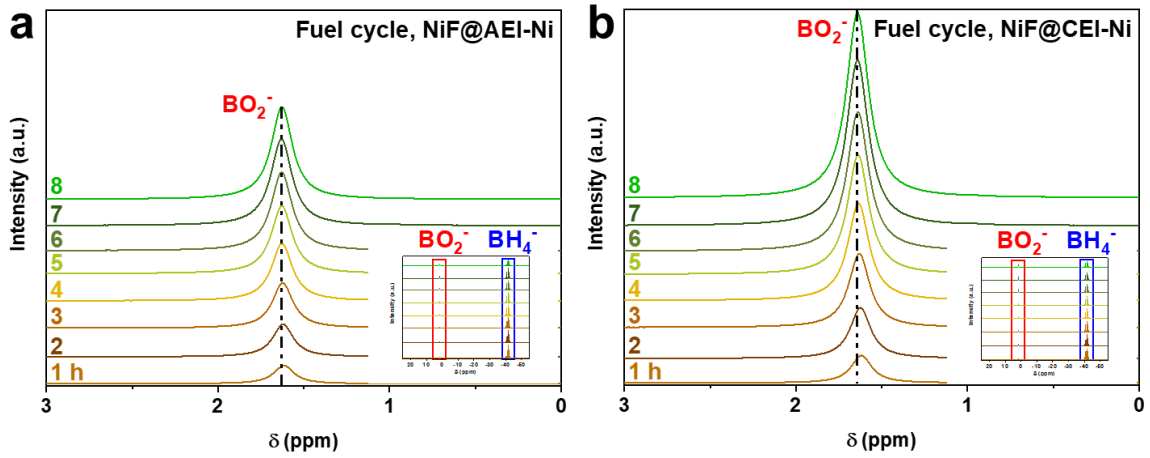

Figure S3.13 ^{11}B NMR of outlet anolyte during fuel cycling test (1 V potentiostat) for (a) NiF@AEI-Ni, and (b) NiF@CEI-Ni (solvent: D_2O).

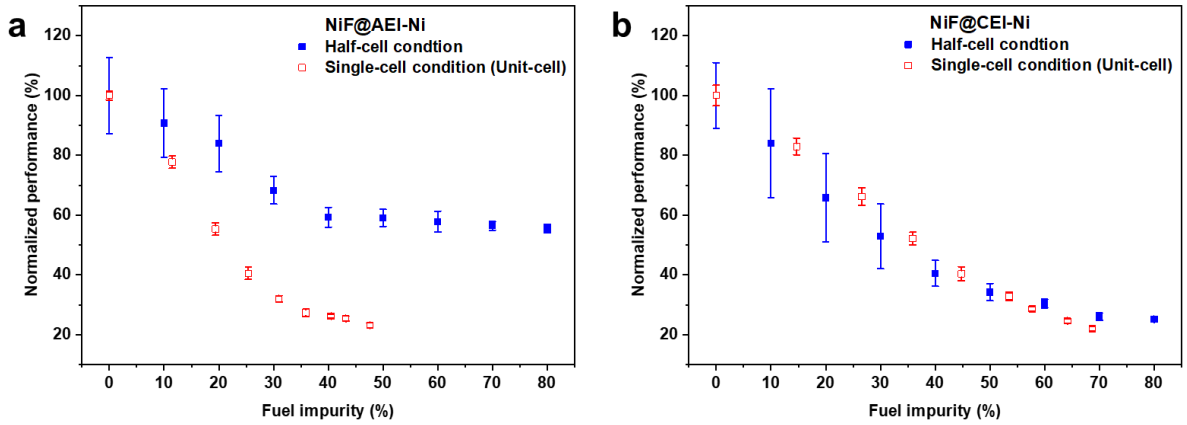

Figure S3.14 Normalized performance of (a) NiF@AEI-Ni and (b) NiF@CEI-Ni at different impure fuel concentration in half-cell and single-cell (unit-cell) configuration. The BOR current is used in half-cell configuration. The power density during fuel cycling is used in single-cell configuration.

References

(1) Cheng, H.; Scott, K. Influence of Operation Conditions on Direct Borohydride Fuel Cell Performance. *Journal of Power Sources* 2006, *160* (1), 407–412. https://doi.org/10.1016/j.jpowsour.2006.01.097.

(2) Qin, H. Y.; Zhu, K. N.; Ye, L. Q.; Li, Z. P. Oxygen Reduction Reaction on a Polypyrrole-Modified, Carbon-Supported Cobalt Hydroxide Catalyst. *Journal of Power Sources* 2012, *208*, 203–209. https://doi.org/10.1016/j.jpowsour.2012.02.040.

(3) Hjelm, R. M. E.; Lafforgue, C.; Atkinson, R. W.; Garsany, Y.; Stroman, R. O.; Chatenet, M.; Swider-Lyons, K. Impact of the Anode Catalyst Layer Design on the Performance of H2O2-Direct Borohydride Fuel Cells. *J. Electrochem. Soc.* 2019, *166* (15), F1218. https://doi.org/10.1149/2.0681914jes.

(4) Wang, Z.; Parrondo, J.; He, C.; Sankarasubramanian, S.; Ramani, V. Efficient PH-Gradient-Enabled Microscale Bipolar Interfaces in Direct Borohydride Fuel Cells. *Nature Energy* 2019, *4* (4), 281–289. https://doi.org/10.1038/s41560-019-0330-5.

(5) Wang, Z.; Sankarasubramanian, S.; Ramani, V. Reactant-Transport Engineering Approach to High-Power Direct Borohydride Fuel Cells. *Cell Reports Physical Science* 2020, *1* (7), 100084. https://doi.org/10.1016/j.xcrp.2020.100084.

(6) Liu, B. H.; Li, Z. P.; Arai, K.; Suda, S. Performance Improvement of a Micro Borohydride Fuel Cell Operating at Ambient Conditions. *Electrochimica Acta* 2005, *50* (18), 3719–3725. https://doi.org/10.1016/j.electacta.2005.01.018.

(7) Lam, V. W. S.; Kannangara, D. C. W.; Alfantazi, A.; Gyenge, E. L. Electrodeposited Osmium Three-Dimensional Anodes for Direct Borohydride Fuel Cells. *Journal of Power Sources* 2012, *212*, 57–65. https://doi.org/10.1016/j.jpowsour.2012.03.067.

(8) Li, S.; Shu, C.; Chen, Y.; Wang, L. A New Application of Nickel-Boron Amorphous Alloy Nanoparticles: Anode-Catalyzed Direct Borohydride Fuel Cell. *Ionics* 2018, *24* (1), 201–209. https://doi.org/10.1007/s11581-017-2180-0.

(9) Oshchepkov, A. G.; Braesch, G.; Ould-Amara, S.; Rostamikia, G.; Maranzana, G.; Bonnefont, A.; Papaefthimiou, V.; Janik, M. J.; Chatenet, M.; Savinova, E. R. Nickel Metal Nanoparticles as Anode Electrocatalysts for Highly Efficient Direct Borohydride Fuel Cells. *ACS Catal.* 2019, 8520–8528. https://doi.org/10.1021/acscatal.9b01616.

(10) Braesch, G.; Oshchepkov, A. G.; Bonnefont, A.; Asonkeng, F.; Maurer, T.; Maranzana, G.; Savinova, E. R.; Chatenet, M. Nickel 3D Structures Enhanced by Electrodeposition of Nickel Nanoparticles as High Performance Anodes for Direct Borohydride Fuel Cells. *ChemElectroChem* 2020, *7* (7), 1789–1799. https://doi.org/10.1002/celc.202000254.

(11) Ma, J.; Li, J.; Yang, S.; Lu, H.; Liu, L.; Wang, R. Ultrathin Veil-like SnO2 Supported Co3O4 Nanoparticles for Direct Borohydride Fuel Cell Anode. *Journal of Power Sources* 2020, *453*, 227866. https://doi.org/10.1016/j.jpowsour.2020.227866.

(12) Chu, W.; He, Y.; Chu, Y. S.; Meng, L.; Liu, J.; Qin, H.; Tao, S. A Highly Stable Cu(OH)2-Poly(Vinyl Alcohol) Nanocomposite Membrane for Dramatically Enhanced Direct Borohydride Fuel Cell Performance. *Journal of Power Sources* 2020, *467*, 228312. https://doi.org/10.1016/j.jpowsour.2020.228312.

(13) Braesch, G.; Wang, Z.; Sankarasubramanian, S.; G. Oshchepkov, A.; Bonnefont, A.; R. Savinova, E.; Ramani, V.; Chatenet, M. A High Performance Direct Borohydride Fuel Cell Using Bipolar Interfaces and Noble Metal-Free Ni-Based Anodes. *Journal of Materials Chemistry A* 2020. https://doi.org/10.1039/D0TA06405J.

Chapter 4 All platinum group metal-free catalysts using in liquid fuel operated direct borohydride fuel cells

Youngdon Ko[1,2], Junkil Park[3], Xiong Zhang[4,5], Liqun Kang[6], Thi Ha My Pham[1,2], Victor Boureau[7], Cuong Pham-Huu[4], Jihan Kim[3], Liping Zhong[1,2*], Andreas Züttel[1,2]

[1] Institute of Chemical Sciences and Engineering, Basic Science Faculty, École polytechnique fédérale de Lausanne (EPFL) Valais/Wallis, Energypolis, Rue de l'Industrie 17, 1951 Sion, Switzerland.
[2] Empa Materials Science and Technology, 8600 Dübendorf, Switzerland.
[3] Department of Chemical and Biomolecular Engineering, Korea Advanced Institute of Science and Technology (KAIST), 291 Daehak-ro, Yuseong-gu, 34141 Daejeon, Republic of Korea.
[4] Institute of Chemistry and Processes for Energy, Environment and Health (ICPEES), UMR 7515 CNRS-Université de Strasbourg, 25 rue Becquerel, 67087 Strasbourg Cedex 02, France.
[5] CAS Key Laboratory of Science and Technology on Applied Catalysis, Dalian Institute of Chemical Physics, Chinese Academy of Sciences, 116023 Dalian, China.
[6] Department of Inorganic Spectroscopy, Max-Planck-Institute for Chemical Energy Conversion, Stiftstr. 34-36, 45470 Mülheim an der Ruhr, Germany.
[7] Interdisciplinary Center for Electron Microscopy, École polytechnique fédérale de Lausanne (EPFL), 1015 Lausanne, Switzerland.
*Corresponding author: liping.zhong@epfl.ch

Preprint version: this section will be submitted to the journal.

Edit: caption numbers of figures, tables, and equations were edited to match the thesis chapter number.

Abstract

The atomically dispersed transition metal with nitrogen-doped carbon (M-N-C) has been studied as a possible replacement for platinum group metal (PGM) catalysts in fuel cell electrodes. In this work, the Fe-N-C and Co-N-C are used as a hydrogen peroxide reduction reaction (PRR) catalysts in direct borohydride fuel cells (DBFCs). Using half-cell and membrane electrode assembly (MEA) configurations, the PRR activity and durability of M-N-C are assessed. The Fe-N-C has higher activity on PRR than Co-N-C. Co-N-C is however more stable than Fe-N-C under DBFC operating conditions. To examine M-N-C degradation, post-mortem XPS and Raman spectroscopy measurements are conducted. In addition, the density functional theory (DFT) simulation supports the Co-N-C stability on the catholyte. In the DBFC durability test, Fe-N-C demonstrates a performance loss of 18.6% following an accelerated durability test, whereas Co-N-C shows a more stable performance with a performance loss of only 6.7%.

4.1 Introduction

The electrochemical catalysts have attracted enormous attention with the increasing demand for renewable energy storage and conversion.[1,2] The hydrogen produced by water splitting from a renewable energy source is regarded as one of the clean energy technologies without CO_2 emission. The green hydrogen from the renewable electrolysis of water could be utilized in the fuel cell for supplying electricity and heat. Liquid fuel-based fuel cells have been looked into for use in portable devices due to the simple recharging of fuel.[3] The direct borohy-

dride fuel cells (DBFCs) are operated by sodium borohydride solution and hydrogen peroxide solution on the anode and cathode, respectively. The DBFC is operated by liquid fuel, with several simultaneous reactions occurring on the catalyst electrode.[4] At the anode side, the borohydride oxidation reaction (BOR) is the main reaction, as shown in Equation 1. The hydrogen evolution reaction (HER), hydrogen oxidation reaction (HOR), and borohydride decomposition are competitive reactions on the anode side. On the other hand, the hydrogen peroxide reduction reaction (PRR) is the main reaction at the cathode side of DBFC (Equation 2).[5] Several different reactions are involved in the cathode side of DBFC, such as the oxygen reduction reaction (ORR), hydrogen peroxide oxidation reaction (POR), and hydrogen peroxide decomposition. Consequently, the DBFC could not reach its theoretical maximum potential (3.01 V, Equation 3).

$$\text{Anode: } BH_4^- + 8OH^- \rightarrow BO_2 + 6H_2O + 8e^- \qquad (E^{0,a} = -1.24 \text{ V vs. SHE}) \qquad (1)$$

$$\text{Cathode: } 4H_2O_2 + 8H^+ + 8e^- \rightarrow 8H_2O \qquad (E^{0,c} = 1.77 \text{ V vs. SHE}) \qquad (2)$$

$$\text{Overall: } BH_4^- + 4H_2O_2 + 8H^+ + 8OH^- \rightarrow BO_2^- + 14H_2O \quad (E^0 = 3.01 \text{ V}) \qquad (3)$$

The modeling of mixed potential in hydrogen peroxide solution was demonstrated by Zhao et al.[6] The open circuit potential of DBFC contributed by the cathode needs to be considered with the mixed potential of PRR, POR, and ORR (Equations 4, 5, and 6).[7] The reduction reactions (PRR and ORR) and oxidation reaction (POR) can be spontaneously established at the cathode of DBFCs. As a result, the mixed potential of reduction and oxidation determines the potential of the cathode (≈ 0.8 V to 0.9V vs. SHE). Among the reduction reaction, the much faster kinetics of PRR (2-electrons transfer) than ORR (4-electrons transfer) is resulting that ORR having the minimal contribution of the cathode in the modeling.

$$H_2O_2 + 2H^+ + 2e^- \rightarrow 2H_2O \qquad (E^{0,PRR} = 1.77 \text{ V vs. SHE}) \qquad (4)$$

$$H_2O_2 \rightarrow O_2 + 2H^+ + 2e^- \qquad (E^{0,POR} = 0.67 \text{ V vs. SHE}) \qquad (5)$$

$$O_2 + 4H^+ + 4e^- \rightarrow 2H_2O \qquad (E^{0,ORR} = 1.23 \text{ V vs. SHE}) \qquad (6)$$

Mayrhofer et al. demonstrate the hydrogen peroxide reduction, oxidation, and decomposition on Pt catalyst.[8] The PRR and POR could be happening in all the voltage ranges, depending on the state of the catalyst surface. This finding lends credence to the mixed-potential hypothesis in the DBFC cathode. Also, the decomposition rate of hydrogen peroxide is proportional to the bulk concentration of hydrogen peroxide. It means that the catholyte fed to the cathode electrode decomposes when it contacts the catalyst electrode, especially on a Pt-based catalyst. Therefore, the investigation of the reaction on the cathode is important to find a suitable catalyst as well as consider the fuel efficiency aspect.

The hydrogen peroxide redox catalysts have not been investigated deeply in the heterogenous catalysis area. On the other hand, extensive research efforts have been devoted to ORR catalysts such as metal-air batteries and fuel cells. Platinum group metal (PGM)-based catalysts (e.g. Pd, Pt) are generally considered the most active ORR catalysts. In addition, the alloy with Pt and other metals (e.g. Co, Fe, Ni, Pd, or Ir) are used to enhance activity and durability.[1] However, the precious metal usage at the electrode limits the cost of the fuel cell system. In this regard, PGM-based catalyst replacement for transition metal catalysts has been intensively studied in many research groups.[9–16] The active site of M-N-C for ORR is known as M-N_4, which foams during the pyrolysis step. The Fe-N-C catalyst has been investigated for ORR by half-cell and membrane electrode assembly (MEA) with fuel cell configuration. Although the high activity of the Fe-N-C catalyst, the durability of the catalyst was overlooked during the activity test. The degradation mechanism of M-N-C could be divided into two different aspects. One is the demetallation of metal moieties from the active sites (M-N_xC_y). Second, the carbon support including

nitrogen degradation during the operation. The protonation of N functional groups, carbon corrosion, and carbon surface oxidation have been considered as possible degradation routes of the M-N-C catalysts as well.[17,18] Even though Fe-N-C is known to be the most active of the M-N-C catalysts, its durability is even more important from an application point of view.

Due to the harsh catholyte condition, which consists of a sulfuric acid and hydrogen peroxide solution mixture, a limited number of catalysts could be used at the cathode side of the DBFC. Platinum-supported carbon (Pt/C) has been used for PRR at the DBFC cathode electrode. The catholyte consists of 15% hydrogen peroxide with 1.5 M sulfuric acid solution, which is a much harsher condition compared to the oxygen-fed cathode of proton exchange membrane fuel cells (PEMFCs). The demetallation mechanism at the active site may be induced by a hydrogen peroxide attack, which is produced by a two-electron reaction of oxygen reduction in PEMFC.[19] Choi et al. described the degradation mechanism as a result of demetallation at low potential and carbon oxidation at high potential.[17] The DBFCs utilize hydrogen peroxide for the catholyte indeed making more harsh conditions for M-N-C catalysts. In addition, the open circuit potential of DBFCs (OCP ≈ 1.9 V) is two times higher than PEMFC (OCP ≈ 0.9 V) which could cause higher carbon oxidation. For those reasons, durable M-N-C catalysts are required for harsh reaction conditions. The hydrogen peroxide reduction and oxidation reaction (PROR) and ORR are taking place together at the active site of M-N-C. The activity of the PRR and ORR reactions, which are the main reactions in the DBFC cathode, need to be tested. Because of its high equilibrium potential in the Pourbaix diagram, the Co-N-C catalyst is regarded as one of the more durable M-N-C catalysts under acid conditions.[20]

In this study, the PGM-based catalysts in DBFC electrodes are all replaced with transition metal catalysts in both the anode and cathode electrodes. Previous research on replacing Pd with Ni catalyst at the anode electrode of DBFC has successfully demonstrated that Ni is more selective on BOR than Pd.[21] The Pt/C is replaced by the M-N-C at the DBFC cathode, resulting in the PGM-free DBFC system described in this paper. In addition, the activity and durability of M-N-C (Fe-N-C and Co-N-C) catalysts are compared with half-cell and DBFC unit-cell configurations. The half-cell measurements for ORR and PROR give insight into what degradation mechanism are happening on the cathode side of DBFC. The post-mortem XPS and Raman spectroscopy results support the degradation mechanism and durability of M-N-C catalysts. The predicted free energy of demetallation on Fe-N-C and Co-N-C is calculated by density functional theory (DFT) simulation. It is found that Fe-N-C has higher activity on ORR and PRR, but Co-N-C is a more suitable catalyst for DBFC cathode in terms of durability under harsh DBFC catholyte condition.

4.2 Experimental section

4.2.1 Preparation of M-N-C catalysts

The M-N-C catalysts were prepared based on the previous report.[22] In a typical procedure, 2 g of citric acid (10.4 mmol), 5 g of $(NH_4)_2CO_3$ (52 mmol) and 1.2 g silica (Fume, Φ = 7 nm) were dissolved in 25 mL of ultrapure water (Veolia Ultra Analytique, 18.2 MU cm, TOC < 2 ppb). Afterwards, the mixture was stirred until a uniform gel suspension was formed. $FeCl_3 \cdot 6H_2O$ (0.024 g, 0.087 mmol) and $ZnCl_2$ (0.2435 g, 1.75 mmol) were then dissolved in 3 mL of distilled water, and the resulting solution was added dropwise to the above colloidal suspension. For the Co-N-C catalyst synthesis, the $CoCl_2$ were replaced to $FeCl_3 \cdot 6H_2O$. After 30 minutes of stirring, the mixture was placed in an oven and dried at 110 ^oC overnight. The resulting solid was then crushed into powder and calcined at 900 ^oC for 2 h in an Ar atmosphere. The as-obtained black solid was then suspended in 120 mL of a 2 M NaOH solution, stirred at 80 ^oC for 8 h to remove the silica template. The solid recovered by successive water-washing/centrifugation/drying steps underwent a second calcination step at 900 ^oC for 1 h in Ar atmosphere.

4.2.2 Catalyst Characterization

X-ray photoelectron spectroscopy (XPS) spectra were collected in a Kratos Axis Supra system equipped with a monochromated Al Kα (1486.61 eV) X-ray source at a nominal power of 225 W. The binding energies (BEs) were referenced to the C 1s BE of adventitious carbon on the sample surface at 284.8 eV. The XPS spectra is deconvoluted by the CasaXPS software. The degradation of carbon species was examined in M-N-C sample by Raman spectroscopy, which was performed using a Renishaw inVia at 457 nm excitation. X-ray diffraction (XRD) spectra was measured in Bruker D8 Discover, Cu Kα (λ = 0.1543 nm) radiation (40 kV and 40 mA). The N_2 isothermal adsorption/desorption was recorded at 77 K on a Belsorp max Ⅱ. Samples were degassed at 120 °C for 5 h under vacuum before nitrogen physisorption measurements. The transmission electron microscopy and high-angle annular dark-field scanning TEM (TEM and HAADF-STEM, Thermo-Scientific Tecnai Osiris) with energy-dispersive X-ray spectroscopy (EDX, Super-X SDD) were used to observe the morphology and elemental distribution of M-N-C catalysts. The aberration-corrected HAADF-STEM images were obtained by Thermo-Scientific Titan Themis for atomic resolution at 200 kV high tension. The Fe K-edge (7.112 keV) and Co K-edge (7.709 keV) X-ray absorption fine structure (XAFS) of the Fe-N-C and Co-N-C catalysts were collected at the P65 beamline of PETRA III (P65 Applied X-ray Absorption Spectroscopy). For Fe K-edge, monochromatic beam between 6.912 and 8.112 keV was introduced through an 11-periods undulator (1st harmonic) and Si(111) double crystal monochromator (DCM). For Co K-edge, the incident beam energy was adjusted to 7.509 to 8.709 keV from the 3rd harmonic beam though the same Si(111) DCM. The beam size at the sample was approx. 0.5 x 1.0 mm^2 (V x H) and the photon flux was ~1011 ph s^{-1} (without attenuation). The XAFS spectra were collected in transmission mode, and the intensity of incident beam (I_0) and the transmitted beam (I_t) was monitored by ionization chambers (filled with a mixture of Ar and N_2). The sample powder was sealed into PEEK-made solid powder cells (9 mm in diameter) using Kapton tapes and mounted on the transfer rods of a liquid He cryostat for the measurement. The XAFS measurements of the Fe and Co samples were performed under 10 K to reduce the thermal vibration of the chemical bonds (to get smaller Debye-Waller factors), as well as to prevent potential beam damage to the samples. The XAFS of each sample was measured 3 times and merged to improve the signal-noise ratio. Fe foil or Co foils were measured simultaneously for each Fe or Co sample, correspondingly, as a reference for energy calibration. In addition, FeO, Fe_2O_3, CoO and Co_3O_4 powder were pressed into pellets and measured as well for reference. XAFS data was analyzed using xraylarch (version 0.9.65) and in-house developed python scripts. Pre-edge background subtraction, post-edge normalization, and the forward Fourier Transform of XAFS data were processed by xraylarch. The k^2-weighted wavelet transform EXAFS (WT-EXAFS) was generated using the Cauchy wavelet method (built-in function in xraylarch). The fitting of EXAFS spectra (R range: 1-3.2 Å, k range: 3-14 $Å^{-1}$) was performed using lmfit (built-in function in xraylarch) based on scattering paths generated from FEFF8L. The amplitude reduction factor S_0^2 is determined to be 0.688 and 0.772 for Fe and Co by fitting of k^2-weighted R-space EXAFS of Fe and Co foils based on the standard crystal parameters of iron and cobalt metal (data from Crystal Open Database, COD ID: 9008536 and 9008466). For the EXAFS fitting of other Fe and Co samples, the S_0^2 values were used as fixed parameters.

4.2.3 Density functional theory (DFT) calculation

Structure optimization and free energy calculation were conducted using DFT calculations implemented in the Vienna ab initio software package (VASP).[23] The project augmented wave method was used with kinetic energy cutoff of 400 eV.[24] The generalized gradient approximation (GGA) using the Perdew-Burke-Ernzerhof (PBE) exchange-correlation functional was imposed with dispersion correction using Grimme's D3 approach.[25,26] Spin polarization was considered in all calculations. The Brillouin zone was sampled using 4×4×1 Monkhost-Pack k-point grid.[27] During the structure optimization, the convergence criterion of 0.02 eV $Å^{-1}$ was applied for the ionic force and 10^{-5} eV for the electronic energy. 14 Å thickness of vacuum was introduced to avoid the interaction

between adjacent layers. For vibrational frequency calculations, all the C atoms and attached H atoms were fixed and only vibrational motion of the N atoms, central metal atom, and adsorbates were considered. The computational hydrogen electrode method was used for the free energy calculation.[28] The free energy change was calculated following the equation 7.

$$\Delta G = \Delta E_{DFT} + \Delta E_{ZPE} + \int C(T)dT - T\Delta S \qquad (7)$$

Where ΔE_{DFT} is the DFT calculated electronic energy change, ΔE_{ZPE} is zero-point energy change, $\int C(T)dT$ is enthalpy change, and ΔS is entropy change.

4.2.4 Electrochemical Measurements

Electrochemical half-cell tests were conducted using a rotating disk electrode or a rotating ring disk electrode as a working electrode (RDE or RRDE, 3 mm GC disk RDE or Pt ring electrode with outer diameter of 7 mm, an inner diameter of 5 mm; the GC disk electrode is a 4 mm diameter RRDE), with a graphite counter electrode, and 3.5 M KCl filled Ag/AgCl as a reference electrode. The working electrode was connected with the constant rotating system (RRDE-3A, ALS), and electrochemical measurements were performed with potentiostats (Metrohm Autolab PGSTAT204 and ALS2325). The catalyst inks are composed of 10 mg sample, 100 mg 5wt% Nafion solution, and 300 mg iso-propyl alcohol mixture. The catalyst ink was dropped and deposited on a glassy carbon substrate for the ORR test and accelerated durability test (ADT). The catalyst loading on glassy carbon is around 700 μg cm^{-2}. The linear sweep voltammetry (LSV) at the 1600 rpm rotating speed under O_2-saturated 0.5 M H_2SO_4 or O_2-saturated 0.02 M H_2O_2 with 0.5 M H_2SO_4 solution. Before starting the ORR and PROR tests, the catalysts are conditioned under N_2-saturated 0.5 M H_2SO_4 with 20 cycles of potential sweep. The freshly deposited catalyst ink (referred Fresh in ADT test) is conducted over 20 potential cycles from 0.075 to 1.2 V_{RHE} under N_2-saturated 0.5 M H_2SO_4 and become the beginning of the test (B.O.T) samples. The ORR current was measured under O_2-saturated 0.5 M H_2SO_4. And the ORR current subtracted to the current measured under N_2-saturated 0.5 M H_2SO_4 to correct the capacitance of samples. The hydrogen production peroxide selectivity (H_2O_2 %) were calculated using the equation 7. The $\boldsymbol{i_r}$ is the ring current, $\boldsymbol{i_d}$ is the disk current, and $\boldsymbol{N}$ is the current collection efficiency of Pt ring electrode ($\boldsymbol{N}$ = 0.28). The collection efficiency of Pt ring electrode was measured and calculated by the oxidation of ferrocyanide to ferricyanide current in 10 mM potassium ferricyanide in 1 M potassium nitrate solution.[29] For the samples to measure the postmortem XPS and Raman spectroscopy were deposited on glassy carbon electrode which contact to the RDE electrode and closed with the cap (Supplementary Fig. S6). The sample for the XPS and Raman spectroscopy were prepared by dropping catalyst ink on GC electrode and the GC electrode were prepared each of potential cycles samples (total 5 samples each Fe-N-C and Co-N-C, Fresh, B.O.T, 3K, 5K, 10K). The accelerated durability test (ADT) for ORR and PROR in half-cell configuration were conducted in two different sets. The potential sweep ranges are divided into two sections: 0.6 V to 1.0 V and 1.0 V to 1.5 V. The potential cycles are 3K, 5K, and 10K. The PROR durability test was only conducted in the 0.6 V to 1.0 V range due to the severe bubble formation at 1.0 V to 1.5 V.

$$H_2O_2 \text{ production selectivity: } H_2O_2\ (\%) = 200 \times (\boldsymbol{i_r}/\boldsymbol{N})/(\boldsymbol{i_d} + \boldsymbol{i_r}/\boldsymbol{N}) \qquad (8)$$

$$n = 4\boldsymbol{i_d}/\ (\boldsymbol{i_d} + \boldsymbol{i_r}/\boldsymbol{N}) \qquad (9)$$

4.2.5 Direct borohydride fuel cell performance measurement

The preparation of nickel catalyst on nickel foam for the anode electrode and membrane electrode assembly (MEA) was described in our previous study.[21] The nickel catalyst coated with cation exchange ionomer on nickel foam was used as an anode in the DBFC. The M-N-C (Fe-N-C or Co-N-C) catalyst was mixed in isopropyl alcohol and predetermined Nafion amount. The M-N-C catalyst was sprayed directly to the perfluorosulfonic acid (PFSA)

membrane (Nafion 115, Thickness: 127 µm) on a hot plate at 70 °C. The M-N-C catalyst loading was fixed to 2.5 mg cm^{-2} after optimization of electrode preparation. The prepared MEA is assembled in the fuel cell set-up to measure the DBFC performance. Firstly, the manufactured MEA in the fuel cell was conditioned with pre-electrolyte for 10 min at 80 °C. Pre-anolyte and pre-catholyte are 3 M NaOH and 1.5 M H_2SO_4 solution, respectively. To activate the anode and cathode, the anolyte (1.5 M $NaBH_4$ in 3 M NaOH) and the catholyte (15% H_2O_2 in 1.5 M H_2SO_4) were flown to the anode and cathode, respectively. The electrolyte flow was fixed to 7 ml min^{-1} on both anode and cathode sides by a peristaltic pump (Reglo ICC, Ismatec). At the same time, the voltage changed from open circuit potential to 0.35 V for 5 cycles. The fuel cell performance was conducted with a test station (SMART2, WonA-Tech). The protocol for the durability test of DBFC is described in Figure S4.15. The polarization curve for the DBFC unit-cell is measured at the test station and is not IR corrected.

4.3 Results and discussion

4.3.1 Atomically dispersed transition metal with nitrogen doped carbon (M-N-C)

The M-N-C catalysts are synthesized based on the previous report.[22] The mass transport of the reactant is enhanced by the meso porous structure created by the sacrificial silica template during the synthesis process. Various physical characterizations indicated that most of the metals are embedded in the form of single-atoms with nitrogen-doped carbon (Figure S4.1–4.4). The meso pore structure is clearly shown in transmission electron microscopy (TEM) images and pore-size distribution by N_2 physisorption analysis (Figure 4.1 and Figure S4.4). The XRD spectra of Fe-N-C and Co-N-C only show the amorphous carbon structure and did not detect any crystalline Fe and Co species in the catalyst (Figure S4.1). Meanwhile, the high-angle annular dark-field scanning TEM with energy-dispersive X-ray spectroscopy (HAADF-STEM with EDX) elemental maps suggest a homogeneous distribution of doped Fe and Co with N in the Fe-N-C and Co-N-C catalysts, respectively (Figure S4.3). The iron and cobalt metal are atomically distributed on N-C by aberration corrected-STEM analysis as bright dots (Figure 4.1c, d). The nanoparticles are not observed in the Fe-N-C and Co-N-C. The position of the detected atomically dispersed metal is changed depends on the focal point of STEM. Despite the atomically dispersed metals existing homogeneously, the focal point of the single dot changed in the area due to the 3D carbon structures are winkled. The Fe-N-C and Co-N-C catalysts are characterized by using X-ray absorption spectroscopy (XAS). The X-ray absorption near edge structure (XANES) of the Fe K-edge and the Co K-edge are shown in Figure 4.1e and 4.1f for Fe-N-C and Co-N-C catalysts, respectively. The XANES spectra of Fe-N-C catalyst is highly closed to the Fe_2O_3 reference sample. It means that Fe-N-C catalyst has a 3+ valence for the isolated Fe atoms. The Fourier transformed extended X-ray absorption fine structure (FT-EXAFS) of the Fe-N-C catalyst is shown in Figure 4.1g. The structure of the Fe-N-C catalyst is mostly made up of isolated Fe-N(O) bonds. However, only a small amount of Fe cluster was detected based on the FT-EXAFS fitting and wavelet transforms (WT) plot (Figure S4.5 and Table S4.1). The WT plot shows a high intensity at ~ 4 $Å^{-1}$ in *k* space for the Fe-N(O), and slight intensity at ~ 7 $Å^{-1}$ in *k* space for the Fe-Fe. Even though a small amount of Fe cluster was detected from the XAS measurements, the atomically dispersed Fe-N_x is the dominant structure in the Fe-N-C catalyst. Figure 4.1f and 4.1h show the XANES of the Co K-edge and the FT-EXAFS of the Co-N-C catalyst. The Co K-edge XANES spectra of edge energy for the Co-N-C catalyst is similar to that for the CoO reference sample, which shows that the valence state of Co is 2+, consistent with previous results.[30,31] Similar to the Fe-N-C catalyst, a small amount of Co cluster was detected by XAS measurement and shown in the FT-EXAFS fitting and WT plot (Figure S4.6 and Table S4.2). The major structure in Co-N-C is Co-N_x, the active site of ORR and PROR.

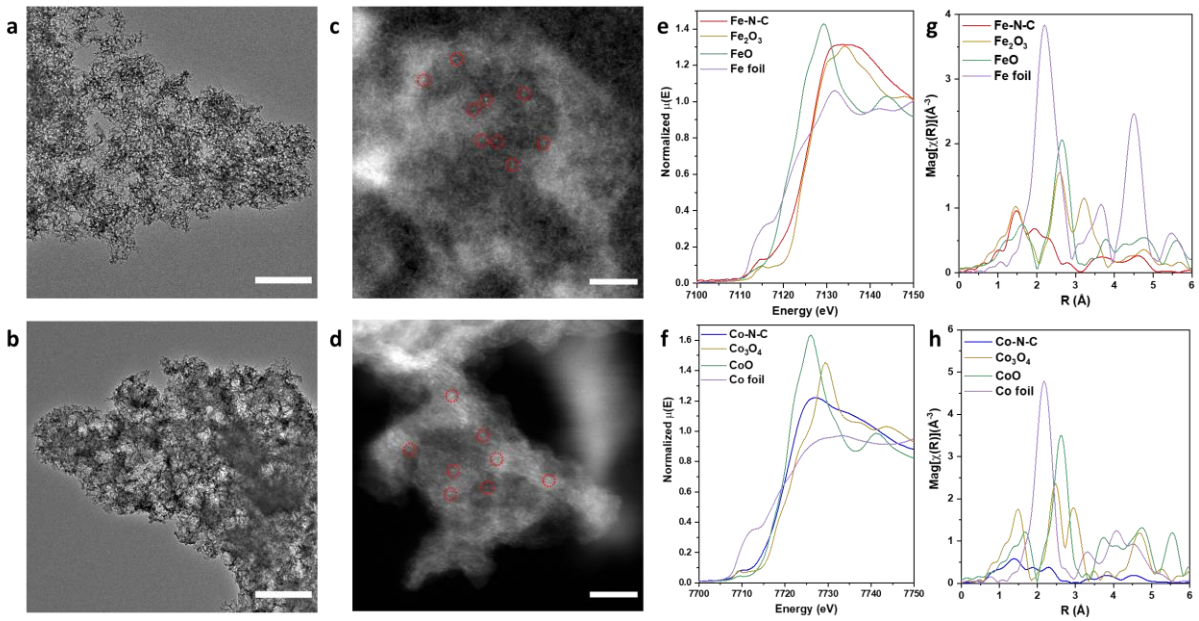

Figure 4.1 Structural characterization of the Fe-N-C and Co-N-C catalysts. TEM images of (a) Fe-N-C and (b) Co-N-C (scale bar: 200 nm). (c) Aberration-corrected HAADF-STEM images of Fe-N-C and (d) Co-N-C (scale bar: 5 nm). (e) Fe K-edge and (f) Co K-edge XANES spectra. (g) Fourier transformed EXAFS spectra of Fe-N-C and (h) Co-N-C.

4.3.2 M-N-C catalysts for ORR and PROR catalytic performance in half-cell and DBFC unit-cell

The M-N-C catalysts are tested in half-cell configuration for the ORR and PROR activities. The electrolyte for the ORR half-cell measurement is O_2-saturated 0.5 M H_2SO_4. The electrolyte for the PROR is O_2-saturated 0.02 M H_2O_2 with 0.5 M H_2SO_4 solution. The ORR and PROR are occurring together at the cathode of the DBFC; hence, two reactions need to be considered both. The active sites of M-N-C catalyst are exhibited wide range of different moieties such as Fe-N_x, metal-free, N-containing moieties, and Fe-containing nanoparticles.[14] Damjanovic model for the ORR mechanism is composed of a direct 4-electron reduction of O_2 to H_2O and a consecutive 2 × 2 electron reduction via the formation of H_2O_2 intermediate.[32] Ohsaka et al. explained the iron role at the Fe-N-C catalyst for 4- and 2-electron reduction in ORR.[33] They claimed that H_2O_2 is produced by 2-electron ORR at one iron active site, and subsequent 2-electron H_2O_2 reduction occurs at the other iron active site. Firstly, the ORR catalytic performances of Fe-N-C and Co-N-C were measured by a rotating ring disk electrode (RRDE). The ORR current was measured by linear sweep voltammetry at the disk electrode with a 1600 rpm rotation speed. The Pt ring electrode voltage was fixed at 1.2 V versus the reversible hydrogen electrode (RHE) to oxidize the H_2O_2 produced and escape from the disk electrode. The Pt ring electrode current shows that the H_2O_2 production on Fe-N-C catalyst is lower than that on Co-N-C catalyst. The Fe-N-C has a more selective 4-electron ORR than the Co-N-C (Figure 4.2a and S4.7). The relatively higher H_2O_2 production by the Co-N-C (41.8%) suggested that the 2-electron ORR coexist strongly at the disk electrode current.

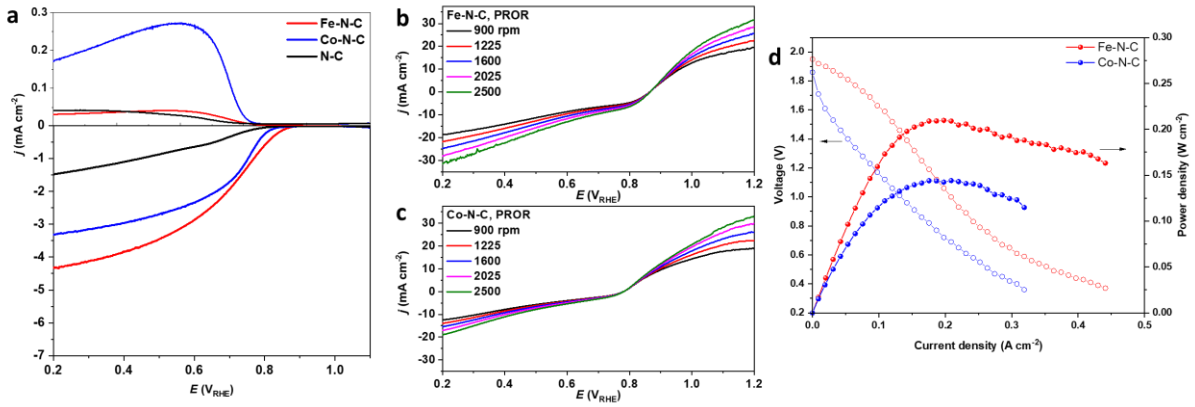

Figure 4.2 Electrochemical ORR, PROR and DBFC test. (a) Steady-state RRDE polarization curves of Fe-N-C, Co-N-C, and N-C, recorded in O_2-saturated 0.5 M H_2SO_4 at a scan rate of 10 mV s^{-1} and a rotating electrode speed of 1600 rpm. Ring potential fixed on 1.2 V_{RHE}. (b) Steady-state PROR polarization curves of Fe-N-C and (c) Co-N-C, recorded in O_2 saturated 0.02 M H_2O_2 with 0.5 M H_2SO_4 electrolyte solution at a scan rate of 10 mV s^{-1}. (d) Direct borohydride fuel cell polarization curves of Fe-N-C or Co-N-C comprised at the cathode electrode and nickel catalyst at the anode electrode. Polarization curves were measured with a 9 cm^2 active area at 80 °C. The anolyte is 1.5 M $NaBH_4$ with 3 M NaOH solution and catholyte is 15 % H_2O_2 with 1.5 M H_2SO_4 solution. The flow rate is 7 ml min^{-1} at both anode and cathode.

Fe-N-C exhibits superior catalytic activity in terms of the highest onset potential (E_{onset}, 0.86 V) and half-wave potential ($E_{1/2}$, 0.68 V) for ORR. The higher kinetic current density at 0.8 V of Fe-N-C (-1.39 mA cm^{-2}) than Co-N-C (-0.65 mA cm^{-2}) shows that the Fe center is a better active site than the Co center for the ORR. The PRR activity of M-N-C catalysts is observed from the RDE measurement in O_2-saturated 0.02 M H_2O_2 with 0.5 M H_2SO_4 solution (Figure 4.2b, c). The O_2-saturated H_2SO_4 with H_2O_2 condition has a closer atmosphere in the DBFC cathode than the N_2-saturated H_2SO_4 with H_2O_2 condition. The PRR activity can be estimated using the mixed potential of PROR. Mayrhofer and Katsounaros et al. described the mixed potential of hydrogen peroxide with thermodynamic considerations.[8] In that work, they used the Pt-based catalyst for the PROR activity test with RDE. The curves of all rotation rates do cross at the same point near the current zero; however, the current zero point does not really correspond to the zero reaction. The crossing point around 0.8 V to 0.9 V indicates that the rates of PRR and POR are equal. In PROR measurement, the crossing point of Fe-N-C (0.87 V) is more positively located than Co-N-C (0.79 V). It means that Fe-N-C is intrinsically active on PRR compared to Co-N-C. In addition, the current in the reduction-dominated potential region (0.2 to 0.79 V) is asymmetrically lower than that in the higher potential region (0.79 to 1.2 V) on Co-N-C, which indicates the PRR is less active than the POR in Co-N-C.

Above all, the reasons and evidences for the high activity on the PRR for Fe-N-C are clearly shown in the DBFC unit-cell measurement (Figure 4.2d). The open circuit voltage (OCV) and peak power density (PPD) of the Fe-N-C catalyst with MEA are 1.95 V and 0.209 W cm^{-2}, respectively. The OCV and PPD of the Co-N-C catalyst with MEA are 1.86 V and 0.144 W cm^{-2}, respectively. The activation loss at the low current region (OCV to 1.6 V) in Fe-N-C is lower than that in the Co-N-C catalyst. All the performance for the unit-cell measurement is higher on Fe-N-C than Co-N-C. The Fe-N-C catalyst has been known as the most active ORR catalyst among M-N-C catalyst, and it is also more active on PRR than Co-N-C.

4.3.3 Durability of M-N-C catalysts

The durability of catalysts is important as activity of catalyst in practical applications for stable operation. The activity of the Fe-N-C exceed that of the Co-N-C based on the half-cell and unit-cell measurements as described earlier. Despite high activity of Fe-N-C on ORR and PRR, the degradation of catalyst must be carefully considered

during the durability test. The degradation mechanism of M-N-C catalysts is characterized with post-mortem XPS and Raman spectroscopy. The mixture of M-N-C catalyst and Nafion ionomer is coated on a glassy carbon (GC) electrode (Figure S4.8). The fresh samples in Figure 4.3 were not touching electrolyte or cycling potential before XPS and Raman spectroscopy measurements. The beginning of test (B.O.T) samples are conditioned over 20 cycles of the 0.075 V to 1.2 V_{RHE} potential ranges. The accelerated durability test (ADT) for half-cell measurement is tested under the potential cycle (B.O.T to 10,000 cycles) at 0.6 V to 1.0 V or 1.0 V to 1.5 V with a 1600 rpm rotation speed. The electrolytes are O_2-saturated 0.5 M H_2SO_4 solution for ORR and O_2-saturated 0.02 M H_2O_2 with 0.5 M H_2SO_4 solution for PROR. Due to the severe bubble formation at 1.0 V to 1.5 V potential cycling, PROR durability can only be performed at 0.6 V to 1.0 V. After the potential cycle, the GC electrode was delicately washed with deionized water and dried under an atmosphere for the XPS and Raman spectroscopy measurements. The potential cycling is divided into two potential regions: one is the generally operating potential of PEMFC (0.6 V to 1.0 V), and the other is the high potential region (1.0 V to 1.5 V), which is known as the destructive potential during fuel cell start-up and shut-down conditions.[34] In the case of DBFC, the peak power density appeared around 1.0 V that is nearly twice higher than PEMFC (≈ 0.5 V). The operation potential of DBFC can be below 1.0 V to avoid carbon corrosion and parasitic losses due to water electrolysis. In M-N-C, the multiple sites of transition metal with nitrogen exist in either in-plane M-N_4 or edge M-N_x (x<4). Nitrogen also exists as pyrrolic-N, pyridinic-N and graphitic-N which could be bound with a proton depending on the pH of the electrolyte.[35] The normalized kinetic current density at 0.8 V in O_2-saturated 0.5 M H_2SO_4 is calculated from the ORR polarization curves for Fe-N-C and Co-N-C (Figure S4.9). The normalized kinetic current density gradually decreased in Fe-N-C and Co-N-C catalysts during the durability test at the 0.6 V to 1.0 V potential region (Figure 4.3c).

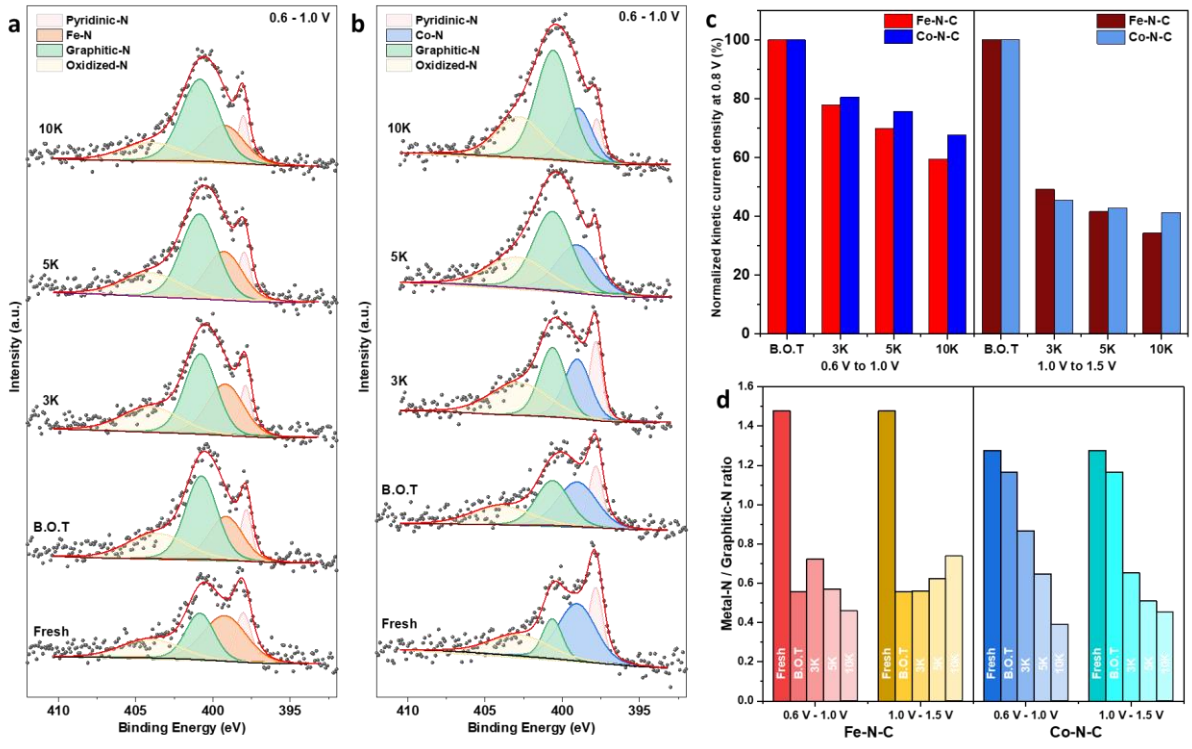

Figure 4.3 Degradation of M-N-C materials. (a) N 1s XPS spectra of M-N-C with accelerated degradation test (ADT) on glassy carbon electrode from the fresh and beginning of the test (B.O.T) to 10,000 cycles for Fe-N-C and (b) Co-N-C at 0.6 V to 1.0 V under O_2-saturated 0.5 M H_2SO_4. (c) Normalized kinetic current density at 0.8 V_{RHE} in ORR under O_2-saturated 0.5 M H_2SO_4 with 1600 rpm rotation speed. (d) The ratio of metal-N/graphitic-N in N 1s XPS spectra with two different voltage cycling region (0.6 V to 1.0 V and 1.0 V to 1.5 V) on Fe-N-C and Co-N-C.

The ORR performance degradation may be due to the M-N_x sites leaching during the 0.6 V to 1.0 V potential cycle. Choi et al. use a scanning flow cell connected to an inductively coupled plasma mass spectrometer (SFC/ICP-MS) to show that Fe leaching can be found with the potential cycles.[18] The Fe leached out mainly during electrochemical measurements below 0.7 V. The potential cycles under the inert gas condition also show Fe leaching from Fe-N-C. The normalized ORR kinetic current density degradation of the Fe-N-C is more severe than the Co-N-C. The higher rate of Fe demetallation may be the main reason for the faster degradation of Fe-N-C. Because of the lower redox potential of Fe (Fe^{2+}/Fe^{3+} = 0.77 V_{SHE}) than Co (Co^{2+}/Co^{3+} = 1.92 V_{SHE}) in the Pourbaix diagram, Fe is easier to leach out of the M-N-C.[20] The XPS spectra of Fe-N-C or Co-N-C show the evolution and decrease in area of the deconvoluted peak after potential cycle in durability test (Figure 4.3a, b). The ratio of metal-N/graphitic-N is compared after potential cycling (Figure 4.3d). To estimate the metal-N amount in the XPS measurement, the graphitic-N structure is chosen as the reference structure. Even though we used the same catalyst ink on each GC sample to obtain the XPS measurement on each sample (Fresh, B.O.T, 3K, 5K, 10K samples), due to the small measurement area of XPS, the M-N-C samples could be differently covered depending on the GC samples. In addition, the graphitic-N in M-N-C structure is less influenced during the ORR and PROR. It is noted that the metal-N/graphitic-N ratio rapidly decreased on Fe-N-C after 20 potential cycles (0.075 to 1.2V_{RHE}) for the activation of the catalyst (Fresh to B.O.T). The activation of catalyst is procced in N_2-saturated 0.5 M H_2SO_4 during potential cycles. It means that the demetallation even occurs without O_2 or H_2O_2 during the potential cycle. The voltage cycling is continuously going on until 10,000 cycles under O_2 purging and 1600 rpm rotation. The increase of the metal-N/graphitic-N ratio on Fe-N-C observed after 3,000 cycles under 0.6 to 1.0 V may come from the graphitic-N degradation. The carbon structure destruction (including graphitic-N) or metal-N sites are revealed with detachment of impurities. The metal-N/graphitic-N ratio continuously decreased after 3,000 cycles. It seems that Fe demetallation continuously occur as described earlier. The metal-N/graphitic N ratio of Fe-N-C continuously increases after B.O.T in the 1.0 V to 1.5 V potential range (Fig. 4.3d and S4.10). In this case, the Fe-N_x sites degradation rate is lower than the graphitic-N degradation rate. It was also noticeable that the oxidized-N amount increased in the 1.0 V to 1.5 V potential cycling range. The increase of catalyst capacitance was also observed at high potential cycling due to the oxidation and destruction of carbon (Figure S4.11). The increase of redox peaks is detected in 0.5 to 0.7 V range in the high potential cycling of M-N-C samples due to the new species of oxygen group. The decrease of graphitic-N sites and increase of oxidized-N sites occur due to the carbon destruction and oxidation in the high potential range (1.0 V to 1.5 V). On the other hand, the metal-N/graphitic-N ratio on the Co-N-C gradually decreased in both the low and high potential cycling ranges. The demetallation rate of cobalt in Co-N-C is slower than Fe-N-C. Raman spectroscopy results of Fe-N-C and Co-N-C also follow the trend of XPS results (Figure S4.12). The ratio of defective carbon intensity to graphitic carbon intensity on Fe-N-C at 1.0 V to 1.5 V gradually increases. It is indicated that the graphitic carbon degradation rate is rapid on Fe-N-C compared to Co-N-C. The faster graphitic carbon degradation rate on Fe-N-C than on Co-N-C needs further study to understand the phenomenon. The demetallation of Fe-N-C and Co-N-C containing H_2O_2 was also investigated in Figure S4.13-S4.16. The active site of iron leached out faster than cobalt in 0.02 M H_2O_2 with 0.5 M H_2SO_4 solution, as similar phenomena as O_2 environment which are described earlier.

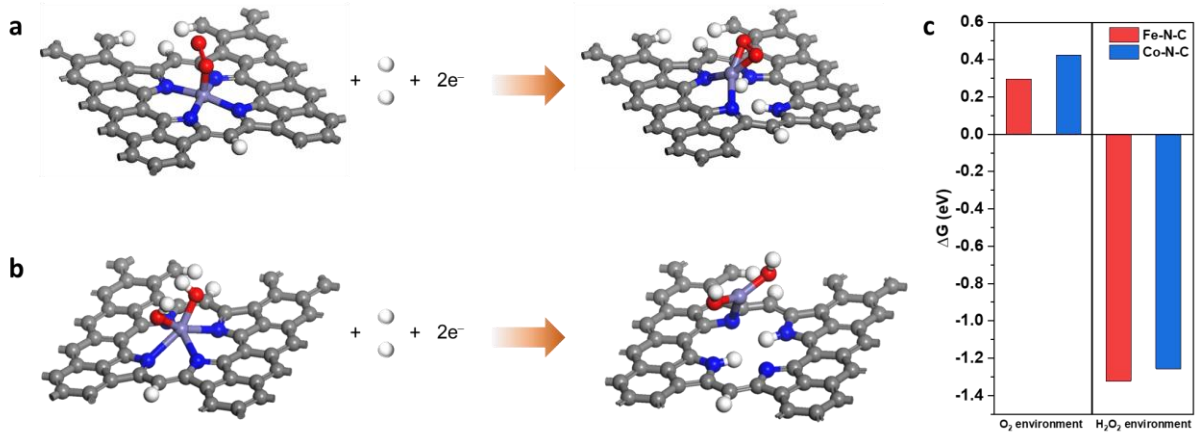

Figure 4.4 Degradation of M-N-C catalysts Atomistic structures of simulation models for leaching of the central M atoms in pyrrolic-N, MN_4C_{12} (M = Fe or Co) active sites under (a) O_2 environment (b) H_2O_2 environment. (c) Calculated free energy change of demetallation on Fe-N-C (O_2: 0.297, H_2O_2: −1.323 eV) and Co-N-C (O_2: 0.426, H_2O_2: −1.257 eV).

The low stability of Fe-N-C against demetallation compared to Co-N-C was further investigated using density functional theory (DFT) calculations. The free energy change during the leaching process of the central metal atom was calculated in the presence of adsorbed O_2 and H_2O_2, respectively (Figure 4.4a and 4.4b). Recent studies have reported that adsorbed H_2O_2 is spontaneously dissociated into two *OH groups.[36,37] The dissociation of H_2O_2 during the structure optimization process was also confirmed in this work, and this structure was used as the initial form of M-N-C with adsorbed H_2O_2. Three different types of M-N-C structures (Pyrrolic-N, Pyridinic-N, and In-plane) were considered for the calculation, and the calculation results of the pyrrolic-N structure, which is known as the most dominant structure, are shown in Figure 4.4. The results of the other two types of structures are summarized in Figure S4.17 and S4.18. In the presence of O_2 adsorbates, the free energy change of demetallation in Fe-N-C (0.297 eV) was calculated to be lower than that of Co-N-C (0.426 eV). A similar trend was observed in the case of H_2O_2 adsorbates, with Fe-N-C showing a lower free energy change (-1.323 eV) than Co-N-C (-1.257 eV). The lower value of the free energy change during the leaching process of the central metal atom shown for Fe-N-C implies that Fe-N-C is more vulnerable to demetallation under both conditions, which is consistent with our experimental observation. It is also noteworthy that, for both structures (Fe-N-C and Co-N-C), demetallation would occur more easily with H_2O_2 adsorbates compared to O_2 adsorbates since the free energy changes were calculated to be much lower in the case of H_2O_2 (Figure 4.4c).

4.3.4 Durability of M-N-C catalysts in cathode of direct borohydride fuel cell

The M-N-C catalyst's activity and durability evaluation are conducted in unit-cell DBFC. Both catalysts were incorporated into MEAs as the cathode and the Ni catalyst as the anode to test PGM-free DBFC. The Ni catalyst anode electrode preparation is described in our previous report.[21] The accelerated durability test (ADT) protocol for the DBFC is described in Figure S4.19. The modified ADT protocol for non-PGM electrocatalysts is applied for DBFC unit-cell testing.[38] Five potential cycles from the open circuit voltage (OCV) to 0.35 V at the beginning of the test refer to the activation region. The 100 times potential cycled from 1.0 V to 0.6 V in 2 sec steps at 1.0 V and 4 sec steps at 0.6 V. After every 100 cycles, up to 500 cycles, three cycles of performance testing from the OCV to the 0.35 V are performed.

The performances of DBFC are shown in Figure 4.5. The maximum peak power density is reached after 100 potential cycles (0.6 to 1.0 V). The performance enhancement is due to the material conditioning of the electrode. The adsorbed species at the active site may be detached during the potential cycle, and the electrode structure may be modified for the best performance condition. The OCV of MEA shows 1.95 V and 1.86 V for Fe-N-C and

Co-N-C, respectively (Figure 4.5a and 4.5b). Those values are highly related to the mixed potential that was observed in the PROR half-cell test. The gap between the mixed potential of Fe-N-C (0.87 V) and Co-N-C (0.79 V) is 0.08 V which is close to the gap of MEAs' OCV (0.09 V). The mixed potential in half-cell could be used as one of the important indicators for the OCV of MEA and catalytic performance of PRR. The peak power density (PPD) of MEA at 100 cycles shows that the Fe-N-C catalyst (0.209 W cm^{-2}) has higher activity than the Co-N-C catalyst (0.144 W cm^{-2}). The normalized PPD of Fe-N-C and Co-N-C that comprised MEA in 100 periods is summarized in Figure 4.5c. The performance of Fe-N-C is reached maximum at 100 cycles and decreased continuously until 500 cycles (0.172 W cm^{-2}, 81.4 % of PPD at 100 cycles). The performance of Co-N-C also follows similar trends as that of Fe-N-C but the performance degradation limited to 93.3 % of PPD at the 100 cycles (0.136 W cm^{-2}). The PPD degradation percentage of Co-N-C is almost same as Pt/C catalyst MEA degradation (93.2 %, Figure S4.20). It could be caused by the degradation of the carbon oxidation at the electrode as well as the degradation of the gas diffusion layer due to O_2 evolution. The ohmic region resistance is increased in every case of MEA by 500 cycles. The increase in ohmic resistance may be due to membrane and ionomer degradation caused by the high concentration of H_2O_2 in the catholyte. The development of durable membranes and ionomers is required to obtain long-term stable DBFC performance.

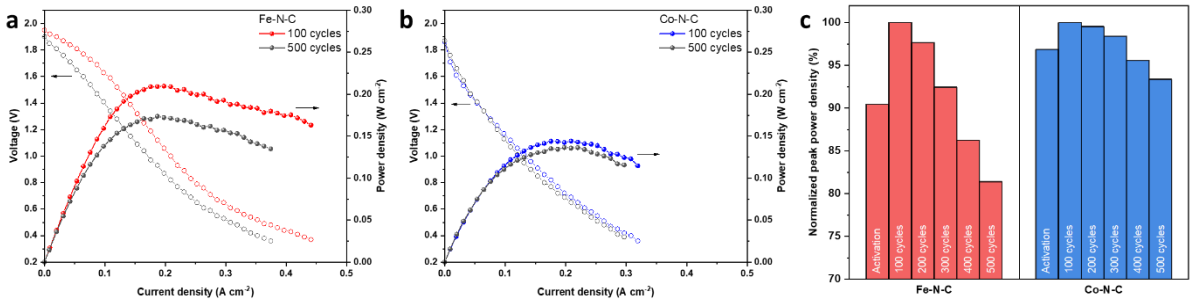

Figure 4.5 Performance of DBFC during ADT (a) Direct borohydride fuel cell polarization curves of accelerated durability test (ADT) in unit-cell configuration after 100 and 500 cycles for Fe-N-C and (b) Co-N-C. (c) The normalized peak power density of DBFC unit-cell from activation to 500 cycles.

4.4 Conclusions

PGM-free catalysts in DBFC are demonstrated with nickel catalyst at the anode and M-N-C catalyst at the cathode, respectively. The activity and durability of Fe-N-C and Co-N-C are compared by electrochemical measurement, spectroscopy, and DFT simulation. The activity of Fe-N-C is higher than Co-N-C for both ORR and PRR by half-cell and DBFC measurement. By using a three-electrode half-cell measurement, the candidate material for PRR can be easily compared to the mixed potential value. Where the mixed potential shifted to the higher potential, which means high activity for the PRR catalyst. At the mixed potential region, the PRR and POR rates are the same, which is independent of the mass transport and more likely related to the intrinsic activity of the catalyst. The durability of Fe-N-C and Co-N-C is conducted to find the suitable catalyst in harsh DBFC conditions. The half-cell and MEA tests showed that the Co-N-C is a durable catalyst under H_2O_2 with H_2SO_4 catholyte. The post-mortem XPS results show that the active site of the Fe-N-C degrades faster than Co-N-C in terms of demetallation of central atom. In addition, the DFT simulation supports the degradation mechanism based on the low predicted free energy of iron with nitrogen bonding (FeN_x) than cobalt with nitrogen bonding (CoN_x) in O_2 and H_2O_2 atmosphere. All PGM-group catalyst free DBFCs are achieved for economically viable DBFC. Even though the fuel cell performance needs to further improved to be reach the high performance of a DBFC with a PGM-group catalyst, this study will be a guideline for finding durable and high performance DBFCs.

References

(1) Wang, X. X.; Swihart, M. T.; Wu, G. Achievements, Challenges and Perspectives on Cathode Catalysts in Proton Exchange Membrane Fuel Cells for Transportation. *Nat Catal* **2019**, *2* (7), 578–589. https://doi.org/10.1038/s41929-019-0304-9.

(2) Wei, C.; Rao, R. R.; Peng, J.; Huang, B.; Stephens, I. E. L.; Risch, M.; Xu, Z. J.; Shao-Horn, Y. Recommended Practices and Benchmark Activity for Hydrogen and Oxygen Electrocatalysis in Water Splitting and Fuel Cells. *Advanced Materials* **2019**, *31* (31), 1806296. https://doi.org/10.1002/adma.201806296.

(3) Index. In *Direct Liquid Fuel Cells*; Akay, R. G., Yurtcan, A. B., Eds.; Academic Press, 2021; pp 307–312. https://doi.org/10.1016/B978-0-12-818624-4.09990-8.

(4) Oshchepkov, A. G.; Braesch, G.; Bonnefont, A.; Savinova, E. R.; Chatenet, M. Recent Advances in the Understanding of Nickel-Based Catalysts for the Oxidation of Hydrogen-Containing Fuels in Alkaline Media. *ACS Catal.* **2020**, *10* (13), 7043–7068. https://doi.org/10.1021/acscatal.0c00101.

(5) Wang, Z.; Parrondo, J.; He, C.; Sankarasubramanian, S.; Ramani, V. Efficient PH-Gradient-Enabled Microscale Bipolar Interfaces in Direct Borohydride Fuel Cells. *Nature Energy* **2019**, *4* (4), 281–289. https://doi.org/10.1038/s41560-019-0330-5.

(6) An, L.; Zhao, T. S.; Chai, Z. H.; Zeng, L.; Tan, P. Modeling of the Mixed Potential in Hydrogen Peroxide-Based Fuel Cells. *International Journal of Hydrogen Energy* **2014**, *39* (14), 7407–7416. https://doi.org/10.1016/j.ijhydene.2014.02.169.

(7) Perry, S. C.; Pangotra, D.; Vieira, L.; Csepei, L.-I.; Sieber, V.; Wang, L.; Ponce de León, C.; Walsh, F. C. Electrochemical Synthesis of Hydrogen Peroxide from Water and Oxygen. *Nat Rev Chem* **2019**, *3* (7), 442–458. https://doi.org/10.1038/s41570-019-0110-6.

(8) Katsounaros, I.; B. Schneider, W.; C. Meier, J.; Benedikt, U.; Ulrich Biedermann, P.; A. Auer, A.; J. Mayrhofer, K. J. Hydrogen Peroxide Electrochemistry on Platinum: Towards Understanding the Oxygen Reduction Reaction Mechanism. *Physical Chemistry Chemical Physics* **2012**, *14* (20), 7384–7391. https://doi.org/10.1039/C2CP40616K.

(9) Xie, X.; He, C.; Li, B.; He, Y.; Cullen, D. A.; Wegener, E. C.; Kropf, A. J.; Martinez, U.; Cheng, Y.; Engelhard, M. H.; Bowden, M. E.; Song, M.; Lemmon, T.; Li, X. S.; Nie, Z.; Liu, J.; Myers, D. J.; Zelenay, P.; Wang, G.; Wu, G.; Ramani, V.; Shao, Y. Performance Enhancement and Degradation Mechanism Identification of a Single-Atom Co–N–C Catalyst for Proton Exchange Membrane Fuel Cells. *Nature Catalysis* **2020**, *3* (12), 1044–1054. https://doi.org/10.1038/s41929-020-00546-1.

(10) Liu, S.; Li, C.; Zachman, M. J.; Zeng, Y.; Yu, H.; Li, B.; Wang, M.; Braaten, J.; Liu, J.; Meyer, H. M.; Lucero, M.; Kropf, A. J.; Alp, E. E.; Gong, Q.; Shi, Q.; Feng, Z.; Xu, H.; Wang, G.; Myers, D. J.; Xie, J.; Cullen, D. A.; Litster, S.; Wu, G. Atomically Dispersed Iron Sites with a Nitrogen–Carbon Coating as Highly Active and Durable Oxygen Reduction Catalysts for Fuel Cells. *Nat Energy* **2022**, 1–12. https://doi.org/10.1038/s41560-022-01062-1.

(11) Kaiser, S. K.; Chen, Z.; Faust Akl, D.; Mitchell, S.; Pérez-Ramírez, J. Single-Atom Catalysts across the Periodic Table. *Chem. Rev.* **2020**, *120* (21), 11703–11809. https://doi.org/10.1021/acs.chemrev.0c00576.

(12) Hai, X.; Xi, S.; Mitchell, S.; Harrath, K.; Xu, H.; Akl, D. F.; Kong, D.; Li, J.; Li, Z.; Sun, T.; Yang, H.; Cui, Y.; Su, C.; Zhao, X.; Li, J.; Pérez-Ramírez, J.; Lu, J. Scalable Two-Step Annealing Method for Preparing Ultra-High-Density Single-Atom Catalyst Libraries. *Nat. Nanotechnol.* **2021**, 1–8. https://doi.org/10.1038/s41565-021-01022-y.

(13) Bai, L.; Hsu, C.-S.; Alexander, D. T. L.; Chen, H. M.; Hu, X. Double-Atom Catalysts as a Molecular Platform for Heterogeneous Oxygen Evolution Electrocatalysis. *Nat Energy* **2021**, *6* (11), 1054–1066. https://doi.org/10.1038/s41560-021-00925-3.

(14) Asset, T.; Atanassov, P. Iron-Nitrogen-Carbon Catalysts for Proton Exchange Membrane Fuel Cells. *Joule* **2020**, *4* (1), 33–44. https://doi.org/10.1016/j.joule.2019.12.002.

(15) Li, J.; Sougrati, M. T.; Zitolo, A.; Ablett, J. M.; Oğuz, I. C.; Mineva, T.; Matanovic, I.; Atanassov, P.; Huang, Y.; Zenyuk, I.; Di Cicco, A.; Kumar, K.; Dubau, L.; Maillard, F.; Dražić, G.; Jaouen, F. Identification of Durable and Non-Durable FeNx Sites in Fe–N–C Materials for Proton Exchange Membrane Fuel Cells. *Nat Catal* **2021**, *4* (1), 10–19. https://doi.org/10.1038/s41929-020-00545-2.

(16) Mehmood, A.; Gong, M.; Jaouen, F.; Roy, A.; Zitolo, A.; Khan, A.; Sougrati, M.-T.; Primbs, M.; Bonastre, A. M.; Fongalland, D.; Drazic, G.; Strasser, P.; Kucernak, A. High Loading of Single Atomic Iron Sites in Fe–NC Oxygen Reduction Catalysts for Proton Exchange Membrane Fuel Cells. *Nat Catal* **2022**, *5* (4), 311–323. https://doi.org/10.1038/s41929-022-00772-9.

(17) Choi, C. H.; Baldizzone, C.; Grote, J.-P.; Schuppert, A. K.; Jaouen, F.; Mayrhofer, K. J. J. Stability of Fe-N-C Catalysts in Acidic Medium Studied by Operando Spectroscopy. *Angewandte Chemie International Edition* **2015**, *54* (43), 12753–12757. https://doi.org/10.1002/anie.201504903.

(18) Choi, C. H.; Baldizzone, C.; Polymeros, G.; Pizzutilo, E.; Kasian, O.; Schuppert, A. K.; Ranjbar Sahraie, N.; Sougrati, M.-T.; Mayrhofer, K. J. J.; Jaouen, F. Minimizing Operando Demetallation of Fe-N-C Electrocatalysts in Acidic Medium. *ACS Catal.* **2016**, *6* (5), 3136–3146. https://doi.org/10.1021/acscatal.6b00643.

(19) Bae, G.; Chung, M. W.; Ji, S. G.; Jaouen, F.; Choi, C. H. PH Effect on the H2O2-Induced Deactivation of Fe-N-C Catalysts. *ACS Catal.* **2020**, *10* (15), 8485–8495. https://doi.org/10.1021/acscatal.0c00948.

(20) Banham, D.; Ye, S.; Pei, K.; Ozaki, J.; Kishimoto, T.; Imashiro, Y. A Review of the Stability and Durability of Non-Precious Metal Catalysts for the Oxygen Reduction Reaction in Proton Exchange Membrane Fuel Cells. *Journal of Power Sources* **2015**, *285*, 334–348. https://doi.org/10.1016/j.jpowsour.2015.03.047.

(21) Ko, Y.; Lombardo, L.; Li, M.; Pham, T. H. M.; Yang, H.; Züttel, A. Selective Borohydride Oxidation Reaction on Nickel Catalyst with Anion and Cation Exchange Ionomer for High-Performance Direct Borohydride Fuel Cells. *Advanced Energy Materials* **2022**, *12* (16), 2103539. https://doi.org/10.1002/aenm.202103539.

(22) Zhang, X.; Truong-Phuoc, L.; Liao, X.; Papaefthimiou, V.; Pugliesi, M.; Tuci, G.; Giambastiani, G.; Pronkin, S.; Pham-Huu, C. Inducing Atomically Dispersed Cl–FeN 4 Sites for ORRs in the SiO 2 -Mediated Synthesis of Highly Mesoporous N-Enriched C-Networks. *Journal of Materials Chemistry A* **2022**, *10* (11), 6153–6164. https://doi.org/10.1039/D1TA09519F.

(23) Kresse, G.; Furthmüller, J. Efficiency of Ab-Initio Total Energy Calculations for Metals and Semiconductors Using a Plane-Wave Basis Set. *Computational Materials Science* **1996**, *6* (1), 15–50. https://doi.org/10.1016/0927-0256(96)00008-0.

(24) Blöchl, P. E. Projector Augmented-Wave Method. *Phys. Rev. B* **1994**, *50* (24), 17953–17979. https://doi.org/10.1103/PhysRevB.50.17953.

(25) Perdew, J. P.; Burke, K.; Ernzerhof, M. Generalized Gradient Approximation Made Simple. *Phys. Rev. Lett.* **1996**, *77* (18), 3865–3868. https://doi.org/10.1103/PhysRevLett.77.3865.

(26) Grimme, S.; Antony, J.; Ehrlich, S.; Krieg, H. A Consistent and Accurate Ab Initio Parametrization of Density Functional Dispersion Correction (DFT-D) for the 94 Elements H-Pu. *J. Chem. Phys.* **2010**, *132* (15), 154104. https://doi.org/10.1063/1.3382344.

(27) Monkhorst, H. J.; Pack, J. D. Special Points for Brillouin-Zone Integrations. *Phys. Rev. B* **1976**, *13* (12), 5188–5192. https://doi.org/10.1103/PhysRevB.13.5188.

(28) Nørskov, J. K.; Rossmeisl, J.; Logadottir, A.; Lindqvist, L.; Kitchin, J. R.; Bligaard, T.; Jónsson, H. Origin of the Overpotential for Oxygen Reduction at a Fuel-Cell Cathode. *J. Phys. Chem. B* **2004**, *108* (46), 17886–17892. https://doi.org/10.1021/jp047349j.

(29) Paulus, U. A.; Schmidt, T. J.; Gasteiger, H. A.; Behm, R. J. Oxygen Reduction on a High-Surface Area Pt/Vulcan Carbon Catalyst: A Thin-Film Rotating Ring-Disk Electrode Study. *Journal of Electroanalytical Chemistry* **2001**, *495* (2), 134–145. https://doi.org/10.1016/S0022-0728(00)00407-1.

(30) Pan, F.; Zhang, H.; Liu, K.; Cullen, D.; More, K.; Wang, M.; Feng, Z.; Wang, G.; Wu, G.; Li, Y. Unveiling Active Sites of CO2 Reduction on Nitrogen-Coordinated and Atomically Dispersed Iron and Cobalt Catalysts. *ACS Catal.* **2018**, *8* (4), 3116–3122. https://doi.org/10.1021/acscatal.8b00398.

(31) Zitolo, A.; Ranjbar-Sahraie, N.; Mineva, T.; Li, J.; Jia, Q.; Stamatin, S.; Harrington, G. F.; Lyth, S. M.; Krtil, P.; Mukerjee, S.; Fonda, E.; Jaouen, F. Identification of Catalytic Sites in Cobalt-Nitrogen-Carbon Materials for the Oxygen Reduction Reaction. *Nat Commun* **2017**, *8* (1), 957. https://doi.org/10.1038/s41467-017-01100-7.

(32) Damjanovic, A.; Genshaw, M. A.; Bockris, J. O. Distinction between Intermediates Produced in Main and Side Electrodic Reactions. *J. Chem. Phys.* **1966**, *45* (11), 4057–4059. https://doi.org/10.1063/1.1727457.

(33) Muthukrishnan, A.; Nabae, Y.; Ohsaka, T. Role of Iron in the Reduction of H 2 O 2 Intermediate during the Oxygen Reduction Reaction on Iron-Containing Polyimide-Based Electrocatalysts. *RSC Advances* **2016**, *6* (5), 3774–3777. https://doi.org/10.1039/C5RA23162K.

(34) Zhao, J.; Tu, Z.; Chan, S. H. Carbon Corrosion Mechanism and Mitigation Strategies in a Proton Exchange Membrane Fuel Cell (PEMFC): A Review. *Journal of Power Sources* **2021**, *488*, 229434. https://doi.org/10.1016/j.jpowsour.2020.229434.

(35) Rojas-Carbonell, S.; Artyushkova, K.; Serov, A.; Santoro, C.; Matanovic, I.; Atanassov, P. Effect of PH on the Activity of Platinum Group Metal-Free Catalysts in Oxygen Reduction Reaction. *ACS Catal.* **2018**, *8* (4), 3041–3053. https://doi.org/10.1021/acscatal.7b03991.

(36) Chen, L.; Liu, X.; Zheng, L.; Li, Y.; Guo, X.; Wan, X.; Liu, Q.; Shang, J.; Shui, J. Insights into the Role of Active Site Density in the Fuel Cell Performance of Co-N-C Catalysts. *Applied Catalysis B: Environmental* **2019**, *256*, 117849. https://doi.org/10.1016/j.apcatb.2019.117849.

(37) Yang, N.; Peng, L.; Li, L.; Li, J.; Liao, Q.; Shao, M.; Wei, Z. Theoretically Probing the Possible Degradation Mechanisms of an FeNC Catalyst during the Oxygen Reduction Reaction. *Chem. Sci.* **2021**, *12* (37), 12476–12484. https://doi.org/10.1039/D1SC02901K.

(38) Zhang, H.; Osmieri, L.; Park, J. H.; Chung, H. T.; Cullen, D. A.; Neyerlin, K. C.; Myers, D. J.; Zelenay, P. Standardized Protocols for Evaluating Platinum Group Metal-Free Oxygen Reduction Reaction Electrocatalysts in Polymer Electrolyte Fuel Cells. *Nat Catal* **2022**, *5* (5), 455–462. https://doi.org/10.1038/s41929-022-00778-3.

Supporting information

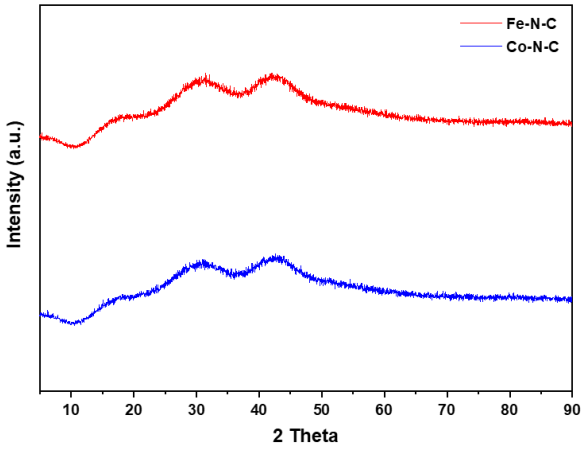

Figure S4.1 XRD pattern of Fe-N-C and Co-N-C.

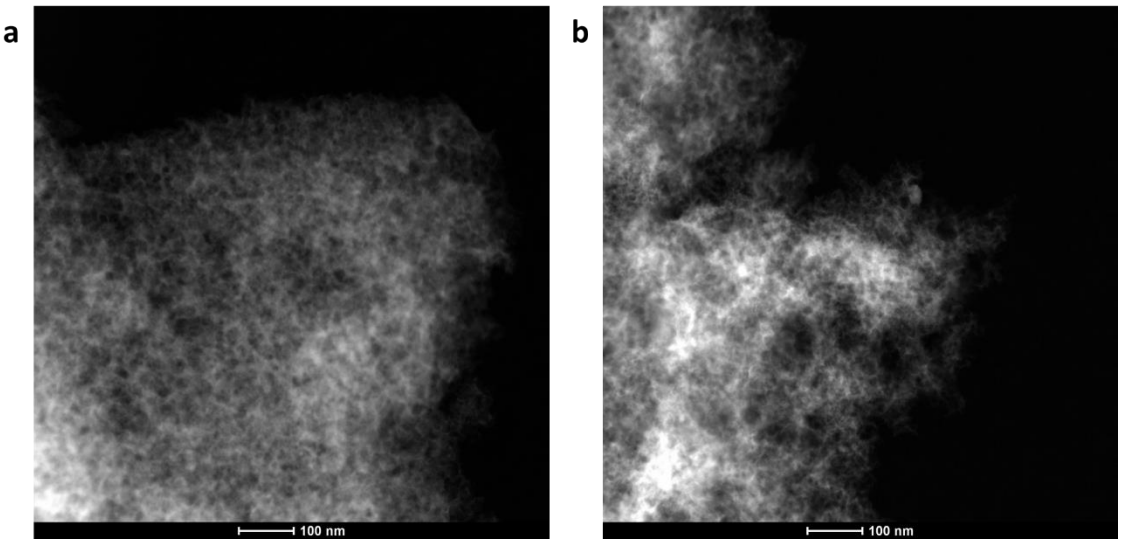

Figure S4.2 STEM images of (a) Fe-N-C and (b) Co-N-C (scale bar: 100 nm).

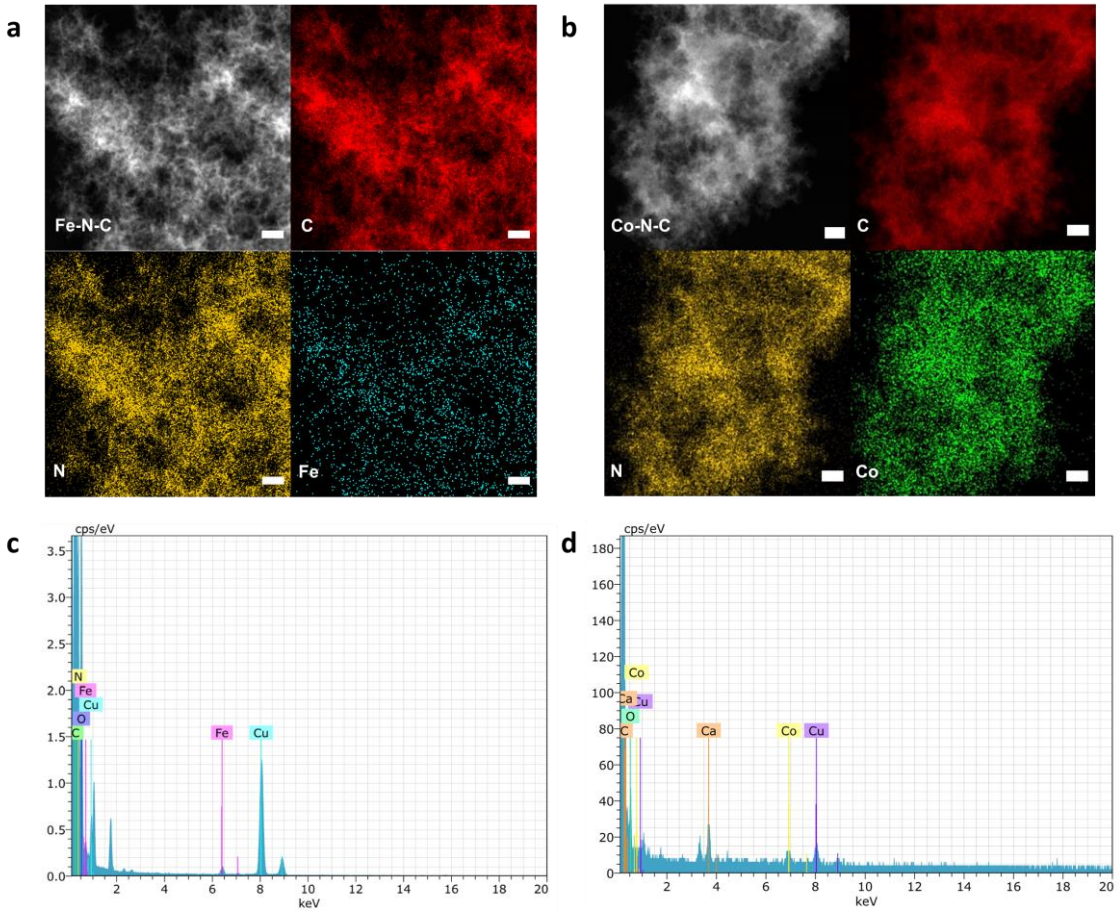

Figure S4.3 HAADF-STEM images and corresponding elemental mapping of (a) Fe-N-C and (b) Co-N-C (scale bar: 50 nm). (c) EDX spectra of Fe-N-C and (d) Co-N-C.

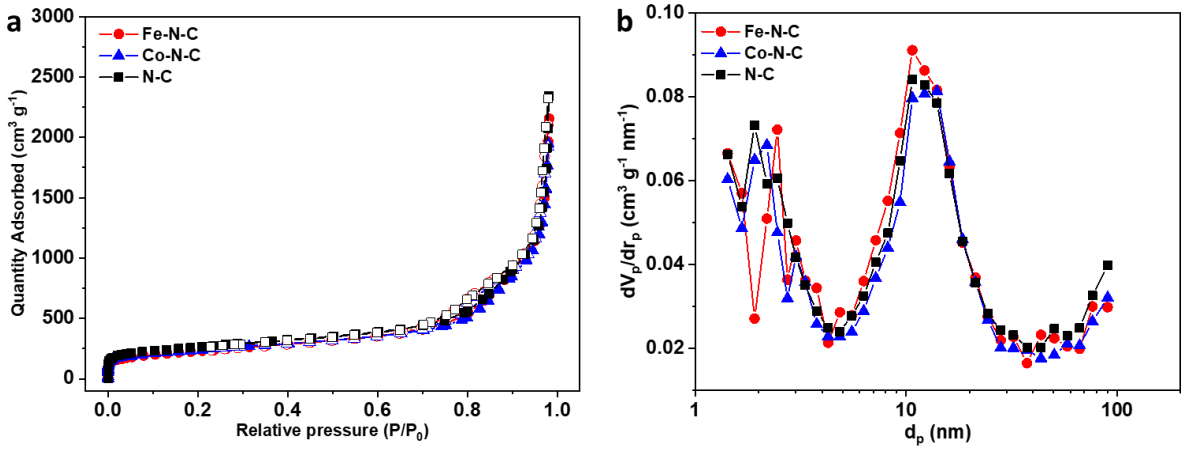

Figure S4.4 (a) N_2 isotherm adsorption/desorption of Fe-N-C, Co-N-C, and N-C and (b) pore size distributions by BJH method.

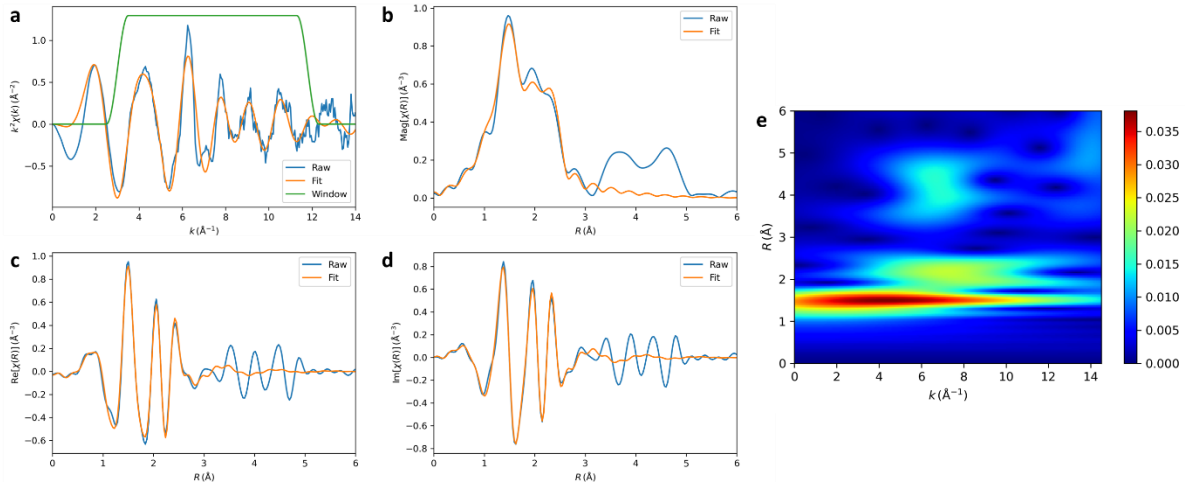

Figure S4.5 (a) EXAFS fitting of Fe-N-C in *k* and (b, c, d) R space. (e) Wavelet transforms (WT) plot of Fe-N-C. The maxima at approximately 4 and 7 $Å^{-1}$ are associated with the Fe-N(O, C) and Fe-Fe contribution, respectively.

Table S4.1. Structural data from the fitting of Fe K-edge EXAFS signal in Fe-N-C catalyst

Sample	Path	S_0^2 (amp)	C.N.	R [Å]	R_{ref} [Å]	σ^2	ΔE_0 [eV]	R-factor
Fe-N-C (10K)	Fe-C/N/O	0.688 (fixed)	2.60 ± 0.43	1.938 ± 0.022	1.946	0.0020 ± 0.0012	-0.6 ± 2.0	0.0151
	Fe-C/N/O		2.00 ± 0.34	2.097 ± 0.036	2.100	0.0020 ± 0.0012		
	Fe-Fe		1.67 ± 0.49	2.553 ± 0.012	2.550	0.0040 ± 0.0025		

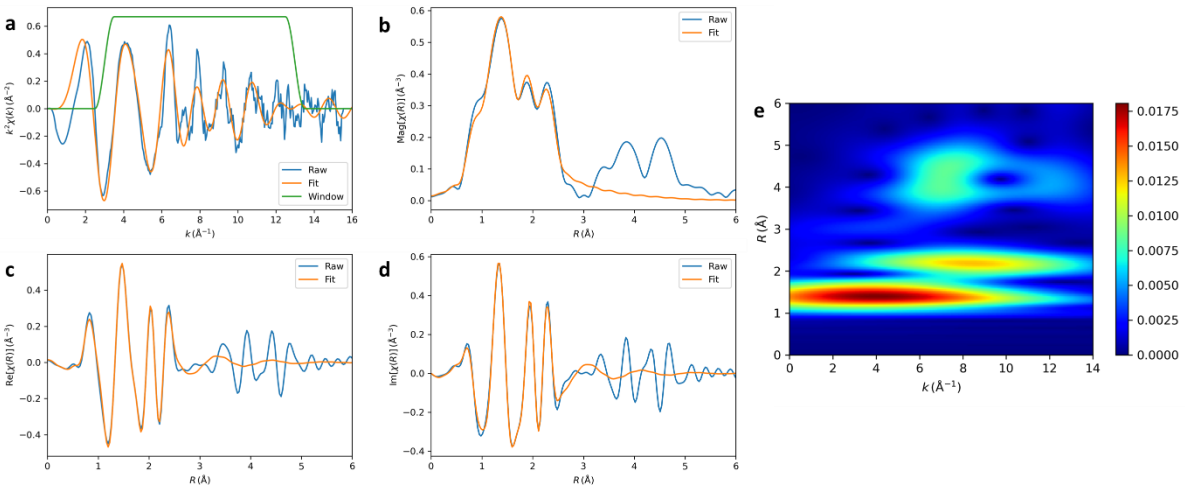

Figure S4.6 (a) EXAFS fitting of Co-N-C in *k* and (b, c, d) R space (e) Wavelet transforms (WT) plot of Co-N-C. The maxima at approximately 4 and 8 $Å^{-1}$ are associated with the Co-N(O, C) and Co-Co contribution, respectively.

Table S4.2. Structural data from the fitting of Co K-edge EXAFS signal in Co-N-C catalyst

Sample	Path	S_0^2 (amp)	C.N.	R [Å]	R_{ref} [Å]	σ^2	ΔE_0 [eV]	R-factor
Co-N-C (10K)	Co-C/N/O	0.772 (fixed)	1.82 ± 0.35	1.889 ± 0.015	1.900	0.0034 ± 0.0002	-1.9 ± 1.6	0.0112
	Co-C/N/O		1.35 ± 0.20	2.075 ± 0.024	2.080	0.0034 ± 0.0002		
	Co-Co		0.74 ± 0.20	2.075 ± 0.009	2.509	0.0023 ± 0.0017		

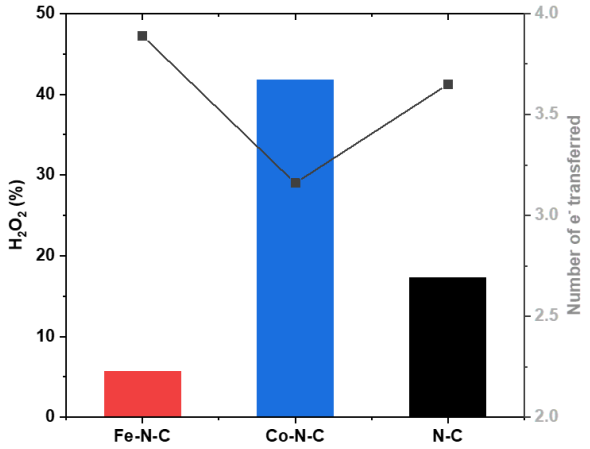

Figure S4.7 Hydrogen peroxide production and electron transfer number at 0.3 V on Fe-N-C, Co-N-C, and N-C catalyst. Fe-N-C (electron transfer number: 3.89, H_2O_2 production: 5.7%), Co-N-C (electron transfer number: 3.16, H_2O_2 production: 41.8%), N-C (electron transfer number: 3.65, H_2O_2 production: 17.3%).

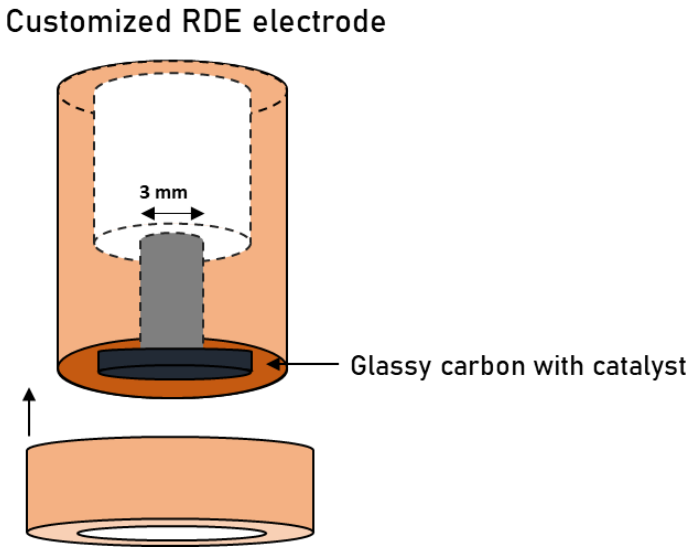

Figure S4.8 Drawing of customized RDE electrode, a piece of glassy carbon with the catalyst is contacted with RDE electrode and fixed with the cap for post-mortem XPS and Raman spectroscopy after durability test.

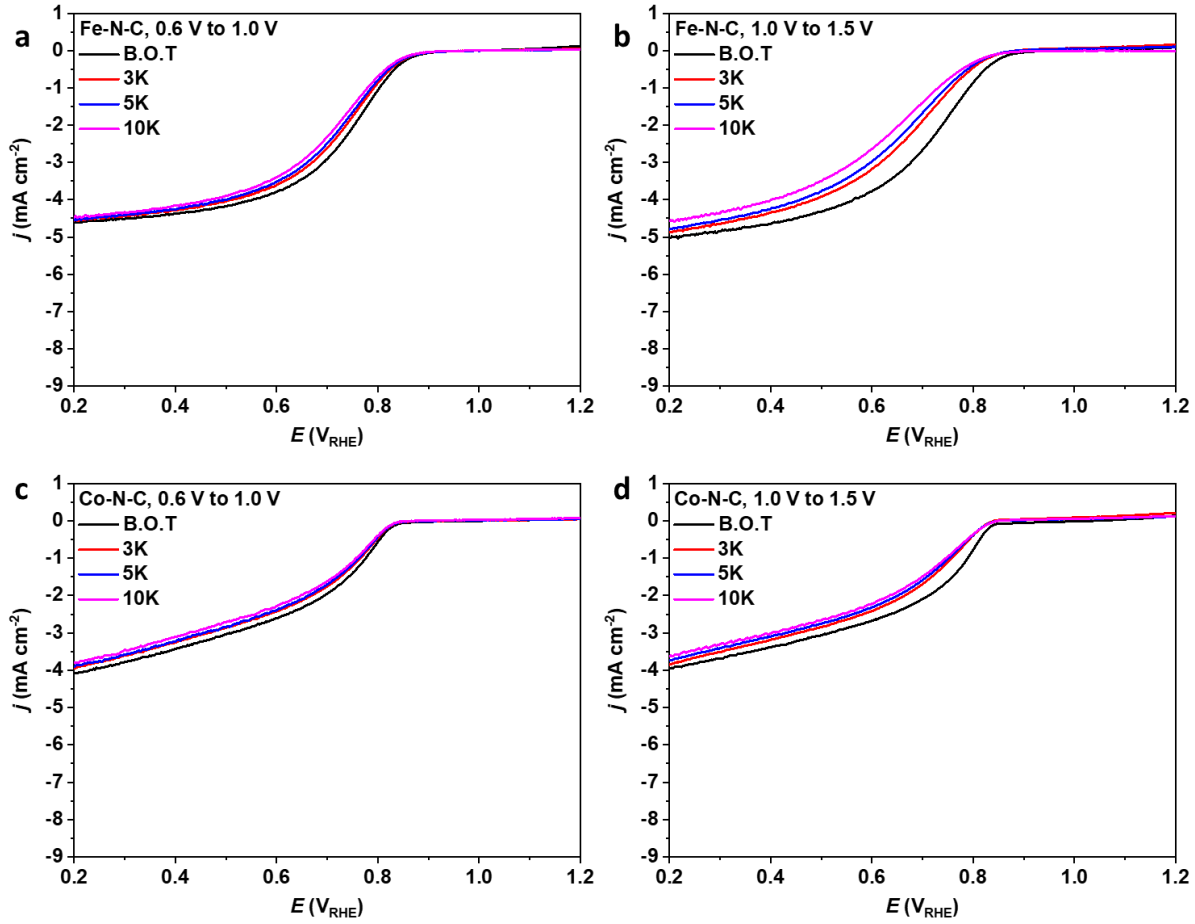

Figure S4.9 ORR polarization curves for Fe-N-C and Co-N-C during accelerated durability test (ADT) from beginning of the test (B.O.T) to 10,000 cycles for an electrode rotating speed of 1600rpm. (a) Fe-N-C under the potential range 0.6 V to 1.0 V, (b) 1.0 V to 1.5 V. (c) Co-N-C under the potential range 0.6 V to 1.0 V, (d) 1.0 V to 1.5 V under O_2-saturated 0.5 M H_2SO_4.

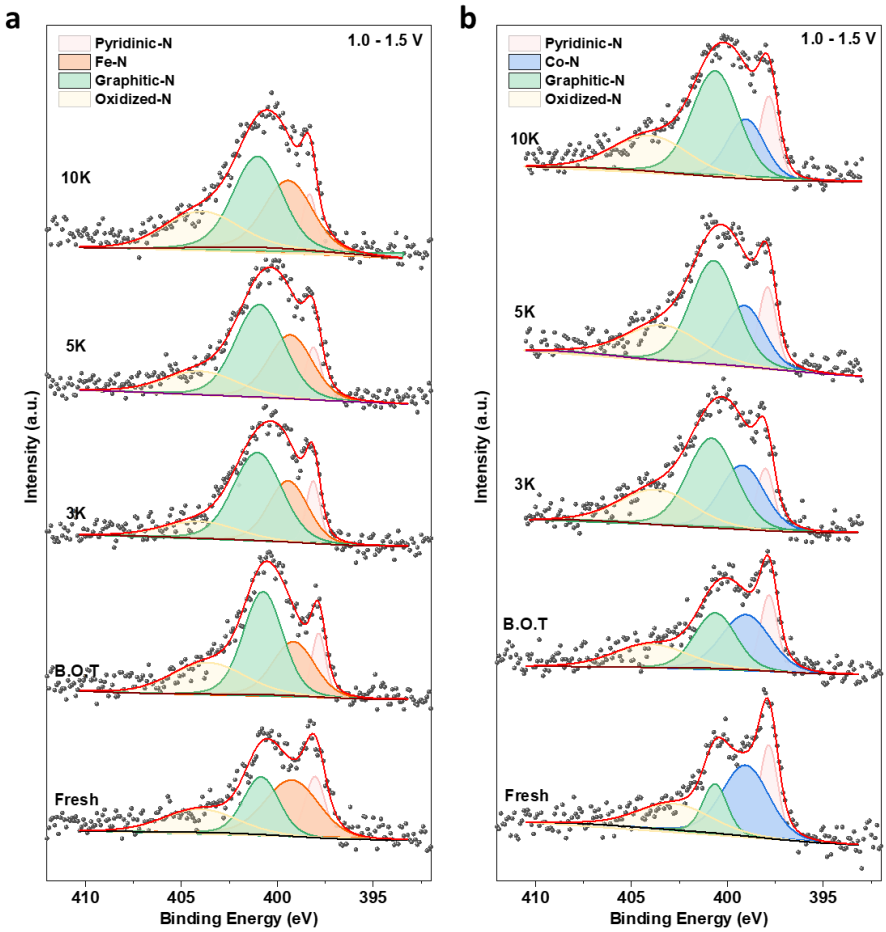

Figure S4.10 N 1s XPS spectra of M-N-C with accelerated degradation test (ADT) on glassy carbon electrode from the fresh and beginning of the test (B.O.T) to 10,000 cycles for (a) Fe-N-C and (b) Co-N-C at 1.0 V to 1.5 V under O_2-saturated 0.5 M H_2SO_4.

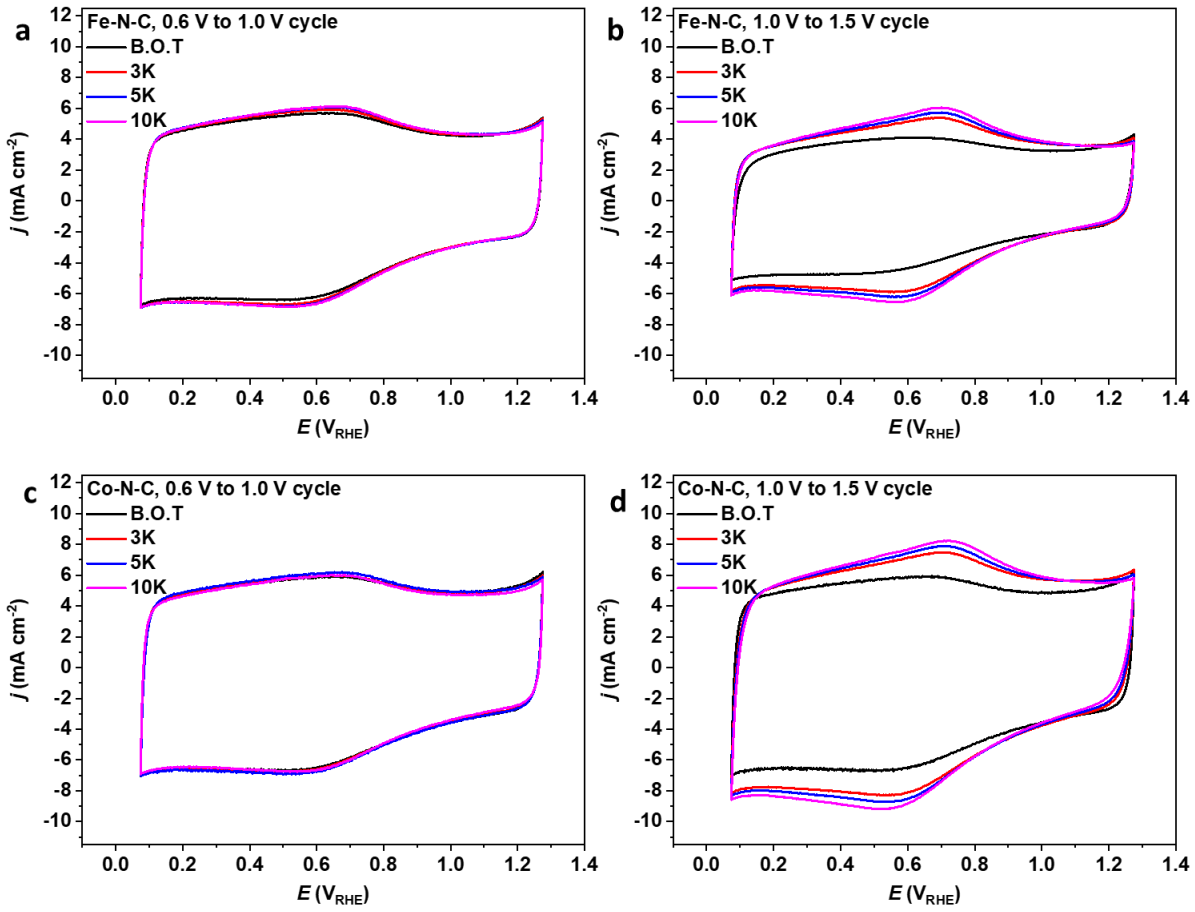

Figure S4.11 Cyclic voltammetry for the Fe-N-C and Co-N-C during accelerated durability test (ADT) from fresh and beginning of the test (B.O.T) to 10,000 cycles. (a) Fe-N-C under the potential range 0.6 V to 1.0 V, (b) 1.0 V to 1.5 V. (c) Co-N-C under the potential range 0.6 V to 1.0 V, (d) 1.0 V to 1.5 V under N_2-saturated 0.5 M H_2SO_4.

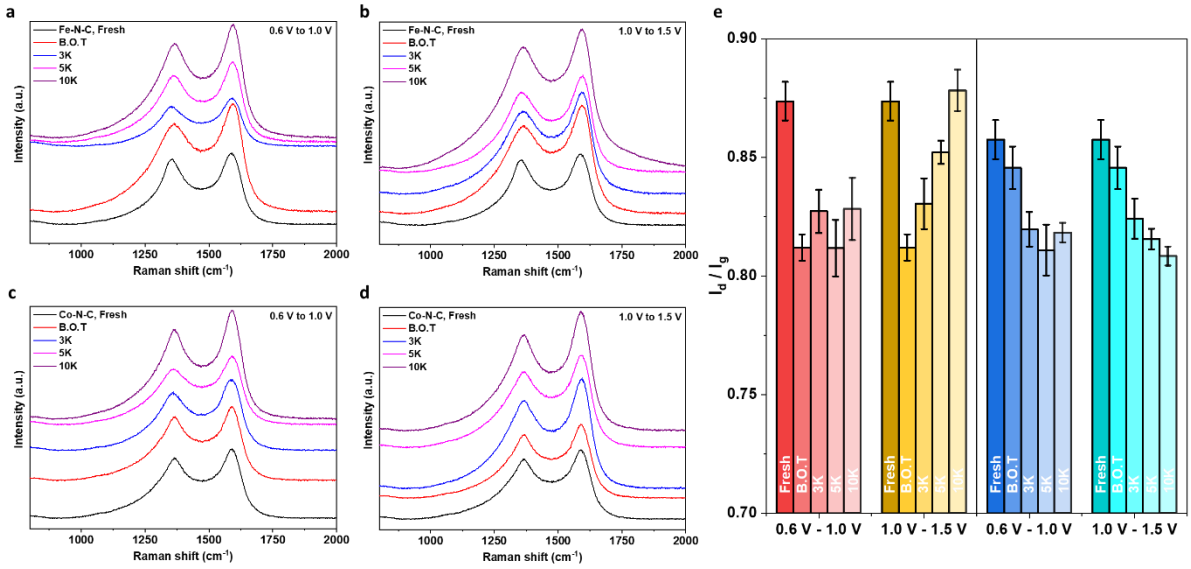

Figure S4.12 Raman spectra of the Fe-N-C and Co-N-C during accelerated durability test (ADT) from fresh and beginning of the test (B.O.T) to 10,000 cycles. (a) Fe-N-C under the potential range 0.6 V to 1.0 V, (b) 1.0 V to 1.5 V. (c) Co-N-C under the potential range 0.6 V to 1.0 V, (d) 1.0 V to 1.5 V under O_2-saturated 0.5 M H_2SO_4. (e) I_d/I_g ratio changing during ADT.

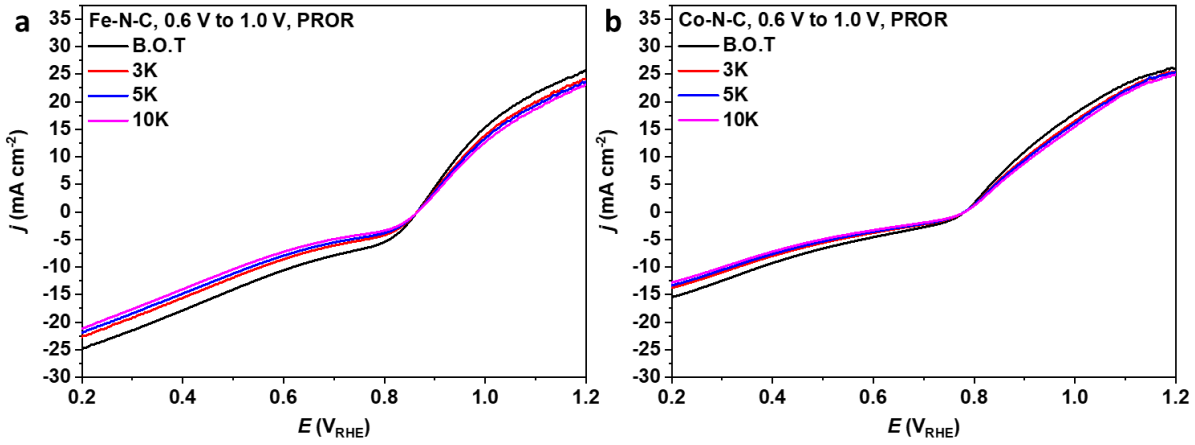

Figure S4.13 PROR polarization curves for Fe-N-C and Co-N-C during accelerated durability test (ADT) from fresh and beginning of the test (B.O.T) to 10,000 cycles for an electrode rotating speed of 1600rpm. (a) Fe-N-C under the potential range 0.6 V to 1.0 V (b) Co-N-C under the potential range 0.6 V to 1.0 V under O_2-saturated 0.02 M H_2O_2 with 0.5 M H_2SO_4.

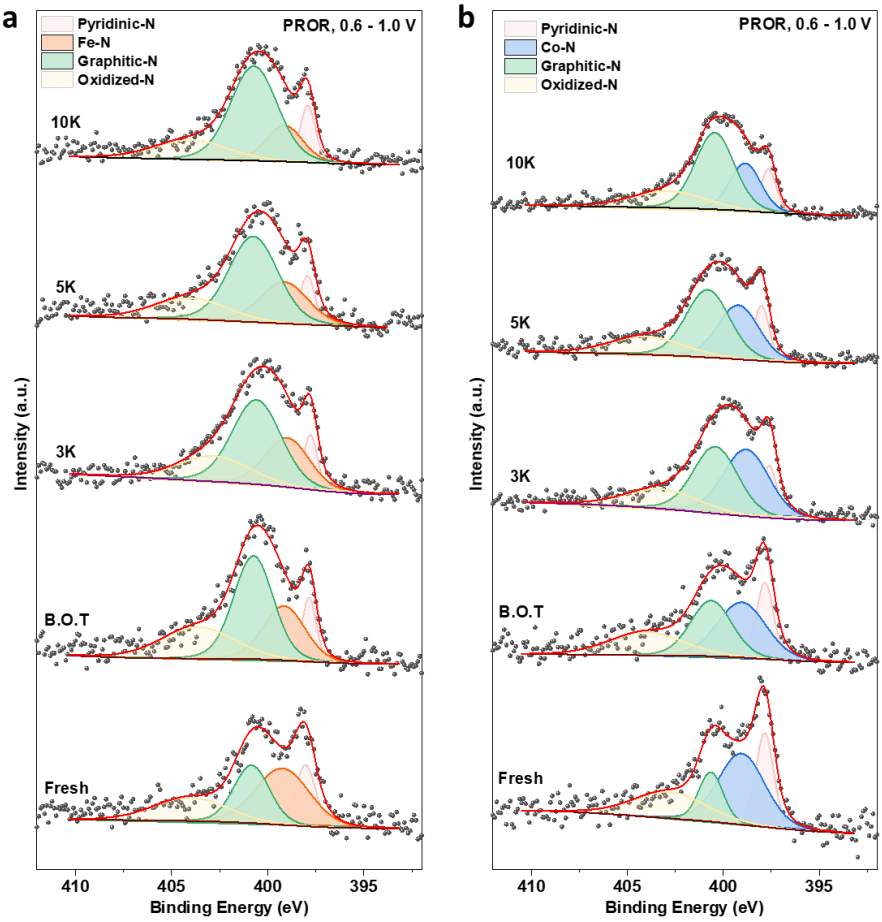

Figure S4.14 N 1s XPS spectra of M-N-C with accelerated degradation test (ADT) on glassy carbon electrode from the fresh and beginning of the test (B.O.T) to 10,000 cycles for (a) Fe-N-C and (b) Co-N-C at 0.6 V to 1.0 V under 0.02 M H_2O_2 with O_2-saturated 0.5 M H_2SO_4.

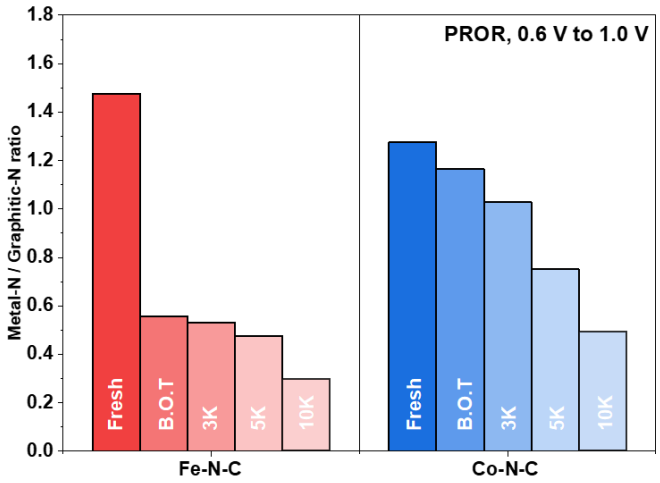

Figure S4.15 The ratio of metal-N/graphitic-N in N 1s XPS spectra from the fresh and beginning of the test (B.O.T) to 10,000 cycles for (a) Fe-N-C and (b) Co-N-C at 0.6 V to 1.0 V under 0.02 M H_2O_2 with O_2-saturated 0.5 M H_2SO_4.

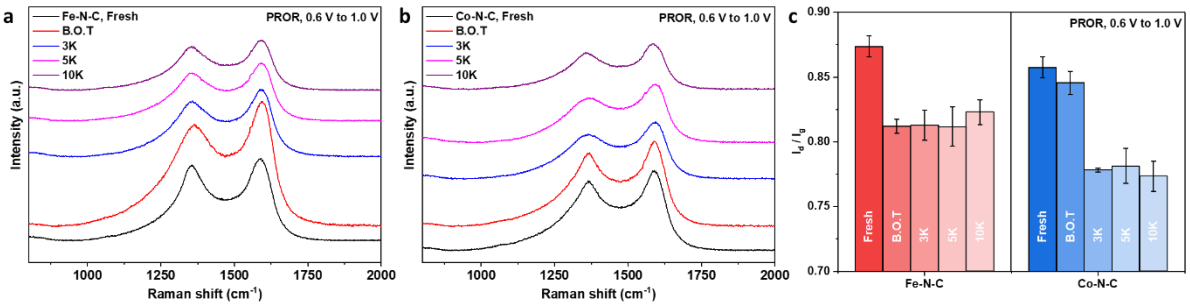

Figure S4.16 Raman spectra of the Fe-N-C and Co-N-C during accelerated durability test (ADT) from fresh and beginning of the test (B.O.T) to 10,000 cycles. (a) Fe-N-C under the potential range 0.6 V to 1.0 V, (b) Co-N-C under the potential range 0.6 V to 1.0 V under O_2-saturated 0.5 M H_2SO_4. (c) I_d/I_g ratio changing during ADT.

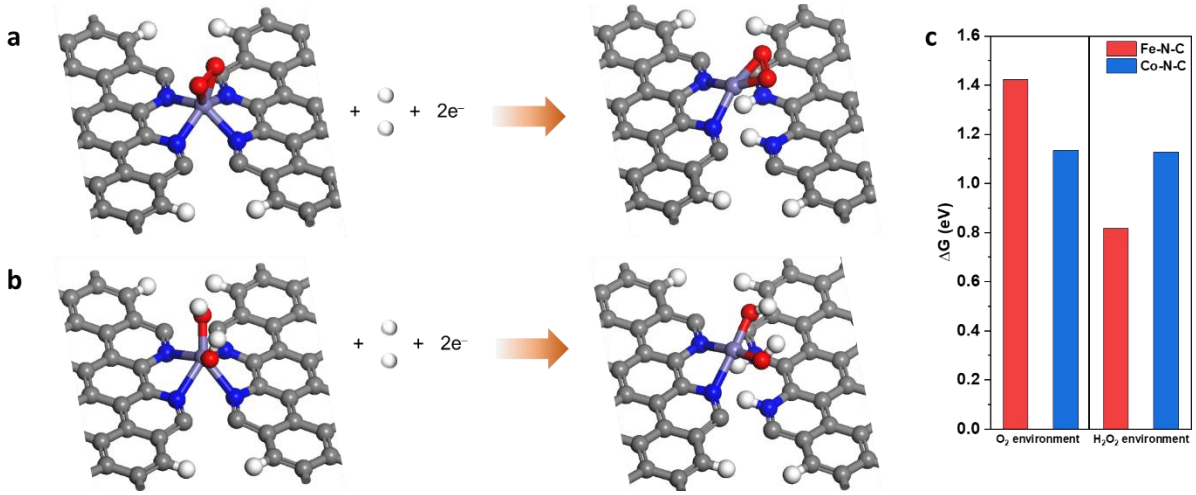

Figure S4.17 Atomistic structures of simulation models for leaching of the central M atoms in pyridinic-N, $MN_{2+2}C_{4+4}$ (M = Fe or Co) active sites under (a) O_2 environment (b) H_2O_2 environment. (c) Predicted free energy of demetallation on Fe-N-C (O_2: 1.422, H_2O_2: 0.818 eV) and Co-N-C (O_2: 1.135, H_2O_2: 1.128 eV).

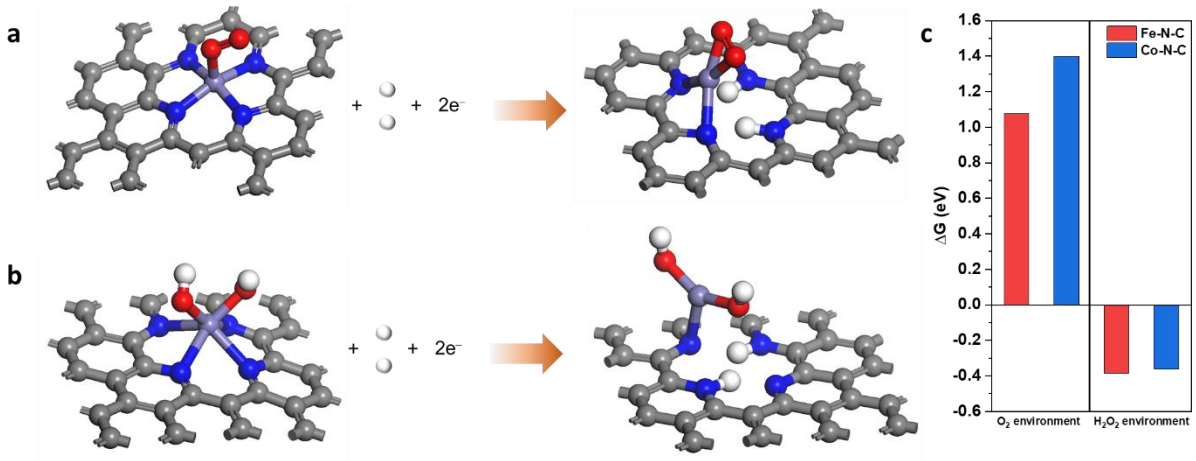

Figure S4.18 Degradation of M-N-C catalysts Atomistic structures of simulation models for leaching of the central M atoms in in-plane, MN_4C_{10} (M = Fe or Co) active sites under (a) O_2 environment (b) H_2O_2 environment. (c) Predicted free energy of demetallation on Fe-N-C (O_2: 1.077, H_2O_2: −0.386 eV) and Co-N-C (O_2: 1.400, H_2O_2: −0.361 eV).

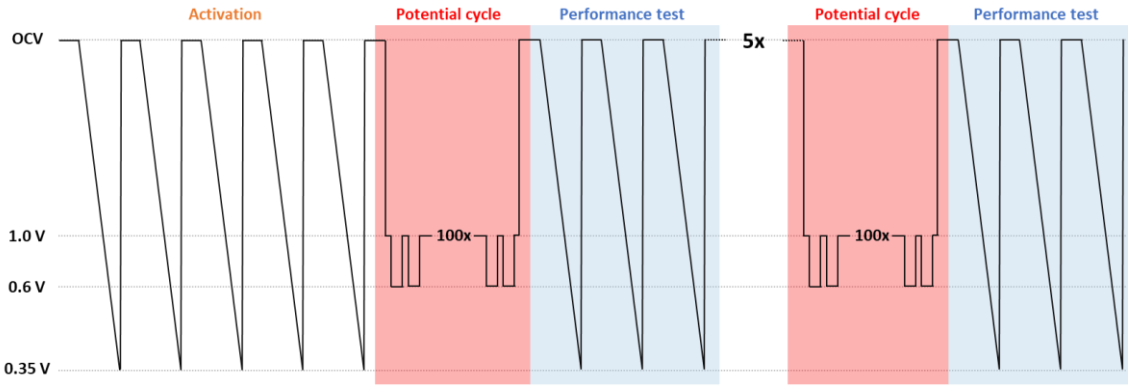

Figure S4.19 Accelerated durability test (ADT) protocol of DBFC in unit-cell configuration.

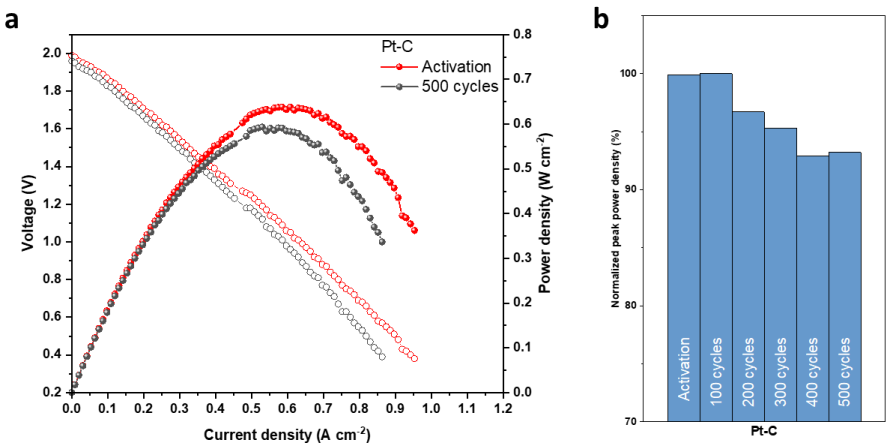

Figure S4.20 (a) Direct borohydride fuel cell polarization curves of accelerated durability test (ADT) in unit-cell configuration after 100 and 500 cycles for Pt-C (Pt loading at the cathode: 1 mg cm^{-2}). (c) The normalized peak power density of DBFC unit-cell from activation to 500 cycles.

Table S4.3. Comparison of recent DBFC performance data (PGMs based, PGM free anode, All PGM free DBFC).

Anode (loading, mg cm^{-2})	Cathode (loading, mg cm^{-2})	Separator (thickness, µm)	Oxidant	Operation temperature (^oC)	P_{max} (mW cm^{-2})	OCV (V)	Year published
Au/C (2)	Pt/C (2)	Nafion 117 (175)	O_2	85	72	1.0	2006[1]
Ni-Pt/C (10)	$Co(OH)_2$-PPY-C (5)	Nafion 117 (183)	O_2	80	550	1.1	2012[2]
Pt/C (0.3)	Pt/C (0.3)	Nafion 117 (183)	H_2O_2	25	275	1.67	2015[3]
Pd/C (0.3)	Pt/C (0.3)	Nafion 117 (183)	H_2O_2	25	211	1.72	2015[3]
Pd/C (3) + Ni	Pt/C (3)	Bipolar interface (175)	H_2O_2	70	630	1.95	2019[4]
Pd/C (3) + Ni	Pt/C (3)	Bipolar interface (175)	H_2O_2	70	890	1.96	2020[5]
Pd/C (0.5) + Ni	Pt/C (1)	Bipolar interface (127)	H_2O_2	80	391	1.88	2022[6]
PGM free anode (loading, mg cm^{-2})	**Cathode (loading, mg cm^{-2})**	**Separator (thickness, µm)**	**Oxidant**	**Operation temperature (^oC)**	**P_{max} (mW cm^{-2})**	**OCV (V)**	**Year published**
Ni powder (167)	Pt/C (1)	Nafion 211 (25)	Air	40	40	1.0	2005[7]
Os/C (1.7)	Pt/C (4)	Nafion 117 (175)	O_2	60	109	1.1	2012[8]
Ni_{ED}/C (0.6)	Pt/C (2)	Nafion 212 (50)	O_2	60	240	1.21	2019[9]
NiED/eNFT (1.2)	Pt/C (2)	Nafion 212 (50)	O_2	60	180	1.24	2020[10]
Ni_{ED}/eNFT-D	Pt/C (1)	Bipolar interface (175)	H_2O_2	70	446	2.0	2020[11]
NiF@AEI-Ni (10)	Pt/C (1)	Bipolar interface (127)	H_2O_2	80	440	1.95	2022[6]
NiF@CEI-Ni (10)	Pt/C (1)	Nafion 115 (127)	H_2O_2	80	609	1.92	2022[6]
PGM free anode (loading, mg cm^{-2})	**PGM free cathode (loading, mg cm^{-2})**	**Separator (thickness, µm)**	**Oxidant**	**Operation temperature (^oC)**	**P_{max} (mW cm^{-2})**	**OCV (V)**	**Year published**
NiB/C (70)	$LaNi_{0.9}Ru_{0.1}O_3$/C (7.5)	Nafion	O_2	25	180	1.09	2018[12]
u-SnO_2/Co_3O_4 (10)	$LaNiO_3$ (7.5)	Poly fiber membrane (140)	Air	25	52	1.02	2020[13]
$Co(OH)_2$-PPy-BP (5)	$Co(OH)_2$-PPy-BP (5)	Cu-AEM (120)	O_2	60	403	1.05	2020[14]
Co-Ni-B (30)	$LaNiO_3$ (7.5)	Poly fiber membrane (140)	O_2	25	209	1.06	2021[15]
NiF@CEI-Ni (10)	Co-N-C (2.5)	Nafion 115 (127)	H_2O_2	80	144	1.86	This work
NiF@CEI-Ni (10)	Fe-N-C (2.5)	Nafion 115 (127)	H_2O_2	80	209	1.95	This work

References

(1) Cheng, H.; Scott, K. Influence of Operation Conditions on Direct Borohydride Fuel Cell Performance. *Journal of Power Sources* **2006**, *160* (1), 407–412. https://doi.org/10.1016/j.jpowsour.2006.01.097.

(2) Qin, H. Y.; Zhu, K. N.; Ye, L. Q.; Li, Z. P. Oxygen Reduction Reaction on a Polypyrrole-Modified, Carbon-Supported Cobalt Hydroxide Catalyst. *Journal of Power Sources* **2012**, *208*, 203–209. https://doi.org/10.1016/j.jpowsour.2012.02.040.

(3) Hjelm, R. M. E.; Lafforgue, C.; Atkinson, R. W.; Garsany, Y.; Stroman, R. O.; Chatenet, M.; Swider-Lyons, K. Impact of the Anode Catalyst Layer Design on the Performance of H2O2-Direct Borohydride Fuel Cells. *J. Electrochem. Soc.* **2019**, *166* (15), F1218. https://doi.org/10.1149/2.0681914jes.

(4) Wang, Z.; Parrondo, J.; He, C.; Sankarasubramanian, S.; Ramani, V. Efficient PH-Gradient-Enabled Microscale Bipolar Interfaces in Direct Borohydride Fuel Cells. *Nature Energy* **2019**, *4* (4), 281–289. https://doi.org/10.1038/s41560-019-0330-5.

(5) Wang, Z.; Sankarasubramanian, S.; Ramani, V. Reactant-Transport Engineering Approach to High-Power Direct Borohydride Fuel Cells. *Cell Reports Physical Science* **2020**, *1* (7), 100084. https://doi.org/10.1016/j.xcrp.2020.100084.

(6) Ko, Y.; Lombardo, L.; Li, M.; Pham, T. H. M.; Yang, H.; Züttel, A. Selective Borohydride Oxidation Reaction on Nickel Catalyst with Anion and Cation Exchange Ionomer for High-Performance Direct Borohydride Fuel Cells. *Advanced Energy Materials* **2022**, *12* (16), 2103539. https://doi.org/10.1002/aenm.202103539.

(7) Liu, B. H.; Li, Z. P.; Arai, K.; Suda, S. Performance Improvement of a Micro Borohydride Fuel Cell Operating at Ambient Conditions. *Electrochimica Acta* **2005**, *50* (18), 3719–3725. https://doi.org/10.1016/j.electacta.2005.01.018.

(8) Lam, V. W. S.; Kannangara, D. C. W.; Alfantazi, A.; Gyenge, E. L. Electrodeposited Osmium Three-Dimensional Anodes for Direct Borohydride Fuel Cells. *Journal of Power Sources* **2012**, *212*, 57–65. https://doi.org/10.1016/j.jpowsour.2012.03.067.

(9) Oshchepkov, A. G.; Braesch, G.; Ould-Amara, S.; Rostamikia, G.; Maranzana, G.; Bonnefont, A.; Papaefthimiou, V.; Janik, M. J.; Chatenet, M.; Savinova, E. R. Nickel Metal Nanoparticles as Anode Electrocatalysts for Highly Efficient Direct Borohydride Fuel Cells. *ACS Catal.* **2019**, 8520–8528. https://doi.org/10.1021/acscatal.9b01616.

(10) Braesch, G.; Oshchepkov, A. G.; Bonnefont, A.; Asonkeng, F.; Maurer, T.; Maranzana, G.; Savinova, E. R.; Chatenet, M. Nickel 3D Structures Enhanced by Electrodeposition of Nickel Nanoparticles as High Performance Anodes for Direct Borohydride Fuel Cells. *ChemElectroChem* **2020**, *7* (7), 1789–1799. https://doi.org/10.1002/celc.202000254.

(11) Braesch, G.; Wang, Z.; Sankarasubramanian, S.; G. Oshchepkov, A.; Bonnefont, A.; R. Savinova, E.; Ramani, V.; Chatenet, M. A High Performance Direct Borohydride Fuel Cell Using Bipolar Interfaces and Noble Metal-Free Ni-Based Anodes. *Journal of Materials Chemistry A* **2020**. https://doi.org/10.1039/D0TA06405J.

(12) Li, S.; Shu, C.; Chen, Y.; Wang, L. A New Application of Nickel-Boron Amorphous Alloy Nanoparticles: Anode-Catalyzed Direct Borohydride Fuel Cell. *Ionics* **2018**, *24* (1), 201–209. https://doi.org/10.1007/s11581-017-2180-0.

(13) Ma, J.; Li, J.; Yang, S.; Lu, H.; Liu, L.; Wang, R. Ultrathin Veil-like SnO2 Supported Co3O4 Nanoparticles for Direct Borohydride Fuel Cell Anode. *Journal of Power Sources* **2020**, *453*, 227866. https://doi.org/10.1016/j.jpowsour.2020.227866.

(14) Chu, W.; He, Y.; Chu, Y. S.; Meng, L.; Liu, J.; Qin, H.; Tao, S. A Highly Stable Cu(OH)2-Poly(Vinyl Alcohol) Nanocomposite Membrane for Dramatically Enhanced Direct Borohydride Fuel Cell Performance. *Journal of Power Sources* **2020**, *467*, 228312. https://doi.org/10.1016/j.jpowsour.2020.228312.

(15) Duan, Y.; Li, S.; Tan, Q.; Chen, Y.; Zou, K.; Dai, X.; Bayati, M.; Xu, B. B.; Dala, L.; Liu, T. X. Cobalt Nickel Boride Nanocomposite as High-Performance Anode Catalyst for Direct Borohydride Fuel Cell. *International Journal of Hydrogen Energy* **2021**, *46* (29), 15471–15481. https://doi.org/10.1016/j.ijhydene.2021.02.064.

Chapter 5 Electrochemical H_2O_2 Production via 2-electron Oxygen Reduction Reaction and Identification of Active Site on Co-N-C

Youngdon Ko[1, 2], Liqun Kang[3], Xiong Zhang[4, 5], Victor Boureau[6], Thi Ha My Pham[1, 2], Cuong Pham-Huu[4], Liping Zhong[1,2*], Andreas Züttel[1,2]

[1] Laboratory of Materials for Renewable Energy (LMER), Institute of Chemical Sciences and Engineering (ISIC), Basic Science Faculty (SB), École Polytechnique Fédérale de Lausanne (EPFL) Valais/Wallis, Energypolis, Rue de l'Industrie 17, 1951 Sion, Switzerland

[2] Empa Materials Science and Technology, 8600 Dübendorf, Switzerland

[3] Department of Inorganic Spectroscopy, Max-Planck-Institute for Chemical Energy Conversion, Stiftstr. 34-36, 45470 Mülheim an der Ruhr, Germany.

[4] Institute of Chemistry and Processes for Energy, Environment and Health (ICPEES), UMR 7515 CNRS-Université de Strasbourg, 25 rue Becquerel, 67087 Strasbourg Cedex 02, France.

[5] CAS Key Laboratory of Science and Technology on Applied Catalysis, Dalian Institute of Chemical Physics, Chinese Academy of Sciences, 116023 Dalian, China.

[6] Interdisciplinary Center for Electron Microscopy, École polytechnique fédérale de Lausanne (EPFL), 1015 Lausanne, Switzerland.

[*]Corresponding author: liping.zhong@epfl.ch

Preprint version: this section will be submitted to the journal.

Edit: caption numbers of figures, tables, and equations were edited to match the thesis chapter number.

Abstract

Electrochemical hydrogen peroxide (H_2O_2) production is demonstrated with cobalt with nitrogen-doped carbon (Co-N-C). The high selectivity of the 2-electron oxygen reduction reaction (ORR) is one of the main requirements for the electrochemical H_2O_2 production catalysts. The atomically dispersed Co with nitrogen bonding is known as a highly selective 2-electron ORR active site. The nanoparticle Co can be formed during the synthesis of atomically dispersed Co active site. In this study, the H_2O_2 production selectivity is compared for atomically dispersed Co and nanoparticle Co. The cation shielding effect is utilized to investigate the identification of active sites on atomically dispersed Co and nanoparticle Co. The small amount of cation in the electrolyte repels the proton ion around the nanoparticle Co and prevents the further reduction of H_2O_2. The cation shielding effect improves the selectivity of H_2O_2 production on a mixture of atomically dispersed Co and nanoparticle Co.

5.1 Introduction

Hydrogen peroxide (H_2O_2) is used in a variety of industry areas, such as bleaching and deodorizing textiles, wood pulp, removal of organic compounds from wastewater, disinfectants, and rocket fuel[1]. The global H_2O_2 market demand is expected to grow continuously due to the increase in paper production and water treatment in the end-user industry.[2] Currently, most of the H_2O_2 is produced by the anthraquinone process, which is a multistep method. It requires significant energy input and generates waste.[3] The electrochemical two-electron oxygen reduction reaction (ORR) produces H_2O_2 on-site and in real time, making it an appealing process for antiseptic and fuel production. The H_2O_2 fuel could be used in space missions and energy conversion devices such as direct

borohydride fuel cells (DBFCs)[4,5]. The DBFC uses H_2O_2 in the catholyte to supply electricity and heat. Through electrochemical reactions, H2O2 usage and production could be accomplished reversibly on-site.

The catalyst for H_2O_2 production via electrochemical reaction could be divided into two groups. The water oxidation reaction and oxygen reduction reaction via $2e^-$ transfer reactions are two different methods that can produce H_2O_2. Both oxidation and reduction reactions compete with $4e^-$ transfer reactions, which are oxygen evolution reaction (OER) and water production via ORR, respectively. Therefore, the selective oxidation or reduction for $2e^-$ is one of the important properties of electrochemical H_2O_2 production catalysts. In this article, we focus on the method for H_2O_2 production via 2-electron ORR. The carbon materials, such as nitrogen-doped graphene, carbon nanotube, Pd with carbon, and transition metal with nitrogen-doped carbon (M-N-C) are used as H_2O_2 production catalysts for 2-electron ORR[6–9]. The ORR has two competing pathways: two-electron transfer for H_2O_2 production and four-electron transfer for H_2O production in acidic and alkaline solutions.[10] High selective 4-electron ORR is required for fuel cell and metal-air battery applications. On the other hand, high 2-electron ORR selectivity and low H_2O_2 decomposition rate are needed on catalysts to produce H_2O_2. For the M-N-C catalysts, using an alkaline electrolyte is preferred for the 4-electron transfer ORR reaction due to its smaller overpotential than an acid electrolyte. Furthermore, the H_2O_2 produced by the 2-electron reaction in an alkaline environment could be reduced further to foam H_2O. In this study, the selectivity of H_2O_2 production is tested under acidic and alkaline conditions. Recently, Wang et al. reported the cation shielding effect of H_2O_2 production at industrially high current densities. The cation shielding effect at the surface of the electrochemical catalysts suppresses the proceeding H_2O formation, which enhances the selectivity of H_2O_2 production on carbon materials such as CNT, rGO, and Zn-N-C.[11] The solvated alkali metal cations could preferentially be attracted to the catalyst/electrolyte interface and squeeze out local protons, suppressing the further reduction to H_2O.

The atomically dispersed metal catalysts known as single metal atom catalysts (SACs) have attracted much attention due to their high catalytic performance and selectivity.[12,13] However, the synthesis method for SACs is tricky, and most of the methods require an additional step to remove unwanted nanoparticles. The atomically dispersed cobalt with nitrogen-doped carbon demonstrated the highest H_2O_2 selectivity among the M-N-C catalysts due to the optimized adsorption energy of the *OOH intermediate by density functional theory (DFT) calculation and experimentally.[14,15] Herein, we could differentiate the active site for H_2O_2 production in Co-SAC and Co nanoparticles with a cation shielding effect. The H_2O_2 production selectivity in the Co-N-C SAC sample is decreased from 60.2% to 43.1% when the cation is added to the acid electrolyte due to the blockage of active sites by the cation charge. The cation shielding effect, on the other hand, increases the H_2O_2 production selectivity in Co SAC and the nanoparticle mixture (Co-N-C mixture sample) from 39.5% to 61.5%.

5.2 Experimental section

5.2.1 Synthesis of Co-N-C catalysts

Co-N-C SAC was prepared through the synthesis method from the previous study.[16] The 2 g of citric acid and 5 g of $(NH_4)_2CO_3$ were dissolved in 25 ml of deionized (D.I.) water. The 1.2 g of silica was added to the solution, and it forms a uniform colloidal suspension. The 3 ml of iron (0.024 g of $FeCl_3$) and zinc precursor (0.2435 g of $ZnCl_2$) mixture solution was added dropwise to the colloidal suspension. The mixture solution was dried in a 110 °C oven after 30 minutes of stirring. The dried solid was crushed into a fine powder and calcined at 900 °C for 2 h in Ar atmosphere. Afterward, the silica was removed with a 2 M NaOH solution at 80 °C for 8 h. The obtained powder was calcined at 900 °C again after washing by centrifugation.

Co-N-C mixture was synthesized by a molecular organic framework (MOF) template carbonization method. The 6.4 g of $Zn(NO_3)\cdot 6H_2O$ and 0.16 g of $CoCl_2$ were mixed in 400 ml D.I. water. The 14.5 g of 2-methylimidazole was

dissolved in 400 ml D.I. water. The two mixture solutions were mixed rapidly and stirred for 2 h. The purple-color colloidal solution was formed, and it was aged 12 h without stirring. After obtaining the precipitant by centrifuging, the purple-colored powder was obtained by freeze drying. The 2 g of powder was mixed with 2 g of silica in 100 ml D.I. water. After drying by freeze drier, the mixed powder was calcined to 700 °C for 5 h and increased temperature to 900 °C in N_2 atmosphere. The silica was then removed using a 2 M NaOH solution at 80 °C for 8 hours, and the powder was dried in a vacuum oven at 80 °C to obtain the Co-N-C mixture sample.

5.2.2 Structural characterization

XRD was measured by Bruker D8 Discover, using copper, a with Cu Kα (λ = 0.1543 nm) radiation (40 kV and 40 mA). The Brunauer–Emmett–Teller (BET) specific surface area of Co-N-C samples was estimated using N_2 adsorption, at 77 K (Microtrac MRB, BELSORP Max II). X-ray photoelectron spectroscopy (XPS) spectra were collected in a Kratos Axis Supra system equipped with a monochromated Al Kα (1486.61 eV) X-ray source. The TEM (Thermo-Scientific Tecnai Osiris) with energy-dispersive X-ray spectroscopy (EDX, Super-X SDD) was used to observe the morphology of the Co-N-C SAC and Co-N-C mixture. The aberration-corrected HAADF-STEM images were obtained by Thermo-Scientific Titan Themis for atomic resolution with 200 kV high tension. The Fe K-edge (7.112 keV) and Co K-edge (7.709 keV) X-ray absorption fine structure (XAFS) of the Fe-N-C and Co-N-C catalysts were collected at the P65 beamline of PETRA III (P65 Applied X-ray Absorption Spectroscopy). For Fe K-edge, monochromatic beam between 6.912 and 8.112 keV was introduced through an 11-periods undulator (1st harmonic) and Si(111) double crystal monochromator (DCM). For Co K-edge, the incident beam energy was adjusted to 7.509 to 8.709 keV from the 3rd harmonic beam though the same Si(111) DCM. The beam size at the sample was approx. 0.5 x 1.0 mm^2 (V x H) and the photon flux was ~10^{11} ph s^{-1} (without attenuation). The XAFS spectra were collected in transmission mode, and the intensity of incident beam (I0) and the transmitted beam (I_t) was monitored by ionisation chambers (filled with mixture of Ar and N_2). The sample powder was sealed into PEEK-made solid powder cells (9 mm diameter) using Kapton tapes and mounted on the transfer rods of a liquid He cryostat for the measurement. The XAFS measurements of the Fe and Co samples were performed under 10 K to reduce the thermal vibration of the chemical bonds (to get smaller Debye-Waller factors), as well as to prevent potential beam damage to the samples. The XAFS of each sample was measured 3 times and merged to improve the signal-noise ratio. Fe foil or Co foils were measured simultaneously for each Fe or Co sample correspondingly as reference for energy calibration. In addition, FeO, Fe_2O_3, CoO and Co_3O_4 powder was pressed into pellets and measured as well for reference. XAFS data was analyzed using xraylarch (version 0.9.65) and in-house developed python scripts. Pre-edge background subtraction, post-edge normalization and forward Fourier Transform of XAFS data were processed by xraylarch. The k^2-weighted wavelet transform EXAFS (WT-EXAFS) was generated using the Cauchy wavelet method (built-in function in xraylarch). The fitting of EXAFS spectra (R range: 1-3.2 Å, k range: 3-14 $Å^{-1}$) was performed using lmfit (built-in function in xraylarch) based on scattering paths generated from FEFF8L. The amplitude reduction factor S02 is determined to be 0.688 and 0.772 for Fe and Co by fitting of k^2-weighted R-space EXAFS of Fe and Co foils based on the standard crystal parameters of iron and cobalt metal (data from Crystal Open Database, COD ID: 9008536 and 9008466). The S_0^2 values were used as fixed parameters for the EXAFS fitting of other Fe and Co samples, respectively.

5.2.3 Electrochemical measurements

The electrochemical performance of the catalysts was carried out by a three-electrode system potentiostat (ALS Model 2325 Bipotentiostat). The RRDE working electrode is connected to the ALS RRDE-3A for controlling the rotation speed. The Pt ring electrode has an outer diameter of 7 mm, an inner diameter of 5 mm; the glassy carbon disk electrode is a 4 mm diameter. The counter and reference electrodes are Pt wire and Ag/AgCl electrodes, respectively. The catalyst ink was prepared by 5 mg catalyst into a mixture of 100 µL isopropyl alcohol

and 300 µL 5 wt.% Nafion dispersion. The catalyst ink was sonicated for 5 min before dropping the ink to the disk electrode. The catalyst loading amounts on the disk electrode were adjusted by dropped catalyst ink volume. The cyclic voltammetry (CV) curves were recorded under the N_2-saturated 0.5 M H_2SO_4 solution. The linear sweep voltammetry (LSV) curves were measured under the O_2-saturated 0.5 M H_2SO_4 and 0.1 M KOH solution. The Pt ring electrode potential is fixed at 1.2 V_{RHE} to measure the anodic current of the H_2O_2 and avoid the O_2 reduction. The cation shielding effects for the Co-N-C catalyst were measured under the O_2-saturated 0.5 M H_2SO_4 with 0.05 M Na_2SO_4 and 0.1 M KOH with 0.05 M Na_2SO_4. The H_2O_2 production selectivity was calculated by the following equations:

$$H_2O_2 \text{ production selectivity: } H_2O_2\ (\%) = 200 \times (\boldsymbol{i_r/N})/(\boldsymbol{i_d} + \boldsymbol{i_r/N})$$

The $\boldsymbol{i_r}$ is the ring current, $\boldsymbol{i_d}$ is the disk current, and $\boldsymbol{N}$ is the current collection efficiency of Pt ring electrode ($\boldsymbol{N}$ = 0.28). The collection efficiency of Pt ring electrode was measured and calculated by the oxidation of ferrocyanide to ferricyanide current in 10 mM potassium ferricyanide in 1 M potassium nitrate solution.[17]

5.3 Results and discussion

5.3.1 Nanoparticle and atomically dispersed cobalt with nitrogen-doped carbon

The atomically dispersed transition metal sites are generally obtained through the pyrolysis of metal-, nitrogen-, and carbon-containing polymeric precursors.[18] Most atomically dispersed M-N-C synthesis results in the formation of nanoparticles. The nanoparticles are leached out with an acidic solution treatment to obtain only atomically dispersed transition metal sites. Atomically dispersed transition metals with nitrogen bonding remain in the structure during acid leaching due to their higher stability under the acidic conditions than nanoparticles. The cobalt single atom catalyst (SAC) detected both Co-N-C SAC and Co-N-C mixture samples, as shown in Figure 5.1. The nanoparticles are only observed in the Co-N-C mixture sample by transmission electron microscopy (TEM), and scanning transmission electron microscopy-energy-dispersive X-ray spectroscopy (STEM-EDX) images (Figure 5.1d-f). On the other hand, Co is detected on both STEM-EDX images (Figure 5.1c and 1f) and the aberration-corrected high angle annular dark field-STEM (HAADF-STEM) images confirmed that both Co-N-C SAC and Co-N-C mixture have atomically dispersed Co (Figure 5.1b, 1e, and S5.1). The structure of cobalt in the Co-N-C SAC and Co-N-C mixture is investigated using X-ray absorption spectroscopy (XAS, Figure 5.2a and 2b). The X-ray absorption near edge structure (XANES) of Co K-edge is shown in Figure 5.2a. The XANES spectra of Co-N-C SAC is highly closed to the CoO reference sample. It means that the Co-N-C SAC has a 2+ valence for the isolated Co atoms. On the other hand, the XANES spectra of the Co-N-C mixture have a similar structure to the Co foil sample. It shows that the Co-N-C mixture have Co nanoparticles in the structure. Even though co-existence of the atomically dispersed Co in the Co-N-C mixture, the nanoparticles dominate Co K-edge XANES spectra that makes hard to check the isolated Co atom existence in the sample. Nevertheless, the AC-STEM images of Co-N-C mixture showed the existence of atomically dispersed Co (Figure 5.1e and S5.1). Fourier transform (FT) extended X-ray absorption fine structure (EXAFS) were carried out to check the bonding of cobalt in Co-N-C SAC and Co-N-C mixture samples (Figure 5.2b). The Co-N-C SAC sample showed prominent peak at about 1.39 Å which corresponded to the scattering interaction between the Co atoms and the nearest shell coordination of the Co-N(O) bond and agreed well with the other literatures.[19,20] The Co-N-C mixture showed the peak at about 2.2 Å which corresponded to the Co-Co bond and matched well with the Co foil sample peak. The wavelet transforms (WT) of the K^3-weighted Co K-edge EXAFS further confirm the above conclusion (Figure S5.2). The WT contour plot of the Co-N-C SAC showed that the Co-N-C SAC mostly have atomically dispersed Co. On the other hand, the Co-N-C mixture mostly has Co nanoparticles in the structure. The EXAFS fitting curves were carried out, and corresponding parameters were summarized in Figure S5.2 and Table S5.1. The X-ray diffraction (XRD) spectra of Co-N-C

SAC and Co-N-C mixture show that the nanoparticles only existed in the Co-N-C mixture samples (Figure 5.2c). A small amount of Co cluster in the Co-N-C SAC, which was detected by XAS, cannot be observed in the XRD spectra.

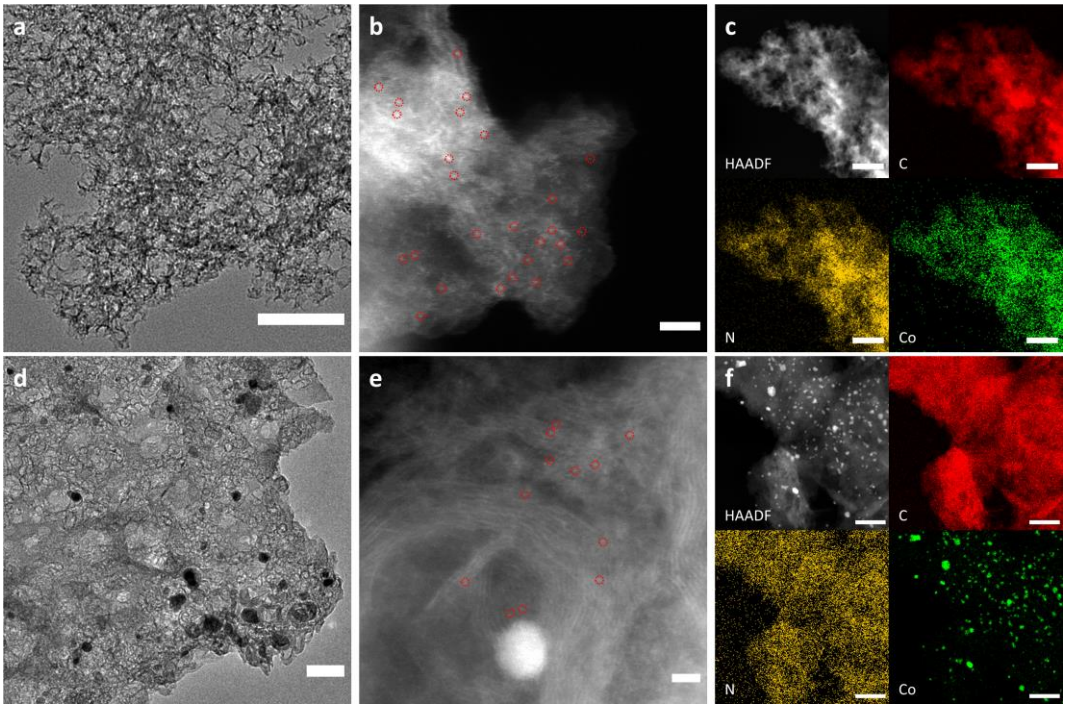

Figure 5.1 Structural characterization for (a-c) Co-N-C SAC and (d-f) Co-N-C mixture. (a, d) TEM images, (b, e) aberration-corrected STEM images (Bright spots assigned to heavier Co atoms within red circles), (c, f) EDS analysis of Co-N-C SAC and Co-N-C mixture, color code: C (red), N (orange), and Co (green). (Scale bar: 100 nm in TEM, 2 nm in AC-STEM, 200 nm in EDS images).

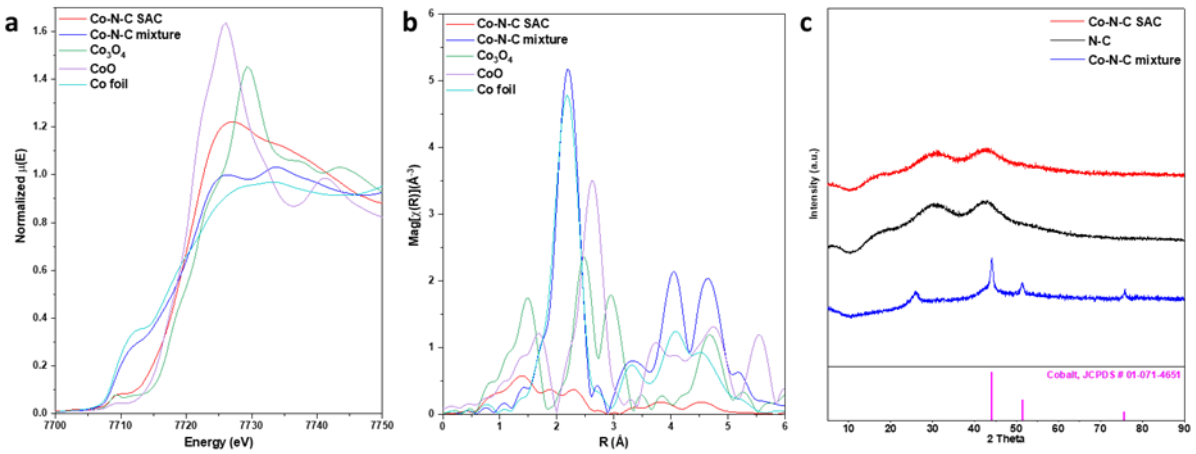

Figure 5.2 (a) Co K-edge XANES spectra and (b) Fourier transformed EXAFS spectra of Co-N-C SAC and Co-N-C mixture samples. (c) XRD patterns of Co-N-C SAC, N-C, and Co-N-C mixture. The cobalt reference (JCPDS #01-071-4651) is indicated at the below.

The electrocatalytic active surface area (ECSA) is calculated based on the capacitance of samples at different scan rates (Figure 5.3). The Co-N-C SAC has a higher ECSA value than the Co-N-C mixture. The high conductivity of Co nanoparticles in the Co-N-C mixture may make a difference in capacitance. The ECSA estimation and comparison method for SAC and nanoparticle-containing carbon materials still needs improvement for future studies. Although comparing each material is difficult, the ECSA value with various loading amounts can be calculated. The capacitance of Co-N-C SAC is increased almost three times (14.2 to 38.6 mF cm^{-2}) when the loading amount increases two times (175 to 350 µg cm^{-2}) as shown in Figure 5.3a. That means the low density of Co-N-C SAC is more deposited on the working electrode and forms the thick catalyst layer. The thick catalyst layer affects the H_2O_2 escape amount and limits the approach of O_2 at the active site. On the other hand, the capacitance of the Co-N-C mixture follows the catalyst loading amount (175 to 350 µg cm^{-2}, 3.5 to 6.6 mF cm^{-2}) which has a lower ECSA value than the Co-N-C SAC (Figure 5.3b). The catalyst deposition amounts are optimized with capacitance and H_2O_2 production selectivity afterward, with an electrochemical activity test.

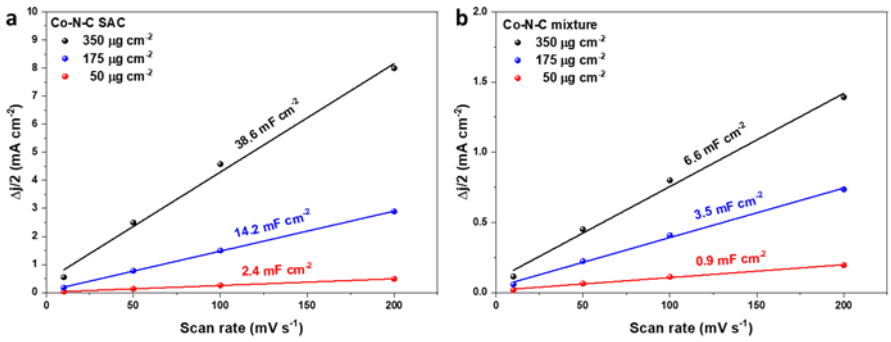

Figure 5.3 Charge currents of (a) Co-N-C SAC and (b) Co-N-C mixture plotted as a function scan rate.

5.3.2 Electrocatalytic peroxide production using Co-N-C via 2e-ORR

The catalytic activity of the Co-N-C SAC and Co-N-C mixture for H_2O_2 production is measured with different catalyst loading amounts in acidic and alkaline conditions (Figure 5.4). The rotating ring disk electrode (RRDE) is used for calculating the selectivity of ORR ($2e^-$ or $4e^-$). The 0.5 M H_2SO_4 and 0.1 M KOH electrolytes are used for acidic and alkaline conditions. The ORR activity of Co-N-C materials varies significantly with electrolyte conditions. The linear sweep voltammetry (LSV) curves for Co-N-C SAC and Co-N-C mixture with three different catalyst amounts (50, 175, and 350 µg cm^{-2}) are shown in Figure 5.4a-d, in which the disk electrode detected the oxygen reduction currents while the Pt ring electrode monitored the yield of H_2O_2. The Pt ring electrode potential is fixed at 1.2 V versus a reversible hydrogen electrode (RHE) to avoid the ORR current and only detect the H_2O_2 oxidation current. Due to different ORR mechanisms in acidic and alkaline conditions, the ORR onset potential at the disk electrode begins earlier in both Co-N-C SAC and Co-N-C mixture catalysts in 0.1 M KOH solution than in 0.5 M H_2SO_4 solution. In addition, the onset potential of Co-N-C SAC at the disk electrode started earlier on high catalyst loading case, 0.86 V and 0.98 V for 350 µg cm^{-2} in 0.5 M H_2SO_4 and 0.1 M KOH solution, respectively (Figure 5.4a and b). The high-loading catalyst (350 µg cm^{-2}) has the most positive onset potential and highest ORR current density of -3.84 mA cm^{-2} and -3.05 mA cm^{-2} on Co-N-C SAC and Co-N-C mixture in 0.5 M H_2SO_4 at 0.2 V_{RHE}, respectively (Figure 5.4a and c). However, the H_2O_2 escaped amount from the electrode is less than two catalyst loading amounts (175 and 50 µg cm^{-2}). It may be the produced H_2O_2 was further reduced to H_2O during escaping the thick disk electrode. The different phenomena occurred on high loading catalyst in 0.1 M KOH solution, the most positive onset potential is shown on 350 µg cm^{-2}, while the highest ORR current density is shown on 175 µg cm^{-2} of -3.96 mA cm^{-2} and -3.84 mA cm^{-2} on Co-N-C SAC and Co-N-C mixture in 0.1 M KOH at 0.2 V_{RHE}, respectively (Figure 5.4b and d). The low overpotential for the ORR at the alkaline condition makes H_2O_2 production less selective compared to the acidic condition. In alkaline condition, the ORR can more easily proceed to direct 4-

electron reduction or continuous 2+2-electron reduction. Although low overpotential exist in alkaline electrolytes, the thick catalyst layer on the disk electrode reduces the O_2 transport to the catalyst, resulting in the low ORR current density in 350 μg cm^{-2} loading. In addition, the H_2O_2 oxidation current (Pt ring electrode) at high catalyst loading shows that a higher amount of H_2O_2 is further to H_2O before escaping the disk electrode in an alkaline electrolyte than an acid electrolyte due to the low overpotential. The H_2O_2 production selectivity in acid and alkaline electrolytes is summarized in Figure 5.4e and f. The H_2O_2 production selectivity is highest at the 50 μg cm^{-2} loading in both acidic and alkaline conditions. It is highly correlated with the H_2O_2 escape amount from the catalyst layer at the disk electrode. The low catalyst loading (50 μg cm^{-2}) has a thin catalyst layer on the disk electrode, so most of the H_2O_2 escaped the disk and reached the Pt ring electrode. It is also worth noting that the onset potential of disk and ring electrodes begins more similarly at 50 μg cm^{-2} loading than 175 and 350 μg cm^{-2} loading samples. However, the low catalyst loading causes a low current density and high overpotential for ORR. Thus, the catalyst loading is optimized to 175 μg cm^{-2} for further study. The H_2O_2 production selectivity is higher at the Co-N-C SAC than the Co-N-C mixture due to the intrinsically high activity of 2e-ORR at single atom Co active sites. On the other hand, the low H_2O_2 production selectivity of the Co-N-C mixture is attributed to the activity of H_2O_2 reduction on nanoparticle Co. The H_2O_2 production selectivity in alkaline solution is decreased at high loading catalyst amount, as the same reason for the acid condition. The H_2O_2 production selectivity on Co-N-C SAC is even lower than the Co-N-C mixture. The single atom Co active site seems less selective for H_2O_2 production in alkaline solution than in acid solution.

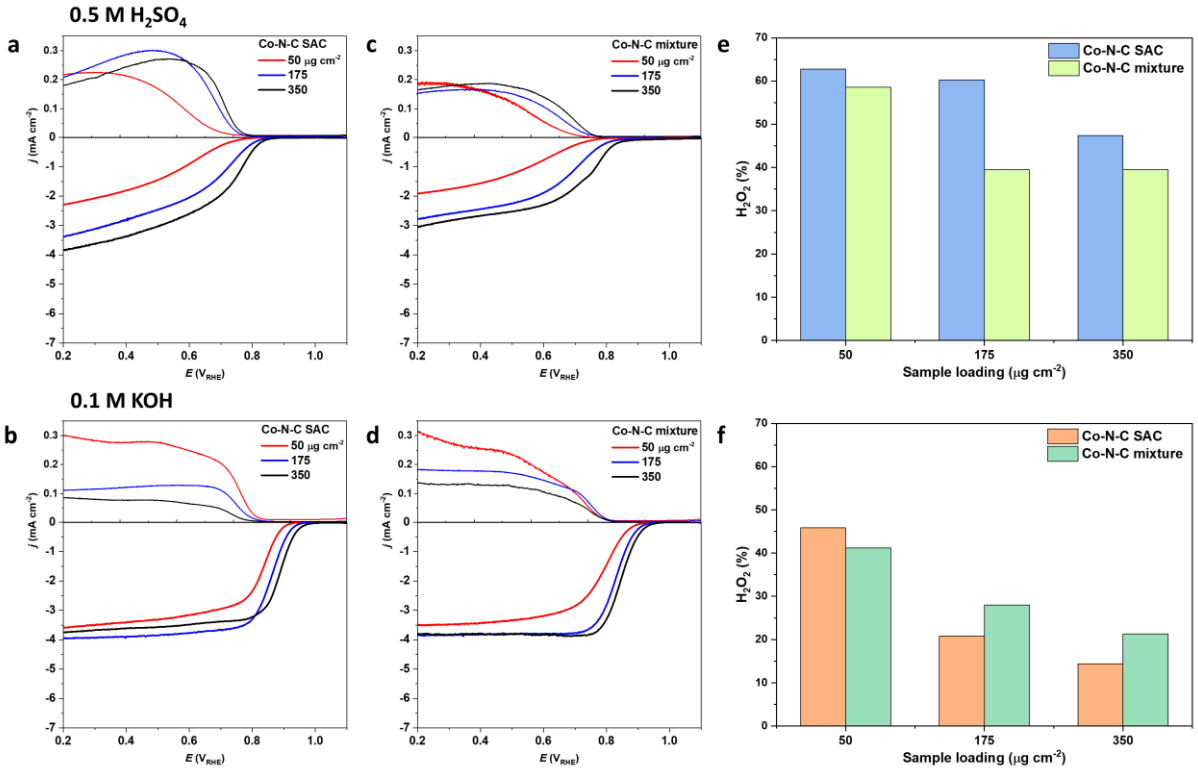

Figure 5.4 ORR performance of Co-N-C SAC and Co-N-C mixture tested via RRDE. (a, b) LSV of Co-N-C SAC and (c, d) Co-N-C mixture depends on the sample loading (50, 175, and 350 μg cm^{-2}) on glassy carbon working electrode in 0.5 M H_2SO_4 and 0.1 M KOH electrolyte at 1600 rpm and 10 mV s^{-1}, with the Pt ring electrode at a fixed potential of 1.2 V_{RHE}. (e) H_2O_2 production selectivity of Co-N-C SAC and Co-N-C mixture in 0.5 M H_2SO_4 and (f) 0.1 M KOH solution.

5.3.3 Cation shielding effect of oxygen reduction reaction selectivity on Co-N-C

The cation shielding effect is reported to obtain selective H_2O_2 production by Wang et al.[11] The small amount of cation in the electrolyte changes the H_2O_2 production selectivity due to the limited H^+ ion at the active site that inhibits further H_2O_2 reduction to H_2O. In our study, the cation shielding effect is used for the active site identification of single atoms and nanoparticles of Co. The H_2O_2 production selectivity is measured on pure electrolytes (0.5 M H_2SO_4 and 0.1 M KOH) and with Na_2SO_4 to observe the cation shielding effect (Figure 5.5). The H_2O_2 production selectivity is highly acquired Co-N-C SAC than Co-N-C mixture in 0.5 M H_2SO_4 solution. However, adding 0.05 M Na_2SO_4 to the 0.5 M H_2SO_4 solution reduces H_2O_2 selectivity on Co-N-C SAC (60.2 to 43.1%). On the other hand, the H_2O_2 selectivity on the Co-N-C mixture is enhanced with 0.05 M Na_2SO_4 in 0.5 M H_2SO_4 (39.5 to 61.5%). The RRDE polarization curves of Co-N-C SAC and Co-N-C mixture with and without cation addition are shown in Figure S5.3. These phenomena are explained by the different active sites on Co-N-C SAC and Co-N-C mixture. The cation shielding effect on Co-N-C SAC and Co-N-C mixture is described by the schematic illustration in Figure 5.6. The 0.5 M H_2SO_4 electrolyte is represented in Figure 5.6a and the 0.5 M H_2SO_4 with 0.05 M Na_2SO_4 electrolyte is represented in Figure 5.6b. The Co-N-C SAC sample is illustrated on the left, and the right one is for the Co-N-C mixture illustration. The Co-SAC active sites are intrinsically selective for 2e-ORR but Co nanoparticles are active on H_2O_2 reduction to produce H_2O shown in Figure 5.6a. The H_2O_2 production selectivity in alkaline electrolytes also shows that the cation shielding effect can be used for the identification of active sites on Co-N-C SAC and Co-N-C mixture (Figure 5.6b). Although the H_2O_2 production selectivity is higher in the Co-N-C mixture in 0.1 M KOH, which is the difference in 0.5 M H_2SO_4, the H_2O_2 selectivity enhancement is observed in the Co-N-C mixture by the cation shielding effect. The low H_2O_2 production selectivity in Co-N-C SAC in 0.1 M KOH originated from the less selective H_2O_2 production than acid electrolytes in Co-SAC, as explained earlier.

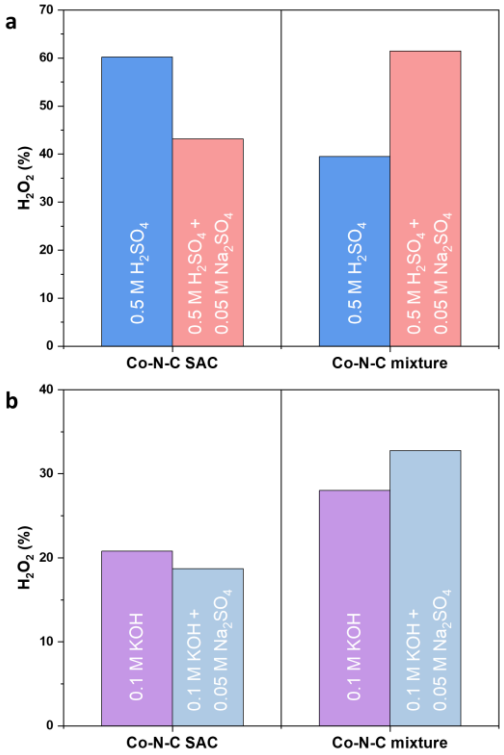

Figure 5.5 The cation shielding effects on H_2O_2 molar fraction selectivity of Co-N-C SAC and Co-N-C mixture in (a) 0.5 M H_2SO_4 and 0.5 M H_2SO_4 + 0.05 M Na_2SO_4, (b) 0.1 M KOH and 0.1 M KOH + 0.05 M Na_2SO_4 electrolytes.

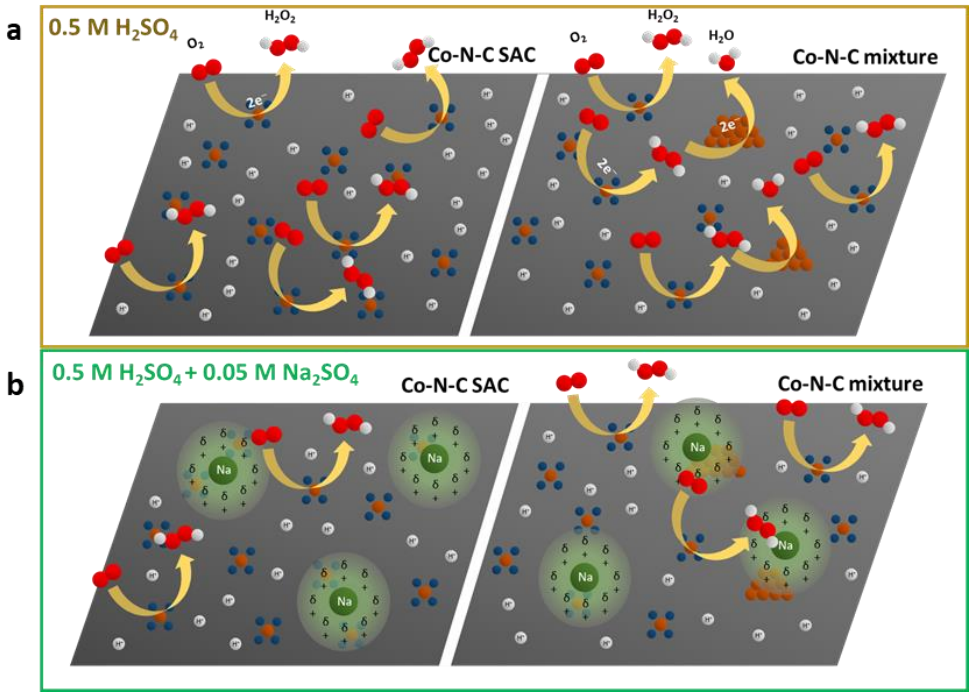

Figure 5.6 Schematic illustration of cation shielding effects on Co-N-C SAC and Co-N-C mixture, which affects the selectivity of H_2O_2 production. Surrounding charge of Na^+ ion repulse H^+ ion and screen the active site of Co-N_x and Co nanoparticles. The Co-N-C SAC and Co-N-C mixture are described on left and on right black sheet, (a) 0.5 M H_2SO_4 and (b) 0.5 M H_2SO_4 with 0.05 M Na_2SO_4 electrolyte.

5.4 Conclusions

The electrochemical H_2O_2 production via 2-electrons ORR is demonstrated with Co-N-C based electrocatalysts. High-selective H_2O_2 production can be obtained in the acidic electrolyte with Co-N-C catalysts. The catalyst loading amounts are optimized based on the H_2O_2 escape amount from the disk electrode by the H_2O_2 oxidation current at the ring electrode. Also, the onset potential and current density of ORR are considered to select the catalyst loading amount. The low overpotential of 4-electron ORR activity on Co-N-C materials in alkaline electrolytes causes the low selectivity of H_2O_2 production. In addition, the different role of the active site on Co SAC and nanoparticle is revealed with the cation shielding effect. The intrinsically high selectivity for H_2O_2 production occurs on the Co SAC active site, while the Co nanoparticle has H_2O_2 reduction activity, which decreases the H_2O_2 production selectivity. The selectivity of H_2O_2 production is enhanced with a small amount of cation in the electrolyte. The cation charge repels the proton ion at the active site of the Co nanoparticle which inhibits further H_2O_2 reduction to H_2O. On the other hand, the selectivity of H_2O_2 production is decreased at the active site of the Co SAC due to the blockage of the active site by the cation charge.

References

(1) Kim, H. W.; Ross, M. B.; Kornienko, N.; Zhang, L.; Guo, J.; Yang, P.; McCloskey, B. D. Efficient Hydrogen Peroxide Generation Using Reduced Graphene Oxide-Based Oxygen Reduction Electrocatalysts. *Nat Catal* **2018**, *1* (4), 282–290. https://doi.org/10.1038/s41929-018-0044-2.

(2) *Hydrogen Peroxide Market Expected to Reach $6.2 Billion by 2026*. Global Market Insights Inc. https://www.gminsights.com/pressrelease/hydrogen-peroxide-market (accessed 2022-09-06).

(3) Campos-Martin, J. M.; Blanco-Brieva, G.; Fierro, J. L. G. Hydrogen Peroxide Synthesis: An Outlook beyond the Anthraquinone Process. *Angewandte Chemie International Edition* **2006**, *45* (42), 6962–6984. https://doi.org/10.1002/anie.200503779.

(4) Ko, Y.; Lombardo, L.; Li, M.; Pham, T. H. M.; Yang, H.; Züttel, A. Selective Borohydride Oxidation Reaction on Nickel Catalyst with Anion and Cation Exchange Ionomer for High-Performance Direct Borohydride Fuel Cells. *Advanced Energy Materials* **2022**, *12* (16), 2103539. https://doi.org/10.1002/aenm.202103539.

(5) Wang, Z.; Parrondo, J.; He, C.; Sankarasubramanian, S.; Ramani, V. Efficient PH-Gradient-Enabled Microscale Bipolar Interfaces in Direct Borohydride Fuel Cells. *Nature Energy* **2019**, *4* (4), 281–289. https://doi.org/10.1038/s41560-019-0330-5.

(6) Kim, H. W.; Bukas, V. J.; Park, H.; Park, S.; Diederichsen, K. M.; Lim, J.; Cho, Y. H.; Kim, J.; Kim, W.; Han, T. H.; Voss, J.; Luntz, A. C.; McCloskey, B. D. Mechanisms of Two-Electron and Four-Electron Electrochemical Oxygen Reduction Reactions at Nitrogen-Doped Reduced Graphene Oxide. *ACS Catal.* **2020**, *10* (1), 852–863. https://doi.org/10.1021/acscatal.9b04106.

(7) Jiang, K.; Back, S.; Akey, A. J.; Xia, C.; Hu, Y.; Liang, W.; Schaak, D.; Stavitski, E.; Nørskov, J. K.; Siahrostami, S.; Wang, H. Highly Selective Oxygen Reduction to Hydrogen Peroxide on Transition Metal Single Atom Coordination. *Nat Commun* **2019**, *10* (1), 3997. https://doi.org/10.1038/s41467-019-11992-2.

(8) Jung, E.; Shin, H.; Lee, B.-H.; Efremov, V.; Lee, S.; Lee, H. S.; Kim, J.; Hooch Antink, W.; Park, S.; Lee, K.-S.; Cho, S.-P.; Yoo, J. S.; Sung, Y.-E.; Hyeon, T. Atomic-Level Tuning of Co–N–C Catalyst for High-Performance Electrochemical H2O2 Production. *Nat. Mater.* **2020**, *19* (4), 436–442. https://doi.org/10.1038/s41563-019-0571-5.

(9) Zhang, B.-W.; Zheng, T.; Wang, Y.-X.; Du, Y.; Chu, S.-Q.; Xia, Z.; Amal, R.; Dou, S.-X.; Dai, L. Highly Efficient and Selective Electrocatalytic Hydrogen Peroxide Production on Co-O-C Active Centers on Graphene Oxide. *Commun Chem* **2022**, *5* (1), 1–7. https://doi.org/10.1038/s42004-022-00645-z.

(10) Ge, X.; Sumboja, A.; Wuu, D.; An, T.; Li, B.; Goh, F. W. T.; Hor, T. S. A.; Zong, Y.; Liu, Z. Oxygen Reduction in Alkaline Media: From Mechanisms to Recent Advances of Catalysts. *ACS Catal.* **2015**, *5* (8), 4643–4667. https://doi.org/10.1021/acscatal.5b00524.

(11) Zhang, X.; Zhao, X.; Zhu, P.; Adler, Z.; Wu, Z.-Y.; Liu, Y.; Wang, H. Electrochemical Oxygen Reduction to Hydrogen Peroxide at Practical Rates in Strong Acidic Media. *Nat Commun* **2022**, *13* (1), 2880. https://doi.org/10.1038/s41467-022-30337-0.

(12) He, Y.; Wu, G. PGM-Free Oxygen-Reduction Catalyst Development for Proton-Exchange Membrane Fuel Cells: Challenges, Solutions, and Promises. *Acc. Mater. Res.* **2022**, *3* (2), 224–236. https://doi.org/10.1021/accountsmr.1c00226.

(13) He, Y.; Guo, H.; Hwang, S.; Yang, X.; He, Z.; Braaten, J.; Karakalos, S.; Shan, W.; Wang, M.; Zhou, H.; Feng, Z.; More, K. L.; Wang, G.; Su, D.; Cullen, D. A.; Fei, L.; Litster, S.; Wu, G. Single Cobalt Sites Dispersed in Hierarchically Porous Nanofiber Networks for Durable and High-Power PGM-Free Cathodes in Fuel Cells. *Advanced Materials* **2020**, *32* (46), 2003577. https://doi.org/10.1002/adma.202003577.

(14) Sun, Y.; Silvioli, L.; Sahraie, N. R.; Ju, W.; Li, J.; Zitolo, A.; Li, S.; Bagger, A.; Arnarson, L.; Wang, X.; Moeller, T.; Bernsmeier, D.; Rossmeisl, J.; Jaouen, F.; Strasser, P. Activity–Selectivity Trends in the Electrochemical Production of Hydrogen Peroxide over Single-Site Metal–Nitrogen–Carbon Catalysts. *J. Am. Chem. Soc.* **2019**, *141* (31), 12372–12381. https://doi.org/10.1021/jacs.9b05576.

(15) Yang, X.; Zeng, Y.; Alnoush, W.; Hou, Y.; Higgins, D.; Wu, G. Tuning Two-Electron Oxygen-Reduction Pathways for H2O2 Electrosynthesis via Engineering Atomically Dispersed Single Metal Site Catalysts. *Advanced Materials* **2022**, *34* (23), 2107954. https://doi.org/10.1002/adma.202107954.

(16) Zhang, X.; Truong-Phuoc, L.; Liao, X.; Papaefthimiou, V.; Pugliesi, M.; Tuci, G.; Giambastiani, G.; Pronkin, S.; Pham-Huu, C. Inducing Atomically Dispersed Cl–FeN 4 Sites for ORRs in the SiO 2 -Mediated Synthesis of Highly Mesoporous N-Enriched C-Networks. *Journal of Materials Chemistry A* **2022**, *10* (11), 6153–6164. https://doi.org/10.1039/D1TA09519F.

(17) Paulus, U. A.; Schmidt, T. J.; Gasteiger, H. A.; Behm, R. J. Oxygen Reduction on a High-Surface Area Pt/Vulcan Carbon Catalyst: A Thin-Film Rotating Ring-Disk Electrode Study. *Journal of Electroanalytical Chemistry* **2001**, *495* (2), 134–145. https://doi.org/10.1016/S0022-0728(00)00407-1.

(18) Fei, H.; Dong, J.; Feng, Y.; Allen, C. S.; Wan, C.; Volosskiy, B.; Li, M.; Zhao, Z.; Wang, Y.; Sun, H.; An, P.; Chen, W.; Guo, Z.; Lee, C.; Chen, D.; Shakir, I.; Liu, M.; Hu, T.; Li, Y.; Kirkland, A. I.; Duan, X.; Huang, Y. General Synthesis and Definitive Structural Identification of MN4C4 Single-Atom Catalysts with Tunable Electrocatalytic Activities. *Nat Catal* **2018**, *1* (1), 63–72. https://doi.org/10.1038/s41929-017-0008-y.

(19) Rong, C.; Shen, X.; Wang, Y.; Thomsen, L.; Zhao, T.; Li, Y.; Lu, X.; Amal, R.; Zhao, C. Electronic Structure Engineering of Single-Atom Ru Sites via Co–N4 Sites for Bifunctional PH-Universal Water Splitting. *Advanced Materials* **2022**, *34* (21), 2110103. https://doi.org/10.1002/adma.202110103.

(20) Wang, K.; Liu, J.; Tang, Z.; Li, L.; Wang, Z.; Zubair, M.; Ciucci, F.; Thomsen, L.; Wright, J.; M. Bedford, N. Establishing Structure/Property Relationships in Atomically Dispersed Co–Fe Dual Site M–N x Catalysts on Microporous Carbon for the Oxygen Reduction Reaction. *Journal of Materials Chemistry A* **2021**, *9* (22), 13044–13055. https://doi.org/10.1039/D1TA02925H.

Supporting information

The oxygen reduction reaction (ORR) pathway under acid and alkaline condition

In acid solution, the two-electron and four-electron transfer pathway are shown in Reaction 1 and 2.

$$O_2 + 2H^+ + 2e^- \rightarrow H_2O_2 \qquad E° = 1.776\ V \qquad (1)$$

$$O_2 + 4H^+ + 4e^- \rightarrow H_2O \qquad E° = 1.229\ V \qquad (2)$$

In alkaline solution, the two-electron and four-electron transfer pathway are shown in Reaction 3 and 4.

$$O_2 + H_2O + 2e^- \rightarrow HO_2^- + OH^- \qquad E° = -0.076\ V \qquad (3)$$

$$O_2 + 2H_2O + 4e^- \rightarrow 4OH^- \qquad E° = 0.401\ V \qquad (4)$$

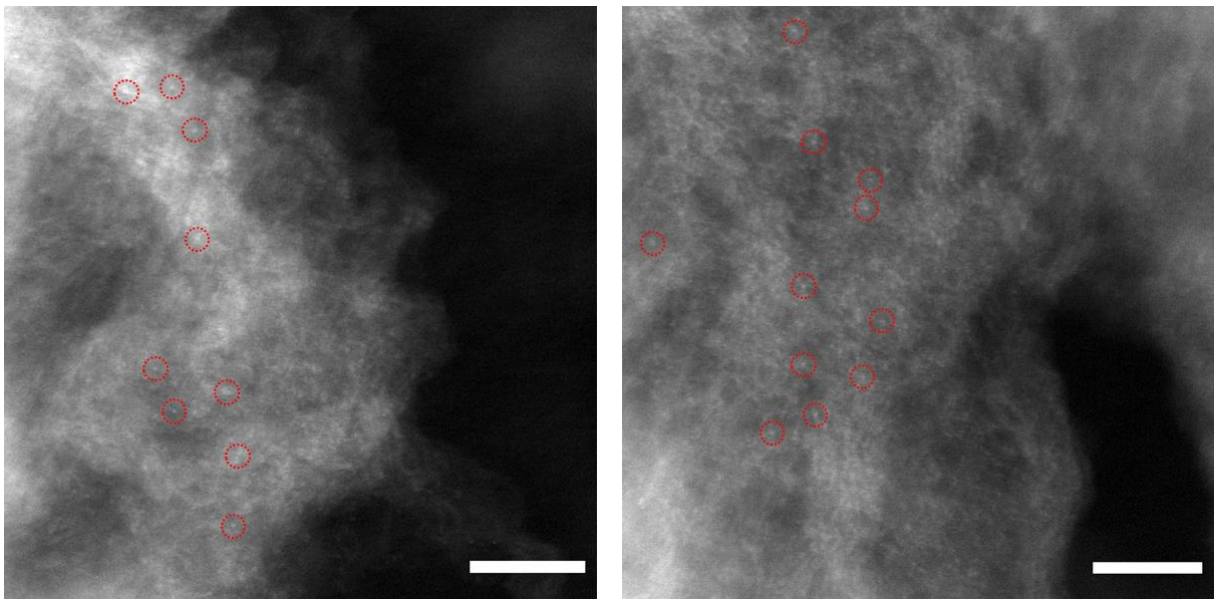

Figure S5.1 Aberration-corrected STEM images of Co-N-C mixture, the region without nanoparticle existence (Bright spots assigned to heavier Co atoms within red circles, scale bar: 5 nm).

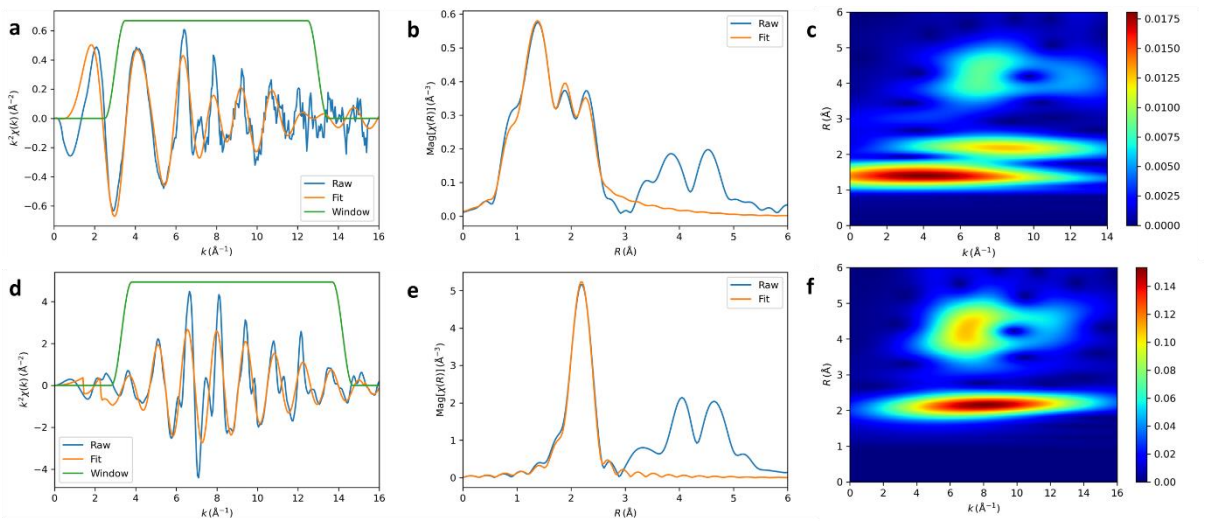

Figure S5.2 EXAFS fitting in *k* and R space on (a, b) Co-N-C SAC and (d, e) Co-N-C mixture. Wavelet transforms (WT) plot of (c) Co-N-C SAC and (f) Co-N-C mixture. The maxima at approximately 4 and 8 Å^{-1} are associated with the Fe-N(O) and Fe-Fe contribution, respectively.

Table S5.1 Structural data from the fitting of Co K-edge EXAFS signal in Co-N-C catalysts.

Sample	Path	S_0^2 (amp)	C.N.	R [Å]	R_{ref} [Å]	σ^2	ΔE_0 [eV]	R-factor
Co-N-C SAC (10K)	Co-C/N/O	0.772 (fixed)	1.82 ± 0.35	1.889 ± 0.015	1.900	0.0034 ± 0.0002	-1.9 ± 1.6	0.0112
	Co-C/N/O		1.35 ± 0.20	2.075 ± 0.024	2.080	0.0034 ± 0.0002		
	Co-Co		0.74 ± 0.20	2.075 ± 0.009	2.509	0.0023 ± 0.0017		
Co-N-C mixture (10K)	Co-O		0.55 ± 0.05	2.133 (fixed)	2.133	0.0036 ± 0.0005	7.4 ± 0.8	0.0068
	Co-Co		6.86 ± 0.38	2.705 ± 0.002	2.689	0.0046 ± 0.0003		

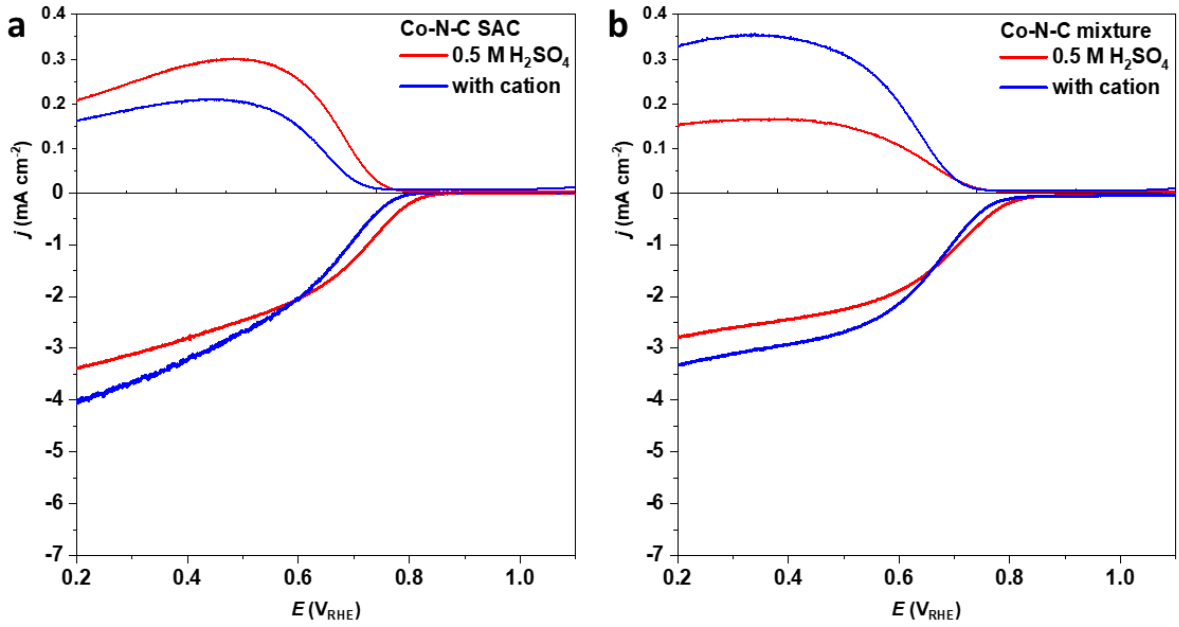

Figure S5.3 Steady-state RRDE polarization curves of (a) Co-N-C SAC and (b) Co-N-C mixture recorded in O_2-saturated 0.5 M H_2SO_4 and O_2-saturated 0.5 M H_2SO_4 with 0.05 M Na_2SO_4 at a scan rate of 10 mV s^{-1} and a rotating electrode speed of 1600 rpm. Ring potential fixed on 1.2 V_{RHE}.

Chapter 6 Conclusions and Perspectives

6.1 Achieved results

In this thesis, I investigated the complex hydride for hydrogen storage and direct borohydride fuel cells (DBFCs) for electricity production.

(1) lowering the hydrogen release temperature and preventing material expansion on alanate complex hydrides by incorporating nickel with porous carbon sheets.
(2) replacement of palladium catalyst at the DBFC anode with a readily synthesized nickel catalyst.
(3) replacement of platinum catalyst with nitrogen-doped carbon (M-N-C) materials for atomically dispersed transition metal and evaluation of durability.
(4) Production of H_2O_2 via the 2-electron oxygen reduction reaction (ORR) and identification of the active site of atomically dispersed and nanoparticle cobalt.

First, a material-based hydrogen storage method is implemented. The complex hydride has a high gravimetric hydrogen density and covalent and ionic bonds in its structure. Hydrogen could be extracted from complex hydrides via hydrolysis and decomposition. In Chapter 2, the decomposition properties of complex hydrides were investigated. The introduction of nickel catalyst to aluminum-based complex hydrides decreased the temperature of hydrogen release. In addition, porous carbon sheets play a role in complex hydrides. It could prevent expansion when hydrogen was released from complex hydride, thereby creating a pathway for hydrogen release.

The nickel catalyst for the DBFC anode was synthesized using a simple, direct method on nickel foam. The nickel catalyst can replace costly palladium catalysts with its superior selectivity and fuel utilization. Multiple anode reactions are evaluated in both half-cell and DBFC arrangements. Two kinds of ionomer were utilized: anion-exchange ionomer (AEI) and cation-exchange ionomer (CEI). The ionomer type generates either a high (AEI) or low (CEI) local pH at the active site of the catalyst in a DBFC configuration, resulting in distinct catalytic reaction on Ni and Pd. Good performance is determined by the selective catalytic activities for the borohydride oxidation reaction (BOR) and the hydrogen oxidation reaction (HOR). In addition, measurements of fuel consumption and H_2 evolution in a DBFC configuration provide additional information regarding the complex anode reaction in DBFC.

In DBFC, the PGM-based catalysts are subsequently replaced entirely with transition metal catalysts. M-N-C materials are utilized for the hydrogen peroxide reduction reaction (PRR) in the DBFC cathode. Using half-cell and DBFC configurations, the PRR activity and durability of M-N-C are evaluated. Fe-N-C has greater PRR activity than Co-N-C. Co-N-C is however more stable than Fe-N-C under DBFC operating conditions. To observe M-N-C degradation, post-mortem XPS and Raman spectroscopy measurements are conducted. In addition, the density functional theory (DFT) calculation solidifies the catholyte's Co-N-C stability compared to the Fe-N-C. In the DBFC durability test, Fe-N-C demonstrates a performance loss of 18.6% after an accelerated durability test, whereas Co-N-C demonstrates a more stable performance loss of 6.5%.

The Co-N-C catalysts demonstrate the electrochemical production of hydrogen peroxide through 2-electron ORR. Utilization and production of H_2O_2 could be accomplished reversibly on-site via electrochemical reactions.

High selective H_2O_2 production is a characteristic of the atomically dispersed CoN_4 site. In acidic and alkaline electrolytes, the H_2O_2 production activity of nanoparticle Co and atomically dispersed Co is compared. A small quantity of cation can affect the selectivity of H_2O_2 production and distinguish between the active sites on nanoparticle Co and atomically dispersed Co. The cation shielding effect increases the selectivity of H_2O_2 production on Co nanoparticles while blocking the active site of atomically dispersed Co.

6.2 Perspectives

When the hydrogen economy is fully integrated into our daily lives, more attention will be paid to hydrogen storage and utilization technology. Hydrogen production and utilization could be decentralized in the future energy system. The hydrogen storage methods require a breakthrough in terms of safety and inexpensive long-term storage. In addition, the hydrogen will be utilized with a variety of energy conversion devices. For the future development of the topic of DBFC, additional research can be conducted on other aspects for the system's high performance, sustainability, and durability.

6.2.1 Durable and ion selective membrane for DBFC

The liquid-based DBFC is a system with a large pH gradient between the anode and cathode. The sodium borohydride is only stable at high pH levels, while hydrogen peroxide is only stable at low pH levels. Consequently, the significance of membrane in the DBFC system cannot be disputed. By observing the increase in ohmic resistance, membrane and ionomer degradation can be noticed during operation. Hydrogen peroxide in the system severely degrades the membrane. Addition of a radical scavenger to the membrane and cathode electrode, it may be possible to control the hydrogen peroxide-induced radical. The radical scavenger has been incorporated to the PEMFC system to increase the durability of the ionomer and membrane.[1,2] The CeO_2 acts as a radical scavenger, and the structure's oxygen vacancy is the site of the reaction. CeO_2 could be used as a supporting material for Pt in the DBFC system, resulting in a more durable DBFC system.

In the DBFC system, ion transport through the membrane and charge carrier remain to discover. The sodium ion migration during operation is revealed by the ICP measurements at the cathode electrolyte outlet. The transformation of the anode electrolyte from sodium hydroxide to potassium hydroxide decreases the performance of the DBFC in regions of high current density. The difference in transport rates between potassium and sodium ions may be the main reason. It appears that the sodium ion ion transport rate is lower than that of the potassium ion, which does not hamper proton ion transport in the membrane. Graphene oxide layer coating could be applied to improve DBFC performance for selective proton ion transport to the cathode side. Our preliminary tests indicate that coating the anode side of the membrane with graphene oxide improves performance by approximately 15%. The improvement in DBFC performance has not yet been conclusively linked to selective ion transport in the membrane, but it appears to be closely associated with this phenomenon.

6.2.2 Regeneration of sodium borohydride for sustainable system

The DBFC uses sodium borohydride as a fuel at the anode, which is then converted to sodium metaborate. The cost and extreme conditions of sodium borohydride regeneration raised questions on its eco-friendly regeneration for a sustainable economy. Several papers have been published on the mechanochemical transformation of sodium metaborate to sodium borohydride using magnesium and aluminum metals.[3–6] The energy efficiency of sodium borohydride hydrolysis and regeneration were investigated.[7] The energy input to regenerate sodium borohydride is used to produce hydrogen, vaporize ethylenediamine, and regenerate magnesium. According to the calculation, the maximum energy efficiency is 49.91%, which could be increased by recycling the heat released by the exothermic reaction. For a greener and decentralized system, the removal of metal after regenera-

tion with solvent vaporization process should be avoided. A decentralized system may necessitate the electrochemical regeneration of sodium borohydride. The electrochemical regeneration of sodium borohydride using platinum and lithium electrodes are reported from the report.[8] The electrochemical regeneration of sodium borohydride is an intriguing future research topic.

6.2.3 Utilization of hydrogen and oxygen from the DBFC outlet

The integration of a gas-fed fuel cell next to the DBFC system is required. Due to side reactions, hydrogen evolution and oxygen evolution occur unintentionally in the DBFC system. On each electrode, the decomposition of borohydride and hydrogen peroxide produces hydrogen and oxygen. With the utilization of hydrogen and oxygen from the DBFC outlet, it is possible to increase the efficiency of chemical energy conversion. The modeling of hydrogen and oxygen evolution kinetics is necessary for fuel cell system operation.

6.2.4 Increasement of active site density in M-N-C catalysts

In Chapter 5, the M-N-C catalysts for the hydrogen peroxide reduction catalyst in DBFC cathode are investigated. All PGM-free DBFCs were unable to match the performance of DBFCs with Pt catalyst. The low density of active sites may be the main reason for the low DBFC performance of the M-N-C catalyst. The M-N-C catalyst contains significantly less metal than Pt-based catalysts because the atomically dispersed metal sites are extremely limited. In order to provide more active sites, the M-N-C cathode electrode is thicker than the Pt cathode electrode. One difference between PEMFC and DBFC is the presence of protons in the cathode electrode. Proton transport through the membrane and ionomer to the cathode active site is essential for PEMFCs.[9] Due to the presence of sulfuric acid, a large quantity of proton ion already exists in catholyte. Therefore, proton ion transfer may not be the limiting factor in the case of DBFC. Different electrode support structures, such as materials with a high porosity, could be one of the solutions for a PGM-free, high-performance DBFC system.

References

(1) Rui, Z.; Liu, J. Understanding of Free Radical Scavengers Used in Highly Durable Proton Exchange Membranes. *Progress in Natural Science: Materials International* **2020**, *30* (6), 732–742. https://doi.org/10.1016/j.pnsc.2020.08.013.

(2) Xie, H.; Xie, X.; Hu, G.; Prabhakaran, V.; Saha, S.; Gonzalez-Lopez, L.; Phakatkar, A. H.; Hong, M.; Wu, M.; Shahbazian-Yassar, R.; Ramani, V.; Al-Sheikhly, M. I.; Jiang, D.; Shao, Y.; Hu, L. Ta–TiOx Nanoparticles as Radical Scavengers to Improve the Durability of Fe–N–C Oxygen Reduction Catalysts. *Nat Energy* **2022**, *7* (3), 281–289. https://doi.org/10.1038/s41560-022-00988-w.

(3) Zhu, Y.; Zhong, H.; Wang, H.; Ouyang, L.; Liu, J.; Huang, Z.; Zhu, M. Breaking the Passivation: Sodium Borohydride Synthesis by Reacting Hydrated Borax with Aluminum. *Chemistry – A European Journal* **2021**, *27* (35), 9087–9093. https://doi.org/10.1002/chem.202100552.

(4) Zhu, Y.; Ouyang, L.; Zhong, H.; Liu, J.; Wang, H.; Shao, H.; Huang, Z.; Zhu, M. Closing the Loop for Hydrogen Storage: Facile Regeneration of NaBH4 from Its Hydrolytic Product. *Angewandte Chemie International Edition* **2020**, *59* (22), 8623–8629. https://doi.org/10.1002/anie.201915988.

(5) Zhong, H.; Ouyang, L.; Zeng, M.; Liu, J.; Wang, H.; Shao, H.; Felderhoff, M.; Zhu, M. Realizing Facile Regeneration of Spent NaBH 4 with Mg–Al Alloy. *Journal of Materials Chemistry A* **2019**, *7* (17), 10723–10728. https://doi.org/10.1039/C9TA00769E.

(6) Liu, B. H.; Li, Z. P.; Zhu, J. K. Sodium Borohydride Formation When Mg Reacts with Hydrous Sodium Borates under Hydrogen. *Journal of Alloys and Compounds* **2009**, *476* (1), L16–L20. https://doi.org/10.1016/j.jallcom.2008.09.057.

(7) Ouyang, L. Z.; Zhong, H.; Li, Z. M.; Cao, Z. J.; Wang, H.; Liu, J. W.; Zhu, X. K.; Zhu, M. Low-Cost Method for Sodium Borohydride Regeneration and the Energy Efficiency of Its Hydrolysis and Regeneration Process. *Journal of Power Sources* **2014**, *269*, 768–772. https://doi.org/10.1016/j.jpowsour.2014.07.074.

(8) Wu, Y.; Cell, M. Process for the Regeneration of Sodium Borate to Sodium Borohydride. 32.

(9) Lee, C.; Babu, S. K.; Mukundan, R.; Borup, R. L.; Spendelow, J. S. Groovy Electrodes Enable Facile O2 and H+ Transport in PEMFCs. *Meet. Abstr.* **2022**, *MA2022-01* (35), 1420. https://doi.org/10.1149/MA2022-01351420mtgabs.

Curriculum Vitae

Youngdon Ko
Email: youngdon.ko@epfl.ch, ORCiD: 0000-0001-5558-0258
Tel: +41 78 611 6781
Date of Birth: 26. November. 1992
Nationality: Republic of Korea

Education

Ph.D. **Chemistry and Chemical Engineering,** EPFL, Switzerland. 06/2019 – 03/2023

Advisor: Prof. Andreas Züttel

M.S. **Materials Chemistry and Engineering,** Konkuk university, Seoul, Korea. 03/2017 – 02/2019

Advisor: Prof. Wha Jung Kim

B.S. **Materials Chemistry and Engineering,** Konkuk university, Seoul, Korea. 03/2011 – 02/2017

Research interests

- **Hydrogen Storage and Utilization:** Investigating complex hydrides, metal hydrides, carbon-based materials for hydrogen storage. Utilizing hydrogen and borohydride by PEMFC and DBFC.
- **Oxygen Reduction Reaction and Hydrogen Peroxide Reduction Reaction:** Research on transition metal with nitrogen doped carbon (M-N-C) catalysts to replace the noble metal (Pt, Pd) in fuel cells.
- **eCO_2RR and CO_2 Adsorption for Valuable Chemicals:** Electrochemical CO_2 reduction reaction under the different surface properties and catalysts. CO_2 adsorption with destabilized borohydride.

Honors and Awards

- **Graduate Student Catalyst Research Award,** Catalyst Committee, The Korean Institute of Chemical Engineers, Korea. (2019.01)
- **Graduate School Chief Award,** Konkuk University, Korea. (2019.02)

Peer-reviewed Publications

1. **Y.D. Ko**, L. Kang, X. Zhang, V. Boureau, THM. Pham, C. Huu, L. Zhong[†], A. Züttel, Direct H_2O_2 Production via 2-electron Oxygen Reduction Reaction and Identification of Active Site on Co-N-C, *In preparation*.
2. **Y.D. Ko**, J. Park, X. Zhong, L. Kang, THM. Pham, V. Boureau, C. Huu, J. Kim, L. Zhong[†], A. Züttel, All platinum group metal-free catalysts using in liquid fuel operated direct borohydride fuel cells, *In preparation*.
3. **Y.D. Ko**, L. Lombardo, M. Li, THM. Pham, H.N. Yang, A. Züttel[†], Selective Borohydride Oxidation Reaction on Nickel Catalyst with Anion and Cation Exchange Ionomer for High-Performance Direct Borohydride Fuel Cells, *Advanced Energy Materials,* (2022) 2103539. (Cover image)

4. **Y.D. Ko**, L. Lombardo, M. Li, E. Oveisi, H.N. Yang†, A. Züttel, Interfacial Effect between Aluminum-Based Complex Hydrides and Nickel-Containing Porous Carbon Sheets, *ACS Applied Energy Materials*, 10 (2020) 9685-9695. (Cover image)

5. **Y.D. Ko**, W.J. Kim†, Effect of pH on the physical and electrochemical properties of Pt-hollow-structured TiO_2 and its self-humidifying ability in PEMFC, *, ACS Sustain. Chem. Eng., 6*, (2018) 17134-17141.

6. **Y.D. Ko***, H.N. Yang*, A. Züttel, S.D. Kim, W.J. Kim†, Membrane electrode assembly fabricated with the combination of Pt/C and hollow shell structured-Pt-SiO_2@ZrO_2 sphere for self-humidifying proton exchange membrane fuel cell, *J. Power Sources*, 367 (2017) 8-16. (* Co-first author)

7. H.N. Yang*, **Y.D. Ko***, W.J. Kim†, 3-D structured Pt/rGO-polyethyleneimine-functionalized MWCNTs prepared with different mass ratio of rGO and MWCNT for proton exchange membrane fuel cell*, Int. J. Hydrogen Energy*, 43 (2018) 4439-4447.(* Co-first author)

8. H.N. Yang*, **Y.D. Ko***, W.H. Lee, A. Züttel, and W.J. Kim†, Nitrogen-doped carbon black supported Pt–M (M= Pd, Fe, Ni) alloy catalysts for oxygen reduction reaction in proton exchange membrane fuel cell, *Materials Today Energy* 13 (2019) 374-381. (* Co-first author)

9. L. Lombardo, **Y.D. Ko**, K. Zhao, H.N. Yang†, A. Züttel, Direct CO_2 capture and Reduction to High-End Chemicals with Tetraalkylammonium Borohydrides, *Angewandte Chemie*, 17 (2021) 9666-9675.

10. M. Li, THM. Pham, **Y.D. Ko**, K. Zhao, L. Zhong, W. Luo†, and A. Züttel. Support-Dependent Cu–In Bimetallic Catalysts for Tailoring the Activity of Reverse Water Gas Shift Reaction. *ACS Sustainable Chemistry & Engineering* (2022).

11. THM. Pham, J. Zhang, M. Li, T. H. Shen, **Y.D. Ko**, V. Tileli, W. Luo†, and A. Züttel. Enhanced Electrocatalytic CO_2 Reduction to C_2^+ Products by Adjusting the Local Reaction Environment with Polymer Binders. *Advanced Energy Materials*, (2022) 2103663. (Cover image)

12. J. Zhang, THM. Pham, **Y.D. Ko**, M. Li, S. Yang, C. Koolen, L. Zhong, W. Luo, and A. Züttel. Tandem effect of Ag@ C@ Cu catalysts enhances ethanol selectivity for electrochemical CO_2 reduction in flow reactors. *Cell Reports Physical Science,* (2022) 100949.

13. M. Li, THM. Pham, E. Oveisi, **Y.D. Ko**, W. Luo†, and A. Züttel. Revealing the Surface Chemistry for CO_2 Hydrogenation on Cu/CeO_{2-x} Using Near-Ambient-Pressure X-ray Photoelectron Spectroscopy. *ACS Applied Energy Materials* 4, no. 11 (2021) 12326-12335.

Conference and Symposium

1. 14th International Symposium Hydrogen & Energy combined with 2nd International Symposium "Hydrogenomics", Sapporo, Japan (2020.01). (Poster presentation).

2. 2022 European Young Chemists' Meeting, online (2022.01). (Poster presentation).

3. Europe–Korea Conference on Science and Technology (EKC2022), Marseille, France (2022. 07). (Oral presentation).

4. Gordon Research Seminar – Fuel cells, (2022. 07), Bryant University, USA (Oral presentation).

5. Gordon Research Conference – Fuel cells, (2022. 07), Bryant University, USA (Poster presentation).

6. Future Materials, Rome, Italy (2022. 10). (Invited oral presentation).